

P2mix

Report No. 16568-6028-R000

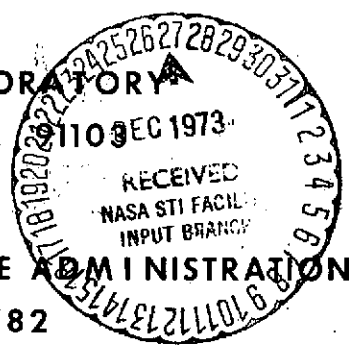
March 1973

STUDY OF ADVANCED TECHNIQUES FOR DETERMINING THE LONG TERM PERFORMANCE OF COMPONENTS

FINAL REPORT

Prepared for
THE JET PROPULSION LABORATORY
PASADENA, CALIFORNIA

Under
NATIONAL AERONAUTICS AND SPACE ADMINISTRATION
CONTRACT NAS 7-782



(NASA-CR-136199) STUDY OF ADVANCED
TECHNIQUES FOR DETERMINING THE LONG TERM
PERFORMANCE OF COMPONENTS Final Report,
14 Feb. 1972 - 14 Mar. 1973 (TRW
Systems Group) 249 p HC \$13.00 CACL 14D G3/15 Unclas
15850

225

N74-13193



ONE SPACE PARK • REDONDO BEACH • CALIFORNIA

FOREWORD

This report was prepared by TRW Systems Group, Redondo Beach, California, and contains the results of work accomplished during the period February 14, 1972 to March 14, 1973. The program was originated in May, 1970 and is managed by the Jet Propulsion Laboratory under the technical direction of Mr. George A. Yankura. An Interim Report was published in March 1972 and contains the results of the work accomplished during the period May 14, 1970 to February 14, 1972. The NASA Program Manager is Mr. William Cohen, Code RPT, Office of Aeronautics and Space Technology.

The work performed on the program was accomplished by the Applied Technology Division of TRW Systems Group. Technical direction of the program is provided by the Chemical Propulsion Department of the Combustion Systems Laboratory. The Program Manager is Mr. R. J. Salvinski. Responsible technical personnel who supported this program are acknowledged in the following:

Mr. H. Baggenstoss	Reliability Assurance
Mr. R. Costello	Reliability Assurance
Mr. N. Doshi	Metrology Department
Mr. F. Muenzer	Product Design & Analysis Department
Mr. D. Pearson	Materials Research Staff
Mr. R. N. Porter	Chemical Propulsion Department
Mr. J. L. Reeve	Product Design & Analysis Department
Mr. J. L. Reger	Materials Research Staff
Mr. T. V. Roszhart	Materials Research Staff

Further acknowledgement is made to the personnel of the School of Chemistry, University of Bradford, who were responsible for investigating the surface properties of Engineering Materials. Professor M. W. Roberts, B.Sc., Ph.D., D.Sc., F.R.I.C. and Dr. J. R. H. Ross, B.Sc., Ph.D. directed the research. The experimental work was carried out by Dr. W. J. Murphy, B.Sc., Ph.D., S. Frost, B.Tech. and J. A. Morris, B.Tech., all of whom were graduate students working for their Ph.D. degrees.

CONTENTS

	Page
1.0 INTRODUCTION, SUMMARY & CONCLUSION	1-1
1.1 General	1-1
1.2 Purpose of Program.	1-2
1.3 Technical Approach.	1-2
1.4 Interim Report.	1-5
1.5 Summary	1-8
1.6 Conclusions	1-8
2.0 METAL VALVE SEAL DESIGN FOR LONG TERM PERFORMANCE.	2-1
2.1 Introduction.	2-1
2.2 Technical Approach.	2-1
2.3 Performance Prediction of a Metal Valve Seat.	2-2
2.4 Development of a Long Life Metal Valve Seal	2-12
2.4.1 Requirements	2-12
2.4.2 Sealing Stress Requirements.	2-12
2.4.3 Analyses of Contained Metal Seal - Bulk Compression.	2-16
2.4.4 Metal Seat Design Configuration.	2-16
2.4.5 Testing Appartus	2-20
2.4.6 Test Description and Test Results.	2-21
3.0 METHODS OF ANALYSIS, CORRELATION AND PREDICTION.	3-1
3.1 Introduction.	3-1
3.2 Time Correlation Method	3-4
3.3 Dimensional Analysis Method	3-5
3.4 Weiner Analysis of Signatures	3-10
4.0 THERMAL CONTACT STUDY.	4-1
4.1 Conclusions and Recommendations	4-1
4.2 Summary of Previous Investigations.	4-3
4.3 Derivation of Equations Used in Contact Thermal Resistance Analysis	4-7
4.4 Determination of Contact Spot Radius C.	4-10
4.5 Determination of Void Volume.	4-13
4.6 Referenced Test Data Analysis	4-14

CONTENTS (CONTINUED)

	<u>Page</u>
4.7 More Recent Thermal Resistance Measurements	4-17
4.7.1 Description of Test Specimens.	4-17
4.7.2 Sensors.	4-19
4.7.3 Test Setup Description (preliminary Tests) . . .	4-20
4.8 Preliminary Test Results.	4-25
4.9 Modification of Test Setup.	4-27
4.10 Thermal Time Constant.	4-29
4.11 Test Results	4-30
4.12 Discussion of Test Results	4-32
4.13 Modification of the Thermal Conductance Experiment Using the Transient Thermal Resistance (TTR) Measurement . .	4-35
4.14 TTR Technique Improvements	4-54
5.0 COHERENT OPTICAL SIGNATURES OF MATERIAL SURFACES	5-1
5.1 Introduction.	5-1
5.2 Coherent Optical Signatures of Surfaces	5-2
5.3 Application of Coherent Optical Signature Technique to the Long Term Performance Valve Seat Development (See Section 2.0).	5-7
5.3.1 Testing Apparatus.	5-11
5.4 Conclusions	5-13A
6.0 FLOW TRANSIENT SIGNATURE STUDIES	6-1
6.1 Introduction.	6-1
6.2 Description of Appartus	6-1
6.2.1 Valve Test Station	6-1
6.2.2 Electronic Instrumentation	6-6
6.3 Results	6-8
6.3.1 Flow Volume Versus Time Signatures	6-8
6.3.2 Flow Rate Versus Time Signatures	6-14
6.4 Fluid Leak Measurement.	6-22
7.0 SURFACE STUDIES.	7-1
7.1 Introduction.	7-1
7.2 Surface Compatibility Study	7-1

CONTENTS (CONTINUED)

	<u>Page</u>
7.2.1 Experimental	7-2
7.2.2 Results and Discussion	7-3
7.2.2.1 Electrolytically Polished Surfaces	7-3
7.2.2.2 Inconel Samples.	7-3
7.2.2.3 Untreated Mechanically Abraded Samples	7-5
7.2.3 Conclusions.	7-11
7.3 Surface Energy and Wetting Studies of Solids.	7-11
7.3.1 Appraisal of the Relationships Between Surface Energy and the Physical Properties of Materials.	7-11
7.3.1.1 Mechanical Interaction of Solids	7-12
7.3.1.2 Quantitative Description of Adhesive Wear.	7-14
7.3.1.3 The Roughness Factor in Metal to Metal Contacts	7-19
7.3.2 Experimental Studies and Some Conclusions.	7-19
7.3.2.1 Determination of the True Value of γ Solutions	7-19
7.3.2.2 Determination of the Butanol Adsorption Isotherm for the Solid-Liquid Interface.	7-24
7.3.2.3 Conclusions and Suggestions for Further Work	7-25
7.4 Auger Spectroscopic Study of the Surfaces of Inconel.	7-28
7.4.1 Introduction and Experimental.	7-28
7.4.2 Results and Discussion	7-28
8.0 NEW TECHNOLOGY	8-1
8.1 Zero Leakage Metal Valve Seat for Long Term Performance	8-1
8.2 Measuring Surface and Interface Topology by Thermal Contact Resistance. Section 4.0.	
8.3 Optical Signature of Metal Valve Seat Surfaces. Section 5.0	8-1
8.4 Flow Transient Signature Technique. Section 6.0.	8-1
8.5 Fluid Leakage Measurement. Section 6.0	8-2
8.6 Contact Angle Measurements to Examine Surface Compatibility. Section 7.0	8-2

1.0 INTRODUCTION, SUMMARY AND CONCLUSIONS

1.1 GENERAL

Components which must operate over a long period of time have been the concern of designers for many years. Better designs have evolved through natural selection of materials based on operational results and because of examination and investigation of the failure process. In most cases real-time testing is simply the exposure of the equipment to its service environment. Now engineers are faced with designing equipment which must operate in the space and planetary environments over long mission durations without the benefit of real-time test support data. Long-term space missions presently planned include the unmanned planetary exploration missions of up to 15 years duration. The manned earth orbiting space shuttle is planned for 10 year service life.

There is a significant difference between these missions. In the case of the unmanned planetary missions the component cannot be examined, maintained or repaired during its operational life. The space shuttle, on the other hand, will return to an earth base periodically allowing equipment to be examined, maintained and repaired prior to the next launch. The problems with insuring long service life for components used in the planetary mission equipment are therefore more severe. One possible solution is the development of teleoperators which can perform certain maintenance, repair and replacement functions aboard the unmanned spacecraft. Other solutions include developing new techniques for determining the long-term performance of equipment. The latter approach is the subject of this document.

1.2 PURPOSE OF PROGRAM

The purpose of this program is to explore the application of existing and new technology to the problem of determining the long-term performance capability of liquid rocket propulsion feed system components. Results of this work should also enhance the understanding of the mechanisms contributing to component deterioration and thereby provide an improved datum for evaluating present and future component designs, and should provide the basis for techniques which could be utilized to verify

the long-term performance capability of hardware.

Probably the most failure sensitive feed system components are the valves. The use of reactive propellants such as liquid fluorine are planned for future propulsion systems and only metal seats are suitable materials under these extreme conditions. The most critical requirement is maintaining zero leakage (10^{-7} scc/sec) using metal valve seats. Therefore the major effort of this program is investigating the long-term performance of metal to metal valve seats.

1.3 TECHNICAL APPROACH

Two main approaches were taken. One approach was simply that of advancing the technology of characterizing components through the development of new or more sensitive measurement (signature) techniques. This approach is based on the premise that one cannot further the understanding of something without being able to measure it. The second approach is directed toward improving the understanding of the physical process of degradation.

The first approach should lead to improved methods for qualifying or acceptance testing of components. The second approach should evolve knowledge of failure processes which can be used to design and build better components. Both approaches are intimately linked, for it is detection and knowledge of the failure mechanism which leads to the better design, and conversely, the more reliable the hardware, the more sensitive the degradation detection method must be to determine its unreliability.

A mechanical part can fail its intended function by either a failure in the bulk material or by failure of a surface. A relatively large amount of technical study has been focused on the bulk properties of materials, while little effort has been devoted to the understanding of surfaces. Surface degradation probably represents the most frequent cause of service failures in mechanical components. Therefore, this study was devoted to the behavior of surfaces and their influence on performance degradation. Determining degradation of a surface was examined in a specific application to a metal-to-metal valve seat.

Laws describing the aging mechanisms must be evolved before prediction of component performance can be made. Hopefully developing better measurement techniques and better understanding physical degradation mechanisms will lead to achieving these goals. An apparent problem is how to use the information that is generated. The flow diagram of figure 1-1 illustrates how test information might be used in characterizing valve performance.

The diagnostic and characterization plan depicted in figure 1-1 is not greatly different from presently used qualification testing methods. The component is cycled, measurements made and the performance noted. The feedback portion of the flow diagram depicts the input of aging stimuli similar to the present method of imposing thermal and vibration environments on a component and noting a change in performance.

The important developments to be made lie in three of the areas represented by the block diagram of figure 1-1. These are 1) signature analysis, 2) accelerated aging stimuli, and 3) understanding the aging mechanisms and their affects on the component performance. For example, increasing temperature has been used as an aging stimuli; however neither the affect of temperature on the aging mechanism or the time/temperature correlation is well known.

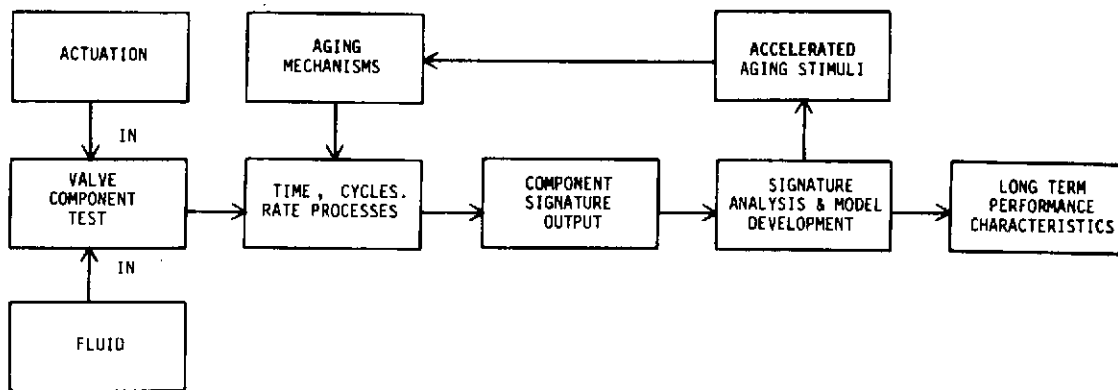


Figure 1-1 Component Diagnostic and Characterization Flow Diagram

Some progress has been made in evaluating and predicting performance by the technique of characterization (signature) of the component, exemplified by the recent application of acoustic signature analysis. By recording component signatures, noting and evaluating any changes in the signatures and correlating these changes to normal operating signals, the condition of the component is measured. For example the optical tracking of a fluid segment moving through the inlet tube on valve opening and closing can be used to characterize valve transient performance. Any change in the flow transient signature is caused by a change in some part of the valve component or actuation unit. This optical technique was developed under this program and is reported in Section 6.0. Other measurements may be necessary to determine the cause of the change, such as the measurement of actuator voltage.

One study made by the military, after World War II, indicated that 43% of equipment failures were due to poor design, 20% were traceable to manufacturing errors, 30% were the result of field conditions and only 7% were due to wearout and other failures. A study of automotive recalls concluded that over 60% of the defects were traceable to faulty design (Ref. 1). This information suggests that any long-term performance evaluation technique will be more effective if it is oriented heavily toward determining the efficacy of the design. Unfortunately only a few design criteria for long-term components are presently available. An effort was made in this program (see Section 2.0) to establish design criteria in a selected area and show how this criteria was used to design a long life metal valve seal.

One such long life design criteria relates to the rate of corrosion. Material compatibility with liquid chemical rocket propellants is of major concern, but an extensive treatment was outside the scope of this program. Results of a limited effort in characterizing surfaces for corrosive degradation is reported in Section 7.0. The reader is referred to work by Boeing (Ref. 2.0) for a more extensive investigation of materials compatibility for long life components.

1.4 INTERIM REPORT

This final report represents a continuing effort under NASA Contract NAS 7-782 during the period February 1972 to March 1973. Results of the program study from May 1970 to February 1972 are reported in the Interim Report (Ref. 3). The interim report contains the results of a survey and review of technologies, valve leakage studies, diffusion tests, acoustic signature study and surface compatibility studies.

The survey and review of technologies provided information on which the efforts of this program was based. Currently used methods of testing components were identified, including accelerated testing techniques and several signature techniques.

A mechanisms effects study was also performed for the purpose of defining the mechanisms which may cause component failure, with emphasis on valve seat leakage. An analysis of valve seat leakage as a function of surface finish was made and a correlation between surface finish and wear theory was attempted.

Accelerated diffusion testing was made at elevated temperature between beryllium copper and inconel. The results of the diffusion tests indicate this method to be a promising one for determining metal interface degradation of valve seat surfaces which are to be in contact for long durations.

An acoustic signature study was undertaken to determine its use for measuring real contact at a metal interface. The results of this effort led to the thermal contact study reported in Section 4.0 of this report.

1.5 SUMMARY

The results of the efforts reported herein represent four areas of study. A major effort was devoted to developing techniques to characterize component performance and some efforts were made toward understanding physical and chemical mechanisms. Analytical techniques were investigated which could be useful in evaluating and predicting component performance. A major development in the program was the analysis, design, fabrication and test of a zero leakage metal valve seal for long life use. Following is a brief summary of each section topic.

Metal Valve Seal Design For Long Term Performance

The long term performance of a zero leakage metal valve seat configuration was studied and the results showed that increasing roughness of the metal surfaces by wear would result in leakage increasing to unacceptable limits. A new technique in metal valve seat design was developed which avoided the normal primary failure mechanisms of wear, fatigue, contamination and stress. A metal valve seal designed to refurbish its metal surface while preventing material strain along each of the three axes was fabricated and tested. Zero leakage (10^{-8} scc/sec He) after 30,000 cycles successfully demonstrated this method for achieving long term performance.

Methods of Analysis, Correlation and Prediction

Current analytical methods used to evaluate and predict the performance of components were reviewed. Time correlation and dimensional analysis methods were investigated. A Wiener analysis of signatures was reviewed in detail and appears to offer a valuable technique in characterizing the performance of components. Two examples of this technique are given. The first is the identification of the process dynamics involved in a steel cold rolling mill. A second example describes the use of the Wiener analysis of a neuron chain, a complex highly nonlinear system and compares the procedure to characterizing valve flow transient signatures.

Thermal Contact Resistance

The dependence on thermal contact resistance of the surface roughness of two flat surfaces in contact was investigated. One of the degradation parameters of a valve which can be detected using this measurement technique is the surface roughness of the valve poppet and seat. The valve leakage is a function of the surface roughness of the poppet and seat surface. Analysis and test results indicated that the thermal resistance measurement can be employed to determine the valve seat/poppet surface degradation on a real time basis. The method would require built-in thermal sensors within the valve. A roughness change as small as 2 rms was detected using this technique.

Coherent Optical Signature of Material Surfaces

The feasibility of an optical signature to characterize surface roughness was demonstrated. The optical technique is based on the use of a coherent wavefront which is diffracted by the material surface. The diffracted light strikes a photocell and an electrical output is recorded on an x-y plotter. A HeNe laser was used as the source light. Surface rms roughness measurements as small as 0.5 rms are believed possible. A surface roughness of 2 rms was monitored using this technique in support of the long term performance metal valve seat development study.

Flow Transient Signature Studies

A highly accurate flow transient signature technique was developed and used to characterize a high response shutoff valve. This was accomplished using an Optron electro-optical strain monitor to measure the movement of a light-dark fluid interface upon valve opening and closing. Data acquisition at the rate of 500 bits during a 2 millisecond transient is contemplated. Valve leakage measurement also was demonstrated using the same optical tracking methods; leakage resolution as low as 7.5×10^{-8} scc/sec alcohol was demonstrated in the laboratory setup.

Surface Studies

Surface studies were conducted through a university grant with the objective to examine the use of contact angle measurements for monitoring changes of surfaces exposed to specific environments. The results of this research indicate that the technique of contact angle measurements can be useful in determining the reactivity of various liquids with metal surfaces. Also the use of contact angle and adsorption measurements were examined as a possible method of determining the work of adhesion in a two material system.

1.6 CONCLUSIONS

The technical efforts expended under this program resulted in the development of several new measurement techniques and an exploratory examination of analytical and research methods. A unique design approach avoiding the more common failure mechanisms proved highly successful in the development of a zero leakage, long life, metal valve seat.

These efforts, however, do not represent a conclusion to the problems of long term performance prediction. The technology of component performance prediction is far from the level of maturity required for general application.

Current investigations of long life prediction techniques represent more a probing rather than a decisive technology. Designing to avoid failure such as exemplified in Section 2.0, will most likely remain the more common approach to the long life problem. Developing aging laws and gaining more insight into the physics of failure mechanisms should play an important role in future studies directed toward determining the long term performance of components.

1.7 REFERENCES

1. R. J. Salvinski, et al, STUDY OF ADVANCED TECHNIQUES FOR DETERMINING THE LONG TERM PERFORMANCE OF COMPONENTS. TRW Intrim Report No. 168-68-6-14-R000, March 1972.
2. MACHINE DESIGN. March 22, 1973, p. 196.
3. R. L. Green, ADVANCED TECHNIQUES FOR DETERMINING THE LONG TERM COMPATIBILITY OF MATERIALS WITH PROPELLANTS. NASA Contract NAS 7-789, Boeing Aerospace Co., Seattle, Wash. (Final Report to be published)

2.0 METAL VALVE SEAL DESIGN FOR LONG TERM PERFORMANCE

2.1 INTRODUCTION

Liquid rocket propulsion system requirements for long term (to 10 years) missions dictate extremely low leakage requirements. The use of highly reactive propellants restricts the material choice to all metal systems. The major impact of the metal seat design constraint is in meeting the zero leakage (10^{-6} scc/sec He) requirements. The major objective of this task is to determine the long term performance of metal valve seats developed within the present technology and to evolve new technology in metal sealing techniques which will enable the valve components to meet the long term requirements.

2.2 TECHNICAL APPROACH

Failure of metal valve seals to meet zero leakage is possible by one or more of the following mechanisms.

- a. Wear
- b. Contamination
- c. Fatigue
- d. Stresses (tension, compression, shear)
- e. Corrosion (long term compatibility with propellants)
- f. Material Transport (adhesion, diffusion)

Metal valve seals are typically finished to approximately a 2 rms ($\approx .05$ micron) surface and for the flat configurations to better than $1/4$ ($\approx .20$ micron) wavelength of monochromatic light. A major factor in degradation of the finish is wear which can roughen the surface after repeated cycles. Contamination is also a serious failure mode especially because metal seals cannot envelope particles where elastomers can. Fatigue and stress failures are not usually serious where sufficient cyclic testing can be accomplished within reasonable time constraints. However, fatigue and stress failures may occur due to synergistic effects; mainly corrosion (oxidation/reduction). These effects are time dependent and are not easily accounted for in cyclic testing typically conducted over a period of only a few weeks or less.

The approach normally taken for proving component capability for long term requirements is to test to failure within short durations by accelerated testing. Long term performance is then based on judgment of the test results. Cyclic testing fits this method of determining performance. The more complex failure modes which are time dependent are not easily recognized or tested for. Possibly the solution to the problem is understanding the failure mechanisms followed by a more creative design approach.

The simplest solution may be to eliminate the failure mechanism. For example, if a structural tension member is subject to failure, how can failure be avoided? In prestressed members (in compression) tension is indeed eliminated within the compression prestressed range.

The scope of the effort reported in this section will concentrate on elimination of the major failure mechanisms of a metal valve seat; that is, the effects of wear and contamination, fatigue and the primary stresses. The reader is referred to work performed by Boeing under NASA Contract NAS 7-789 regarding long term material compatibility (Ref. 1) and the work carried out under this program on metal interface diffusion and reported in the Interim Report (Ref. 2).

2.3 PERFORMANCE PREDICTION OF A METAL VALVE SEAT

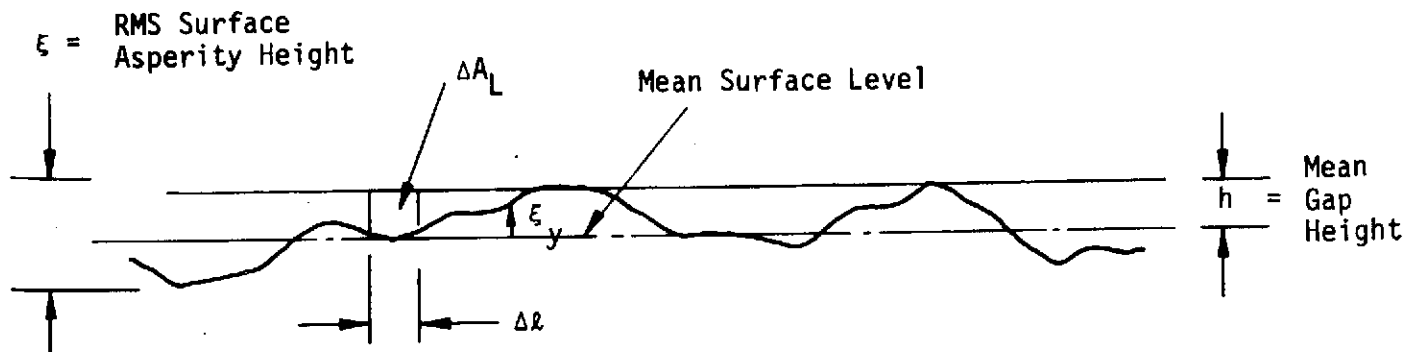
The derivation of the leakage area of a flat annular interface is reported in the Interim Report (Ref. 2). The leakage equation is based on a perfectly rigid flat surface which is in contact with a deformable surface having random surface irregularities.

The equation for the average leakage area is:

$$A_L = \epsilon \ell \left\{ (2\pi)^{-1/2} e^{-h^2/2\epsilon^2} + \frac{h}{2\epsilon} \left[1 + \operatorname{erf} \left(\frac{h}{\sqrt{2} \epsilon} \right) \right] \right\} \quad (2-1)$$

where: A_L = leak area
 ℓ = circumferential length of contact area
 ϵ = rms surface asperity height
 h = gap height between mean surface level and contacting surface
 erf = error function

and:



This equation is plotted in Figure 2-1 in terms of a dimensionless leak area as a function of a dimensionless gap.

The limiting value for $A/\Delta R \xi$ of Figure 2-1 as h/ξ approaches zero is due to the constraint that the approach and contact cannot exceed the mean surface level. Figure 2-2 is a plot of the leak rate of helium as a function of the differential pressure across the two surfaces for a given surface finish and gap height. The valve seat diameter was chosen as 0.050 inch as representative of valves used on small engines. Molecular flow with a small path entrance was assumed as the dominating leak mechanism. For other seat diameters the leakage values must be multiplied by $D/.05$ where D is the diameter of the other seat.

Equation 2-1 and its representation in Figure 2-1 and 2-2 are based on analytical techniques; however, the data appears to be representative of current metal seal leakage. The curve of Figure 2-2 then gives the leakage value at the first cycle. What is the leakage after 10 cycles or 1000 cycles? To answer this question the change in h and ξ as a function of cycles must be known.

One approach to determining the change in ξ is to relate the surface asperity height to the wear particle size which is characteristic of the material in a given environment. Wear particle generation is a function of certain properties of the materials in contact and their surface finishes.

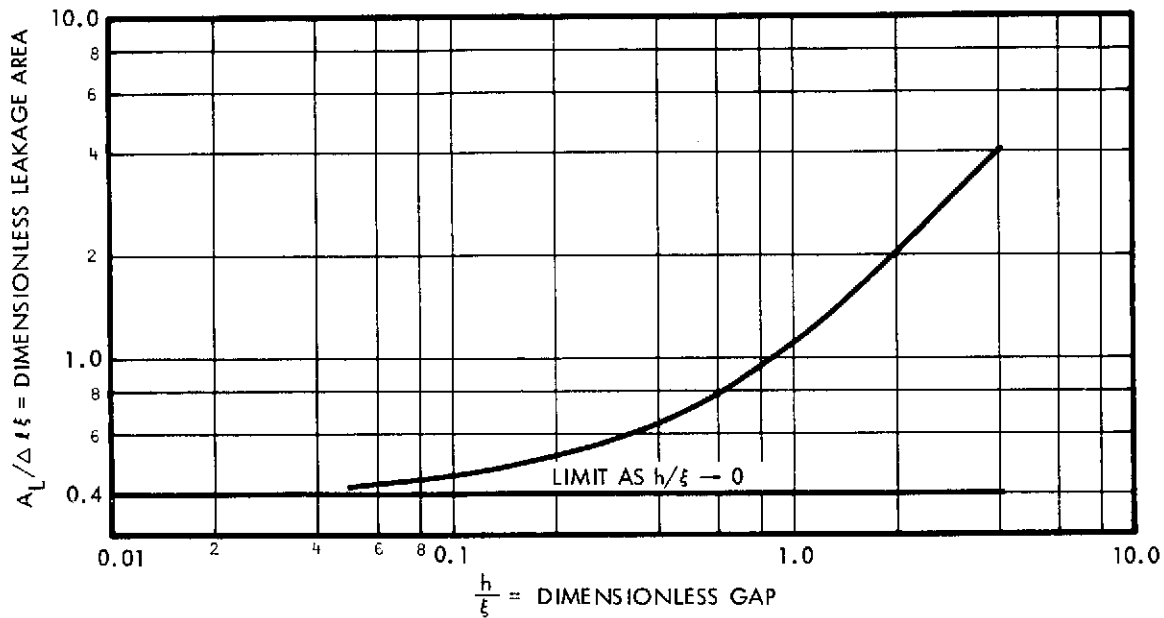


Figure 2-1. Dimensionless Area Vs. Gap

The relationship between wear particle size and adhesive energy has been developed by E. Rabinowicz (Ref. 3) at MIT and is given by the following equation:

$$d = 60 E W_{ab} / \delta_{yp}^2 \quad (2-2)$$

where: d = the average diameter of the wear particle

E = Young's modulus

δ_{yp} = yield stress of the material in compression

W_{ab} = the work of adhesion of the materials a & b in contact and is further defined as:

$$W_{ab} = \gamma_a + \gamma_b - \gamma_{ab} \quad (\text{see Section 7.3.1.2})$$

where: γ_a = surface free energy of material a per unit area

γ_b = surface free energy of material b per unit area

γ_{ab} = interface free energy per unit area.

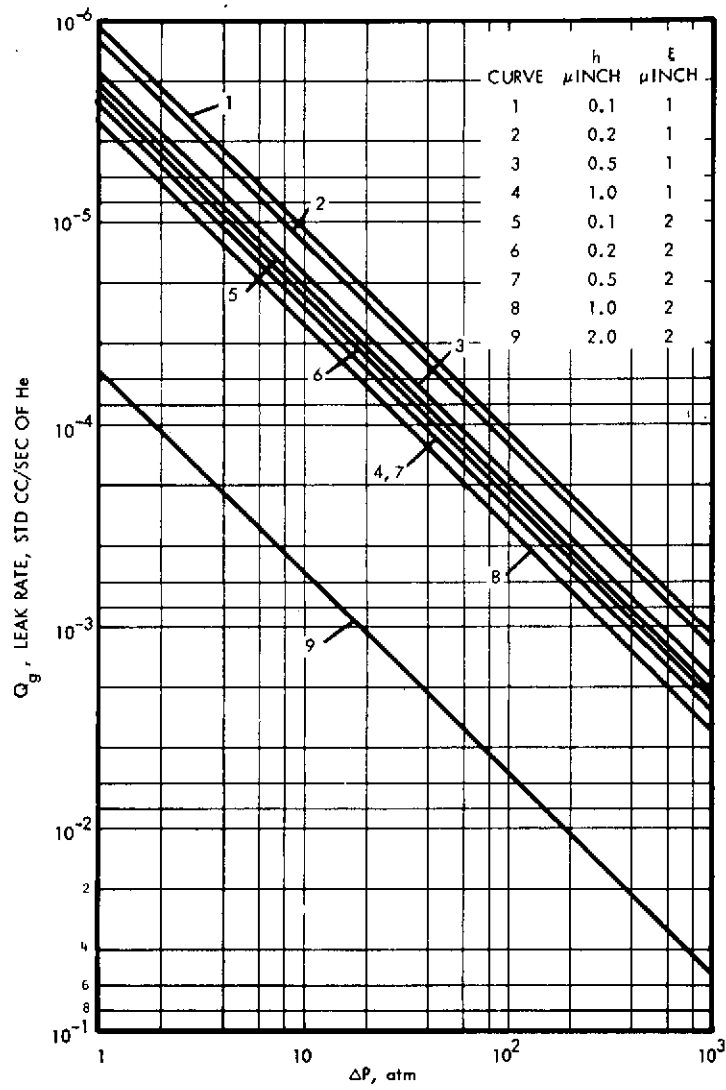


Figure 2-2. Leak Rate Vs. ΔP For Different Finishes

It has been found that δ_{yp} is about one-third the hardness P and that δ_{yp}/E is about 3×10^{-3} for many materials, then:

$$d = 60,000 W_{ab}/P \quad (2-3)$$

Experimental results showing the relation between material and the average wear particle diameter obtained by E. Rabinowicz are presented in Table 2-1.

Table 2-1. Average Wear Particle Size Under Ambient Atmosphere for Different Materials

Metal	P $\frac{\text{dynes}}{\text{cm}^2}$	W $\frac{\text{ergs}}{\text{cm}^2}$	d cm
Lead	4×10^8	440	270×10^{-4}
Tin	6	540	120 "
Bismuth	12	375	50 "
Cadmium	23	600	320 "
Aluminum	30	900	140 "
Zinc	30	750	440 "
Copper	60	1100	250 "
Brass	120	700?	180 "
Mild Steel	200	1000	60 "
Iron (Oxide)	2000?	600?	1 "
Aluminum (Oxide)	2000	900	1 "
Teflon	4	15?	90 "
Nylon	20	30?	? "
Silver	80	920	330 "
Nickel	260	1650	35 "
Glass	550	200?	1 "

Another assumption made is that the wear particle size generated at any given cycle is equal to the surface finish or mean asperity height characterized by the surface of the softer material.

The wear particle size d given by the above equation is the equilibrium size. That is, the particle tends to a certain size and remains at that size. Also the surface finish will generate to a finish equal to the equilibrium size. This equilibrium surface is then the final surface characterized after "wear in", independent of the initial surface condition. In most cases, a valve seat finish is initially, when fabricated, very fine, ranging about 2 rms. If we assume an initial surface finish of .05 microns (2 rms) and using an iron oxide surface model it can be seen the average wear particle will eventually "wear in" to 1.0 micron. The corresponding finish will be 40 rms. For a valve seat this is a severely rough surface and leakage would be considered gross. Conversely if the surface finish is coarser than the average equilibrium wear particle size the surface will become less coarse during wear-in.

What needs to be known is the change in wear particle diameter as a function of cycles. The loss of a tolerable surface may occur due to a cycle "wear in" of too few a number relative to the life usefulness of the valve.

It is important to consider the effect of the reactivity of the environment on the wear particle size. Indications are that the more reactive the environment the smaller will be the equilibrium wear particle. This effect is illustrated in Table 2-2 with copper-copper surfaces and wear particles developed in various environments. In vacuum the wear particle would be expected to be quite large. For a reactive propellant such as fluorine or oxygen difluoride the wear particle should be smaller than those listed in Table 2-1. However, for the fuels such as diborane the wear particle size should be greater, indicating a better leakage performance characteristic of metal valve seats for the oxidizer over the seats used with the fuel.

The design implications of the foregoing analysis are apparent. The use of harder seat materials will result in smaller wear particles and subsequently the wear process will ultimately result in less coarse

finishes. By selecting a seat material with a characteristic small wear particle size it should be possible to predict the final surface finish after N cycles.

Table 2-2. Effect of Environment on the Average Wear Particle Size

<u>Environment</u>	<u>Average Particle Diameter Copper-Copper Surfaces Micrometers (μ)</u>
Nitrogen	480
Helium	380
Carbon Dioxide	300
Dry Air	224
Oxygen	201
Laboratory Air	177
Wet Air	144
Cetane	12
Silicone DC 200-100 cst.	9.5
Ucon Fluid LB-70X	9.5
Palmitic Acid in Cetane	8.0

If the surface finish is approximately equal to the wear particle size for a given seat material combination then prediction is easily obtained. However, it appears that surface roughness can be much smaller than the average wear particle size reported in Table 2-1. Therefore, the initial performance of the valve seal should be better than at "wear-in." It remains to develop a relation between wear particle size as a function of cycle life. In addition, the equilibrium wear particle size of a material exposed to the propellant needs to be determined.

Surface roughness and wear particle generation criteria are valid for the leakage model only when the surfaces at the interface conform in curvature (or flatness) within the dimensions of the minimum surface roughness. If the non-conformity is greater than the surface roughness, the dominant leakage path will be the gaps produced by the non-conformity and the leakage will undoubtedly be much higher than predicted by the model. This design implication favors the use of flat surface geometry for seats which can be most easily fabricated to a high degree of conformance with present day fabrication techniques. Thin elastic seats such as the lip seal can appear to conform to the poppet, however, the conformity on a micro level is not well known.

An example of the analyses that may be applicable to predicting surface roughness vs number of cycles is given in the following.

An expression for the number of cycles to equilibrium would relate the number of asperity junctions (point of contact) which must be destroyed (or created) to equal one junction of the same area at equilibrium. This analysis assumes the real area of contact is always constant.

$$A_r = \frac{\pi d_i^2}{4} N_i = \frac{\pi d_e^2}{4} N_e \quad (2-4)$$

$$N_i = \frac{d_e^2}{d_i^2} N_e \quad (2-5)$$

where N is the number of junctions and d is the average diameter of the loose particles generated. The subscripts i and e represent the i th cycle and equilibrium state, respectively.

The total adhesive energy for a given set of junctions is:

$$W = \frac{d P}{60,000} N \quad (2-6)$$

The adhesive energy required to change N_i junctions of average diameter d_i to N_e junctions of average diameter d_e is:

$$\Delta W = \frac{d_i P}{60,000} \frac{d_e^2}{d_i^2} N_e - \frac{d_e P}{60,000} N_e \quad (2-7)$$

Assuming only one junction at equilibrium, then:

$$\Delta W = \frac{P}{60,000} \frac{d_e}{d_i} (d_e - d_i) \quad (2-8)$$

Further assuming that an equal adhesive energy is used to create a single wear particle per cycle, then:

$$C_e = \frac{\frac{d_e}{d_i} (d_e - d_i)}{d_i} = \frac{d_e}{d_i} \left(\frac{d_e}{d_i} - 1 \right) \quad (2-9)$$

where C_e is the number of cycles to create an equilibrium wear particle.

Taking d_e to be 2.0μ and d_i to be $.05\mu$

$$C = 40(39) = 1,560 \text{ cycles}$$

The reader is cautioned that this analysis is based on gross assumptions that have not been verified by test and is intended to be illustrative of methodology only.

It is useful to plot a relationship between wear particle diameter and cycles. Figure 2-3 is a plot of these parameters based on the above analysis, however, C_e and d_e are now taken to be C_n and d_n where:

C_n = number of cycles to develop d_n and

d_n = diameter of wear particle at n cycles

From Figure 2-2 and Figure 2-3 the initial (1st cycle) leakage can be determined by relating d_i to ξ . The equality of d to ξ is admittedly crude; however, any difference between the two quantities cannot be great since the creation of a wear particle must under equilibrium conditions be closely representative of the surface finish. An important variable is the gap height h of Figure 2-2. h will depend on the interfacial bearing stress applied between the two surfaces. It is conceivable h may be as small as .1 to .5 of ξ depending on the bearing stress. The bearing stress will also determine the real area of contact or number of asperity junctions formed which will influence the effect of equation 2-9 on the cycle life vs. leakage.

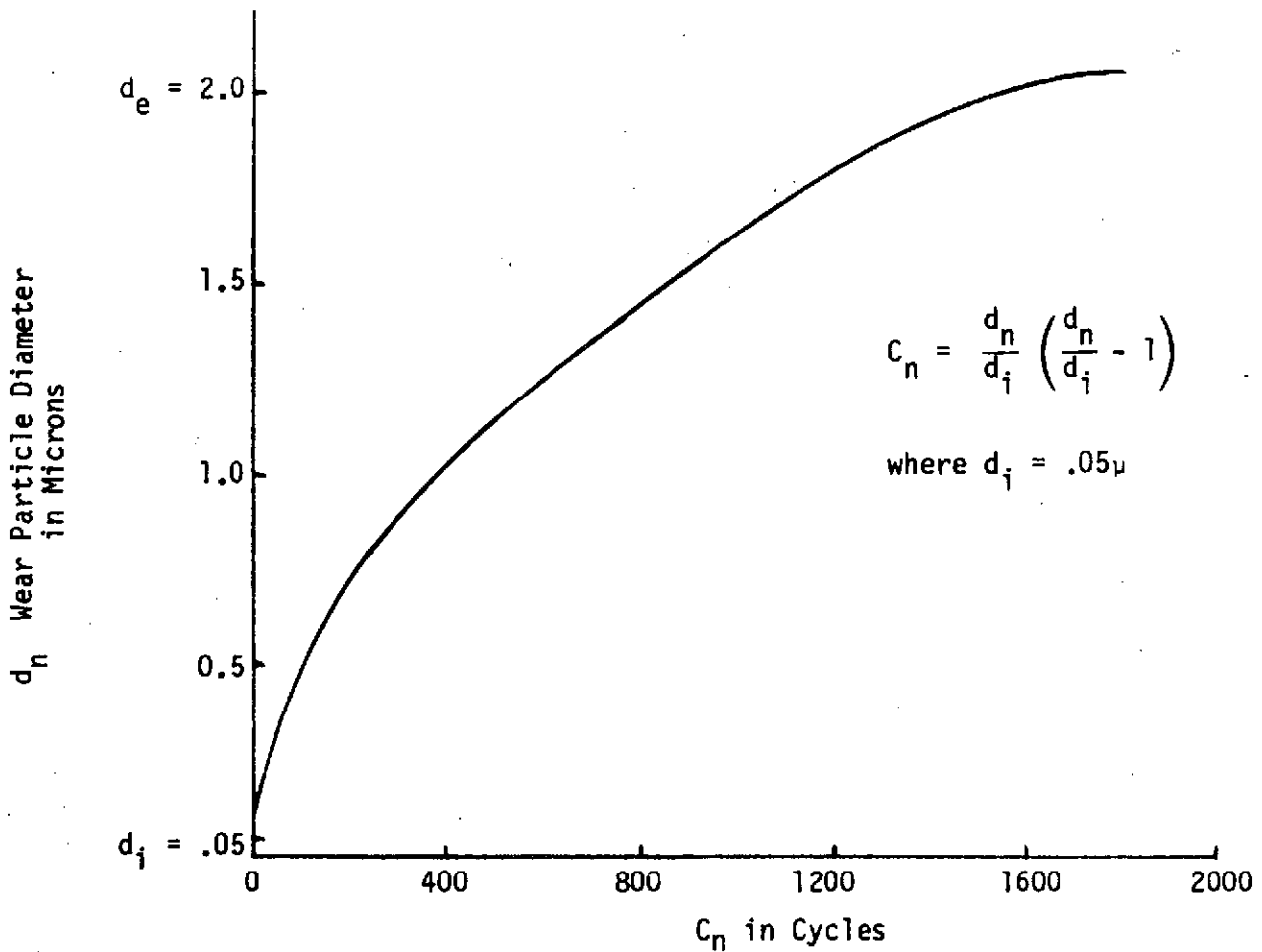


Figure 2-3. Estimated Wear Particle Diameter As a Function of Cycle Life

Assuming all asperities at the valve seat interface are in contact, then it is estimated from Figures 2-2 and 2-3 that leakage will degrade from about 10^{-5} to $<10^{-3}$ ($\Delta P \approx 10$ ATM) within a few cycles corresponding to a surface finish degradation from 2 microinches to about 4 microinches.

Minimizing surface finish degradation during wear based on wear particle size, suggest selecting hard materials which have the smallest equilibrium wear particle size. As can be seen from Table 2-1 the hardest material particles are about 1 micron ($\approx 40 \times 10^{-6}$ inches) in ambient air, which at equilibrium result in rough surfaces. The effect of the liquid propellant on the size of the particle is a decrease in size in oxidizers and an increase in size in reducing fuels.

2.4 DEVELOPMENT OF A LONG LIFE METAL VALVE SEAL

2.4.1 Requirements

A multicycle isolation valve exhibiting zero leakage was selected for the long life study. The valve is to be used on a liquid rocket engine and must operate reliably for up to 10 years. Leakage requirements are 10^{-6} scc/sec of the propellants which are Flox/MMH or fluorine/hydrazine. This valve is presently being developed by JPL in support of an outer planetary mission program.

The actual cycle requirement of the isolation valve is less than 50 cycles. It is desirable, however, to obtain 1000 cycles in test for purposes of assuring a reliability margin.

The analysis performed in Section 2.3 would indicate that zero leakage cannot be sustained for the required number of cycles. In addition, the effects of time dependent mechanisms such as fatigue, stress and propellant compatibility are unknown.

The valve seal design and design requirements provided here are taken from Reference 4, which reports the results of the isolation study program conducted for JPL.

2.4.2 Sealing Stress Requirements

One method of eliminating the influence of wear on surface finish would be to refurbish the seat surface at each cycle. This could be accomplished by coining, using a hard poppet impacting a softer seat. The problem with repeated coining is the flow of the softer material at the edges of the interface. This is avoided by containment of the soft seat material. Containment also restricts plastic strain.

Empirical design practice for hard on hard metal valve seats and static metallic gaskets commonly dictates a seating stress of two to three times the compressive yield stress of the softer material to achieve low leak rates (Ref. 5, p. 6.3.2-6). Plastic metal working theory was applied to the problem of forcing a soft plastic material into the microscopic asperities of a hard elastic material. These stress models were originally developed by the metalworking industry to predict the pressures required to force blanks into hard dies, but should apply as well on the microscopic level as the geometric parameters they contain are non-dimensional. Cyclic work hardening and oxide and fluoride films might increase the effective yield stress of the soft material at its surface, which would be of interest in predicting asperity conformance. In metal working practice the material is deformed a distance equal to many times the thickness of surface films, so the yield stress of the bulk material may be used.

The predictions of two separate plasticity models are summarized in Figure 2-4. Here a random asperity contour is idealized to a sawtooth pattern of opening angle 2α . When the two sealing surfaces are brought into light contact, the hard material has asperities of effective depth of $2h$ NO LOAD.

As the mean contact stress is increased to several times the compressive yield stress of the soft material, the soft material is forced into the asperities of the hard materials. The decrease in effective height of still unfilled asperities is indicated on Figure 2-4. The solid curve shows the prediction of a coining model (Ref. 6) in which a flat soft blank is forced into a depression in a hard die. By this model, the required contact stress is not affected by the angle of the sawtooth and must be very large to fill the last 10 percent of the die depth. The dashed curves of Figure 2-4 represent the prediction of a punching model (Ref. 7) in which a single sharp punch is indented into a soft blank. It can be seen that at applied stresses between two and four times the yield stress the predictions are similar, but the punching model predicts a dependence on asperity sharpness as well as depth. This dependence is shown in Figure 2-5. Consideration of limited data on the asperity angles encountered in practice indicates that at worst real surfaces would be on the relatively flat portion of this curve.

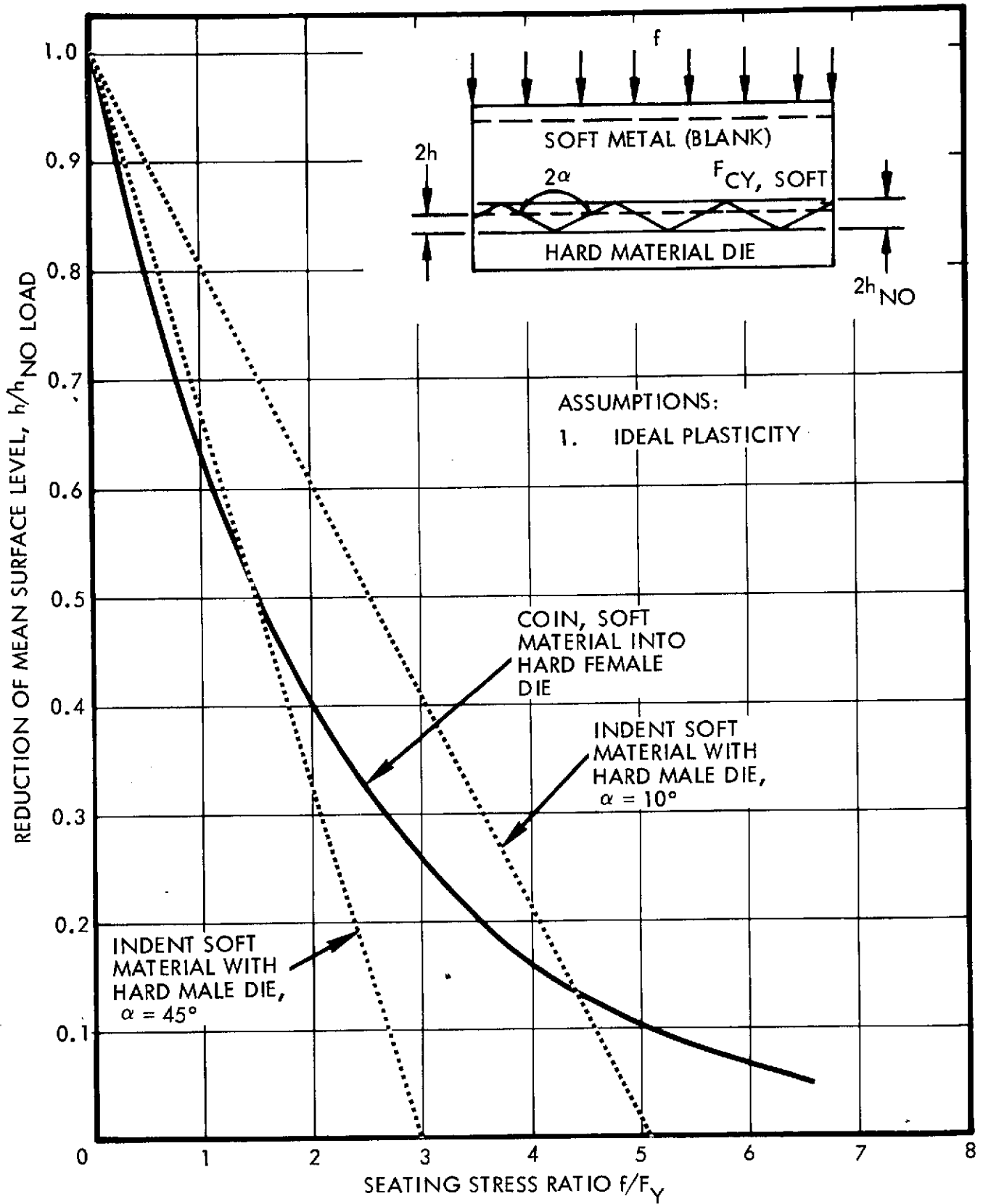


Figure 2-4. Relation of Mean Surface Height to Applied Seating Stress by Plastic Coining and Indentation Theory

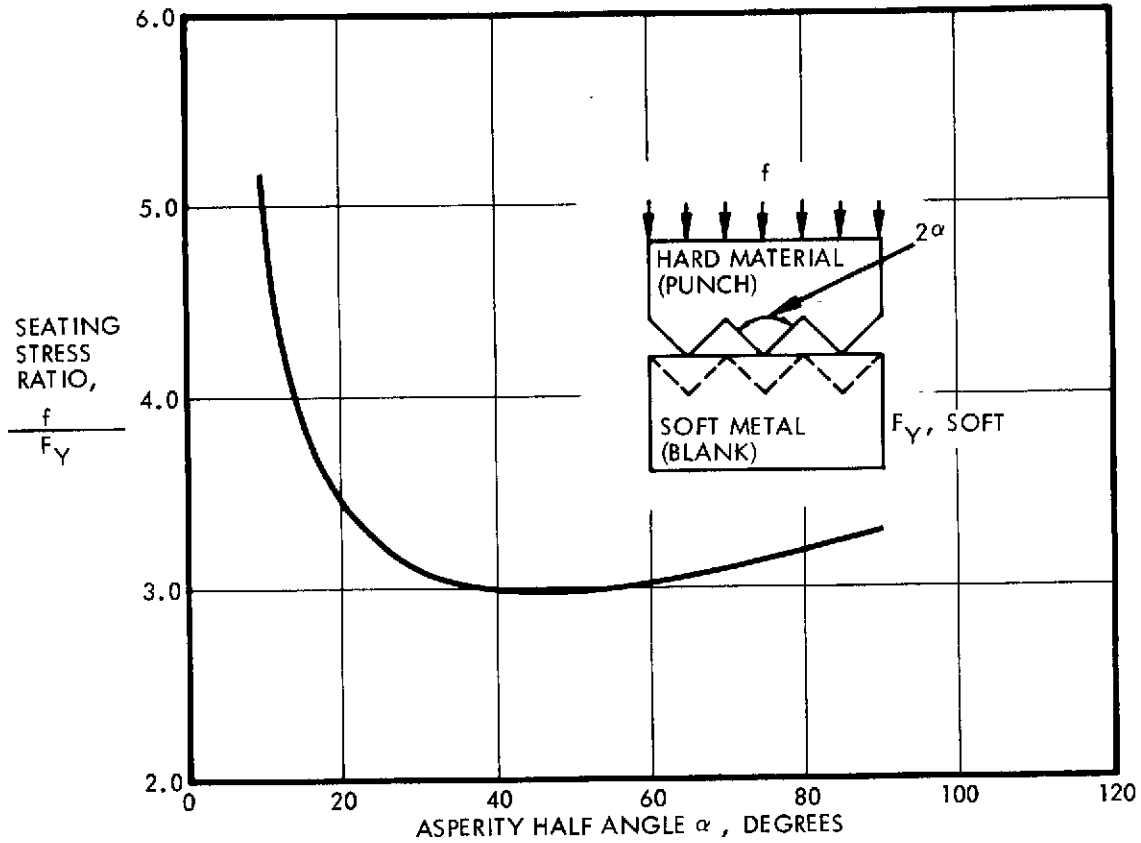


Figure 2-5. Effect of Asperity Sharpness on Required Seating Stress

In an actual soft/hard contact the soft material, as well as the hard will have a significant surface roughness. None of the plastic models in being treat a non-flat soft blank, but presumably very little increase in the contact stress should be necessary to crush down peaks and valleys in the soft surface if it is already being forced into the hard surface at several times yield.

In addition to the soft and hard surface contours, wear particles composed of soft material, hard material and/or their compounds will be trapped between the seats. An upper limit on the depth such particles will be indented into the soft surface can be found with another punching

model, in this case a blunt radiused punch. Figure 2-6 shows the indentation depth versus contact stress for this case. Of particular interest is the stress necessary to indent an approximately spherical wear particle a distance equal to its own diameter into the soft surface.

2.4.3 Analyses of Contained Metal Seal - Bulk Compression

The problems encountered with coining metal is the extrusion of the softer metal at the edge of the interface. This can be prevented by containment of the softer metal. An additional concern is strain hardening as a result of repeated loading. Tension compression and fatigue are also possible failure modes.

By containment of the metal, plastic strain of the metal is eliminated over the cyclic life of the metal seat. Without plastic strain, work hardening and failure due to stress cannot occur. Under bulk compression (tri-axial stress) fatigue failure is eliminated. However, extrusion between the clearances of the poppet and seat is of concern. Also, adhesion between the metal couple is a potential problem.

Figure 2-7 shows the dimensional requirements on gaps between adjacent parts surrounding a soft metal seal according to plastic extrusion theory. For a seal width dimension of 0.100 inch and a seating stress of four times yield, the curve indicates that such a gap should be kept narrower than 0.003 inch.

2.4.4 Metal Seat Design Configuration

The metal poppet and seat design test fixture is illustrated in Figure 2-8. This fixture is attached to a hydraulic actuator capable of automatic cycling. The detailed drawings of the poppet and seat are depicted in Figure 2-9. All dimensions of Figure 2-9 are nominal. The poppet and seat were installed in the test fixture of Figure 2-8 allowing less than .001 inch extrusion gap between the poppet and seat housing. The soft aluminum (1100) was installed requiring a light press fit to the housing. The initial average surface roughness on the stainless steel

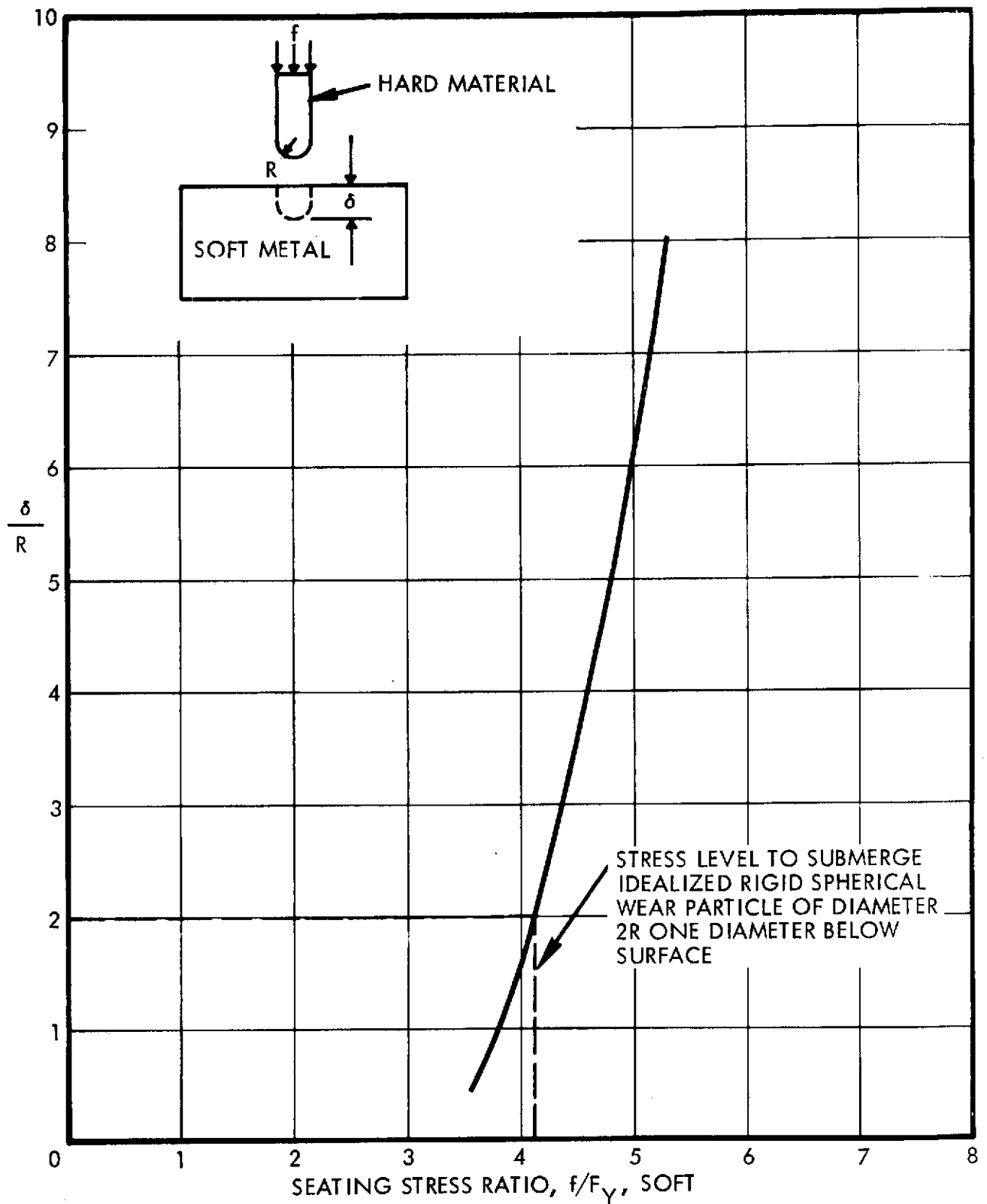


Figure 2-6. Indentation of Hard Radiused Punch Into Soft Material

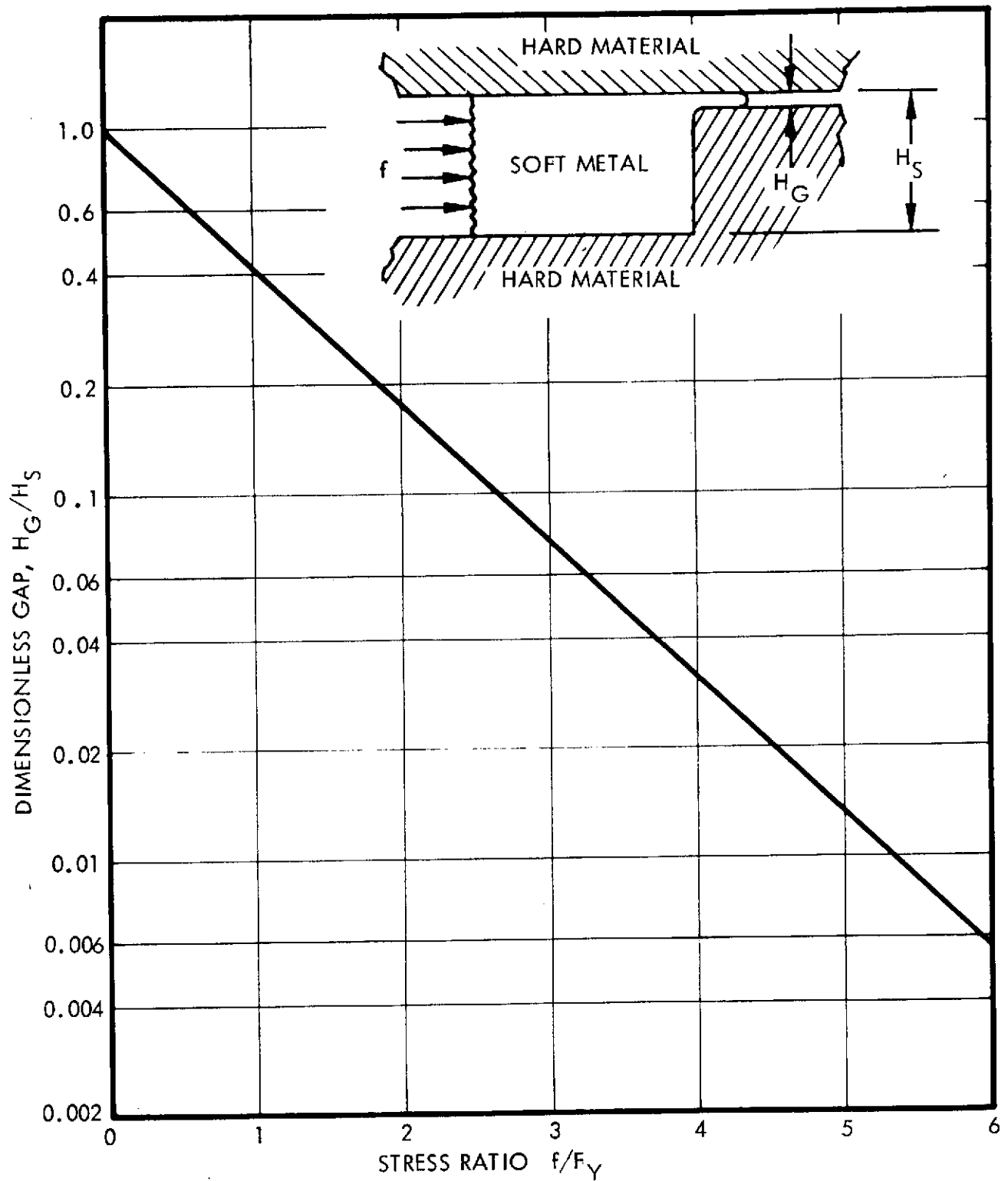


Figure 2-7. Minimum Gap Requirements Between Adjacent Parts to Prevent Extrusion of Seal Material Between Sliding Surfaces

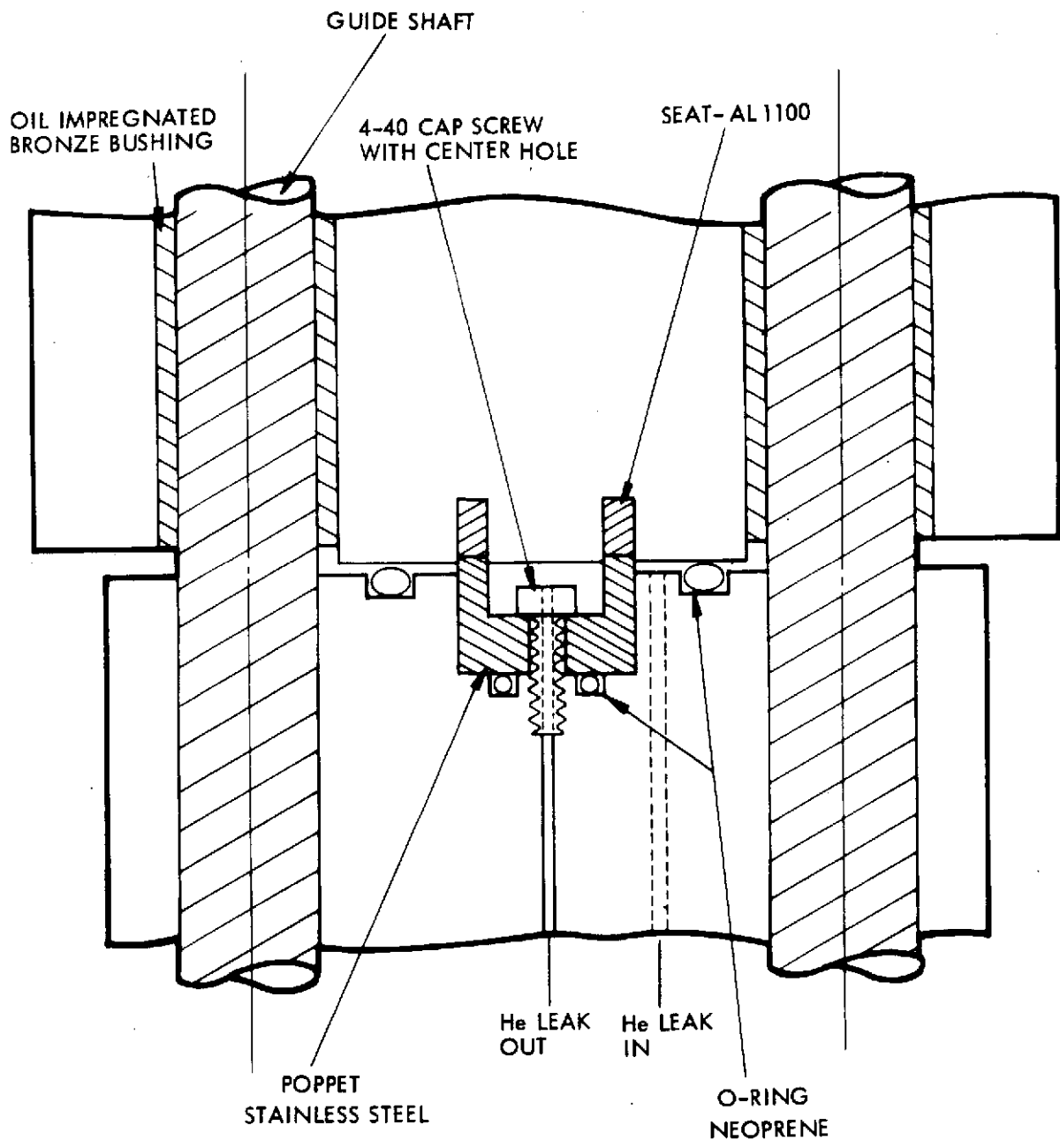


Figure 2-8. Valve Seal Test Fixture

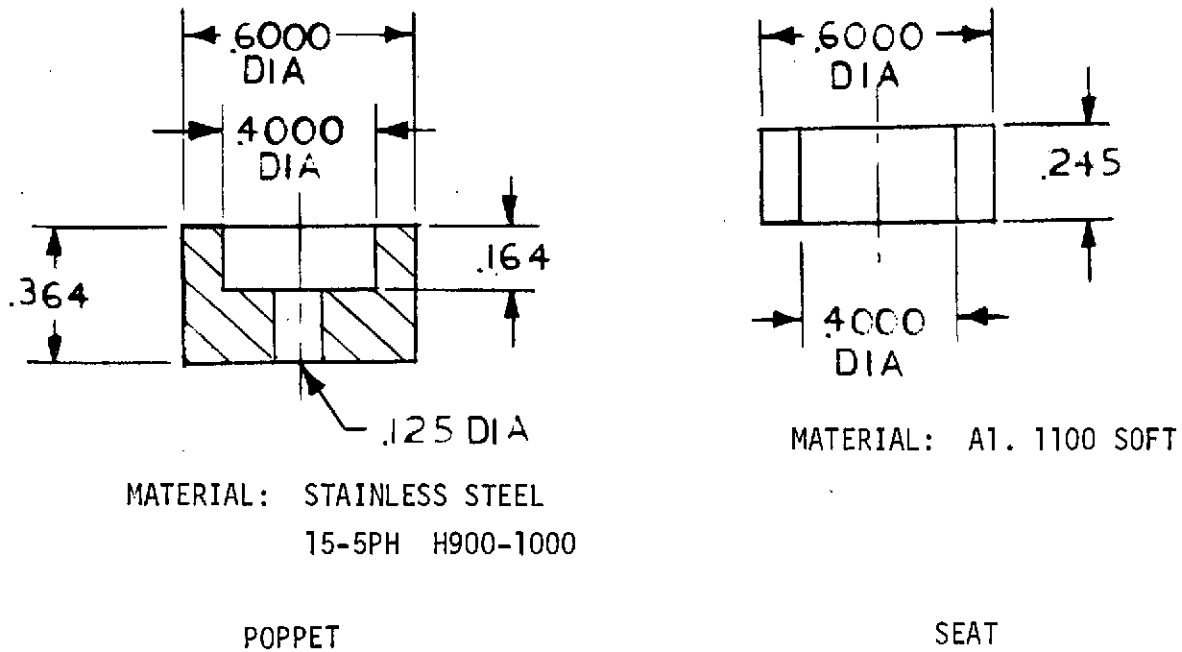


Figure 2-9. Hard and Soft Valve Seat Configuration

poppet (15-5 PH) was about 0.5 microinches and about 2.0 microinches for the soft seat. Flatness of both specimens were held to 1/4 wavelength of monochromatic light. The choice of materials for the poppet and seat were based on 1) low yield strength of the seat material at cryogenic temperatures, 2) compatibility with Flox, and 3) anti-adhesion properties.

2.4.5 Testing Apparatus

The hard or soft seal test fixture is illustrated in Figure 2-8. The fixture was mounted in the TRW Load Control System (Research, Inc. Model 900.02). A photograph of the system is shown in Figure 2-10. The loading machine can achieve up to 50,000 pounds load and is capable of a cyclic rate of up to 10 cps. The ram load is produced by hydraulic pressure and the load is measured by a Ormond Inc. Double Bridge 50,000 lb Transducer Model No. WTL-PM25-CD-50K.

A Hewlett Packard 680 strip recorder is used to record load and cycle rate.

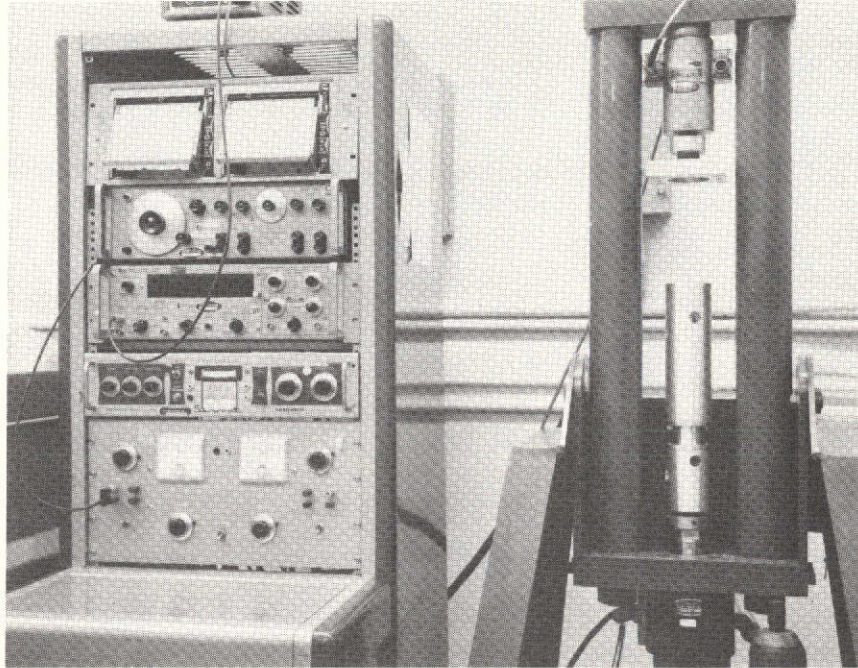


Figure 2-10. Loading Frame and Operating Panel Used for Cyclic Testing Metal Valve Seal

2.4.6 Test Description and Test Results

The procedure employed in the testing program consisted of the following:

1. Inserting the test surfaces into the mechanical loading fixture
2. Opening and closing the valve seat a specified number of cycles
3. Measuring the leakage rate at selected stages of the cycling process
4. Removing the test surfaces for measurement using the coherent optical technique at selected stages of the cycling process.

The beginning of the test series concerned the establishment of the initial conditions of the hard and soft surfaces. These surfaces were not handled directly at any time since they were very sensitive to any form of contact. Following the final polishing operation, they were

cleaned and placed in the coherent optical setup (see Section 4.0) for their first roughness measurement. These measurements, recorded as the cycle number 0, showed that the soft aluminum surface had an average roughness of 2.3 microinches and the hard stainless steel surface had a value of .5 microinches. It was noted that the variability of roughness around the circumference of the sealing faces was greatest on the soft aluminum seat while almost no variation was noted on the stainless steel surface.

The first major contact between the two surfaces occurred when the soft aluminum seat was pressed into the fixture holder (Cycle No. 2). A maximum interfacial pressure of 12.7 ksi was developed during this operation and was the first coining of the hard surface features into the soft seat. The leakage rate during the second cycle was measured at different loading levels. The fixture containing the soft seat was then removed and inserted into the optical setup where the new surface roughness was found to be 1.9 microinches average. Thus the second cycle of valve operation produced a reduction in average surface roughness of .4 microinches on the soft aluminum seat.

The results of the second cycle are illustrated in Figure 2-11 which depicts the coining or wear-in process as a function of increasing seat bearing stress. The leakage showed a dramatic decrease from about 10^{-3} scc/sec He to approximately 10^{-6} scc/sec He between 10,000 and 12,000 psi bearing stress. The third and successive cycles were maintained at a loading of 19,100 psi; with leakage decreasing to about 10^{-8} scc/sec on the 9th cycle. The helium applied across the seat was by the blanket method. At the 10th and successive cycles the helium differential was increased (see Table 2-3).

Successive cycling continued to improve surface quality and decrease the leakage rate as predicted from the "coining" theory analysis. On the 277th valve cycle, the measured leak rate had decreased to 1.2×10^{-9} scc/sec while the surface roughness of the aluminum valve seat decreased .85 microinch to 1.25 microinch. It can be seen that along with the reduction in surface roughness, the variation in roughness around the seal circumference also

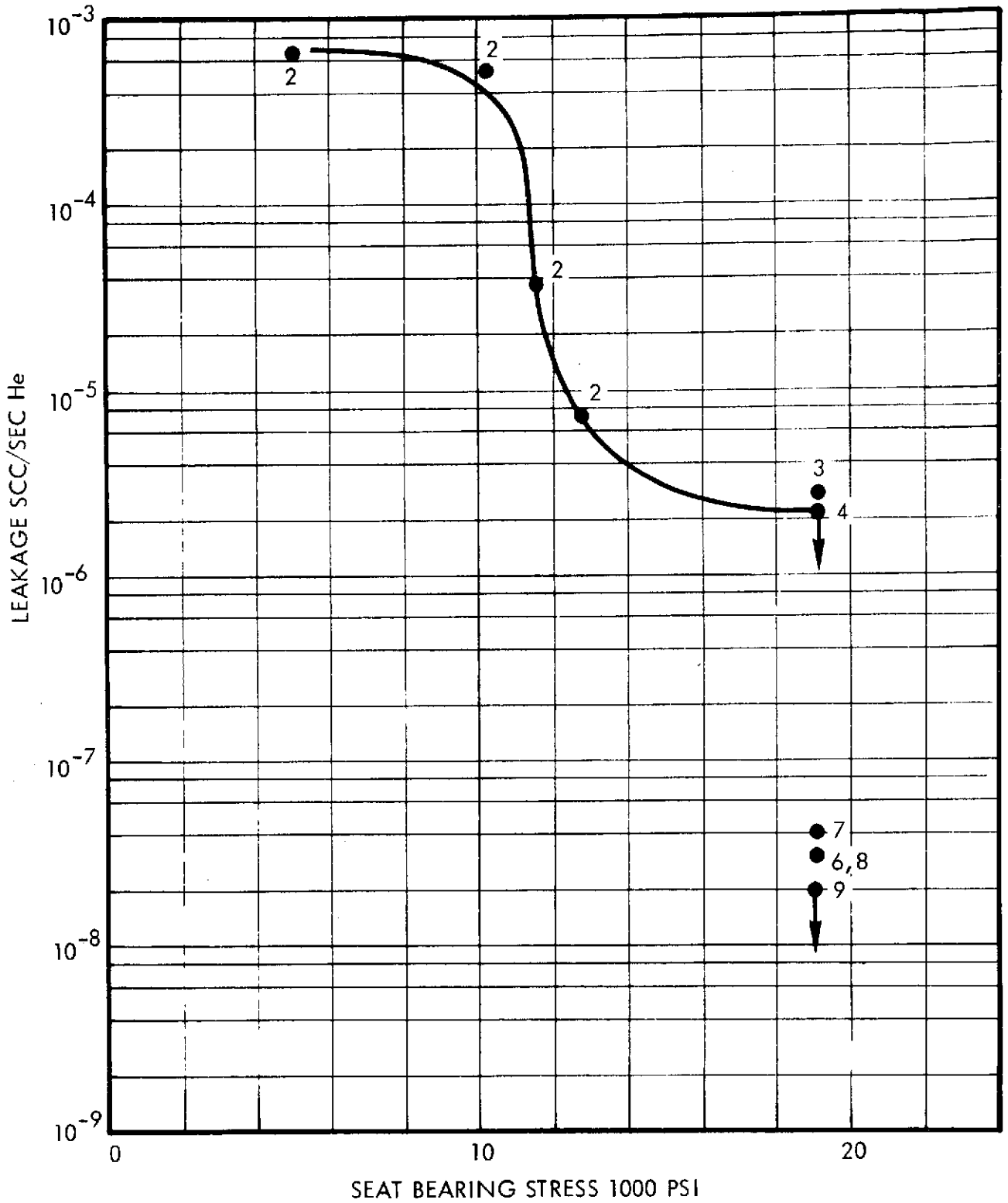


Figure 2-11. Initial Cycle (Wear-In) Effects on Leakage

Table 2-3. Compilation of Long Life Metal Valve Seal Test Data

Run No.	Load lbf	Cycle No.	Leakage scc/sec He	Leakage ΔP, psi	Seat Interface Bearing Stress Psi	Comments
1	0	1	10 ⁻³	14.7 Blanket	0	Fixture Weight Only
2	785 1,630 1,820 2,000	2	7 X 10 ⁻⁴ 6 X 10 ⁻⁴ 4 X 10 ⁻⁵ 7 X 10 ⁻⁶	↓	5,000 10,400 11,600 12,700	Increasing Load ↓
3	3,000	3	1.45 X 10 ⁻⁶ 1.56 X 10 ⁻⁶ 1.65 X 10 ⁻⁶	14.7 Blanket ↓	19,100 ↓	
4	3,000	4	1.38 X 10 ⁻⁶ 1.03 X 10 ⁻⁶ 1.25 X 10 ⁻⁶	14.7 Blanket ↓	19,100 ↓	
5	3,000	5	-	-	19,100	
6	3,000	6	1.89 X 10 ⁻⁸ 2.02 X 10 ⁻⁸ 2.02 X 10 ⁻⁸	14.7 Blanket ↓	19,100 ↓	
7	3,000	7	4.79 X 10 ⁻⁸ 4.28 X 10 ⁻⁸ 3.66 X 10 ⁻⁸ 4.54 X 10 ⁻⁸ 4.79 X 10 ⁻⁸	14.7 Blanket ↓	19,100 ↓	
8	3,000	8	1.26 X 10 ⁻⁸ 1.39 X 10 ⁻⁸ 1.26 X 10 ⁻⁸ 1.39 X 10 ⁻⁸	14.7 Blanket ↓	19,100 ↓	
9	3,000	9	1.51 X 10 ⁻⁸ 1.39 X 10 ⁻⁸ 1.51 X 10 ⁻⁸ 1.39 X 10 ⁻⁸	14.7 Blanket ↓	19,100 ↓	
10	-	-	-	-	-	No Measurements
11	3,000 2,000	11	1.26 X 10 ⁻⁹ 2.52 X 10 ⁻⁹ 3.04 X 10 ⁻⁹ 8.82 X 10 ⁻⁹ 1.38 X 10 ⁻⁸ 3.59 X 10 ⁻⁷ 3.59 X 10 ⁻⁷ 3.59 X 10 ⁻⁷	25 35 45 55 65 25 45 65	19,100 ↓ 12,700 ↓	Decreased Load Increased ΔP He
12	1,000- 6,000	12- 276	-	-	6,370- 42,000	Random Loading Resulting From Setting Machine to 1 cps
13	3,000	277	1.26 X 10 ⁻⁹ ↓	25 35 45 55 65	19,100 ↓	Varied ΔP He ↓
14	3,000	278	1.26 X 10 ⁻⁹	65	19,100	
15	1,000	279	3.02 X 10 ⁻⁸ 3.14 X 10 ⁻⁸ 3.5 X 10 ⁻⁸ 3.75 X 10 ⁻⁸ 4.0 X 10 ⁻⁸ 4.0 X 10 ⁻⁸	20 25 35 45 55 65	6,370 ↓	Decreased Load ↓

Run No.	Load lbf	Cycle No.	Leakage scc/sec He	Leakage ΔP, psi	Seat Interface Bearing Stress Psi	Comments
16	3,000 2,600 2,200 1,800- 2,000 1,300 1,000- 600- 700 300 500	280	1.26 X 10 ⁻⁹ 1.26 X 10 ⁻⁹ 1.26 X 10 ⁻⁹ 2.5 X 10 ⁻⁹ 3.8 X 10 ⁻⁹ 1.75 X 10 ⁻⁸ 1.3 X 10 ⁻⁶ 1.26 X 10 ⁻⁴ 4.0 X 10 ⁻⁶	45 ↓	19,100 16,500 14,000 11,450- 12,700 8,300 6,370- 7,000 3,800- 4,450 1,910 3,180	Decreasing Load ↓ Increased Load
17	3,000	281	4.8 X 10 ⁻⁹	45	19,100	
18	3,000	281- 1281	-	-	19,100	.9 CPS Load Cyclic Rate
19	3,000	1282	1.26 X 10 ⁻⁹	45	19,100	
20	3,000	1283- 4642	-	-	19,100	.935 CPS
21	3,000	4643	1.26 X 10 ⁻⁹	45	19,100	
22	3,000	4644	1.26 X 10 ⁻⁹	50	19,100	
23	3,000	4644- 9644	-	-	19,100	.935 CPS
24		9645	1.26 X 10 ⁻⁹	50	19,100	
25		9645- 14,645	-	-	19,100	.935 CPS
26	3,000	14,646	1.26 X 10 ⁻⁹	50	19,100	
27	3,000	14,646- 19,446	-	-	19,100	3.2 CPS
28	3,000	19,447	1.26 X 10 ⁻⁹	50	19,100	
29	3,000	19,448	1.29 X 10 ⁻⁹	50	19,100	
30	3,000	19,448- 34,208	-	-	19,100	3 CPS
31	3,000	34,209	1.29 X 10 ⁻⁹	50	19,100	
32	3,000	34,209- 72,004	-	-	19,100	3 CPS - Extrusion
33	3,000	72,005	≈1.29 X 10 ⁻⁹ 4.9 X 10 ⁻⁹ -Gross	50 115	19,100	Leakage Not Steady

decreased, indication that the statistical properties of the sealing interface had become more uniform and isotropic.

Surface roughness and leakage data is recorded in Table 2-4. The data of Table 2-4 is taken from Section 4.0 which describes in more detail this new surface optical signature technique.

Table 2-4. Surface Roughness and Leakage Recorded by Valve Cycles

Cycle No.	Orientation Angle θ	Surface Roughness σ in Microinches	Average $\langle\sigma\rangle$	Leakage in Scc/Sec He
0	0°	3.0	2.3	-
	30	2.7		
	80	2.0		
	130	1.3		
	340	2.5		
2	0°	1.3	1.9	7.59×10^{-6}
	115	2.5		
	209	1.6		
	303	2.3		
	355	1.9		
277	0°	1.4	1.25	1.26×10^{-9}
	65	1.4		
	82	1.4		
	182	1.4		
	201	1.6		
	292	1.3		
	303	0.8		
	320	1.2		
	330	1.3		
	72,000	1°		
77		1.6		
100		1.4		
160		1.4		
175		1.6		
206		3.0		
216		2.0		
218		1.4		
234		2.0		
251		1.6		
256		2.0		
292		1.4		

On the 280th cycle the effect on leakage due to relaxing the seat load was tested. The results are plotted in Figure 2-12. Leakage increased at a load of about 1800 lbs, but only slightly. The major change in leakage began around 1000-600 lbs load and continued increasing with lower loads. At 300 lbs, load was increased to 500 lbs and leakage decreased as would be expected.

Cycling was again continued with measurements of leakage made at periodic intervals. The leak rate remained constant (1.2×10^{-9} scc/sec) when checked at 34,000 cycles. At 72,000 cycles leakage increased slightly but unsteady. The helium pressure was increased to 115 psi across the seat at which time the leakage exhibited wide fluctuations and finally gross leakage occurred. The test surface was again removed and inserted in the optical roughness measurement setup where the surface roughness of the soft seal was found to be 1.82 microinch. This increase in surface roughness was paralleled with an increase in variability of roughness around the seal circumference.

Compilation of the test data is included in Table 2-3.

Extrusion of the aluminum through the outer diameter clearance was noted. The test program was terminated.

The photograph of Figure 2-13 clearly depicts the extrusion flashing around the outer circumference of the soft aluminum seat. At 7:00 o'clock a spot appears to be due to material transfer which is also visible on the stainless steel poppet of Figure 2-14 (5:00 o'clock). Small embedded particles were also noticed on the aluminum seat in addition to craters which were probably due to loose particles or contaminants which were impressed in the soft aluminum. Several large adhesive wear particles (aluminum) were seen on the stainless surface in addition to numerous small particles which characterized the surface. The particles did not appear to be strongly adhered to the stainless surface. Upon wiping the surface with a tissue, most of the particles were removed and some smearing indicative of soft aluminum was noticed. The surfaces overall were in relatively good condition after the 70,000 cycles. Except for the extrusion there were no indications of surface degradation that would impair the integrity of the seal.

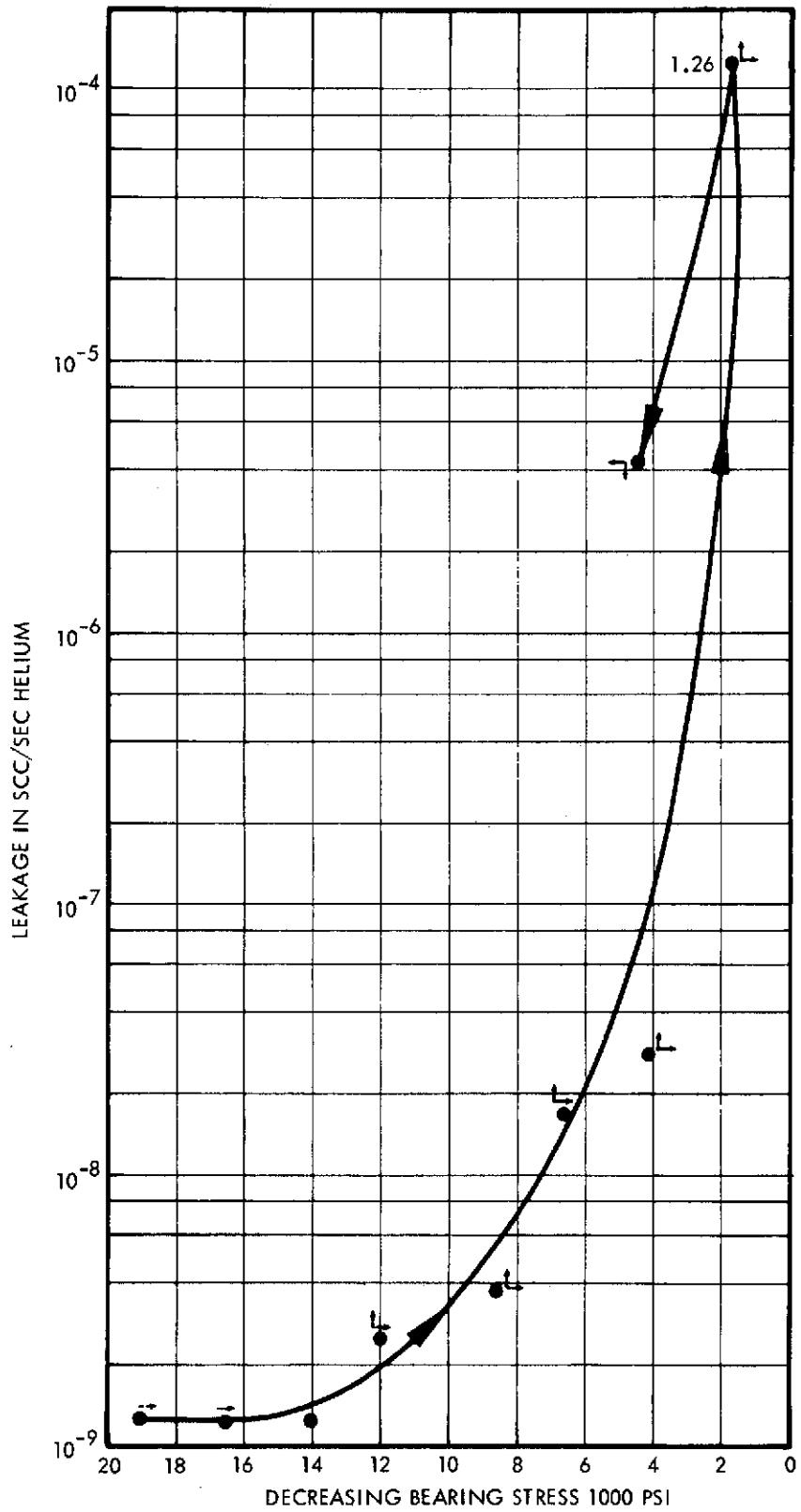


Figure 2-12. Leakage As a Function of Decreasing Bearing Stress After 280 Cycles

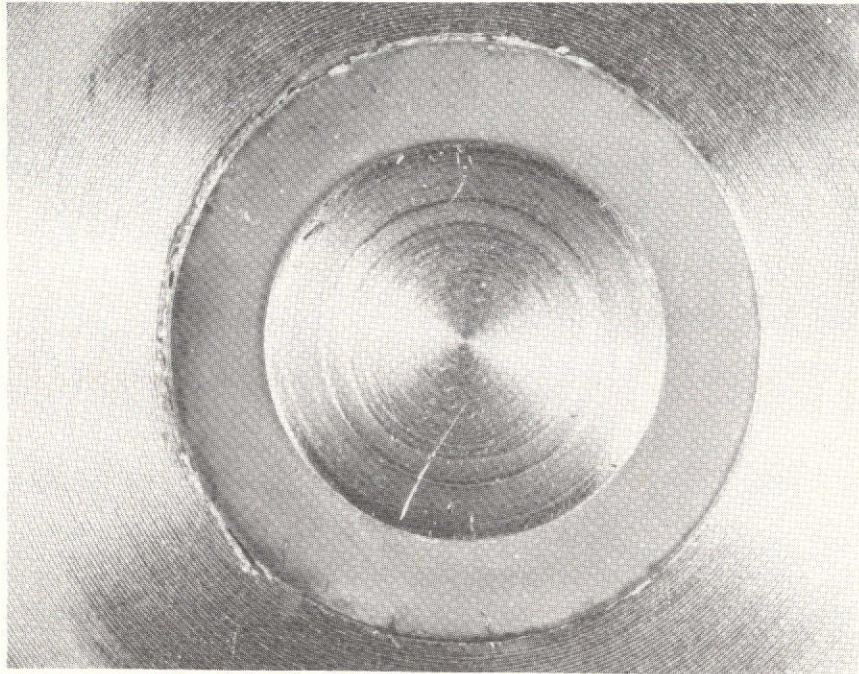


Figure 2-13. Soft Aluminum Seat After 72,000 Cycles Magnified 5x.

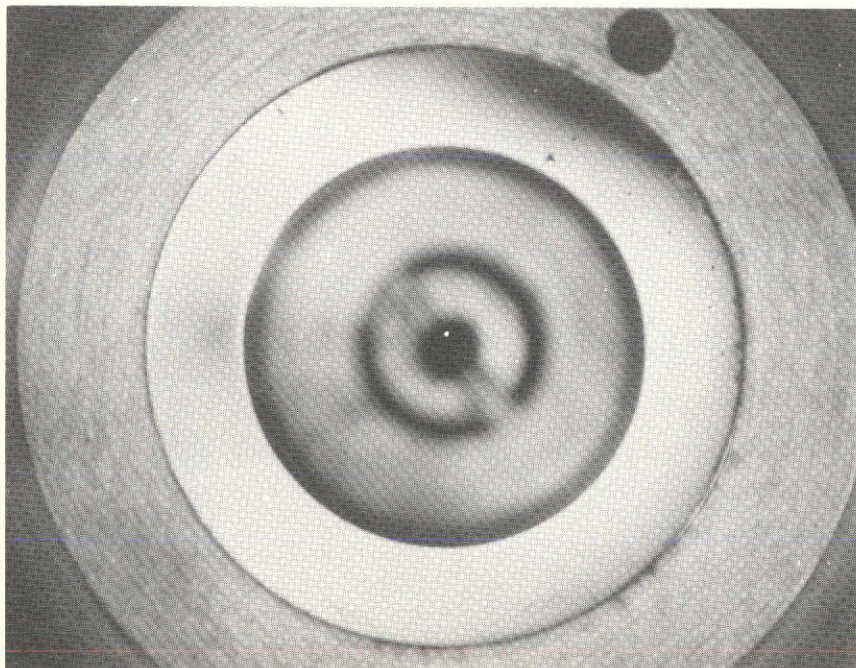


Figure 2-14. Stainless Poppet After 72,000 Cycles Magnified 5x.

2.6 REFERENCES

1. R. L. Green, ADVANCED TECHNIQUES FOR DETERMINING THE LONG TERM COMPATIBILITY OF MATERIALS WITH PROPELLANTS. NASA Contract NAS 7-789, Boeing Aerospace Co., Seattle, Wash. (Final Report to be published)
2. R. J. Salvinski, et al, A STUDY OF ADVANCED TECHNIQUES FOR THE LONG TERM PERFORMANCE OF COMPONENTS. TRW Interim Report No. 168-68-6014-R000, March 1972.
3. E. Rabinowicz, FRICTION AND WEAR OF MATERIALS. John Wiley and Son, New York, New York, 1965.
4. F. L. Merritt, PROPELLANT ISOLATION SHUTOFF VALVE PROGRAM. TRW Report No. 73.4781.6-15, February 1973.
5. G. Howell, AEROSPACE FLUID COMPONENT DESIGNERS' HANDBOOK. Vol. I, Rev. D. TRW Report RPL-TDR-64-25, February 1970.
6. Thomsen, et. al., MECHANICS OF PLASTIC DEFORMATION IN METAL PROCESSING. MacMillan, 1965.
7. J. H. Faupel, ENGINEERING DESIGN. Wiley, New York, 1964.

3.0 METHODS OF ANALYSIS, CORRELATION AND PREDICTION

3.1 INTRODUCTION

The more common techniques used for assessing long life potential of components, subsystems and systems in today's aerospace technology range from elementary to the most sophisticated. Among the elementary techniques are such fluids as fluid compatibility, fluid leakage, spring/mass degradation as a function of time of application, fluid viscometry, test of materials properties (physical, chemical, metallurgical, etc), and other observational types of tests. Results are either compared with results of similar, historical tests from which conclusions are drawn regarding the longevity of the current item or, if sufficient data are available, curves or "trend" lines are plotted to estimate future behavior by observing parametric changes with time. In the first instance acceptability of the item is usually "go-no-go" oriented because accept/reject criteria are specified as a single value or range of values. In Quality Control terminology this is referred to as attributes testing. Disciplines have been evolved utilizing quality control charts which are based on this form of testing.

The analysis of trends is another recognized technique involving a highly developed discipline. Variables testing is amenable to this approach. A common factor for both of these is the need for a significant sample size of the parameter or item being evaluated. A less sophisticated, although perhaps more realistic technique, at least at the component level, is simply to test one or two of a kind for a particular condition, hoping that its presence (or absence) will be sufficient evidence to validate a capability or else eliminate a failure mode from further concern. It must be remembered that testing costs are high at this level (and is even more expensive as configuration complexity increases) so there is an economic reason for minimal testing.

More sophisticated techniques* include such mathematical and statistical

* Refer to the following article for a description of some of these techniques "Some Statistical Techniques Useful in System Aging Studies," E. L. Welker, TRW Systems, Proceedings, 1973 Annual Reliability and Maintainability Symposium, P. 10

treatments as regression analyses, Markov chains, experimental test design, mapping, etc. In TRW's Minuteman Program, for example, the regressing analyses are extensively used to evaluate equipment aging processes where the phenomenon is assumed to be linearly related with time. Higher forms of polynomial expression have been investigated, but these are not conclusive at the present time. Some accelerated aging studies have been performed, although it is difficult to relate the process to the loading factors involved with the process. There simply isn't sufficient data available to correlate aging effects with the process mechanics. A computer program called "LMTAB" has been developed at TRW for extrapolating failure rate and probability over a long period of time using limited statistics obtained in the near-time environment from either controlled or actual use sources. This technique suffers from the scarcity of data which is typical of current long-term investigations.

In a recent proposal, for example, it was necessary to estimate success probability many more times than there was data suitable for this estimate. Coupled with this dearth of data was the fact that zero failures had been observed. The best solution would have been to initiate a test program to simulate this particular mission requirement. This approach was feasible but uneconomical. The immediate solution was to evaluate the thruster failure modes, and hypothesize the inherent capability based on these results. Hopefully, data from this and similar programs will be judiciously analyzed in a time frame to provide dependable aging statistics which can be correlated with the thruster failure mechanisms.

A similar problem exists at higher levels of complexity. Subsystems are tested often for the same characteristics as at the component level. The results are not as well defined because of the interactions both among the various equipments and environments being imposed on these equipments. Thus, for example, valve leakage may be the result of a contaminant particle emanating from the tank. Techniques used at this level tend toward the elementary because of the difficulty in obtaining meaningful measurements. Frequently at this level mission simulation is employed either with or without combining the environments. Thus, thermal vacuum is frequently tested because experience has shown it to be a reliable parameter regarding

the incipency of failures. Vibration, usually three-axes, may be imposed during thermal vacuum, but generally is not imposed because of the added testing complexity costs. Shock, temperature exposure testing (fungus, humidity, etc.), acoustic, radiation, and some of the more exotic, discrete types of tests may be imposed at the component level.

Mission simulation in a reliability testing sense is sometimes performed to evaluate process characteristics. For example, maintenance and repair plans are established and evaluated based on hypothetical failure densities of the hardware configurations. In a sense these models study the aging or wearout process, especially if time-variable rates are used. Such computer techniques as Monte-Carlo, GPSS, SIMSCRIPT or some other programmed algorithms are generally exercised to accomplish their analysis. Hardware failures obviously are descriptive in this form of testing and therefore do not add to one's knowledge of failure mode history.

Real failures resulting from physical mission testing, on the other hand, are too often insufficiently analyzed, and inadequately resolved. Unfortunately, there is often too much emphasis on schedule, and too little on the tests itself. There are many failures that are closed out whether with a relaxation of a procedure requirement or a confession of ignorance coupled with a general disinterest in the problem.

Real-Time Analysis is frequently used during this level of testing using small or mini-computers with suitable data conversion and electronics. Test parameters can be monitored or sampled, and the results either analyzed immediately, or else stored for later analysis. Feedback and correction is a necessary adjunct of this technique. Test results can be plotted as in "trend analysis" for off-site interpretation, tabulated as required for "regression analysis", and/or digitized for Analysis of Variance associated with Experimental Test Design.

Predicting long life capability is frequently accomplished using statistical inference techniques. Considerable theoretical mathematics regarding life-testing has been reported in recent years by such authors as Epstein and Sobel, et al. These theses hypothesized probability

distributions based on component test which were then extrapolated to future expectancy. The TRW "LMTAB" computer program, referred to earlier, is an outgrowth of this technique. These mathematical approaches are characterized by the failure event being generalized rather than being made specific to a particular mode of failure. Thus, although there have been many life tests conducted on various components by various vendors, test laboratories and contractors, much of the work has never been reported, or if it is reported it is so general as to be of little use in failure mode studies.

In a more positive vein, there is some good basic general failure physics being performed by a few agencies. There needs to be more work performed of this nature, particularly since longer space missions are being planned. It is TRW's position that what has been accomplished thus far has been adequate for short (in a time relative sense) spacecraft missions; however, for longer planetary probes, existing knowledge of hardware capability to meet the long-term requirements of space flight simply will not do.

Some of the methods proposed to evaluate long-term or aging characteristics of existing components are presented in the following section. It must be kept in mind that there are discrete hardware analysis techniques not intended for complex mission evaluations. The field is fertile for advancing the state of the art and the rewards are limitless.

3.2 TIME CORRELATION METHOD

This method is developed for correlating operating component test data with impending component performance anomalies malfunction or failures. The method would provide a means of tabulating data points, calculating relative changes in measured parameters and determining influence coefficients which may be used to predict possible failure or identify incipient failures.

In operation, the program would consist of the following operations:

- Recording component signatures for parameters taken simultaneously with time.

- Correlate changes in signature data points per unit time and identify changes which fall outside of specified bands.
- Calculate influence coefficients ($\Delta X_1/\Delta X_2$) where ΔX_1 , ΔX_2 are the changes in parameter X_1 and X_2 in one time interval.
- Printout influence coefficients and slope of data values for evaluation.

Following the program reduction and evaluation of the test data, if failure mode criteria were not available, evaluation would be made to correlate the performance parameters and influence coefficients with possible component malfunction. The evaluation and correlation method relies on the premise that the measured parameters or signatures at a given time are related to the measured parameters or signatures at another time. Each measured set of data at any given time is a calibration point. In initial use, it may be necessary to conduct component tests of the specified components (valves, regulators, etc.) in which components are cycled to failure, in order to establish a correlation (failure criteria) between specific performance parameter influence coefficient shifts with specified malfunctions.

3.3 DIMENSIONAL ANALYSIS METHOD

Dimensional analysis is one method which appears particularly promising as a means of predicting failure modes and operational degradation of components. This method was studied in detail and several dimensional relations were evolved and are reported in the Interim Report (Ref. 1). While correlation with actual test data will be required to verify this method, the general logic of the method appears reasonable. As a demonstration, a simplified dimensional analyses of a valve poppet assembly has been described to illustrate the correlations which could be made.

Example

Defining an electrically actuated valve assembly as shown in the schematic of Figure 3-1

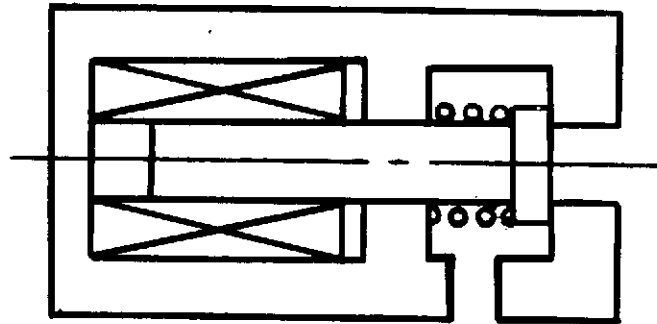


Figure 3-1. Schematic

and selecting response time of the poppet to an electrical command as the dependent parameter of interest, the controlling relationships may be defined by dimensional analysis as follows:

- (1) Establish all relevant parameters

Thus, we say

$$T = f (M, C, K, B, D, i)$$

where: T = response time
M = poppet assembly mass
C = viscous damping coefficient
K = spring constant
B = magnetic flux density
i = current

The techniques outlined in Reference 2 were used to define a unit matrix in the mass, length, time, permittivity system, therefore:

	M	C	K	B	D	i
M	1	1	1	1/2	0	1/2
L	0	0	0	-3/2	2	3/2
t	0	-1	-2	0	0	-2
e	0	0	0	-1/2	0	1/2

also $T = KM^a C^b D^d e_i^f$

or, $T = K(M)^a (M/t)^b \left(\frac{M}{t^2}\right)^d (L^2)^2 \left(\frac{M^{1/2} L^{3/2} E^{1/2}}{t^2}\right)^f$

Solving for the dimensional coefficients

$$(3) T = K \left(\frac{M}{Bi}\right)^{1/2} \left(\frac{C}{M^{1/2} B^{1/2} i^{1/2}}\right)^a \left(\frac{K}{B^{1/2} i^{1/2}}\right)^b$$

Now, if we define a response time degradation coefficient T_D by

$$T = T_D \left(\frac{M}{Bi}\right)^{1/2}$$

equation (3) now becomes

$$T_D = f \left(\frac{C}{M^{1/2} B^{1/2} i^{1/2}}\right)^a \left(\frac{K}{B^{1/2} i^{1/2}}\right)^b = f(N_a, N_b)$$

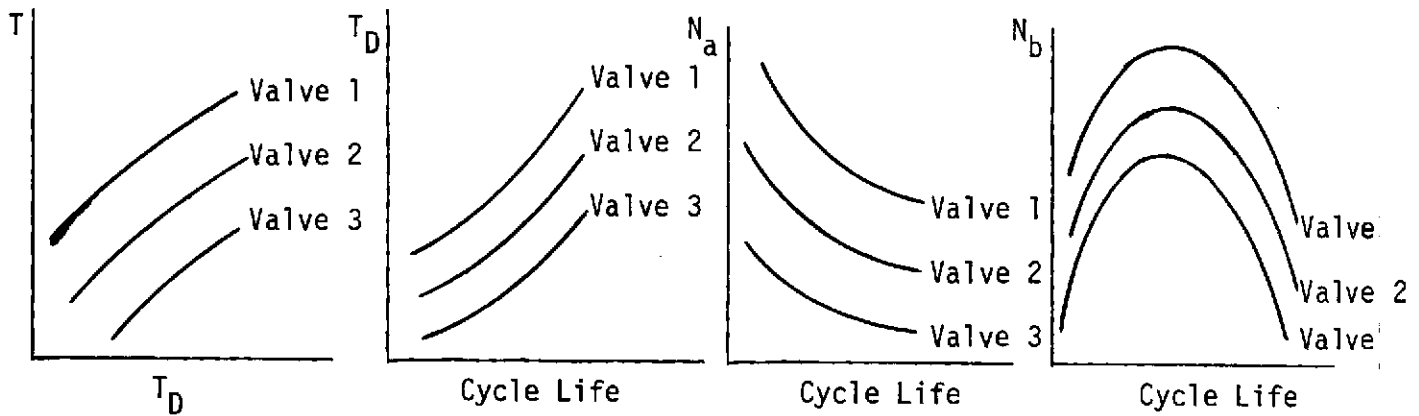
and response time is essentially reduced to a problem involving three dimensional groups,

$$T_D, N_a, N_b$$

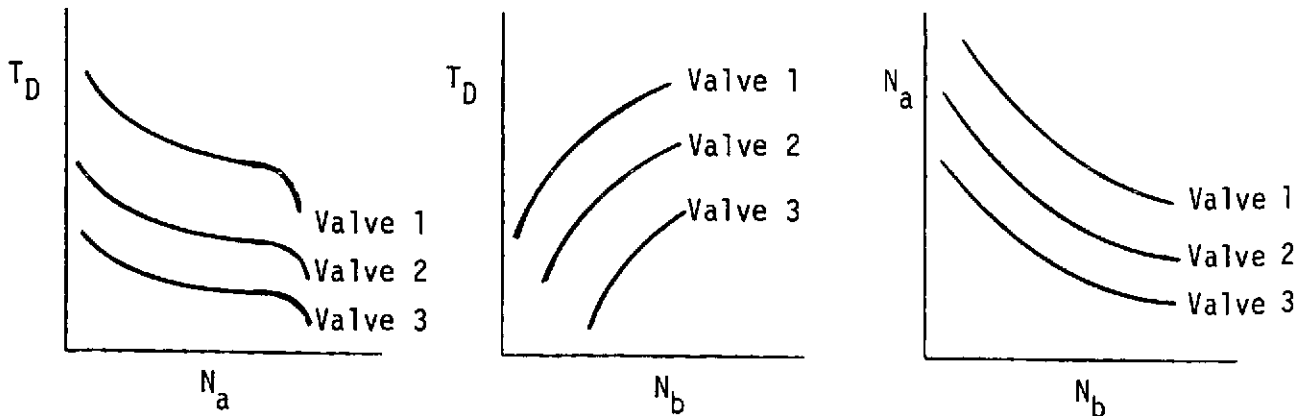
Correlation of Dimensional Groups

Correlation of these relationships to establish predictive trends must be made with empirical data. However, a logical projection of the method for establishing the correlative data would be as follows:

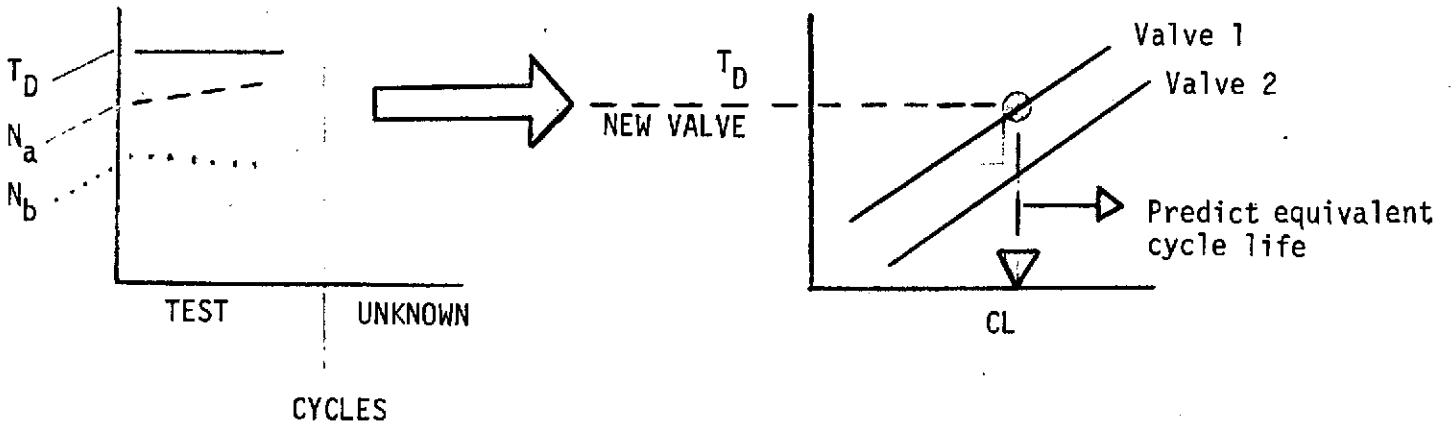
1. Test a specified valve to define empirical data for T_D , M , C , K , B , i as a function of cycle life.
2. Calculate T_D , N_a , N_b and plot. Thus we may obtain:



3. Cross plot, T_D , N_a , N_b



Now, we should be able to establish predicted T , T_D , etc. for a new valve or set of valves by calculating the effective N_a , N_b , T_D for the new components before testing or after a specified number of cycles



Measure data and calculate T , T_D , N_a , N_b for new component

Compare to established data correlation curves

4. Based on correlation with existing data, i.e., (N_a, N_b, T_D)

$$\text{predict } \frac{\Delta T}{\Delta CL} = \frac{\text{change in response time}}{\text{number of cycles}}$$

Also, testing may reveal a parameter relationship similar to the fluid dynamic drag, N_e , N_{MA} relationships whereby C_D is sensitive to Reynolds number at low mach numbers and sensitive primarily to Mach number at high Mach number. Thus, we might find T_D primarily sensitive to N_a only at low values of N_b , etc.

3.4 WIENER ANALYSIS OF SIGNATURES

Signature analysis is widely used in quality assurance programs. In this technique, the item under test is subjected to a set of well-characterized stimuli, and certain aspects of its response are recorded. The item is characterized, to a certain extent, by these responses or signatures. If the experiments are cleverly designed, it is often possible to relate the signatures to some of the underlying physical mechanisms which produce them. If the experiments are performed with care sufficient to obtain an adequate signal-to-noise ratio, small changes in the item will produce recognizable small changes in the signatures. Signature analysis, therefore, is useful both in acceptance tests as an indicator of concealed flaws and in the detection of gradually developing internal changes which may eventually lead to malfunction. In previous portions of this report, it has been shown how flow transient signatures of small fast acting spacecraft valves can be obtained at reasonably good signal-to-noise ratios, and suggestions have been made for obtaining further S/N improvements.

Quite apart from instrumentation problems, signature analysis is rarely as simple as making a set of well-defined measurements of the systems response to a set of well-defined stimuli, and comparing the former measurements with each other in a straightforward manner. First, there is the problem of defining the stimuli. Any desired set of stimuli could be chosen, and the measured system's response would be a signature; however, the problem is to characterize the system in a general manner. How does one define a set of stimuli that are sufficiently rich and varied so that the system's response set signature is a general characterization rather than a particular characterization?

Second, there is the problem of comparing the response sets. Rarely will the response sets be simple sets of discrete scalars which can be compared with elementary mathematical tests for goodness of fit and likelihood of belonging to the same classes. More often, the signature set is a multi-dimensional continuum. In large-scale production line work, it is often possible for a human QA inspector to obtain enough "experience" so that the eye-brain data processor can run an ill-defined

signature "judgement" program well enough to acceptably differentiate the bad items from the good. This traditional comparison procedure, however, is totally unacceptable when relatively few items are involved or when the item is highly critical, especially when it is only one of many critical items in a system. For performance assurance of a small run of deep space components requiring high reliability over a long period, the traditional procedure is (totally unacceptable). How then, does one meaningfully compare signatures of a small group of critical components?

The third problem with signature analysis is knowing when you are right. You may believe that you have an adequate set of stimuli and a valid comparison procedure; but belief is not enough. How do you prove whether you are right?

These are the formidable problems that limit the degree of confidence that can be accorded signature analysis for deep space component performance assurance.

The combination of small production runs on one hand and unprecedented reliability requirements on the other call for a new departure in the signature analysis of components for deep space use. This new departure can be found in the procedure of Wiener analysis. Wiener analysis is a very general and powerful technique for the thorough characterization of non-linear systems. Unlike many approaches which are applicable only to a statistically large ensemble of components, Wiener analysis can characterize a single device. At this point, the question must inevitably occur: If Wiener analysis is so good, why isn't it employed more often? There are several reasons why most engineers have not heard of this technique. First, it was developed recently, the first publication being in 1958 in a MIT graduate school textbook dense with mathematics (Ref. 3). The diffusion of the technique from the original source has been slow. Second, Wiener analysis requires a relatively large amount of computer time, hence applications that are now economic were out of the question several years ago. Finally, the necessary and sufficient conditions for convergence are, in general, mathematically unknown. It has taken some time to develop a corpus of experience sufficient to indicate what sort of problems can be solved with a practical amount of computation. Two examples of this technique

will be given, and its application to the valve problem will be discussed.

The first application is the identification of the process dynamics involved in a five-stand tandem cold rolling mill for steel sheet (Ref. 4). This complex multivariate system contains significant dead times due to the finite speed of the steel sheet and the 13-foot spacing between each of the five pairs of rollers. Although this is not a linear system, its response to sufficiently small perturbations can be considered linear, resulting in a simple exposition. (The second example will introduce the handling of non-linearities of any finite order.)

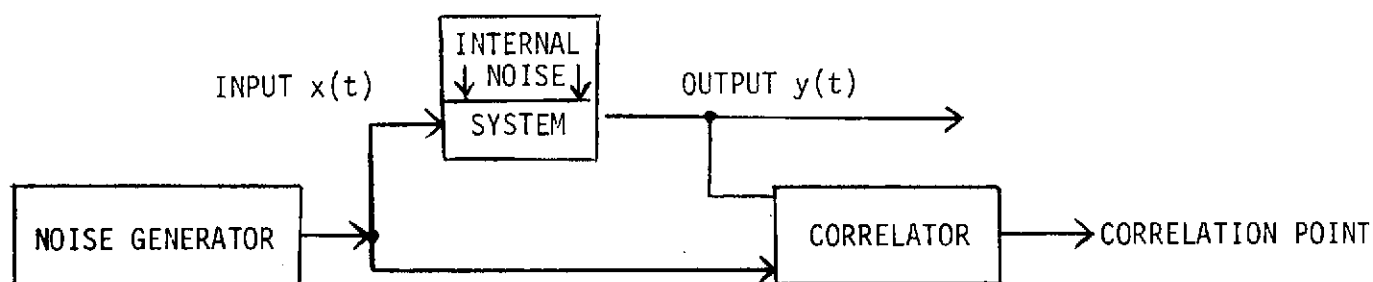


Figure 3-2

A low level random or pseudorandom perturbation signal is applied to the system under test. The use of white noise ensures that the system stimulus will be general rather than merely representing a particular case because any arbitrary particular stimulus can be obtained from the white noise by simplification. It can be quite properly said that white noise contains all possible signals. The mathematical justification for these statements can be found in references 3, 5 and 6. Of course, no physically realizable noise source is truly white since that would imply an infinite power level and infinite variances. Experience has shown, however, that a noise (or pseudonoise) signal with a bandwidth a few times larger than that of the system under test, is adequate to thoroughly exercise the system and such noise sources are readily available.

To the extent that a system is linear, it can be modeled in terms of an impulse response function $h(t)$. The least mean square error value of $h(t)$ can be found from the auto-correlation and cross-correlation functions by solving the Wiever-Hopf equation. (Refs. 5, 7 and 8). (See Appendix 3A)

$$R_{yx}(\tau) = \int_0^{\infty} h(\tau) R_{xx}(\tau-t) dt$$

where

$R_{yx}(\tau)$ is the cross-correlation between the system input $x(t)$ and the system output $y(t)$ as a function of the correlation delay τ

$R_{xx}(\tau)$ is the auto-correlation of $x(t)$ as a function of the correlation delay τ

$h(\tau)$ is the impulse function of the system under test

We have chosen the noise bandwidth to be large compared to the system bandwidth, hence $R_{xx}(\tau)$ can be considered a delta function impulse compared to $h(\tau)$. With the area under $R_{xx}(\tau)$ being A (a measure of the noise power), we have

$$h(\tau) = \frac{1}{A} R_{yx}(\tau)$$

$R_{yx}(\tau)$ can be obtained directly from an on-line correlator (Ref. 9). Alternatively, the $x(t)$ and $y(t)$ data can be recorded, digitalized, and $R_{yx}(\tau)$ obtained by processing in an off-line general purpose computer.

As with most experiments, there are a variety of practical compromises involved. The integrated noise power level A must be set low enough so that it does not grossly interfere with the normal process dynamics (this is due to the acceptance of the assumption of linear behavior for small perturbations about the normal operating point), yet if it is too low, an excessively long correlation period will be required to obtain $h(\tau)$ with the desired accuracy. The noise bandwidth should be large enough so that $R_{xx}(\tau)$ is a good impulse (so that the second equation can be obtained from the first without excessive error) yet if it is too wide, it will again require an unreasonably long correlation period to obtain $h(\tau)$ with the desired accuracy. The resolution of these compromises will be illustrated with the steel rolling mill example.

A five-stand rolling mill is a rather complex system. The control objectives are to hold the sheet tension and thickness constant at the output of each stand in spite of changes in the incoming sheet's thickness, tension, and hardness. The stands (pairs of motor driver rollers) strongly interact with each other in a complex bidirectional manner, assymetric with respect to time. Any change in tension between two stands will immediately affect the thickness coming out of each stand, and any change in thickness will immediately affect the tension on both sides of the stand. Any change in hardness will immediately affect both tension and thickness. Thickness perturbations propagate downstream through the rolling mill with the motion of the sheet and tension perturbations propagate much more rapidly in both directions, inducing thickness changes both upstream and downstream. This system can be considered as a series of instantaneous responses (compared to actuator response time) connected by time delays. The system dynamics are limited by actuator response. The study involved characterizing the effects of the control variables--roll speed, control signal and thickness screw setting control signal--with the controlled variables of thickness and sheet tension and roll speed.

A digital correlator (Ref. 9) was used to compare system inputs and outputs, and pseudorandom noise (Ref. 10) was added to the normal control signals. The internal system noise was characterized by auto-correlating the $y(t)$ output with no noise added to the input. Preliminary tests determined the response times of the actuators, and a 15 Hz bandwidth noise input was chosen; this is several times the system bandwidth. The input noise RMS amplitude was set at 1.8 RPM or 0.4% of the full value of the roll speed; a small enough perturbation so that the quasi-linear behavior assumption was valid. Figure 3-3a shows the speed deviations from the mean value of both the control signal and the roll tachometer signal. The pseudorandom noise perturbations are buried in the system's internal noise. Figure 3-3b shows the cross-correlation between the output speed and the roll speed control signal for various delays τ . The correlator has pulled the value of $R_{yx}(\tau)$ out of the noise, and has calculated $h(\tau)$, the roll speed response of the mill to a speed control impulse perturbation. Figure 3-3c is $\int h(\tau)d\tau$, the speed response of the mill to a control signal step function. It is important to note that this could not have been measured directly by applying

a small control step function since the response would have been buried in the internal system noise. The speed response to any small arbitrary control signal can be calculated by straightforward integration with $h(\tau)$. These preliminary tests were conducted without steel sheet in the mill.

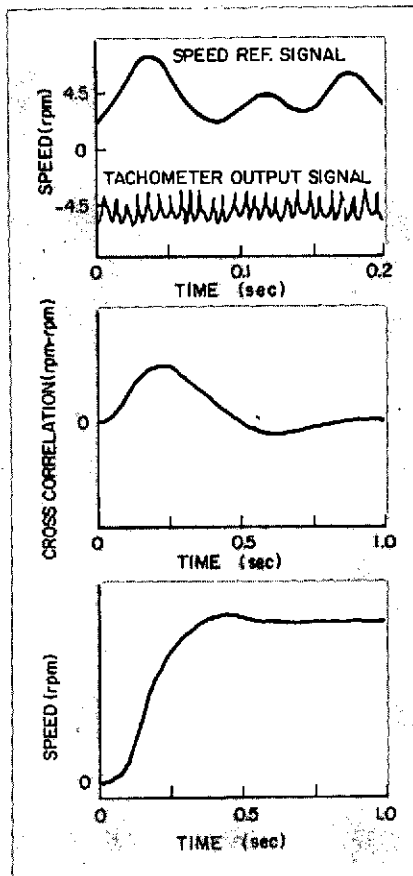


Figure 3-3. Speed Control Actuator

Tests with an input signal having a 15-Hz cutoff a-top) noise signal and speed output time functions, b-middle) cross-correlation between reference speed and roll speed of stand 1, c-bottom) step response, derived by integrating cross-correlation plot. (Taken from Reference 4.)

The mill response was then characterized with steel sheet passing through the five stands. The test noise signal had a bandwidth of 5 Hz (a few times the system bandwidth) and an RMS amplitude of 2.7 RPM (about 0.6% of full speed, and about 1.2% of the mill speed used in this test.) Figure 3-4a shows $-h(\tau)$, the roll speed response to a negative speed control reference impulse, as calculated by the digital correlator. A comparison of 3-4a and 3-4b shows that the former has a better signal-to-noise ratio and the latter has better time resolution, especially during the first 40 milliseconds. This is to be expected since the former was made with 5 Hz bandwidth stimulus noise compared to the latter's 15 Hz stimulus noise bandwidth.

Figure 3-4b shows a different cross-correlation: the reference speed decrease at stand 1 caused by an increase in strip tension between stands 1 and 2. Note the bump in the curve due to the resulting thickness change propagating to stand 2, affecting its speed and hence the sheet tension, and hence effecting automatic control reference speed back at stand 1.

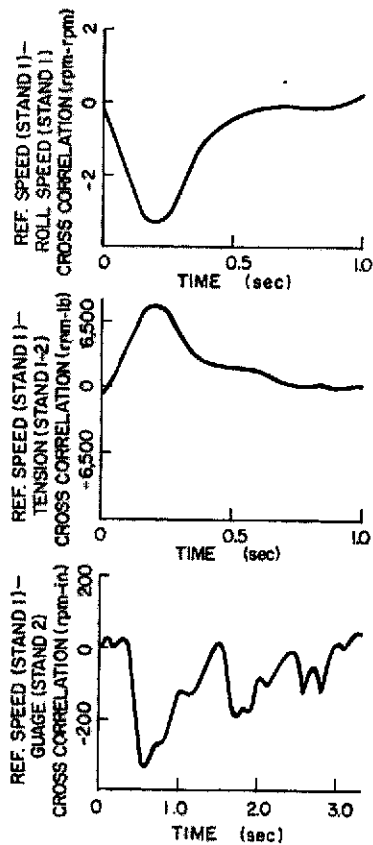


Figure 3-4. Cross-correlations of rolling process, with an input signal having a 5-Hz cutoff a-top) reference speed and roll speed of stand 1, b-middle) reference speed of stand 1 and tension between stands 1 and 2, c-bottom) reference speed of stand 1 and gauge out of stand 2. (Taken from Reference 4.)

Figure 3-4c shows the cross correlation between the reference speed at stand 1 and the thickness at stand 2. In this case, the thickness sensor was four feet from the work rolls, so there was a delay of 0.22 second. The tension increase caused the thickness to decrease simultaneously at both stands 1 and 2, causing the two large peaks separated by the 1.3 seconds required for a change in sheet thickness at stand 1 to propagate to stand 2. The small disturbances at 1.1 and 2.1 seconds on the two main peaks are due to an interaction with stand 3; when the thickness change entered stand 2, the tension changed between stands 2 and 3, resulting in a further thickness change at stand 2. A wide variety of quantitative data can be obtained from these curves. For example $\int_0^{\infty} h(\tau)d\tau$ for the curve

in 3-4b yields 2600 lbs/rpm as the coefficient relating a change in tension between stands 1 and 2 to a change in speed at the first stand. Similar processes were used to measure the different types of interactions between pairs of signals at different points in the five-stand rolling mill, resulting in a quantitative linear (reasonably valid for small perturbations) mathematical model of the behavior of the mill from which an optimum linear control program could be developed.

The above systems characterization study has been pedagogically useful for providing a degree of familiarity with some of the mathematics and instrumentation used in Wiener analysis. Small spacecraft valves, however, cannot be reasonably modeled with any small signal perturbation linear approximation. Small spacecraft valves exhibit extremely nonlinear behavior. Indeed, in many respects, they resemble a neuron of neuron chain; for the most part, they are open or closed, on or off. The next example will consider the successful Wiener analysis of a complex, highly nonlinear system--a chain of three neurons, each of a different type.¹¹ It must be emphasized that this analysis is of a chain of three particular neurons; it is not some sort of statistical averaging over a large ensemble. This example was chosen because the system involved is at least as complex and nonlinear as a small spacecraft valve. In addition, like most biological systems, it is extraordinarily noisy, and provides a far poorer signal-to-noise ratio than can be obtained in our valve studies. Finally, this study provides an application of the Wiener analysis procedure that is almost identical to that which will be suggested for the valves. The Wiener analysis of the neuron chain will be described, followed by a discussion of its application to valve characterization.

The system that was subjected to Wiener analysis was comprised of a horizontal cell which stimulates a bipolar cell which in turn stimulates a ganglion cell, all in the catfish retina. A noise generator injected a current $X(t)$ into the horizontal cell with a microelectrode, and another microelectrode measured the output voltage appearing in the ganglion cell. $Y(t)$ was the ganglion discharge poststimulus histogram. A preliminary inspection established the experimental parameters. A noise bandwidth of 25 Hz was chosen as being a few times as wide as the system bandwidth. The system memory was negligible beyond 300 milliseconds, so the Wiener kernels

were computed for values of their arguments up to 300 milliseconds. The system signal-to-noise ratio was such that the noise input train should exceed 30 seconds in order to limit the error in the calculated kernel values to less than 5%. A noise stimulus record 350 seconds long was used for $X(t)$.

Wiener has shown that³

$$Y(t) = \sum_{n=0}^{\infty} G_n[h_n, X(t)]$$

where t is time,

$Y(t)$ is the system's output

$X(t)$ is a random or pseudorandom input

$\{G_n\}$ is a complete set of orthogonal functionals, and

$\{h_n\}$ is the set of Wiener kernels that characterizes the system

$h(\tau)$ for the steel rolling mill in the previous linear example is a first order Wiener kernel, $h_1(\tau)$. The DC bias level of the system is the zero order kernel, h_0 . The system's non-linearities are characterized by the higher order kernels, $h_2(\tau_1, \tau_2)$, $h_3(\tau_1, \tau_2, \tau_3)$, etc. These kernels are simply higher order cross-correlations between the input white noise and the system response.

Let us take the power density spectrum of the input noise to be

$$\phi_{XX}(f) = P$$

P is the power spectrum level

f is the frequency

Lee and Schetzen have shown that¹²

$$h_n(\tau_1, \tau_2, \dots, \tau_n) = \frac{1}{n!P^n} \left\{ y(t) - \sum_{m=0}^{n-1} G_m[h_m, X(t)] \right\} X(t-\tau_1)X(t-\tau_2)\dots X(t-\tau_n)$$

where τ is the cross-correlation delay time.

h_1 can be obtained with either an on-line correlator or by using a general purpose computer running a correlation program on the recorded data. Higher order kernels are generally obtained by off-line computation, as was the case in this example. Figure 3-5a shows the computed Wiener

kernel $h_1(\tau)$. It represents the least mean square error value of the impulse response of the linear portion of the system. Figure 3-5b shows the computed value of the second order Wiener kernel $h_2(\tau_1, \tau_2)$. Figure 3-5c shows $h_2(\tau_1, \tau_2)$ as viewed from the bottom. $h_2(\tau_1, \tau_2)$ represents the non-linear interaction of two portions of the input signal τ_1 and τ_2 seconds in the past, as it affects the systems output in the present.

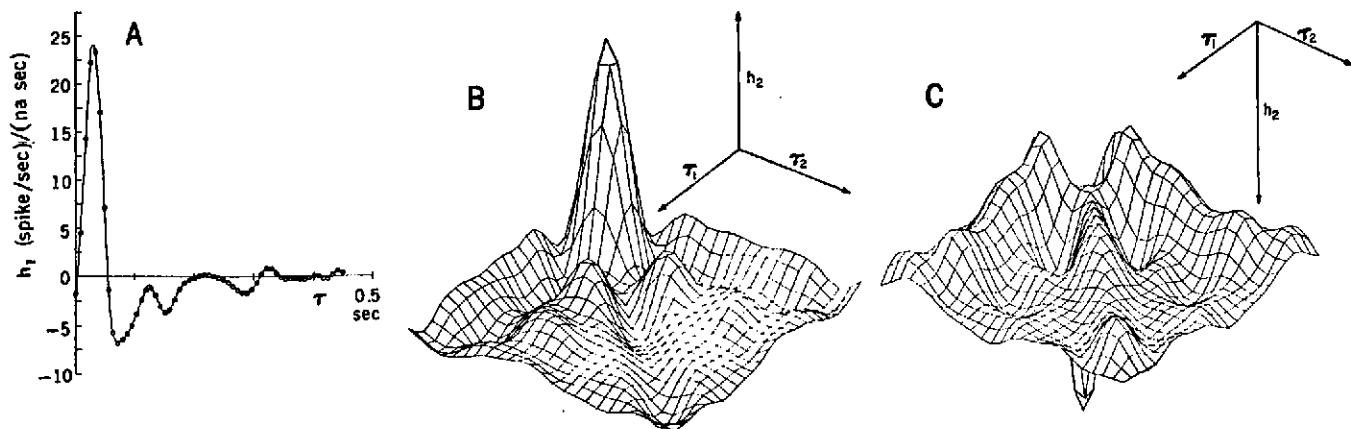


Figure 3-5. The first (A) and second (B and C) order kernels for the neuron chain formed by the horizontal cell, bipolar cell, and ganglion cell in the catfish retina. The first order kernel $h_1(\tau)$ is plotted as a function of time τ , and it is the impulse response of the linear part of the transfer function of the chain. The second order kernel $h_2(\tau_1, \tau_2)$, which describes the nonlinear behavior of the system, is represented by a three-dimensional solid made of the amplitude of the kernel plotted against τ_1 and τ_2 . As seen from the display, the second order kernel is symmetric about the diagonal line $\tau_1 = \tau_2$. For a clear view of the kernel h_2 , the amplitude axis is reversed in polarity in (C). View B shows the peaks well while view C permits a good view of the valleys (appearing as peaks) in $h_2(\tau_1, \tau_2)$. A peak represents a nonlinear interaction that enhances the response (facilitation), while a valley is an inhibitory nonlinear contribution to the response. The grid lines are spaced 8 msec apart. The maximum of h_2 is 53.0 and the minimum is -18.0 (spike/sec)/(na sec)². (Taken from Reference 11.)

Let us now compare the predicted output from the system with that which was determined experimentally. Figure 3-6a shows the noise input stimulus $X(t)$. Figure 3-6b shows the experimentally determined system output $Y(t)$. (Actually, the data are given for an average over ten experimental runs in order to improve the signal-to-noise ratio.) Figure 3-6c shows the linear prediction; i.e., only $h_1(\tau)$ was used. It can be readily seen that the linear prediction is quite poor, as expected. Figure 3-6d shows the predicted $Y(t)$ while using $h_1(\tau)$, $h_2(\tau_1, \tau_2)$, i.e., second order

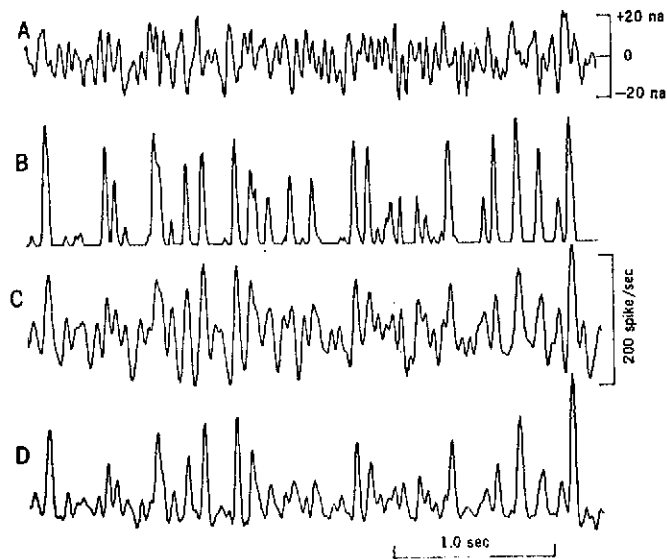


Figure 3-6. (Trace A) White-noise input current to the horizontal cell. (Trace B) Resulting experimental response of the ganglion cell [type B cell in (10)] represented by histograms with a bin width of 8 msec (average of ten experiments). (Trace C) First order Wiener model response to the same white-noise signal (h_1 only, that is, a linear model). (Trace D) Second order Wiener model response (h_1 and h_2 , that is, a nonlinear model). (Taken from Reference 11.)

Wiener analysis. The predicted signal is remarkably similar to the measured signal, especially when it is considered that the analysis was only carried to the second order and that the system was a biological preparation.

The Wiener procedure for characterizing non-linear systems is extraordinarily powerful and general. Let us consider its application, for example, to the valve flow transient signature experiments reported previously under this program. A series of flow transient signatures $Y(t)$ = flow volume versus time or $Y(t)$ = flow rate versus time were produced with $X(t)$ = a voltage step function from 0 to 22, 24, 26 volts. Let us replace, for example, this solenoid voltage step function with a pseudorandom noise $X(t)$, record $Y(t)$, and extract $h_1(\tau)$, $h_2(\tau_1, \tau_2)$ and perhaps $h_3(\tau_1, \tau_2, \tau_3)$ with a computer. The response predicted by the Wiener non-linear model would then be compared to the measured response.

How have we handled the three problems of signature analysis mentioned in the first part of this report? The first problem was of choosing an adequate set of stimuli. We solved this problem by using the most general stimulus possible, a noise stimulus with a bandwidth a few times as great as the system. The second problem, that of comparing response sets, has been solved through the use of the rigorous and well-defined mathematical procedures of correlation and the other mathematics of Wiener analysis. The third problem, that of knowing you are right, is solved by a comparison of the Wiener prediction of $Y(t)$ and the experimental $Y(t)$ for a general noise input $X(t)$.

In so far as any form of signature analysis can detect defects of manufacturing or changes brought about by aging, the Wiener procedures should provide the most general, sensitive and thoroughly defined technique of system characterization. Its practical limits will be in the cost of computer time; the time required to compute a kernel rises exponentially with its order. On the other hand, due to advances in computer production technology, the cost per calculation has been decreasing geometrically with time. The time for cost effective wide spread application of Wiener analysis has very probably already arrived, or if not, will certainly come very soon.

REFERENCES

1. Salvinski, R. J., " Study of Advanced Techniques for Determining Long-Term Performance of Components," TRW Interim Report No. 16568-6028-R000.
2. "Dimensional Analysis," Electro Technology Reference Series, August 1962.
3. Wiener, N., Nonlinear Problems in Random Theory, Massachusetts Institute of Technology Press, 1958.
4. Cumming, I. G., and May, R., "Using Correlation to Identify Process Dynamics," Instruments and Control Systems, July 1972, pp. 59-61.
5. Lee, Y. W., Statistical Theory of Communication, Wiley, New York, 1960.
6. Bose, A. G., Technical Report 309 (Research Laboratory of Electronics, Massachusetts Institute of Technology, Cambridge, 1956); George, D. A., Technical Report 355 (Research Laboratory of Electronics, Massachusetts Institute of Technology, Cambridge, 1959); Barrett, J. F., J. Electron, Control 15, 567 (1963).
7. "A Statistical Analysis of Pupil Noise," paper, pp. 140-152.
8. Wiener, N., "Extrapolation, Interpolation, and Smoothing of Stationary Time Series."
9. Anderson, G. C., Perry, M. A., "A Calibrated Real-Time Correlator/Averager/Probability Analyzer," Hewlett-Packard Journal, November, 1969.
10. Anderson, G. C., Finnie, B. W., Roberts, G. T., "Pseudo-Random and Random Test Signals," Hewlett-Packard Journal, September, 1967.
11. Marmarelis, P. Z., and Ken-Ichi Naka, "White-Noise Analysis of a Neuron Chain: An Application of the Wiener Theory," Science, Vol. 175, March, 1972, pp. 1276-1278.
12. Lee, Y. W., and Schetzen, M., Quarterly Progress Report 60 (Research Laboratory of Electronics, Massachusetts Institute of Technology, Cambridge, 1961).

APPENDIX 3A

CORRELATION, AUTO-CORRELATION, AND CROSS-CORRELATION

The process of correlation of two waveforms $X(t)$ and $Y(t)$ to yield the correlation function $R_{XX}(\tau)$ can be described as follows:

$X(t)$ and $Y(t)$ are multiplied by each other ordinate by ordinate and the products added together to obtain a single number, one value of R_{yx} at a particular ordinate. That is to say

$$\sum_{n=0}^n X(t_n)Y(t_n) \propto R_{xy}(0)$$

or more properly,

$$\lim_{T \rightarrow \infty} \frac{1}{T} \int_0^T X(t)Y(t) dt = R_{xx}(0)$$

to obtain $R_{xy}(\tau)$ for $\tau \neq 0$, the signal $Y(t)$ is time shifted by the amount τ before the ordinate by ordinate multiplication is performed. That is to say

$$\sum_{n=0}^n X(t_n)Y(t_n - \tau) \propto R_{xy}(\tau)$$

or more properly,

$$\lim_{T \rightarrow \infty} \frac{1}{T} \int_0^T X(t)Y(t-\tau)dt = R_{xy}(\tau)$$

Auto-correlation, $R_{xx}(\tau)$, is the correlation of a function with itself for various time shifts .

Cross-correlation $R_{xy}(\tau)$ is the correlation of two different functions for various time shifts τ .

4.0 THERMAL CONTACT STUDY

Thermal resistance techniques were investigated in the area of surface matching. Of interest is the work in contact thermal resistance of metal interfaces exhibiting varying flatness and surface roughness. The contact between two solid surfaces, such as a valve poppet and seat, occurs at individual junctions. Therefore, the real contact area is a very small fraction of the apparent area. Investigations and analysis were performed to establish the relationship of surface conditions and surface loading, on the thermal resistance of metal interfaces. Thus, if the thermal resistance of a metal interface (such as a valve poppet and seat) were measured, the surface conditions (roughness and waviness of the valve poppet/seat combination) could be obtained.

4.1 RESULTS & CONCLUSIONS

Several methods of detecting surface degradation were investigated. The test results and preliminary analysis indicate that the transient thermal resistance technique (TTR) appears to be superior for the following reasons:

1. It is simpler and less expensive than the other techniques considered in this report.
2. It can be employed in most valves and performs the real time degradation measurement unlike optical and stylus techniques.
3. If tested in gases, as shown in the analysis, the void volume can be determined.
4. There are no restrictions on the surface characteristics as in the case of the optical technique where the surface is required to be reflective.

The following table is a performance comparison of the acoustic and TTR techniques of detecting interface surface degradation.

COMPARISON OF THE ACOUSTIC AND TTR TECHNIQUE

<u>Parameters</u>	<u>Acoustic</u>	<u>TTR</u>
Response Time:	Less than one second	Ten seconds or greater depending upon the sensitivity and test configuration.
Sensitivity:	Analysis indicates that roughness detection of the order of microinches is possible. A very high frequency transmission is required to minimize the effect of other acoustic paths.	Tests and analysis indicate that surface degradation of one microinch can be detected. The sensitivity appears to be adequate to offset the effect of other thermal paths.
Modifications:	Requires greater modifications to implement in an existing valve.	Little or no modification is required to implement in an existing valve.
Simplicity and Cost:	Relatively more complex and requires costly equipments such as high frequency (10 Mega Hz) amplifier.	Relatively simpler and requires less costly equipment.

Based on the above discussion, the following recommendations are made:

1. Implement the TTR technique in a selected valve assembly
2. Perform the tests of surface degradation by cycling the valve. Correlate the test data of TTR measurements and leakage with the number of cycles.
3. Perform measurements on void volume and correlate with leakage.

4.2 SUMMARY OF PREVIOUS INVESTIGATIONS

The test results of studies performed by other investigators (Reference 1 and 2) on junction conductance are summarized in the following:

1. The thermal conductance of the interface joint increases with pressure. This increase is appreciable at low pressures but levels off at higher pressures.
2. At any given pressure level, the thermal conductance of the interface joint generally increases as the root square of the surface roughness decreases. However, surface roughness alone is not the dominant parameter in determining thermal conductance of contacts. Over-all flatness has a more important role in determining the intimacy of surface matching.
3. The thermal conductance changes with changes in the heat flow. This is believed due to the changes in the nonlinear stray thermal conductance.
4. In general, interfaces formed between rough specimens give more consistent data than those between smooth specimens.
5. For extremely smooth and flat surfaces in contact, the conductance values are highly sensitive to minute changes in the surface matching.
6. When all experimental conditions are kept constant, interface conductance increases slowly during long heating periods. However, the time effect is only a temporary one and the changes are mostly recoverable after cooling. Therefore, a time-dependent physical property of the metal surface when in contact must also be involved in the interface conductance.

Since the above referenced tests were conducted at very high heating levels (of the order of tens of kilowatts), the resulting high temperature gradients may have caused a change in the dimensional and thermal properties of the metal. Also the long duration measurements at high temperature may have increased

surface corrosion. Thermocouples were used in early tests to measure the temperature gradients (Ref. 1). Since then the state of the art in temperature measurements has improved considerably. The accuracy of the early test measurements could have been improved considerably by employing thermistors. The stability (β) sensitivity (α) and figure of merit (S) of different temperature sensor are given below: (Ref. 3)

Note that the figure of merit S is larger for sensors with a greater sensitivity if all have the same stability, also S is larger for sensors which are more stable (smaller β) given equal sensitivity.

Table 4-1.

<u>Item</u>	<u>Sensor</u>	<u>α = Sensitivity(T/°C)</u>	<u>β = Stability(°C)</u>	<u>$S = \alpha/\beta$</u>
1	Platinum Resistance Thermometer	0.34	± 0.03	11.4
2	Thermistor	4.0	± 0.05	80.0
3	Silicone Resistance	0.7	± 0.1	7.0
4	Quartz Crystal Resonator	0.0035	± 0.01	0.35
5	Thermocouple	0.00083	± 1.0	0.00083

It is apparent from the above data that the use of thermistors would have improved the accuracy of measurement considerably. Since the sensitivity of a thermistor is very high, a high heat flux is not required to measure the temperature gradient accurately.

The dependence of contact thermal resistance on different parameters is summarized in Table 4-2 (Reference 4). The real contact area, which is one of the factors determining the contact thermal resistance, is influenced by the following important factors:

1. Surface geometry which includes roughness and waviness
2. Surface properties which include plasticity, elasticity, hardness and modulus of elasticity.
3. Load and
4. Surface defects.

That the real contact area is independent of the surface roughness and waviness is not inconsistent with the laws of friction, namely

$$A_r = \frac{L}{P} \quad \text{and} \quad F = fL$$

where A_r = Real area of contact

F = Friction force

L = Normal Load

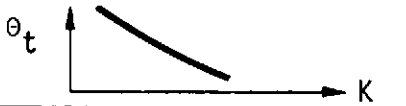
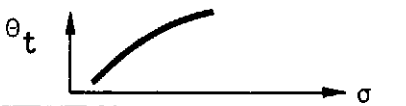
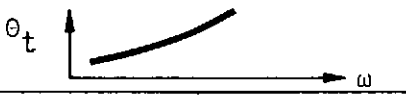
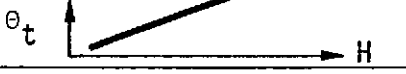
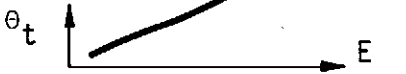
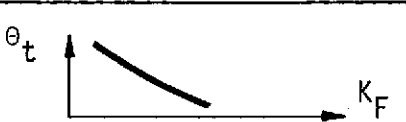
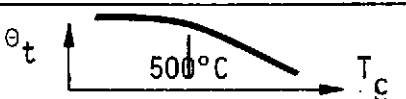
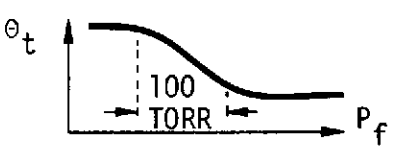
P = Yield stress of the asperities

f = Coefficient of friction

It has been stated (Reference 5) that the friction equation does not apply when surfaces are very smooth and when shear force is present along with the normal force. The friction equation is based on plastic deformation (yielding of asperities). However the contact process for real surfaces cannot be reduced to purely plastic or to purely elastic deformation of the microscopic asperities. Contact interactions of two solids are generally of an elastoplastic nature. This is because the initial contact usually occurs between the highest asperities which are few in number and which will bear all the applied load. There is subsequent redistribution of the pressures to the other asperities after the first contacting asperities have been crushed and the total load is finally supported by the major portions of surfaces of the bodies.

Theory of friction predicts that the real area of contact is independent of the roughness. However, tests indicate that thermal contact resistance increases with increasing roughness. (References 1, 4 and 6) This contradiction may be due to the thermal contact resistance dependence upon the real contact area and also on the height of the asperities. However, it should be noted that the influence of roughness on the thermal resistance is reduced with increasing roughness and contact pressure (Table 4-2). Also note that the degree of elastic deformation appears to be determining the dependence of the thermal resistance to the roughness and waviness of the surfaces in contact.

Table 4.2. PARAMETERS AFFECTING THERMAL CONTACT RESISTANCE (Ref. 4)

ITEM	PARAMETERS	IMPORTANT OBSERVATIONS (θ_t = Thermal Resistance)	GRAPHICAL REPRESENTATION
1	Apparent contact Pressure (P_c)	$\theta_t \propto P_c^{-x}$ For rough surfaces, $x \approx 1$ (Plastic deformation) For smooth surfaces $x = 0.33$ (Elastic deformation) The pressure cycle indicates memory effect.	
2	Metal Thermal Conductivity (K)	$\theta_t \propto K_m^{-1}$ where K_m = harmonic mean thermal conductivity	
3	Surface roughness (σ)	$\theta_t \propto k-(Y)^{-\sigma}$ for smooth surfaces and light loading. The influence is least where contact pressures are high and surfaces rougher	
4	Surface waviness (ω)	$\theta_t \propto (\omega)^Z$. Z is a constant. There is an interdependence between σ , ω , and θ_t	
5	Material hardness (H)	$\theta_t \propto H$ for rough, flat surfaces over a large contact pressure range	
6	Modulus of electricity (E)	$\theta_t \propto E$ for increasing elastic modulus or stiffness)	
7	Interstitial fluid thermal conductivity (K_f)	$\theta_t \propto (K_f)^{-1}$. θ_t decreases with increasing K_f The linear dependence of θ_t on K_f indicates absence of convection effects	
8	Contact temperature level (T_c)	θ_t decreases with increasing T_c . The effect is predominant above 500°C.	
9	Interstitial pressure (P_f)	θ_t is essentially independent of P_f for $P_f > \text{one atm pressure}$ and $P_f < 10^{-5}$ torr. The transition region is about 100 TORR wide and it shifts to left for smoother surfaces, and heavier load.	

4.3 DERIVATION OF EQUATIONS USED IN CONTACT THERMAL RESISTANCE ANALYSIS

NOMENCLATURE

- a_r = The average real area of each asperity contact
- A_r = Total area of contact
- N = Total number of asperities in contacts
- A_a = Total apparent area of contact
- w = Thermal power flowing through the contact area
- T = Temperature
- ΔT = Temperature gradient
- θ = Thermal resistance
- K_b = Effective thermal conductivity of the two metal surfaces in contact
- L = Sum of the center line average (CLA) readings for the two test surfaces
- σ = R.M.S. roughness
- L_1, L_2 = Average roughness of the surfaces 1 and 2
- $\phi(F)$ = Geometric factor dependent on the area ratio
- $K_m = \frac{2K_1K_2}{K_1+K_2}$, the harmonic mean of thermal conductivity of solids (1) and (2)
- $\epsilon^2 = \frac{\text{Real Area}}{\text{Apparent area}} = \frac{A_r}{A_a}$
- β_1 = Maldistribution factor
- S = Number of intersections of the profilogram trace with respect to the baseline per unit length of the trace
- σ_y = Yield stress of the material
- P_a = Apparent contact pressure
- c_i = Radius of the contact junction
- C = Radius of the contour

In deriving the equation for contact thermal resistance of two flat surfaces in contact, the following assumptions are made:

- There are no layers of foreign materials such as oil, contaminants, etc.
- The temperature remains constant over the entire real contact area.
- The waviness of both surfaces is very small compared to the roughness.
- The steadystate heat flow condition exists.
- There is a hard vacuum and low enough temperatures to eliminate gas conduction and radiation effects.
- There are no oxide films.
- Every circular contact spot diameter is much smaller than the radii of curvature of the contacting asperities.

Since the total thermal conductance of the contact between two surfaces is the sum of the conductances of the individual points of contact, the total thermal resistance, θ , which is the reciprocal of thermal conductance is:

$$\theta = \frac{\text{Temperature gradient across the contact area}}{\text{Power through the contact area}}$$

The Fourier heat conduction equation is: (reference 7)

$$w = \frac{-K_b \Delta T A_r}{L}$$

$$\text{Therefore } \theta = \frac{\Delta T}{w} = L/K_b A_r \quad (1)$$

$$\text{Note: } K_b = \frac{L K_1 K_2}{L_2 K_1 + L_1 K_2} \quad (2)$$

$$\text{where } L = L_1 + L_2$$

$$\text{and } a_r = \frac{a_{r1} + a_{r2} + \dots + a_{rn}}{N}$$

$$\therefore A_r = N a_r$$

A general expression for thermal contact resistance based on the

pinching effect (narrowing at asperity contact area) which considers the number, size and distribution of contact spots rather than the magnitude of the total real area, has been derived in reference 4:

$$\theta = \frac{8\phi_1}{\pi K_m \sum_{i=1}^N \frac{c_i}{\beta_i}} + \frac{8\phi_2}{\pi K_m C} \quad (3)$$

Note that the first term in equation (3) is due to the surface roughness, and the second term is due to the surface waviness.

If the maldistribution effect is negligible, $\beta_i = 1$, and if the surface waviness is also negligible, the second term in equation (3) goes to zero. The summation of the radius of the circular spot $\sum_{i=1}^N c_i$ can be obtained from the following equation:

$$\sum_{i=1}^N c_i = \frac{A_s S}{2} \quad (4)$$

The number of intersections of the trace per unit length, 'S' can be obtained from surface profile data. Equation (4) is derived with the assumption that the surfaces are nominally flat and contact spot distribution is the same as for Equation (3).

The geometric factor is defined as: $\phi \approx \left[\frac{\pi}{16} - \frac{\epsilon}{4} \right]$

where the area ratio $\epsilon^2 = \frac{P_a}{3\sigma_y}$ (5)

For lightly loaded wavy smooth surfaces, the thermal resistance component due to waviness will be dominant if the contact function radii c_i are very small compared to the contour radius C and C is extremely small relative to the apparent area. Then equation (3) reduces to the following:

$$\theta = \frac{\bar{\beta}}{2K_m N c} + \frac{1}{2K_m C} \quad (6)$$

where $\bar{\beta}$ = average maldistribution factor = 1.1

4.4 DETERMINATION OF CONTACT SPOT RADIUS C:

The shape and size of the asperities depend upon the mechanical process used to generate the surface. The number, shape and size of individual contacts therefore will depend upon the geometry and material properties. Table 4-3 below gives an indication of the maximum height of asperities σ and the radius of curvature ρ transverse and parallel to the direction of mechanical preparation.

Table 4-3

<u>Process</u>	<u>σ(microns)</u>	<u>ρ(microns)</u>	
		<u>Transverse</u>	<u>Longitudinal</u>
Casting	30-120	1000-1500	1000-1500
Shot Blasting	3-12	100-150	100-150
Turning	3-12	20-80	60-120
Milling	6-20	40-100	80-150
Planing	6-20	40-100	80-150
Grinding	1-5	5-20	250-15,000
Lapping	0.08-0.3	15-250	7000-35,000

The average contact size has been calculated employing the classical theory of Hertz with the following assumptions:

1. The deformation between contacts is elastic.
2. The asperities are hemispherical. For highly polished mirror like surfaces this assumption is valid (reference 4).
3. The contacting asperities touch at the apex only, and not at the shoulder. The average contact radius \bar{c} is:

$$\bar{c} = 1.1 \left[\frac{F_c}{2E \rho} \right]^{1/3} \quad (7)$$

where: F_c = contact force per each asperity
 E = Modulus of elasticity
 ρ = Radius of curvature

Note that the radius of curvature is proportional to the asperity height. \bar{c} is computed for aluminum surfaces of roughness 110 μ inch RMS employing the classical theory of Hertz and it ranges from 16.8 to 17.5 microns for the pressure ranges of 100 to 10,000 psi. The calculation indicates that \bar{c} is essentially independent of apparent pressure. The increase in total real area of contact with pressure is therefore not due to the increase in \bar{c} but N, the total number of contact spots.

\bar{c} is computed for aluminum and steel for different surface roughness of interest, employing equation (7) as shown in Figure 4-1 and Table 4-4 below.

Table 4-4

Surface Roughness Microinches, RMS	Aluminum \bar{c} , micron	Steel \bar{c} , micron
1	3.5	2.5
10	7.6	5.4
50	13.0	9.2
100	16.4	11.6
110	17.0	11.9
200	20.6	14.6

The total number of contact points N can be computed from the following equation:

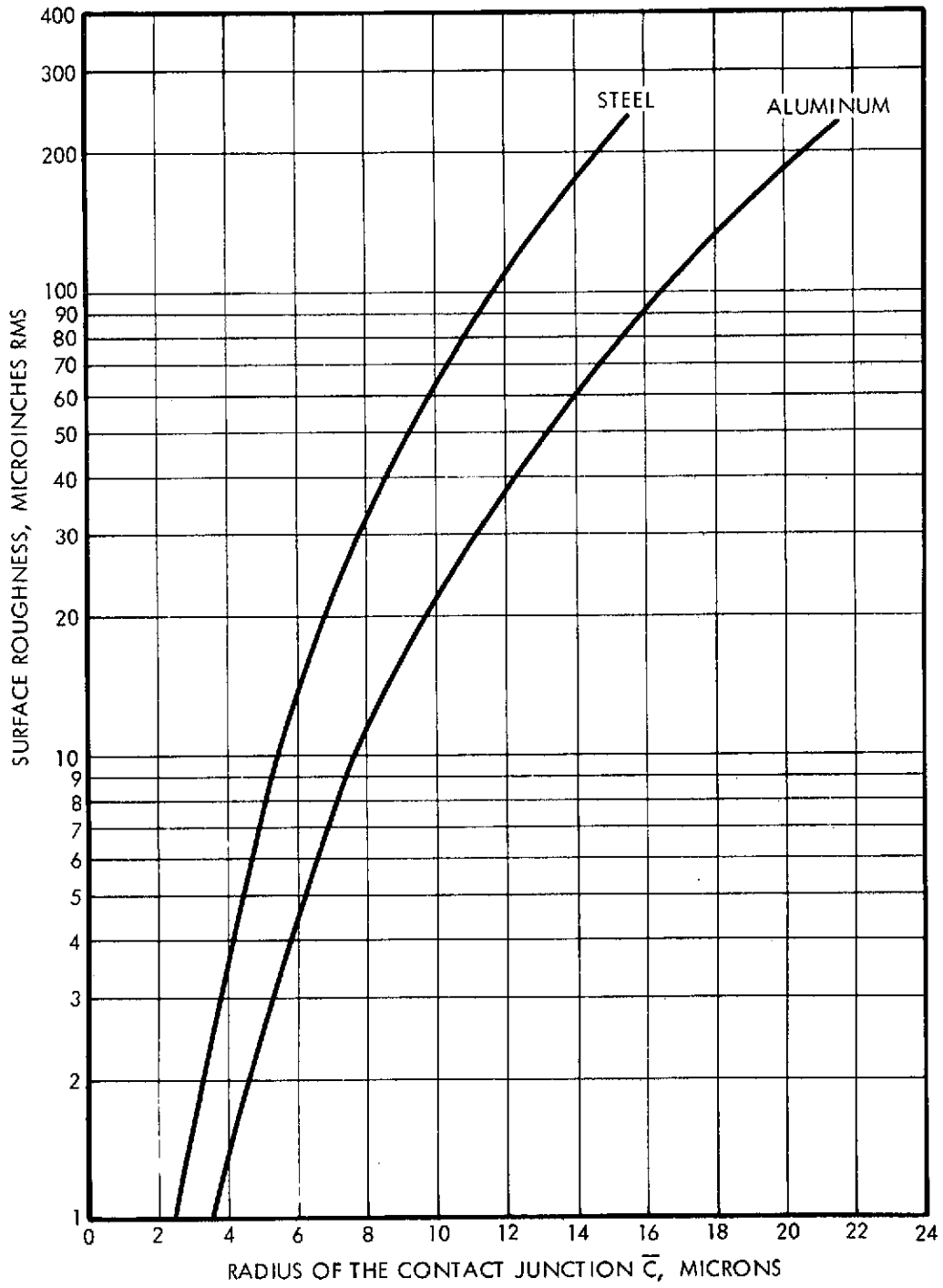
$$n = \frac{P_a}{\pi \bar{c}^2 \cdot 3\sigma_y} \quad (8)$$

It should be noted that \bar{c} represents the average radius of contact spot and c_i the radius of a particular contact spot. For any particular load and surface geometry, there will be a spectrum of contact spot sizes. The average contact spot size represents the largest percentage of actual contacting asperities.

Equation (8) is based on the assumption that the real contact area can support only the stress at which the material begins to yield.

The factor of 3 in Equation (8) may be different if the surfaces are work hardened, or if the RMS slope of the contacting asperities becomes quite small. Equation (8) therefore is approximate.

Figure 4-1
Average Contact Radius, \bar{c}
vs
Surface Roughness



4.5 DETERMINATION OF VOID VOLUME

The thermal conductance of the contact between two surfaces in the presence of gas is the sum of the conductance of the individual points of contact and the conductance of the gas layer. The heat transfer in gas occurs solely by conduction.

The total conductance is:

$$h_T = h_s + h_g$$

where: h_s = conductance associated with solid contacts

h_g = conductance associated with gas medium

$$\begin{aligned} \text{Note that } A_a h_g &= \frac{W}{\Delta t} = \frac{1}{\theta} \\ &= k_g \frac{A_g}{L_g} \end{aligned} \quad (9)$$

Where A_a = apparent areas

k_g = gas conductivity

A_g = Real area through which the power flows across the gas layer by conduction

L_g = Average thickness of the gas layer

Since h_T and h_s are known from the measurement of thermal contact resistances (h_T in presence of gas and h_s in absence of gas), h_g can be found.

$$\text{From the equation } A_a h_g = k_g \frac{A_g}{L_g},$$

the ratio $\frac{A_g}{L_g}$ is obtained since all other quantities are known.

$$\text{or } \frac{A_g}{L_g} = \frac{A_a h_g}{K_g}$$

However A_g is known from the following equation:

$$A_g = A_a - A_r$$

where: $A_r = N a_r$
 $= N\pi c^2$

and $L_g = \frac{K_g}{A_a h_g} (A_a - A_r)$

∴ The void volume V is:

$$V = A_g L_g = \frac{K_g}{A_a h_g} (A_a - A_r)^2$$

4.6 REFERENCED TEST DATA ANALYSIS

The test data of Reference (4) are discussed. A stainless steel 416 sample was tested with the following characteristics:

Surface roughness: $\sigma_1 = 42$ microinches
 $\sigma_2 = \text{small}$

Thermal conductivity: $K_m = 14.6 \frac{\text{BTU}}{\text{Hr-ft-}^\circ\text{F}}$

The measured thermal conductance, h, as a function of apparent pressure P_a and roughness is given in Table 4-5.

The computed contact spot radius, \bar{c} , and number of contact spots per square feet are obtained employing equations (7) and (8). The thermal conductance, h, is related to thermal resistance, θ , as follows:

$$h = \frac{1}{\theta A_a} \quad (10)$$

The thermal conductance for the different pressures is computed employing equations (6) and (10).

The second term in equation (6) which accounts for the effect of waviness, is not computed because of the lack of data on waviness.

Table 4-5. Measured and Computed Thermal Conductance With Pressure and Surface Roughness as Parameters

Material	Roughness μ inches		Total RMS μ inch	Contact Spot Radius \bar{c} μ in/ μ ft	Contact Pressure Pa - Psi	Yield Stress σ_y Psi	Spot Area $\pi \bar{c}^2 = A$ ft ²	Number Density $\frac{p_a}{3\sigma_y A}$ $N = \frac{p_a}{3\sigma_y A}$	Thermal Conductivity K_m BTU Hr-ft ² -°F	Computed Thermal Conductance $h = \frac{2K_m \bar{c} N}{1.1}$	Measured Thermal Conductance BTU Hr-ft ² -°F	Percent Deviation From Measured Conductance
	σ_1	σ_2										
SS 416	42	0	42	360/30	131	110,000	2.85x10 ⁻⁹	1.41x10 ⁵ 1.02x10 ⁶ 4.08x10 ⁶	14.6	113	158	-28.5
					950				800	1080	-24.9	
					3800				3200	3280	- 2.5	
SS 303	190	0	190	568/47.2	131	114,000	7.1x10 ⁻⁹	5.38x10 ⁴ 16.2x10 ⁴ 45.2x10 ⁴	10.0	46.8	100	-52.8
					395				140	200	-30.0	
					1100				394	410	- 4.0	
SS 303	132	76	152	540/45	131	114,000	6.4x10 ⁻⁹	5.97x10 ⁴ 18.2x10 ⁴ 47.8x10 ⁴	10.0	49.0	140	-64.0
					400				148.5	255	-41.5	
					1050				392.0	610	-35.8	
SS 416	131	108	170	560/46.6	131	110,000	6.8x10 ⁻⁹	5.92x10 ⁴ 2.26x10 ⁵ 6.14x10 ⁵	14.6	73.5	170	-56.5
					500				280	326	-14.2	
					1359				760	510	+49.0	

Note that the computed conductance (Table 4-5) is smaller than the measured conductance. If the waviness effect had been included, the deviation would have been larger. However, the effect is insignificant if the waviness term in Equation (6) is small.

The computed conductance can be obtained by employing Equation (4) instead of Equations (7) and (8). A difficulty arising in computing the thermal conductance employing Equation (4) is that there is no way to compute thermal conductance with contact pressure as a parameter. Also Reference (4) did not provide the parameter 'S', the number of intersections of the profilogram trace per unit length of the trace. Therefore, Equation (8) is used in the sample computation below:

Sample Computation of thermal conductance

$$\sigma_1 = 42 \text{ micro inches RMS}$$

$$\sigma_2 = 0 \quad \sigma_T = \sigma_1^2 + \sigma_2^2 = 42 \text{ } \mu\text{inches}$$

$$K_m = 14.6 \text{ BTU/Hr-Ft}^2\text{-}^\circ\text{F}$$

$$\begin{aligned} \text{Contact Spot Area} &= \pi \bar{c}^2 \\ &= \pi(36)^2/10^{12} \text{ inch}^2 \\ &= 2.85 \times 10^{-9} \text{ ft}^2 \end{aligned}$$

$$N \pi \bar{c}^2 = \frac{Pa}{3 y}$$

For Pa = 131 psi from the 1st line of Table 4-5,

$$\begin{aligned} N &= \frac{Pa}{3 \sigma_y \pi \bar{c}^2} = \frac{131}{3 \times 110,000 \times 2.85 \times 10^{-9}} \text{ number per ft}^2 \\ &= 141,000 \text{ lb/ft}^2 \end{aligned}$$

$$\begin{aligned} \text{Thermal Conductance } h &= \frac{1}{A_a \theta} && (10) \\ &= \frac{2 K_m \bar{c} N}{1.1} \end{aligned}$$

$$\begin{aligned}
&= \frac{2 \times 14.6}{1.1} \times \frac{30}{10^6} \text{ ft} \times 0.141 \times 10^6 \\
&= 113 \text{ Btu/Hr-ft}^2\text{-}^\circ\text{F}
\end{aligned}$$

4.7 MORE RECENT THERMAL RESISTANCE MEASUREMENTS

The important objectives of the thermal resistance measurement test are to confirm the test results with those obtained from the analysis and determine if the thermal testing method is practical.

4.7.1 Description of Test Specimens

Sets of Jo blocks were selected as test specimens for the thermal resistance measurement test. The specifications of the Jo blocks are as follows:

Dimensions: 0.500 X 1 3/8" X 0.375

Surface finish of surfaces 0.50" apart: 0.5 μ in RMS

Contact surface dimension: 3/8" X 1 3/16"

Contact surface flatness: less than 3.0 μ inches

Material: Steel

The required roughness of the surface of each test specimen is obtained by employing diamond grit of 3 to 10 micron size. The measured roughness and waviness of each specimen is given in Table 4-6.

The roughness and waviness of each prepared surface were measured on a Bendix profile recorder.

The charts are shown in Figures 4-1a through 4-1p, Appendix 4-a.

TABLE 4-6 CHARACTERISTICS OF TEST SPECIMENS

Item	Test Specimen Identification Number	Width Data		Length Data	
		Waviness Peak to Peak Microinches	Roughness Peak to Peak Microinches	Waviness Peak to Peak Microinches	Roughness Peak to Peak Microinches
1	1-7 (Reference block)	5.0	0.75	5.0	0.75
2	1-9	2.0	0.75	5.0	0.75
3	1-1	2.0	0.75	5.0	0.75
4	10-4	-	-	25.0	10.0
5	50-8	80.0	70.0	80.0	50.0
6	50-5	80.0	125.0	80.0	125.0

4-18

Note that the surface roughness was obtained as desired. However, the waviness was difficult to control in spite of the fact that the lapping was performed under very tightly controlled conditions.

The original Jo blocks did not always pass the manufacturing specification of flatness (waviness). However, the effect of flatness may be minimized by applying large loads.

4.7.2 Sensors

Twelve thermistors, Fenway part number Gb31L4, were selected. Nominal data on each thermistor is as follows:

Nominal resistance at 25°C: $1000 \pm 20\%$ ohms

Assembly description: Glass coated bead

Bead diameter: 0.043"

Lead diameter: 0.004"

Dissipation constant: 0.70 milliwatt/°C in free air

Time constant: 2.0 seconds

Resistance ratio (Resistance at zero°C to that at 50°): 7.3

The thermistors were aged by subjecting them to temperature cycles for two weeks. Each temperature cycle consisted of approximately twelve hours at 250°C and four hours at 25°C. The resistance of each thermistor was measured at $25^\circ\text{C} \pm 0.02^\circ\text{C}$ in an oil bath with ten micro-amps current flowing through the thermistors. The resistance bridge employed was ESI 242B.

The temperature difference ΔT across the interface is measured with a temperature sensor consisting of two matched thermistors having essentially the same resistance/temperature characteristics.

The criteria of the temperature sensor design are:

- o Two bead thermistors should be in as close contact to the mating surfaces of the Jo blocks as possible so that the thermistor will attain essentially the same temperature as the Jo block surfaces.
- o It should be convenient to mount the sensor so that each thermistor is symmetrically located across the interface and close to the interface.
- o The sensor should be mechanically rugged.

One sensor was constructed with the detail shown in Figure 4-2.

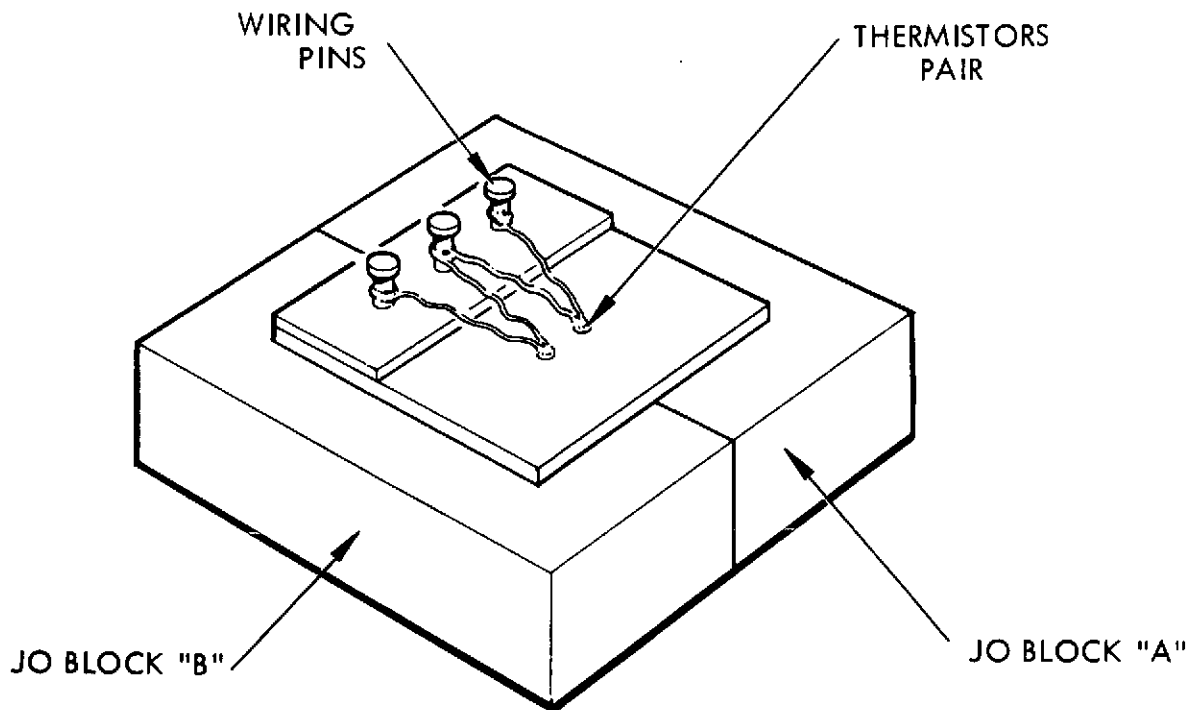


Figure 4-2 Temperature Sensor Configuration

4.7.3 Test Setup Description (Preliminary Tests)

To determine thermal resistance across the interface, the knowledge of accurate heat flow rate through the interface along with temperature difference ΔT is required. The electrical heater (Dale Ohm $45\Omega/25$ watt) is mounted such that the heat leakage through the stray thermal resistances are small and almost all the thermal power flows through the specimen interface.

The test setup schematic is shown in Figure 4-3 and the photographs of Figures 4-4 and 4-5.

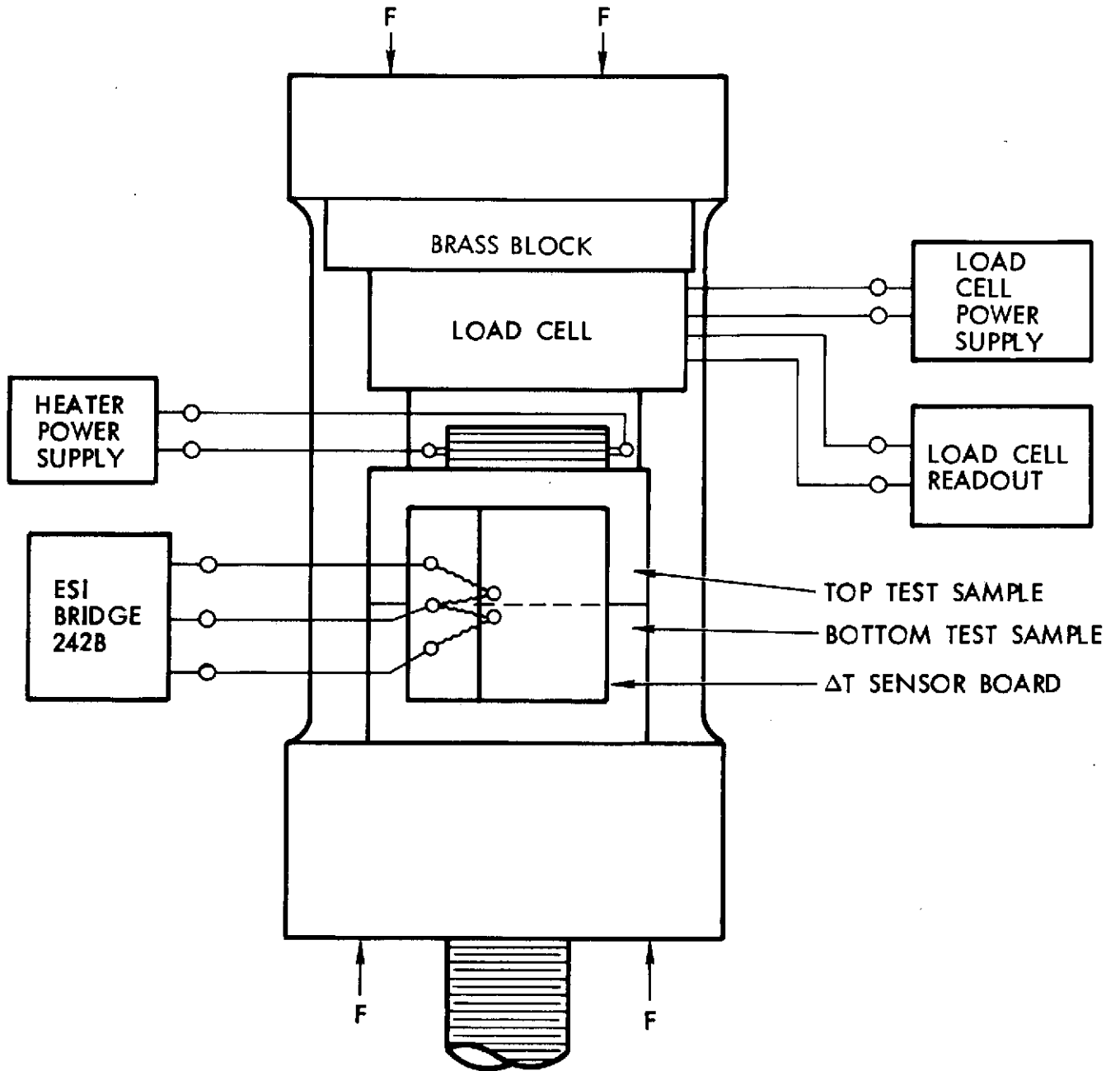


Figure 4-3. Test Setup Schematic



Figure 4-4. Photograph of Test Setup

A heat barrier constructed of phenolic blocks and steel plates is inserted between the load cell and the specimens. A machinist vice is used to generate the pressure across the interface. Since the phenolic is slightly plastic the drop in the load was observed as a function of time. However, the drop was less than 5% in a period of 12 hours.

The instruments employed in the test setup are as follows:

Load cell: Bytrax JP-1KD/1000 lbs full scale

Load cell power supply: Hewlett Packard/Harrison 865

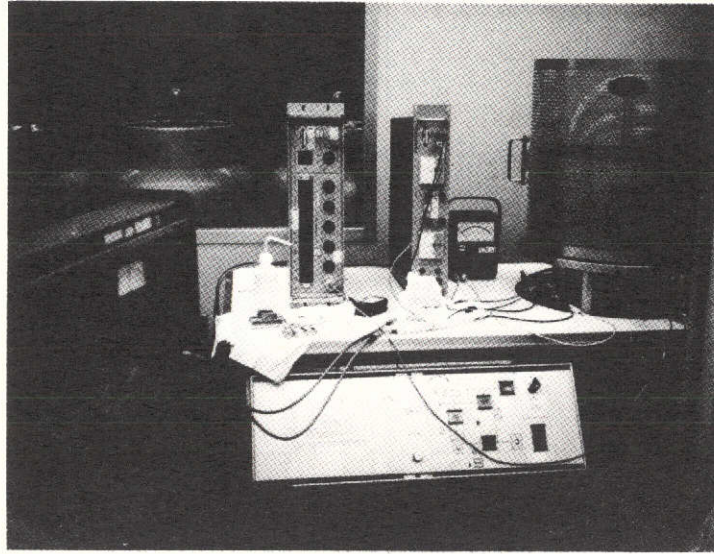
Load cell readout: Digital voltmeter, Cimron 9300

Heater: Dale ohm, 45 ohms/25 watts

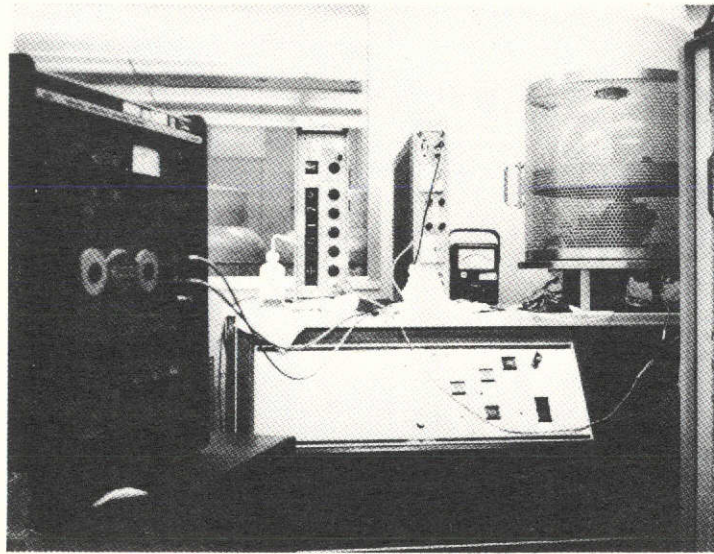
Heater power supply: Hewlett Packard 6271A

Temperature sensor power supply: Fluke 332 Voltage Standard

Sensor readouts: Differential voltmeter Hewlett Packard 3420
ESI Bridge 242B

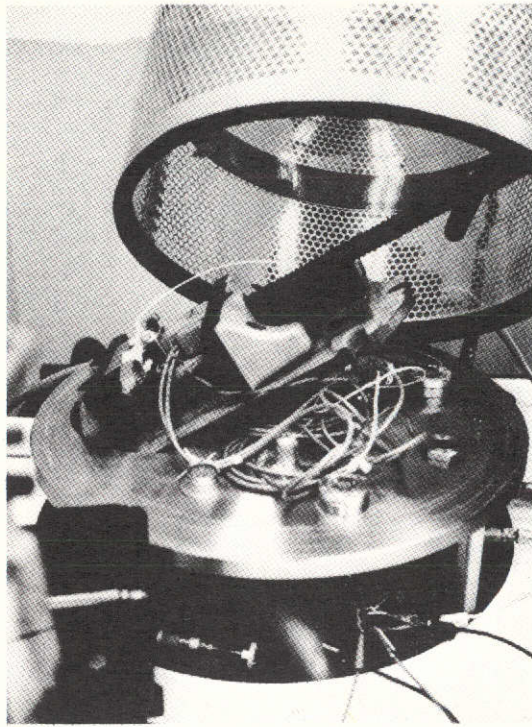


(a)

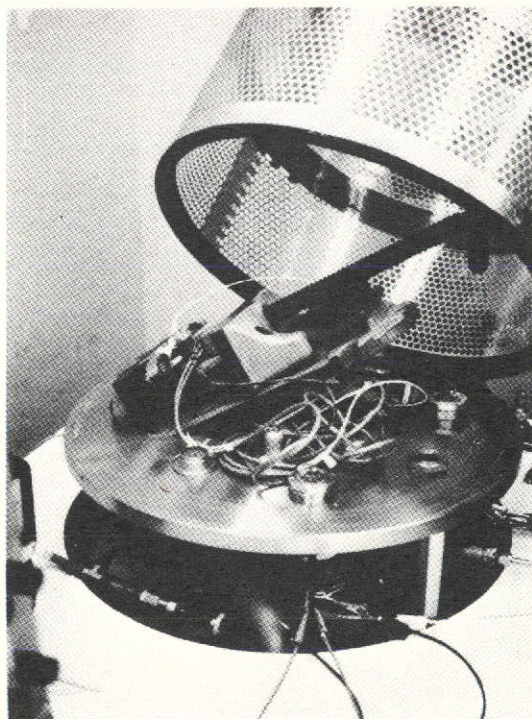


(b)

Figure 4-5. Photographs of Test Setup in Vacuum



(c)



(d)

Figure 4-5. Test Setup - Closeup in Vacuum

4.8 PRELIMINARY TEST RESULTS

The preliminary test was conducted employing two specimens.

The range of load across the interface was varied from 20 to 500 pounds. The thermistor resistance was measured at 0.45 watt and 11.2 watts heater power levels.

The temperature difference ΔT is obtained from the slope of the resistance-temperature curve (Figure 4-6). The thermistor resistance-temperature curve is expressed mathematically as follows:

$$\frac{R}{R_0} = \text{Exp } \beta \left(\frac{1}{T} - \frac{1}{T_0} \right)$$

where: R_0 is the resistance at ambient temperature T_0
 R is the resistance at any other temperature T
 β is the constant dependent on the thermistor material

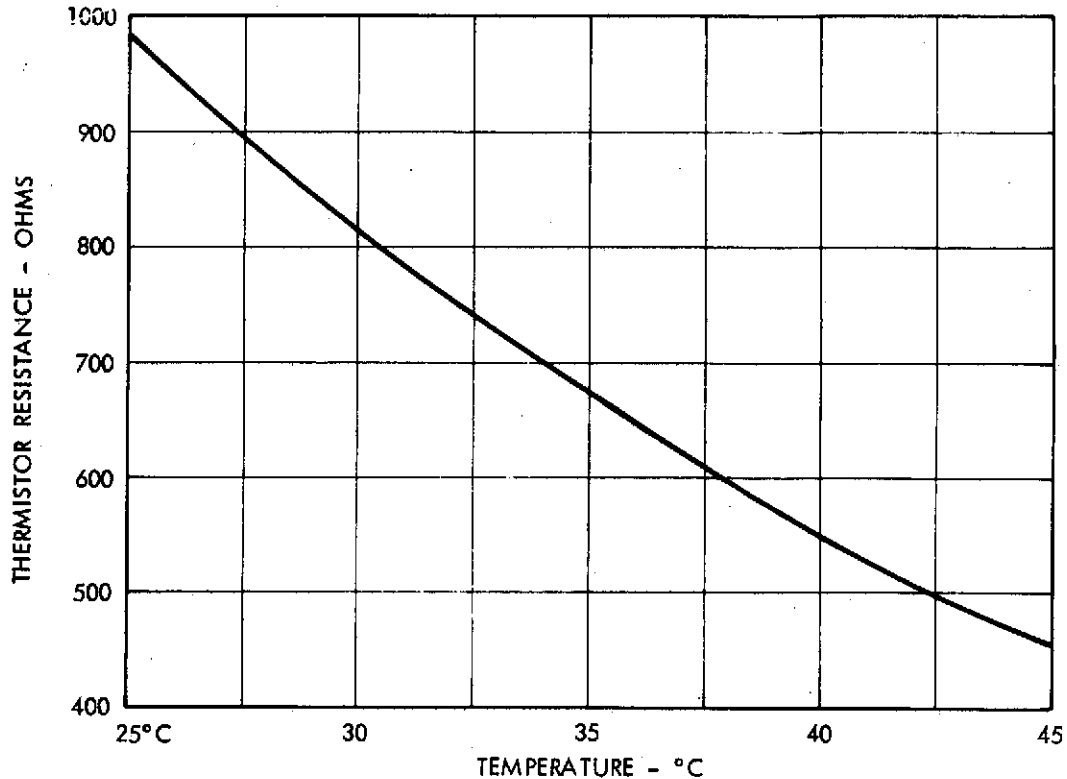


Figure 4-6. Thermistor Resistance Vs. Temperature Curve

Note that for these bead thermistors, the ratio of

$$\text{resistance } \frac{R_0}{R} = 7.3 \text{ where } T_0 = 273^\circ\text{K}$$
$$\text{and } T = 323^\circ\text{K}$$

Substitution of T , T_0 and $\frac{R_0}{R}$ gives the value of $\beta = 3500$.

The preliminary test data taken in air is shown in Table 4-7.

The average temperature difference ΔT obtained from the slope of the resistance-temperature curve for a thermal power, W , of 11.2 watts is:

$$\Delta T = 1.3^\circ\text{C}$$

$$\begin{aligned} \text{The apparent interface area} &= 1.19'' \times 0.375'' \\ &= 0.445 \text{ in}^2 \end{aligned}$$

Assuming all the thermal power flows through the interface the thermal conductance

$$\begin{aligned} h &= \frac{1}{\theta A} = \frac{W}{\Delta T A_p} \\ &= \frac{11.2 \text{ watts} \times 3.41 \text{ Btu/hr/watt} \times 144 \text{ in}^2/\text{ft}^2}{1.3^\circ\text{C} \times 1.8^\circ\text{F}/^\circ\text{C} \times .44 \text{ in}^2} \\ &= 5300 \frac{\text{BTU}}{\text{Hr-}^\circ\text{F-Ft}^2} \end{aligned}$$

It should be noted however that not all of the thermal power flows through the interface. Therefore, the actual thermal conductance is less than 5300 BTU/Hr- $^\circ\text{F-Ft}^2$.

The measured thermal conductance value in Reference 6 for 1.6 micro inch surface roughness for stainless steel is in the range of 2500 to 3000 BTU/Hr- $^\circ\text{F-Ft}^2$.

Table 4-7. Preliminary Thermal Resistance Test Results

Load Lbs	Heater Current Amps	Thermistor Resistance			$\Delta T = \frac{\Delta R}{Slope}$ °C
		R ₁ Ohms	R ₂ Ohms	ΔR Ohms	
220	0.500	461	485	24	1.4
320	0.500	423.2	445	21.8	1.3
458	0.500	412	433	21	1.24

The average slope at R at 450 ohms is 17 ohms/°C.

4.9 MODIFICATION OF TEST SETUP

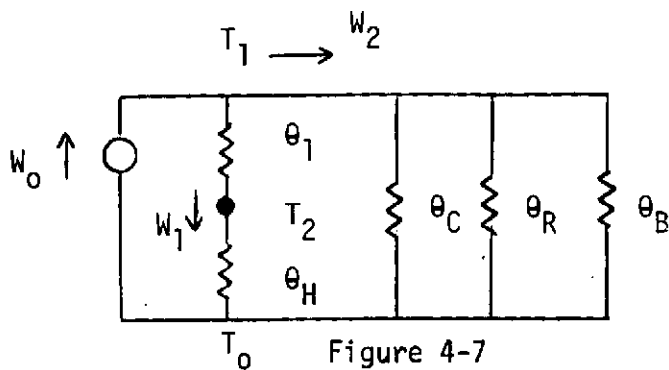
The thermal resistance measurements were conducted employing the setup described in previous pages. It was observed that the temperature difference ΔT across the interface increased with increasing pressure across the interface. However, the analysis predicts that for a constant heat flow through the interface, the ΔT will decrease with increasing pressure. Therefore the test setup was examined carefully. It was determined that the assumption of constant heat flow was not valid as explained below:

Though the heat generation was unchanged with pressure the heat flow through the interface was increasing with pressure. This is apparent from the following equation:

$$\Delta T = W_1 \theta_1$$

where: W_1 = heat flow through the interface
 θ_1 = thermal resistance

For a constant W , θ decreases with increasing pressure (see Table 4-2). Therefore, ΔT is expected to be decreasing with increasing pressure. The conclusion that W_1 was not constant is based on the following simplified thermal circuit diagram (Figure 4-7).



$$W_0 = W_1 + W_2$$

$$W_1 = \frac{(T_1 - T_0)}{\theta_1 + \theta_H}$$

Figure 4-7

θ_C = thermal resistance due to the convective heat flow (for tests in air)

θ_R = thermal resistance due to the radiative heat transfer to the surroundings

θ_B = thermal resistance of the heat barrier introduced between the top Jo block and the load cell

θ_1 = thermal resistance of the two Jo blocks interface. The ΔT is measured across this junction

θ_H = thermal resistance of the junction formed by the Jo block and the heat sink.

Assuming that θ_B , θ_C and θ_R are constant, increasing pressure decreases θ_1 and θ_H . As a result W_1 increases and W_2 decreases.

The effect of pressure on W_1 was minimized by the following steps:

- Insulate the sample completely with insulating material (Dow Corning Sealant 731 RTV). This will increase θ_C , θ_R and θ_B and reduce W_2 . As a result, the effect of pressure on W_1 is reduced.
- Minimize θ_H by cementing the lower sample to the heat sink under pressure. This minimizes θ_H and makes it essentially independent of the pressure.

The corrections stated above gave the desired results. The tests were conducted on five different types of surface roughnesses (0.75 to 125 microinches P-P) in the load range of 10 to 200 pounds. The power level was maintained constant at 1.25 watts. The roughness of each specimen was measured on the Bendix profile recorder (Figure 4-1, Appendix 4-a) and the results tabulated in Table 4-6.

4.10 THERMAL TIME CONSTANT

The analog of the thermal resistance measuring setup can be represented by an electrical circuit consisting of thermal resistances and thermal capacitances.

In the absence of radiation and convection the conductive heat transfer is considered to estimate the thermal time constant. An approximate thermal time constant, τ , defined as the time required to attain 63.3 percent of the final value of temperature is given as follows:

$$\tau = C_{th} \theta_{th}$$

- where: C_{th} = total thermal capacitance
= total mass m_T x heat capacity C_p
 m_T = the sum of the masses of the Jo blocks, the brass block and the heater
 θ_{th} = total thermal resistance
= $3 \theta_{B1} + 3 \theta_J$
 θ_{B1} = thermal resistance of each Jo block
 θ_J = thermal resistance of each junction

$$\begin{aligned} m_T &= \text{volume} \times \text{density} = (3 \times 1.375 \times 0.375 \times 0.5) \times (0.283) \\ &\quad + (2.75 \times 0.75 \times 0.75) \times (0.310) \\ &= 0.75 \text{ lbs} \end{aligned}$$

$$C_p = 0.1 \text{ Btu/lb} - ^\circ\text{F for carbon steel and brass.}$$

$$\begin{aligned} \therefore C_{th} &= 0.75 \times 0.1 = 0.075 \text{ Btu}/^\circ\text{F} \\ &= 143 \text{ Joules}/^\circ\text{C} \end{aligned}$$

$$\begin{aligned} 3 \theta_{B1} &= \frac{3 \times 0.5}{27 \times 0.375 \times 1.375} \\ &= 0.11 \text{ } ^\circ\text{F}/\text{Btu}/\text{hr} = 0.2 \text{ } ^\circ\text{C}/\text{Watt} \end{aligned}$$

where thermal conductivity $k = 27 \text{ Btu}/\text{hr}\text{-ft-}^\circ\text{F}$ for carbon steel

Assume that the maximum $\theta_j = 0.5^\circ\text{C/Watt}$

$$\begin{aligned}\therefore \theta_{th} &= 3 \theta_j + 3 \theta_{B1} \\ &= 1.5 + 0.2 = 1.7^\circ\text{C/Watt}\end{aligned}$$

$$\begin{aligned}\therefore \tau &= 1.7 \times 143.0 \\ &= 255 \text{ seconds}\end{aligned}$$

The measurement readings should be stable after several thermal time constants. Each measurement was taken after approximately 45 minutes. It was observed during the test that after 45 minutes from the time the power was switched on, the readings were reasonably stable.

It should be noted that because of the distributed nature of the thermal circuit having many thermal time constants, there is always going to be a slow and steady temperature rise of the test setup, and therefore the change in thermistor resistances with time.

4.11 TEST RESULTS

The temperature difference ΔT across the solid Jo block was measured at the power level of 1.25 watts. The purpose of this data is to determine the thermal resistance of the slice of a Jo block of thickness equal to the distance between the two thermistors. It is apparent that the ΔT measured across the solid slice of a Jo block must be smaller than ΔT measured across the interface of the two Jo blocks having flattest and smoothest surfaces.

Jo block #7 was used as a reference surface, and the waviness of each Jo block is within 4.0 microinches. The ΔT was computed by dividing ΔR with the slope of the thermistor resistance-temperature curve at the point of thermistor resistance. The slope in ohms per degree centigrade as a function of thermistor resistance obtained from Figure 4-6 is given in Table 4-8.

It should be noted that the data was taken with increasing load. A hysteresis in ΔR was observed with the load decreasing. This appears to be due to the yielding of asperities, however small the yielding may be.

TABLE 4-8 THERMISTOR TEMPERATURE-RESISTANCE VALUES AND THE RESISTANCE-TEMPERATURE SLOPE

Temperature °C	Thermistor Resistance Ohms	Slope Ohms/°C
25.0	1000	40.0
26.2	950	37.5
27.5	900	35.0
29.2	850	32.0
31.0	800	30.0
32.5	750	28.5
34.0	700	27.0
36.0	650	26.0
38.0	600	24.7
40.0	550	22.5
42.0	500	19.4

Sample Calculation

Per Table 4-8 the slope of the temperature-resistance thermistor curve at 695 to 697 ohms is 27 ohms/°C. ΔR at 14.7 psia is 2.0 ohms.

$$\therefore \Delta T = \frac{\Delta R \text{ ohms}}{\text{Slope}} = \frac{2.0}{27} = 0.074^\circ\text{C}$$

$$\therefore \theta_{\text{Slice}} = \frac{0.074^\circ\text{C}}{1.25 \text{ Watt}} = 0.059^\circ\text{C/Watt}$$

Repeating the above calculation for the data in Table 4-9,

$$\text{Average } \theta_{\text{Slice}} = \frac{0.059 + 0.059 + 0.084 + 0.0290}{4} = 0.059$$

$$\text{and Average Thermal Conductance } h = \frac{1}{0.059} \frac{\text{Watt}}{^\circ\text{C}} \times \frac{2.413 \text{ BTU/hr}}{\text{Watt}} \times \frac{1.8^\circ\text{F}}{^\circ\text{C}} \times \frac{1}{3.58 \times 10^{-3} \text{ ft}^2} = 8977 \text{ BTU/hr-}^\circ\text{F-ft}^2$$

CD

TABLE 4-9 MEASUREMENT OF ΔR ACROSS A SOLID JO BLOCK
(NO INTERFACE) WITH HEATING CURRENT OF
50 MA (1.25 WATTS)

<u>Atmospheric Pressure Psi</u>	<u>R₁ Ohms</u>	<u>R₂ Ohms</u>	<u>ΔR Ohms</u>	<u>ΔT °C</u>	<u>θ °C/Watt</u>
14.7	695	697	2.0	0.074	0.059
0.0	752	755	3.0	0.105	0.084
0.0	736	737	1.0	0.036	0.0290
0.0	707	709	2.0	0.074	0.059

4.12 DISCUSSION OF TEST RESULTS

The ΔR measurements as a function of surface roughness and load as a parameter are presented in Table 4-10.

The following is evident from the test data

1. ΔT across the solid slice of Jo block is smaller than Δt across an interface of two smoothest surfaces and a load as high as 200 lbs. This is a good check for the sensor and the technique of measurement.
2. ΔR and therefore ΔT decreases with pressure. This confirms the analysis given in previous pages (Table 4-2).
3. ΔT increases with increasing surface roughness at a constant load in vacuum given constant heater power and approximately the same thermistor resistance as shown in Table 4-11 below.

The necessity of having the same thermistor resistance when comparing ΔT as a function of roughness is important. The thermal circuit as mentioned earlier consists of many thermal resistance capacitances. The temperature of each Jo block increases with time until a thermal equill-

Table 4-10. ΔR and ΔT Across an Interface of Pairs of Jo Blocks*

Jo Block Part #	Surface Roughness Peak to Peak Microinches	Thermistor Resistance			Test Conditions			
		Bottom R_1 ohms	Top R_2 ohms	$\Delta R =$ $R_1 - R_2$ ohms	Load lb	Atmosphere	Slope ohms/ O_c	$\Delta t, O_c$
1-9	0.75	746.2	741.5	4.7	19.3	vacuum	28.4	0.166
		737.5	733.4	4.1	72.5		28.1	0.156
		728.9	726.5	3.4	109.0		27.8	0.122
		738.4	740.3	2.0	130.0		28.2	0.072
1-9	0.75	730.2	724.7	5.5	28.0	Air, Unclean	27.8	0.192
		726.7	721.5	5.2	104.0		27.7	0.138
		726.2	721.2	5.0	130.0		27.7	0.180
		733.1	722.3	10.8	47.0		27.7	0.390
		720.5	732.0	11.5	90.0	Disassembled & then assembled	27.9	0.400
		746.2	741.5	4.7	20.0	Air, Cleaned	28.4	0.165
		737.5	733.4	4.1	73.0		28.1	0.146
		728.4	726.5	3.4	110.0		27.8	0.122
10-4	10	698.6	681.9	16.7	69.0	Vacuum	26.9	0.620
		701.3	686.2	14.1	104.0		27.0	0.530
		858.5	846.6	13.9	110.0	Vacuum 2nd Run	32.0	0.430
		858.7	845.4	13.3	146.0		32.0	0.415
		861.0	847.9	13.1	241.0		32.0	0.400
50-8	50	889.2	870.0	19.2	28.0	Air 1st Run	33.0	0.580
		891.0	872.0	18.8	98.0		33.0	0.570
50-8	50	883.7	866.0	17.7	131.0	Air 2nd Run	32.9	0.535
		892.6	871.0	21.6	7.0		33.0	0.655
		889.0	869.8	19.2	98.0	Vacuum one month later	32.0	0.580
		887.8	869.4	18.4	129.0		33.0	0.560
		886.4	869.4	18.0	232.0		33.0	0.545
		754.0	733.2	20.8	22.0		28.1	0.740
		739.4	723.0	16.4	36.0	Vacuum	27.8	0.590
		744.5	736.5	10.0	47.0		28.1	0.450
		739.5	730.9	9.6	80.0		28.1	0.340
		750.0	742.6	7.5	113.0		28.4	0.265
712.1	690.5	21.6	17.3	26.8	0.810			
745.9	733.2	12.7	82.0	28.1	0.450			
755.2	742.6	12.6	120.0	28.4	0.445			
653.0	634.0	19.0	20.0	25.2	0.744			
675.2	663.3	11.9	76.0	26.3	0.465			
669.2	680.4	11.2	100.0	26.6	0.420			
50-5	125	854.0	833.0	21.0	42.0	Air	31.3	0.670
		847.8	830.6	17.2	112.0		31.2	0.560
		846.1	828.8	17.3	136.0		31.1	0.560
		845.3	828.7	16.6	230.0		31.1	0.535
		709.3	690.1	19.2	19.0	Vacuum	26.8	0.72
		717.0	701.5	15.5	75.0		1st Run	27.0
		707.7	686.5	21.2	18.0	2nd Run	26.7	0.795
		714.4	699.3	16.1	76.0		27.0	0.595
		708.8	692.8	16.0	98.0	3rd Run	26.9	0.592
		693.4	674.1	19.3	20.0		26.5	0.730
		688.6	676.6	12.0	75.0		26.5	0.450
		649.9	677.5	27.6	20.0		26.5	1.040
		696.5	677.5	19.0	75.0	4th Run	26.5	0.715
		700.9	683.9	17.0	111.0		26.7	0.640
		696.6	683.6	13.0	140.0		26.7	0.405

*NOTE: Part # 1-7 was used as a reference Jo block. The heater power was 1.25 watts. The waviness of every Jo block is less than 4 microinches.

Equilibrium is reached. This may take tens of hours. Therefore a time interval based on the most significant thermal time constant was estimated in the previous section. However, the measurements are made intermittently with various test conditions, thus the resistance of each thermistor varied from 860 to 600 ohms indicating a different thermal state of the thermal circuit. The test results therefore should be compared so that the test conditions and the thermal state of each element of thermal circuit are identical. This is accomplished by taking test data and comparing them at the same thermistor resistance. This is essentially the same as having the same thermistor resistance for the same load and power but different surface roughness.

The test results, when compared with the required test condition as discussed above, demonstrate that the thermal resistance technique can be employed to detect surface roughness of the order of a few microinches (Table 4-11).

TABLE 4-11 ΔT FOR DIFFERENT SURFACE ROUGHNESS AT APPROXIMATELY THE SAME LOAD AND THERMISTOR RESISTANCES OBTAINED FROM TABLE 4-10

<u>Part No.</u>	<u>Approx. Top Thermistor Resistance</u>	<u>Approx. Load In Vacuum</u>	<u>Range of ΔT</u>	<u>Surface Roughness Peak-Peak Microinches</u>
Solid Slice No Interface	-	-	0.36 to 0.10	-
1-9	740	20	0.166 0.122	0.75
10-4	690 850	100 110	0.153 0.43	10
50-8	750	20 100	0.75 to 0.81 0.45	50
50-5	700	20 100	0.73 to 1.04 0.590	50

4.13 MODIFICATION OF THE THERMAL CONDUCTANCE EXPERIMENT USING THE TRANSIENT THERMAL RESISTANCE (TTR) MEASUREMENT

As stated earlier, the thermal circuit consisting of thermal resistance and thermal capacitances has many thermal time constants. Therefore, the measurement of a particular thermal resistance in a thermal circuit (Figure 4-7) for different test conditions requires a control of the time which determines the state of the thermal circuit elements. In a steady state thermal resistance (SSTR) measurement, it was assumed that the error in the thermal resistance measurement after the time interval of the order of several significant thermal time constants is insignificant. The time intervals during the cooling cycle were not measured. The TTR measurement does not depend on the above assumptions, since the TTR measurement method requires only that the thermal state of each element of the thermal circuit be the same before the start of the test.

The important advantage of the TTR over SSTR method is that the former is a much faster method and gives more information than the latter. The disadvantage of TTR is that the method is slightly more complex and requires additional instrumentation.

The preliminary transient ΔT measurement was performed under the following conditions:

- o The test setup was in an enclosed volume containing air (no vacuum)
- o The load was varied from 1 pound to 40 pounds. This was accomplished by introducing a helical spring in the test setup.
- o Different thermistors were cemented on each test Jo block employing silicone rubber (Dow Corning 731 RTV, Figure 4-8).
- o Each measurement was taken at different loads and at the same starting temperature. The reason for having the same starting temperature of the setup is to minimize the effect of the non-linearity of the thermistor resistance-temperature curve. This was accomplished by cooling the test samples with a blast of liquified freon and a blower.

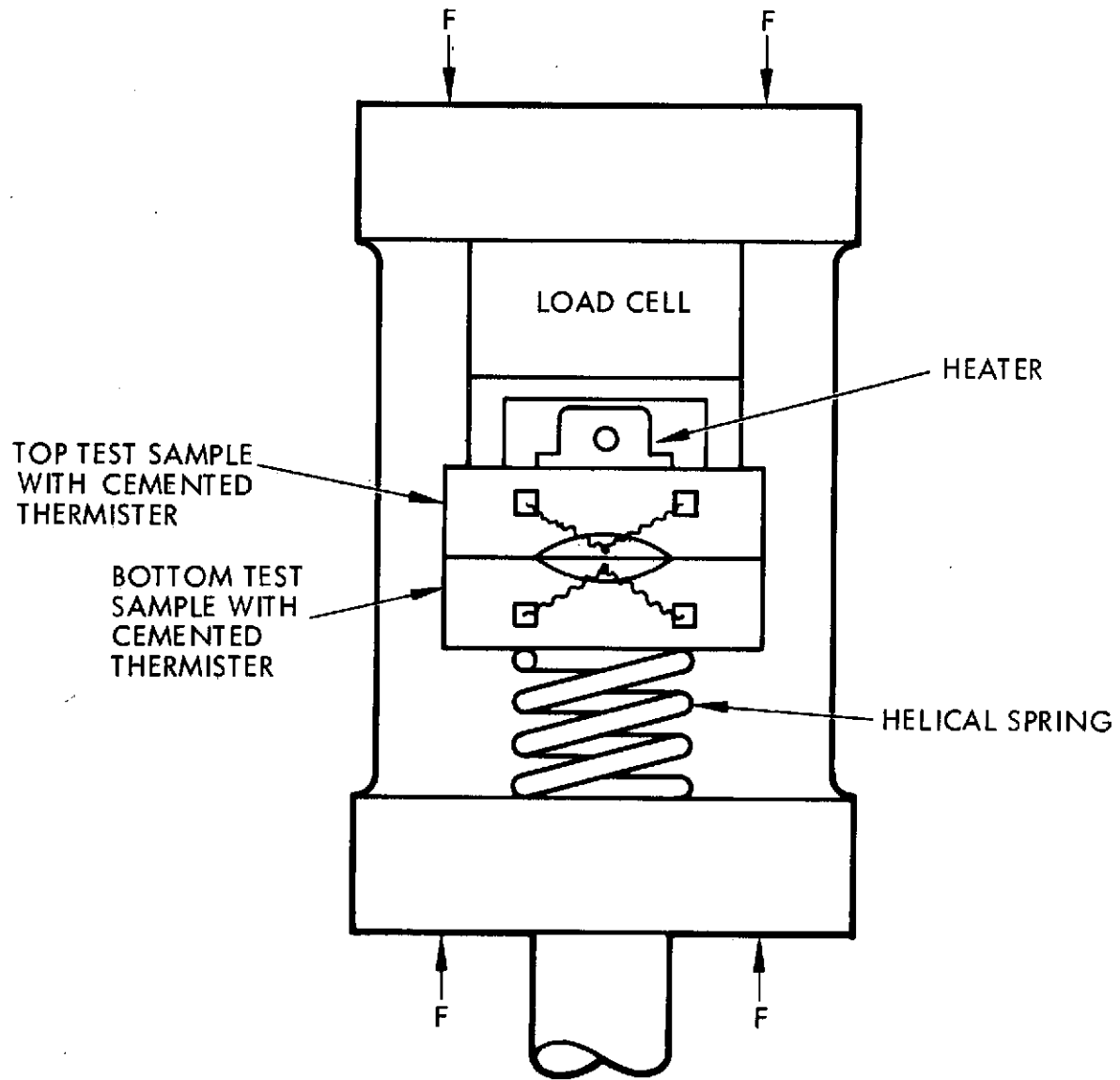


Figure 4-8 Test Setup Schematic for Transient ΔT Measurement

The test setup and the electrical schematic are shown in Figure 4-9. The temperature sensor bridge output plotted on an X-Y plotter is a direct function of ΔT . Note that there is no additional unnecessary mass as in the case of the steady state ΔT measurements due to thermal isolation of the load cell and vise from the test specimens. It was expected that the bridge output would increase as the roughness and waviness of the test specimens increases.

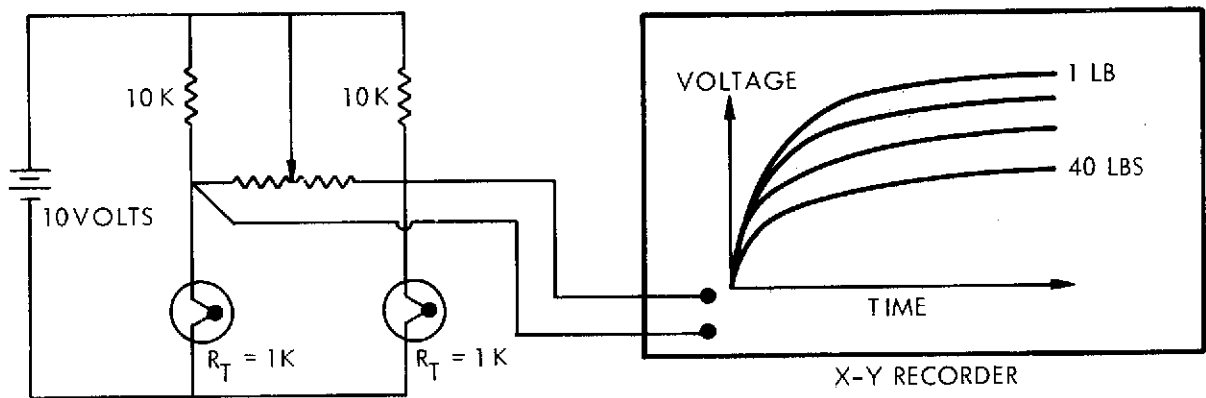


Fig. 4-9 Electrical Schematic for Transient ΔT Measurement

The transient output voltage of the thermistor bridge obtained on an X-Y plotter are shown in Figure 4-10. The steady state output showed some instability most likely due to the natural convective air currents. The value of each thermistor resistance at 24° and 30° centigrade temperatures are shown in Table 4-12. The slope (dR/dT) and correction factor with reference to the thermistor cemented on the Jo block #1-7 are also shown in the same table. The correction factor $\Delta(dR/dT)$ is employed to account for the difference in (dR/dT) of different thermistors.

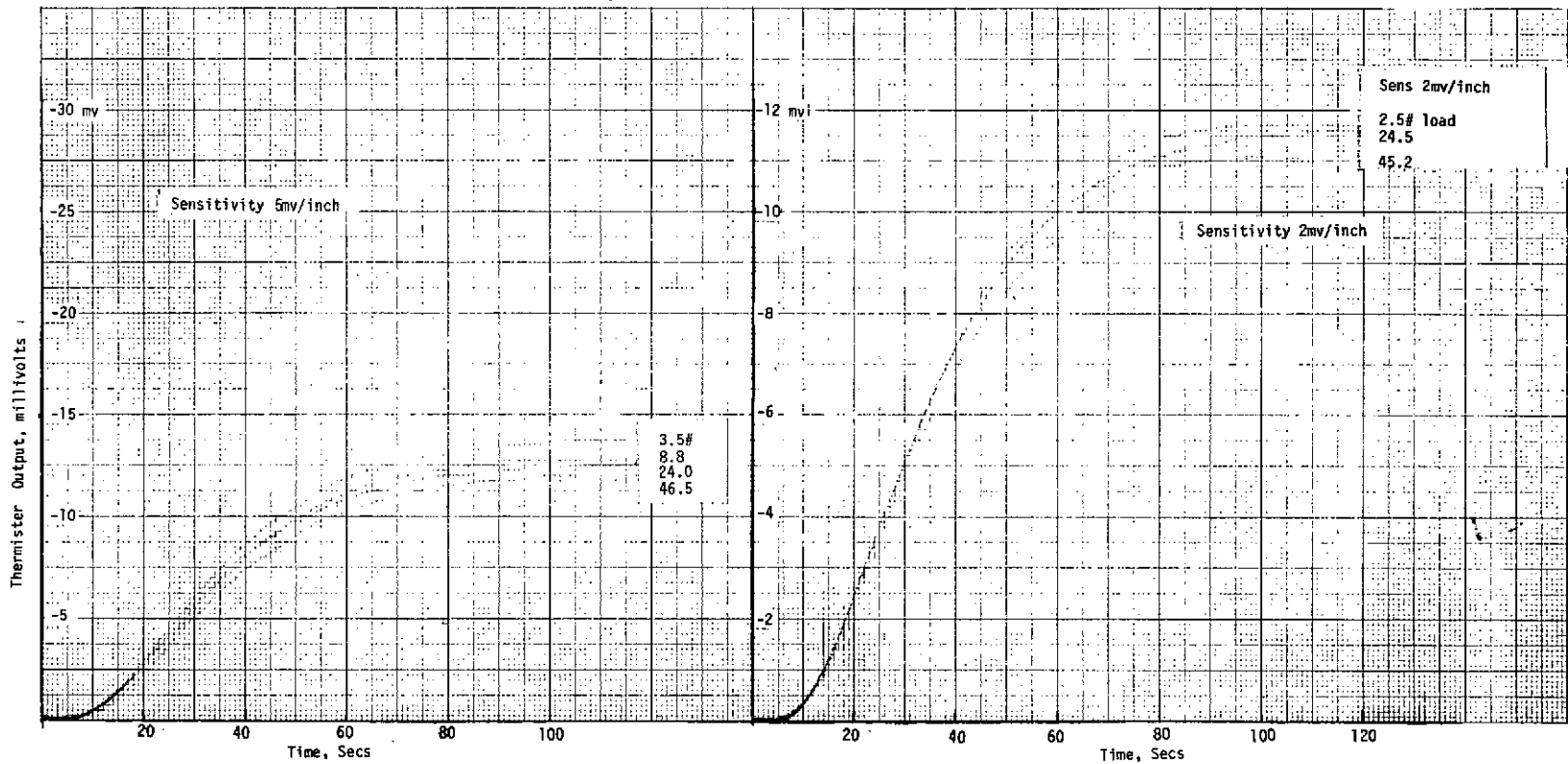


Figure 4-10a

Figure 4-10b

Figures 4-10a and 4-10b THERMISTOR OUTPUT VOLTAGE VS TIME VS LOAD FOR JO BLOCKS #1-7 and #1-9

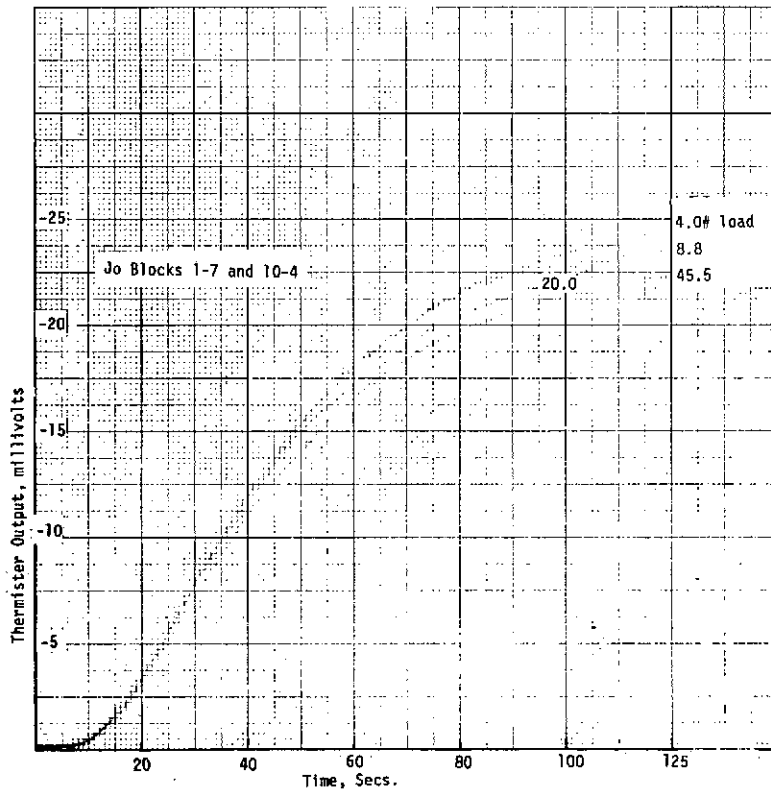


Figure 4-10c

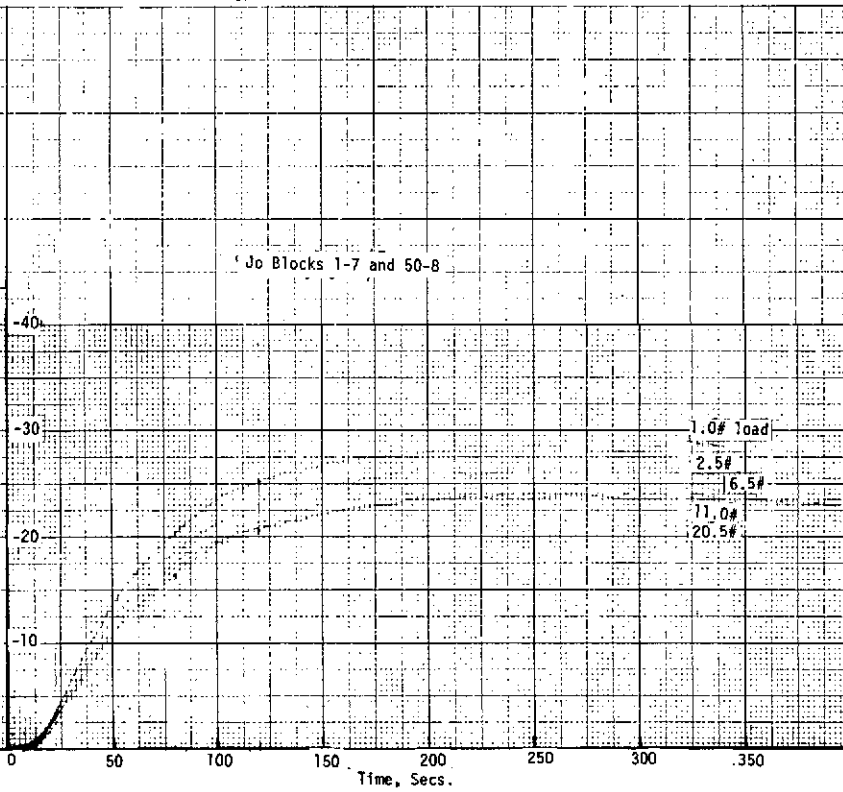


Figure 4-10d

Figures 4-10c and 4-10d THERMISTOR OUTPUT VOLTAGE VS TIME VS LOAD FOR JO BLOCKS 1-7 AND 1-4 AND 1-7 AND 50-8

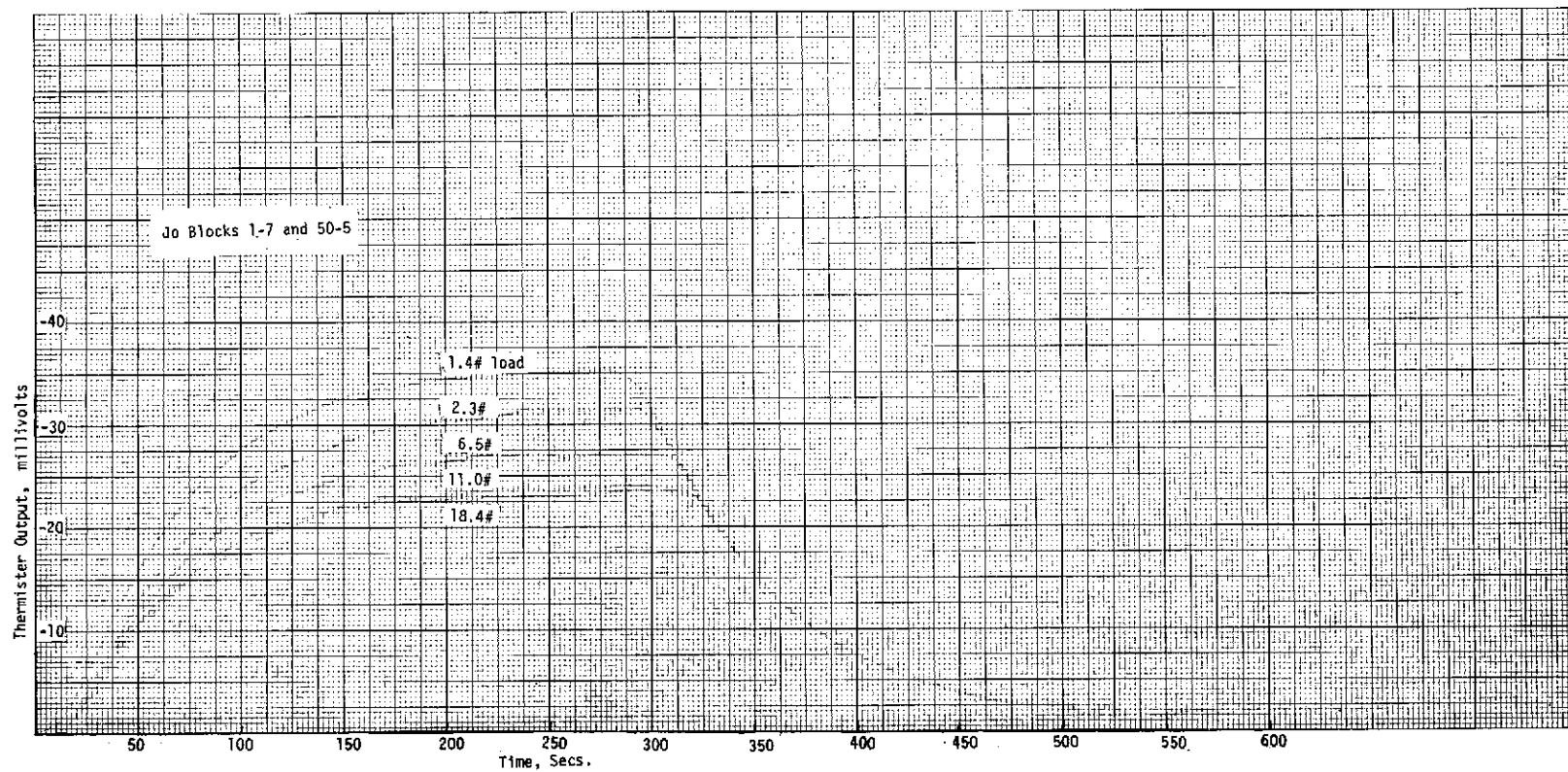


Figure 4-10e THERMISTOR OUTPUT VOLTAGE VS TIME VS LOAD FOR JO BLOCKS 1-7 and 50-5

Sample Computation for the Test Specimens Pair 1-7 and 10-4

The observed output voltage of the bridge e_o is:

$$e_o = \frac{\Delta R V}{10,000} \text{ volts} = \Delta R \text{ millivolts}$$

where: ΔR = the net difference in the thermistor resistances
due to the ΔT across the interface

and V = bridge bias voltage = 10 volts

The corrected output voltage e_o is:

$$e_o = e_o + \Delta (dR/dT) \Delta T$$

The ΔT during the test is obtained from the observed output voltage e_o
as follows:

$$\Delta T = \frac{e_o}{(dR/dT)}$$

The slope dR/dT of the reference Jo block thermistor (1-7) is 30.6
ohms per °C. The thermistor bridge voltage e_o at 4.0 lbs load is
24.5 millivolts.

$$\Delta T = \frac{24.5}{30.6} = 0.800^\circ\text{C}$$

$$\begin{aligned} e_c &= 24.5 - 0.80 \\ &= 23.7 \text{ millivolts} \end{aligned}$$

TABLE 4-12 CORRECTION FACTORS FOR THERMISTORS WITH RESPECT TO THE ONE CEMENTED TO THE REFERENCE BLOCK #1-7

Part No.	Thermistor Resistance at 24°C, ohms	Thermistor Resistance at 30°C, ohms	$\Delta R = (R_{24} - R_{30})$ ohms	$dR/dT = \frac{(R_{24} - R_{30})}{6^\circ C}$	$\Delta(dR/dT)$ With Respect to #1-7
1-7	1009.9	825.4	184.0	30.75	0
1-9	972.1	793.6	178.5	29.75	-1.0
10-4	1050.8	861.3	189.5	31.58	+0.83
50-8	982.6	804.6	178.0	29.67	-1.08
50-5	932.1	763.0	169.1	28.18	-2.57

Note that for positive (dR/dT), the correction term is subtracted from the observed bridge output.

For the test specimens, the output voltage at the end of a 120 second period for a given range of load and the voltage corrections are given in the Table 4-13.

TABLE 4-13 CORRECTED THERMISTOR BRIDGE OUTPUTS FOR DIFFERENT TEST SPECIMENS

Test Block No.	Observed Bridge Output Voltage m Volts	A ΔT °C	B		Corrected Bridge Output m Volts	
			$\Delta(dR/dT)$ Correction Voltage m Volts	$-AXB - \Delta(dR/dT)\Delta T$ m Volts		
1-9	Load High	11.75	0.345	-1.0	0.395	12.145
	Low	13.75	0.462	-1.0	0.462	14.21
10-4	High	22.25	0.705	+0.83	-0.585	21.66
	Low	24.5	0.776	+0.83	-0.644	23.86
50-8	High	20.1	0.677	-1.08	0.731	20.961
	Low	25.0	0.843	-1.08	0.910	25.91
50-5	High	20.0	0.71	-2.57	+1.82	21.82
	Low	30.0	1.06	-2.57	2.72	32.72

Note that the output at load extremes essentially increases with the surface degradation with one exception. The output of the specimen #10-4 at high load is higher than that of specimen #50-8 at the same load. The specific cause of the above anomaly was difficult to determine; however, the transient thermal resistance measurement needed the following improvements.

- o The TTR test in vacuum will improve the sensitivity of measurement and avoid any instability due to air currents caused by the convective heat transfer.
- o The thermistors, though very sensitive detectors of temperature, are not linear devices. As a result the bridge output is also a function of the ambient temperature of the test setup. The dependence of ambient temperature can be minimized by employing linear devices, such as platinum or nickel-iron resistance thermometers.
- o The data would be more reliable if the same pair of temperature detectors were used for all different pairs of specimens.

The improvements mentioned above were incorporated by the following steps:

- o A pair of nickel-iron resistance thermometers were employed for all specimens. Each thermometer was cemented on the test specimen with Eastman 910 cement and removed after the test was completed.
- o The test setup was installed in a vacuum chamber.

To prove the thermal resistance increased with only roughness and was not due to the waviness, the test specimens #1-9 and 1-1, without any surface preparation, were tested. The surface of the test specimen #1-9 was then roughened by liquid bead blasting for 3 to 4 seconds. The surface roughness increased from 0.75 microinches p-p to 5.0 microinches p-p. The waviness was unchanged (Figure 4-2a - 4-2e, Appendix 4-a)

The surface of test specimen #1-1 was roughened by gently rubbing the surface with steelwool a few times longitudinally. The pattern of roughness was obviously different for both cases, and, the test indicated that thermal resistance changed substantially with change in roughness only (Table 4-14).

Conclusions

The following observations of the TTR tests are made:

1. Transient thermometer bridge voltage output increased with increased roughness and waviness simultaneously (item 1 to 3 of Table 4-14).
2. The measurement repeatability without removing the specimen #10-4 from the test setup was 2 percent (Figure 4-2b, Appendix 4-a).
3. The measurement repeatability at different times, for test specimen #1-9 (specimen #1-9 was removed twice from the test setup) was 7.7 percent and 20.0 percent (items 4 thru 7 of Table 4-14).
4. Transient thermometer bridge voltage output increased with increased roughness while maintaining the same waviness (items 4 to 11 of Table 4-14).

The measurement sensitivity of roughness for test specimen 1-9 is:

$$\begin{aligned} S &= \frac{1.05-0.60}{6.75-0.75} \\ &= 75 \text{ microvolt per microinch} \end{aligned}$$

THERMAL CONDUCTANCE VS. ROUGHNESS AS MEASURED USING THE TRANSIENT THERMAL RESISTANCE TECHNIQUE
USING NICKEL-IRON THERMOMETERS

TABLE 4-14

Item	Test Specimen ID # Ref. Specimen #1-7	Roughness p-p Microinches	Waviness p-p Microinches	Nickel-iron Thermometer Bridge Output m Volts at 45 lbs load	Thermal Conductance h, BTU hr-°F-Ft ²	Avg. Thermal Conductance h, BTU hr-°F-Ft ²	Date Tested	Applicable Figure
1	1-9	0.75	5	0.51	1569	1377	10/4/72	4-2c
2	10-4	10.0	25	0.54	1482		10/4/72	4-2a
3	50-8	50.0	80	1.95	410		10/6/72	4-2d
4	1-9	0.75	5	0.65	1230		10/11/72	4-2e
5	1-9	0.75	5	0.60	1333		10/11/72	4-2f
6	1-9A*	5.0	5	1.05	762	851	10/13/72	4-2g
7	1-9A*	5.0	5	0.85	941		10/19/72	4-2h
8	1-1	0.75	5	0.675	1185		10/16/72	4-2j
9	1-1	0.75	5	0.675	1185		10/19/72	4-2k
10	1-1A**	5.0	5	1.45	552	486	10/20/72	4-2m
11	1-1A**	5.0	5	1.90	421		10/21/72	4-2n

*The test specimen surface was liquid bead blasted before the TTR test.

**The test specimen surface was roughened with a steel wool before the TTR test.

4-45

Test Data Analysis

The value of thermal conductance is determined from experimental data and then compared with that obtained from the analysis.

The thermal resistance and conductance are given by the following equations: (Sect. on 4.3)

$$\theta = \frac{1.1}{2K_m \bar{N} \bar{C}} \quad (6) \text{ assuming that the waviness has insignificant effect}$$

$$h = \frac{2K_m \bar{C} \bar{N}}{1.1}$$

$$N = P_a / 330,000 \quad (\pi \bar{C}^2)$$

$$\begin{aligned} \text{Test specimen area } A &= 0.5156 \text{ in}^2 \\ &= 3.58 \times 10^{-3} \text{ ft}^2 \end{aligned}$$

The radius of contact junction \bar{c} is obtained from equation 7, Section 4-3.

Equation 7 can be simplified to the following:

$$\bar{c} = 2.5 (\sigma)^{1/3}$$

Where σ is the rms roughness

The value of thermal conductivity K_m is obtained from the test data in Section 4-9, Table 4-9.

The thermal conductance of a 0.1 inch thick test specimen slice is estimated to be $8977 \frac{\text{BTU}}{\text{hr-}^\circ\text{F-Ft}^2}$

$$\begin{aligned} \circ \circ K_m &= h \times \text{thickness of the slice in feet} \\ &= 8977 \times \frac{1}{120} \\ &= 74.8 \frac{\text{BTU}}{\text{hr-}^\circ\text{F-ft}} \end{aligned}$$

The thermal conductance of the contact junction is:

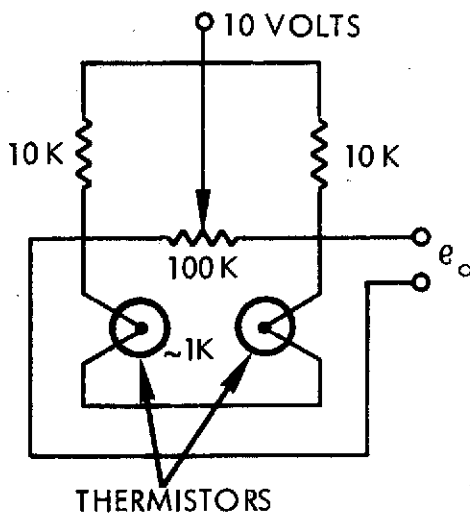
$$h = \frac{2 \times 74.8 \text{ cN}}{1.1}$$

$$= 136 \text{ cN}$$

The values of h for the different junctions are computed in Table 4-15.

Thermal conductance is obtained from measured test data presented in Table 4-13 as follows:

Note that the computations are made for the load of 45 lbs.



$$e_o = e_1 - e_2$$

$$e_o = \frac{\Delta R}{10,000} 10, \text{ volts}$$

$$= \Delta R \text{ millivolts}$$

$$\Delta T = \frac{dT}{dR} \Delta R = \frac{dT}{dR} e_o = \frac{e_o}{\frac{dR}{dT}}$$

thermal conductance $h = \frac{W}{\Delta TA}$, where

W is the heater power (1.25 watts) expressed in BTU/hr

A is the apparent area of the junction.

The values of h for different test specimens based on the test data from Table 4-13 are computed in Table 4-16.

ANALYTICAL DETERMINATION OF THERMAL CONDUCTANCE, h, FOR THE SPECIMEN JUNCTIONS

TABLE 4-15

Test Specimens	Surface Roughness Microinches, RMS	\bar{c} , Micron	\bar{c} Microinches	\bar{c} , feet	A, Ft^2 $= n \bar{c}^2$	N for 45 lbs	$h = \frac{2k_m \bar{c}N}{1.1}$
1-9	0.30	1.8	72	6×10^{-6}	113.1×10^{-12}	2338504	1908
1-9	1.79	3.03	121.2	10.1×10^{-6}	320×10^{-12}	826515	1135
1-1	0.30	1.8	72	6×10^{-6}	113.1×10^{-12}	2338504	1908
1-1	1.79	3.03	121.2	10.1×10^{-6}	320×10^{-12}	826515	1135
10-4	3.5	3.8	152	12.7×10^{-6}	507×10^{-12}	521666	9010
50-8	28	7.6	304	25.3×10^{-6}	2011×10^{-12}	131519	452.8
50-5	28	7.6	304	25.3×10^{-6}	2011×10^{-12}	131519	452.8

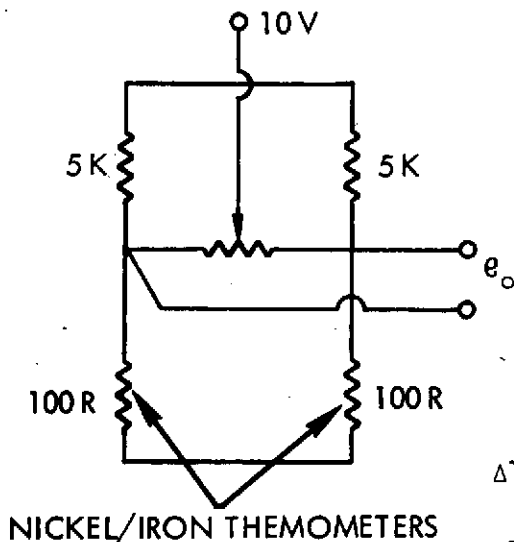
COMPUTATION OF THERMAL CONDUCTANCE, h , FOR THE TEST SPECIMEN JUNCTIONS
 BASED ON EXPERIMENTAL RESULTS USING THERMISTORS

TABLE 4-16

Item	Part # Ref. to 1-7	Thermistor e_o (M Volts at 45 lbs)	$\frac{dR}{dT}$, $\left(\frac{\text{ohm}}{^\circ\text{C}}\right)$	ΔT ($^\circ\text{C}$)	$\left(\frac{h, \text{BTU}}{\text{hr-}^\circ\text{F-Ft}^2}\right)$
1	1-9	12.145	29.75	0.408	1623
2	10-4	21.66	31.58	0.686	965
3	50-8	21.0	29.67	0.708	935
4	50-5	21.8	28.18	0.774	855

The thermal conductance is obtained from measured test data presented in Table 4-14 as follows:

The bridge output voltage $e_o = (e_1 - e_2)$



$$= \left[\frac{100 + \Delta R}{5000} - \frac{100}{5000} \right] \text{V}$$

$$\approx \frac{\Delta R}{5000} \times 10 \text{ volts}$$

$$e_o = 2\Delta R \text{ Milli volts}$$

where ΔR is in ohms

and e_o is in milli volts

$$\Delta T = \frac{dT}{dR} \Delta R$$

$$\Delta T = \frac{dT}{dR} \frac{e_o}{2}$$

For Nickel-iron resistance thermometers at 25°C temperature, the measured slopes dR/dT are:

$$\begin{aligned} \left(\frac{dR}{dT}\right)_1 &= \frac{113.56 - 99.66}{23.22} \\ &= 0.59863 \text{ ohms}/^{\circ}\text{C} = 0.3326 \text{ } \Omega/{}^{\circ}\text{F} \end{aligned}$$

$$\begin{aligned} \left(\frac{dR}{dT}\right)_2 &= \frac{(114.16 - 100.08) \text{ ohms}}{23.22^{\circ}\text{C}} \\ &= 0.6064 \frac{\text{ohms}}{^{\circ}\text{C}} = 0.3369 \text{ } \Omega/{}^{\circ}\text{F} \end{aligned}$$

$$\text{Average } \left(\frac{dR}{dT}\right) = 0.335 \text{ ohms}/{}^{\circ}\text{F}$$

$$\begin{aligned} \Delta T &= \frac{e_o}{2} dR/dT = \frac{e_o}{2 \times 0.335} \text{ }^{\circ}\text{F} \\ &= 1.493 e_o \text{ }^{\circ}\text{F} \end{aligned}$$

$$\begin{aligned} \text{Thermal conductance } h &= \frac{1.25 \text{ watts}}{1.49 e_o \text{ }^{\circ}\text{F} \cdot 3.58 \times 10^{-3} \text{ Ft}^2} \\ &= \frac{800}{e_o} \frac{\text{BTU}}{\text{hr-}^{\circ}\text{F-Ft}^2} \end{aligned}$$

The values of thermal conductance as calculated from equation (6), as determined from the test data presented in Table 4-14, and as determined from the test data presented in Table 4-16, are presented in Table 4-17.

COMPARISON OF CONDUCTANCES AT 45 LBS. LOAD

TABLE 4-17

Item	Test Specimen ID # Ref. Spec. 1-7	Test Specimen p-p Roughness Microinches	Test Specimen p-p Waviness Microinches	Thermal Conductance h is BTU/hr-°F-Ft ²			Percent Deviation $\left(\frac{h_c - h_{m2}}{h_{m2}}\right) 100$
				h _c Obtained From Equation 4-6	h _{m1} Obtained From Measured Data of Table 4-16 (Thermistor data)	h _{m2} Obtained From Measured Data of Table 4-14 (Nickel-iron Thermometer)	
1	1-9	0.75	5.0	1908	1623	1377*	27.8
2	1-9A	5.0	5.0	1135	-	851*	33.4
3	1-1	0.75	5.0	1908	-	1185	61.0
4	1-1A	5.0	5.0	1135	-	486*	135.0
5	10-4	10.0	25.0	901	963	1482	39.2
6	50-8	50.0	80.0	452.8	935	410	10.5
7	50-5	25.0	80.0	452.8	855	-	-

*From Table 4-14, average h

Review of Table 4-17 indicates the following:

1. Thermal conductance obtained from analysis is in good agreement with that obtained from test data in spite of the fact that the waviness effect and the variations in the roughness scratch pattern were not accounted in the analysis. It should also be noted that the repeatability of the test data at different times taken with the same pair of test specimens and the same test conditions, but dismantling and assembling the test setup was of the order of 8 to 20 percent. The unpredicted results obtained with specimen 1-1 appear to be due to the large waviness effect and the variations in scratch pattern. The difference in the profile recordings of specimens 1-1, 1-1A, 1-9 and 1-9A should be noted (Figure 4-3 , Appendix 4-a). If the test data of specimens 1-1 (items 3 and 4) are discarded, the range of deviation of the computed conductance h_c from the measured conductance h_{m2} is from 10 to 39 percent.
2. Thermal conductance obtained from analysis is in general higher than that obtained from the test data. This is expected because the computation does not account for the effect of waviness. The deviation from the above statement is observed in case of items 5, 6 and 7 of Table 4-17. In case of test specimen 10-4 the computed h_c is lower than h_m obtained from the test data. This appears to be due to the matching of waviness; that is, test specimens 1-7 and 10-4 have the least reduction of real contact area due to the waviness effect. To account for the deviation of items 6 and 7 of Table 4-17, it should be noted that the test data of Table 4-13 had greater accuracy limitations as discussed earlier.
3. The computed h_c and measured h_m essentially confirm the prediction that thermal conductance decreases with increasing roughness.

4. The ratio of conductance of test specimen 1-9 before and after bead blasting is obtained as follows:

$$X = \left(\frac{h_{1-9A}}{h_{1-9}} \right) \text{ Measured} = \frac{851}{1377} = 0.618$$

$$Y = \left(\frac{h_{1-9A}}{h_{1-9}} \right) \text{ Computed} = \frac{1135}{1908} = 0.595$$

$$\text{Percent deviation} = \frac{X-Y}{X} \times 100 = 3.7\%$$

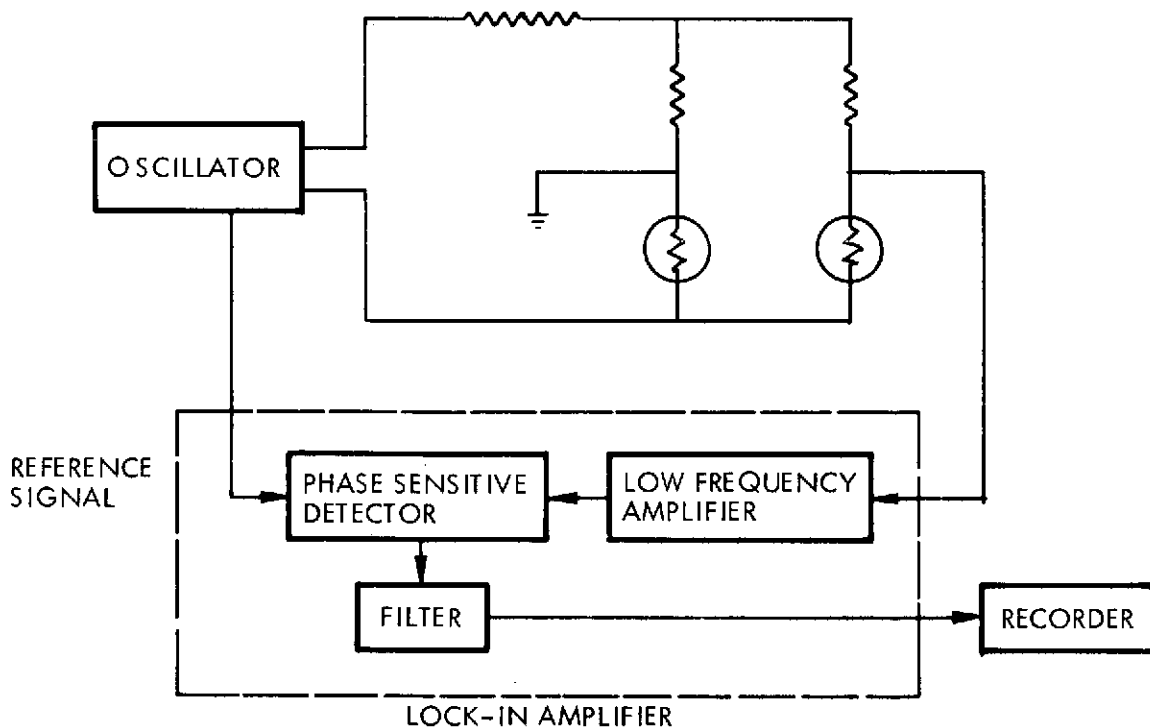
The ratios X and Y are remarkably close. Note that X and Y are essentially independent of waviness effect; however they are not independent of the scratch pattern.

4.14 TTR TECHNIQUE IMPROVEMENTS

The TTR and SSTR techniques employed a DC Wheatstone bridge to measure the output voltage of the bridge as a function of the temperature difference ΔT across the junction of two test specimens. The thermistor bridge can be employed to detect changes in the temperature as small as 0.001°C . It is questionable whether it is required to improve the sensitivity and stability of the set-up employed in the SSTR and TTR tests. However, the DC Wheatstone bridge techniques has the following drawbacks:

1. Errors are introduced by fluctuating thermal emfs in the bridge and connecting leads.
2. A DC amplifier introduces its own baseline drift.

The Wheatstone bridge with an AC bias of frequency 15 Hz minimizes the errors described for the DC Wheatstone bridge. This is achieved employing a lock-in amplifier (Figure 4-13). Since the reactive components of the bridge at 15 Hz are negligible, no phase-shifting arrangement is required to null the bridge. It is claimed that the random fluctuation in an AC Wheatstone bridge technique employing a lock-in amplifier can be reduced by a factor of 50.



The TTR technique can be implemented in a valve, where the surface degradation of the poppet-valve seat is to be measured, as shown in the Figure 4-14. It should be noted that if the technique is employed in a valve containing propellant or oxidizer, the sensitivity of the technique is reduced due to the presence of other thermal paths such as the one through the liquid in void volume. However, the test results indicate that the test setup is adequately sensitive to offset the reduced sensitivity. Furthermore, the sensitivity can be improved by any or all of the following steps:

- o Increase the bridge bias voltage
- o Increase the heater power
- o Employ AC Wheatstone bridge

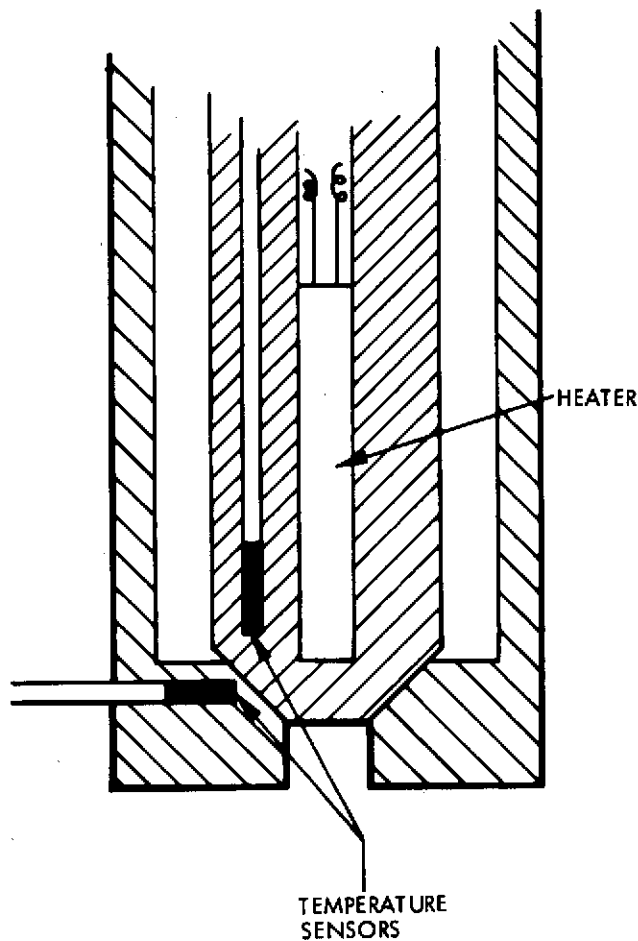


Figure 4-14

4.11 REFERENCES

1. "Effect of Pressure on Thermal Conductance of Contact Joints" by Barzelay, Tong and Holloway, Syracuse University NACA, Washington, May 1955.
2. "Friction and Wear", I. V. Kragelskii, USSR, Academy of Science, Moscow, Translated from Russian by Ronson and Lancaster, Washington, Butterworth, 1965.
3. "Comparison of Temperature Sensors for Space Instrumentation," E. E. Swartzlander, Jr., Hughes Aircraft Company, Aerospace Group, Culver City, California 90230.
4. "Influence of Surface Roughness and Waviness Upon Thermal Contact Resistance" by M. M. Yovanovich and W. M. Rohsenow, MIT, June, 1967.
5. "Friction and Wear of Materials" by E. Rabinowicz, published by John Wiley and Sons, New York, 1965.
6. "Thermal Contact Resistance", by T. W. McDonald, Transactions of the Engineering Institute of Canada, July 1963, Vol. 6, No. B-12.
7. "Heat and Mass Transfer" by Eckert and Drake, McGraw-Hill Book Company, 1959.

A P P E N D I X 4-a

Figure 4-1

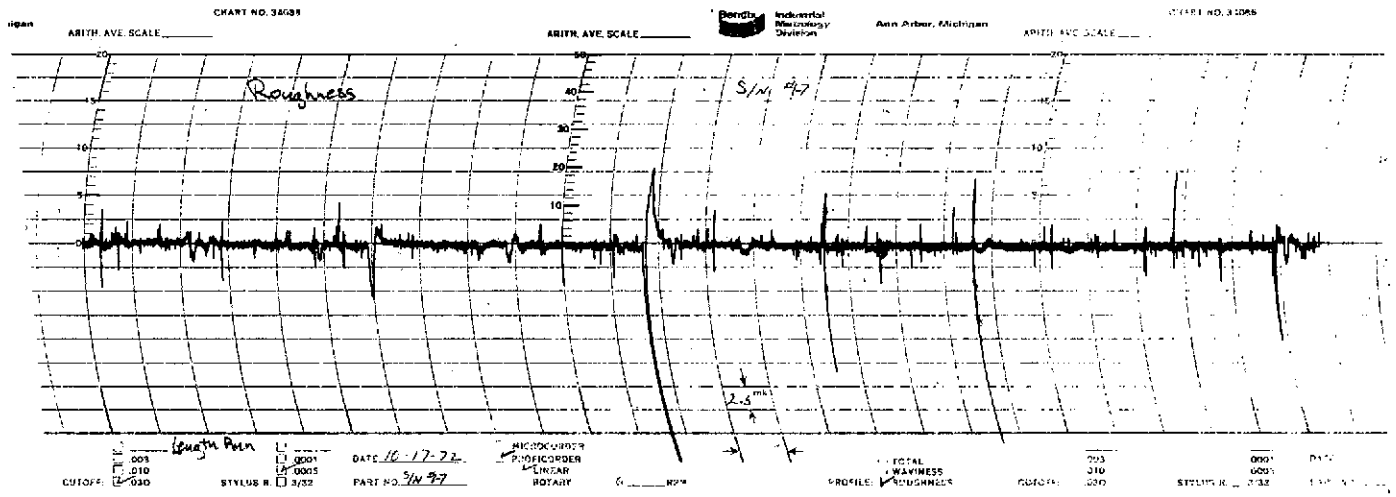


Figure 4-1a Profile of Jo Block Part # 1-7, Roughness, Length run

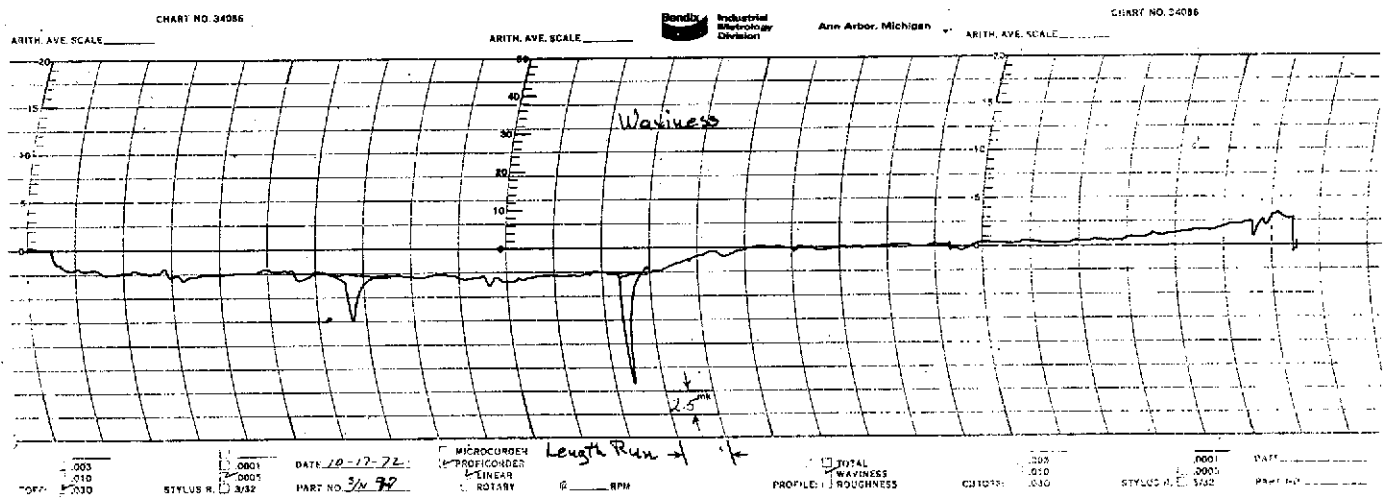


Figure 4-1b Profile of Jo Block Part # 1-7, Waviness, Length Run

4-58

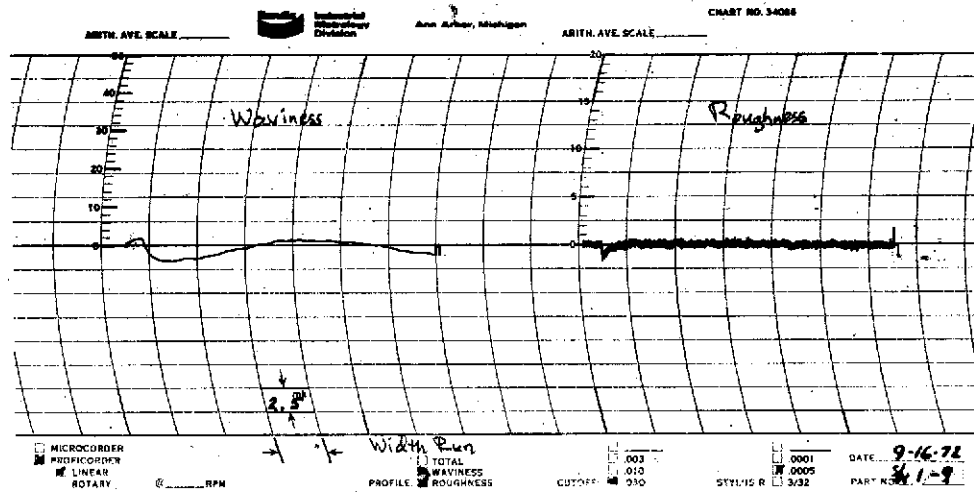


Figure 4-1c Profile of Jo Block Part # 1-9, Waviness and Roughness, Length run

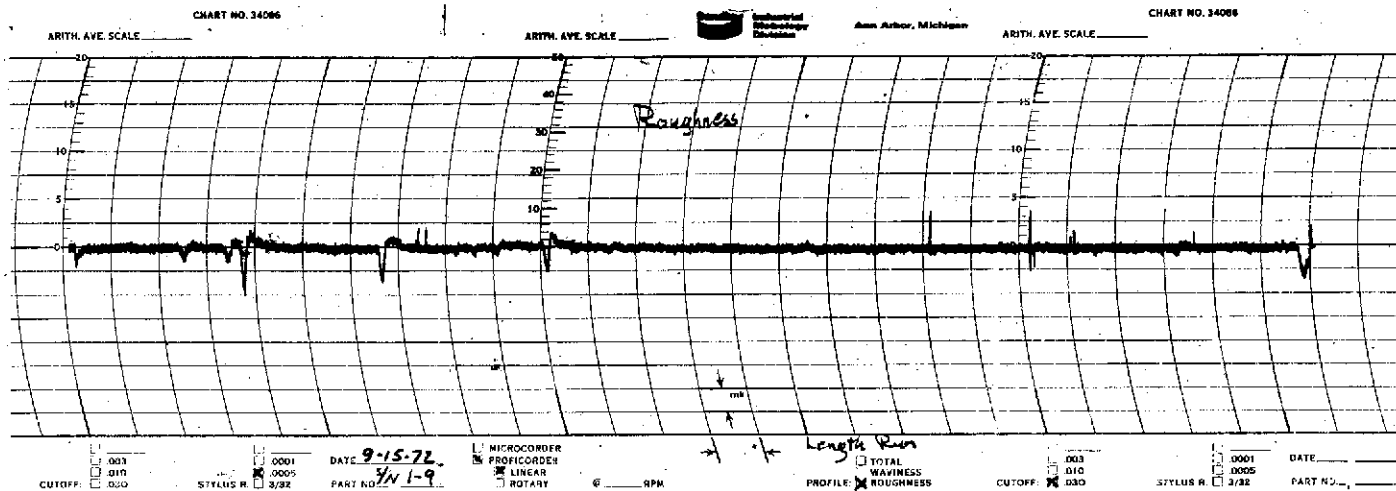


Figure 4-1d Profile of Jo Block Part # 1-9, Roughness, Length Run

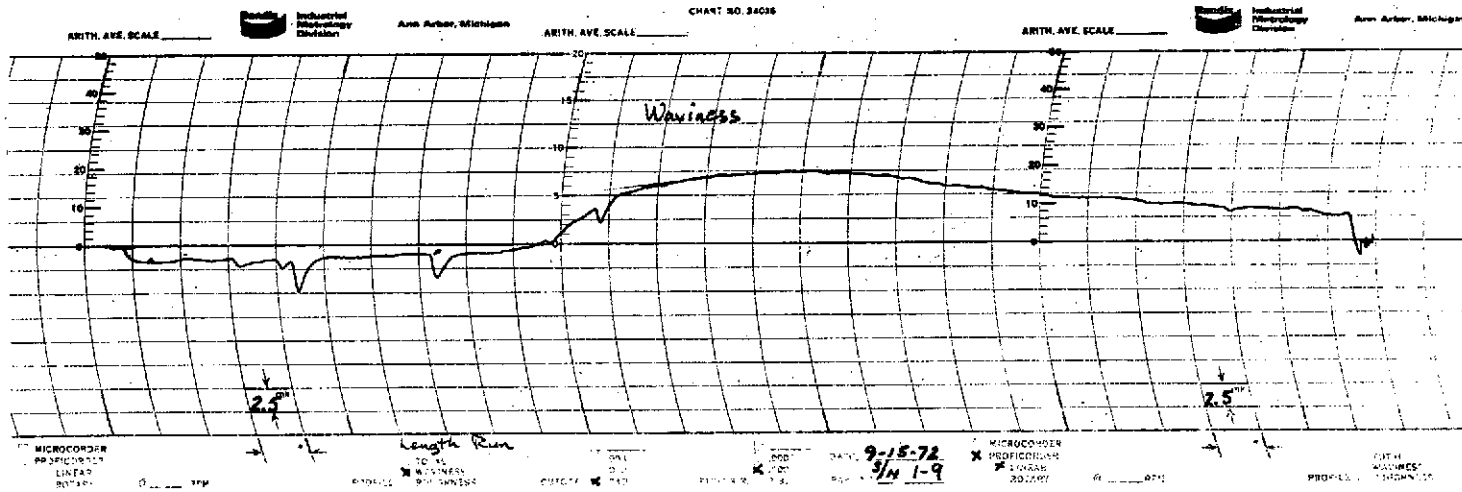


Figure 4-1e Profile of Jo Block Part # 1-9, Waviness, Length Run

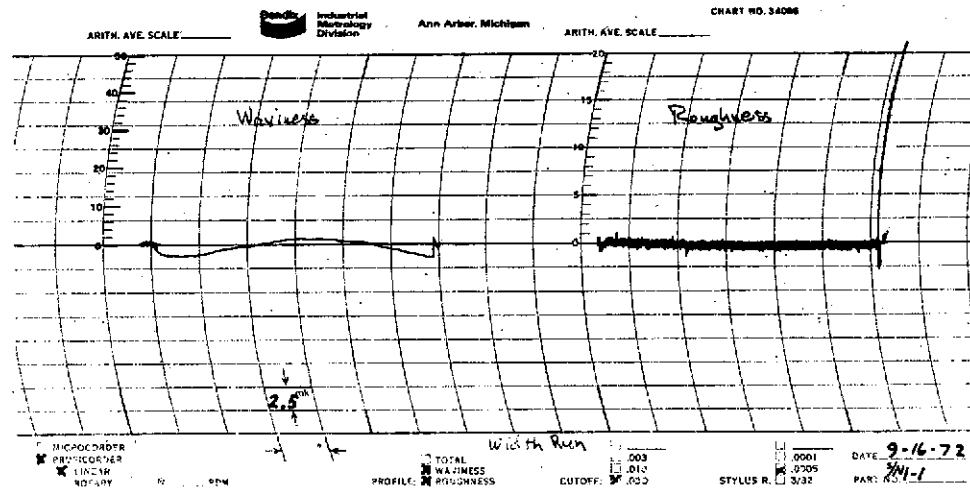


Figure 4-1f Profile of Jo Block Part # 1-1, Waviness and Roughness, Width Run

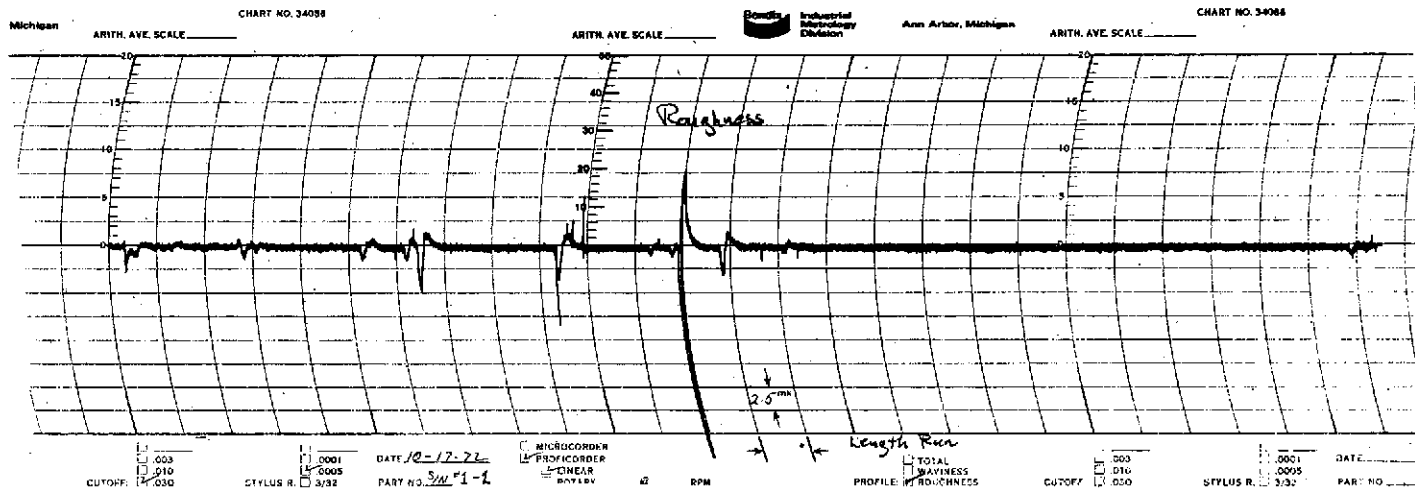


Figure 4-1g Profile of Jo Block Part # 1-1, Roughness, Length Run

4-61

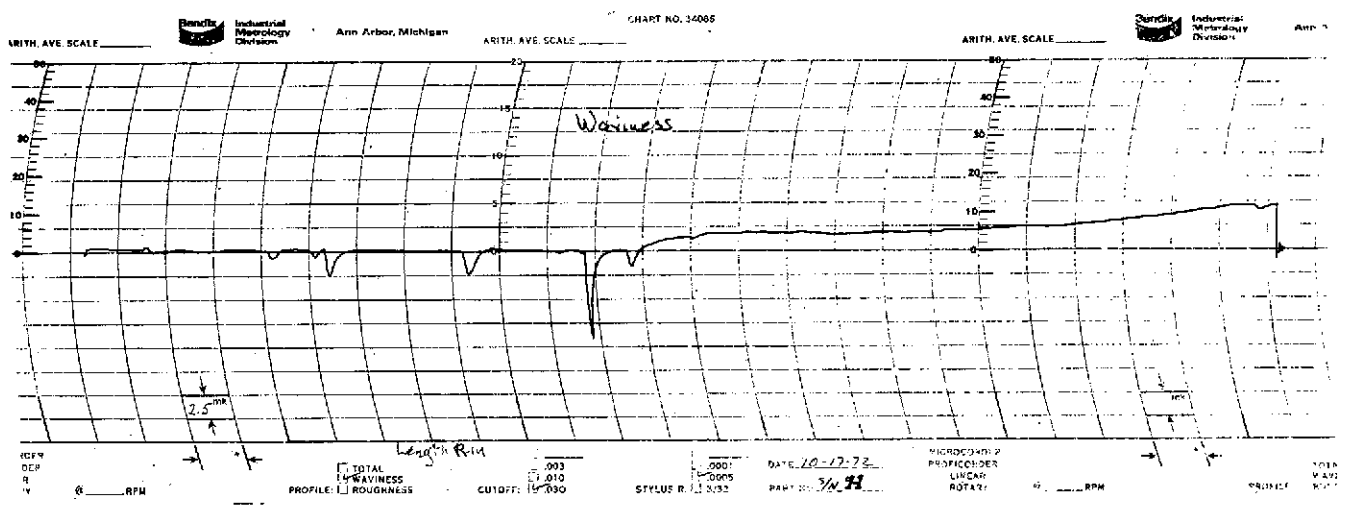


Figure 4-1h Profile of Jo Block Part # 1-1, Waviness, Length Run

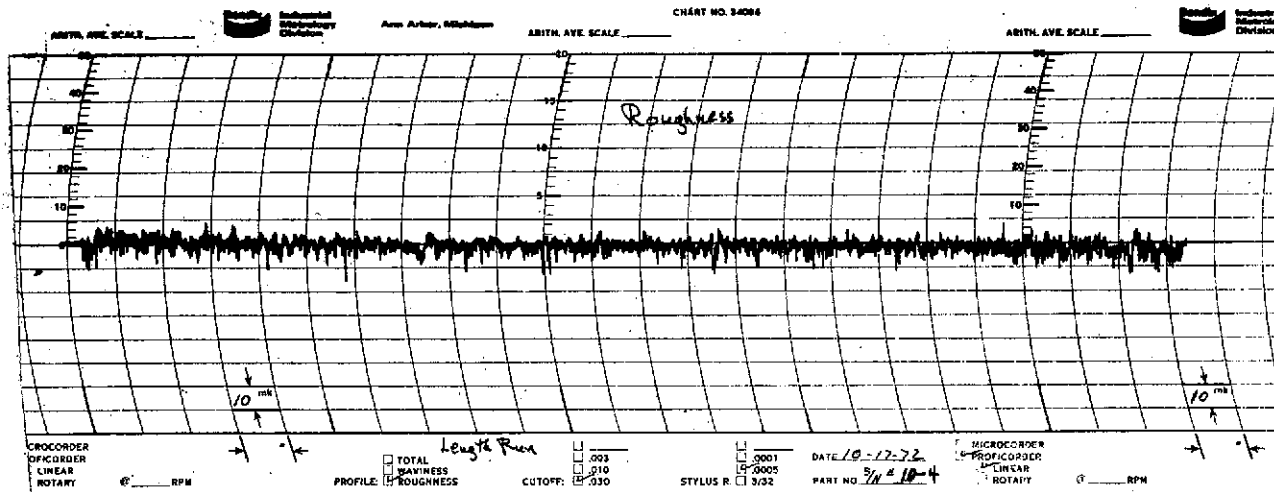


Figure 4-1i Profile of Jo Block Part # 10-4, Roughness, Length Run

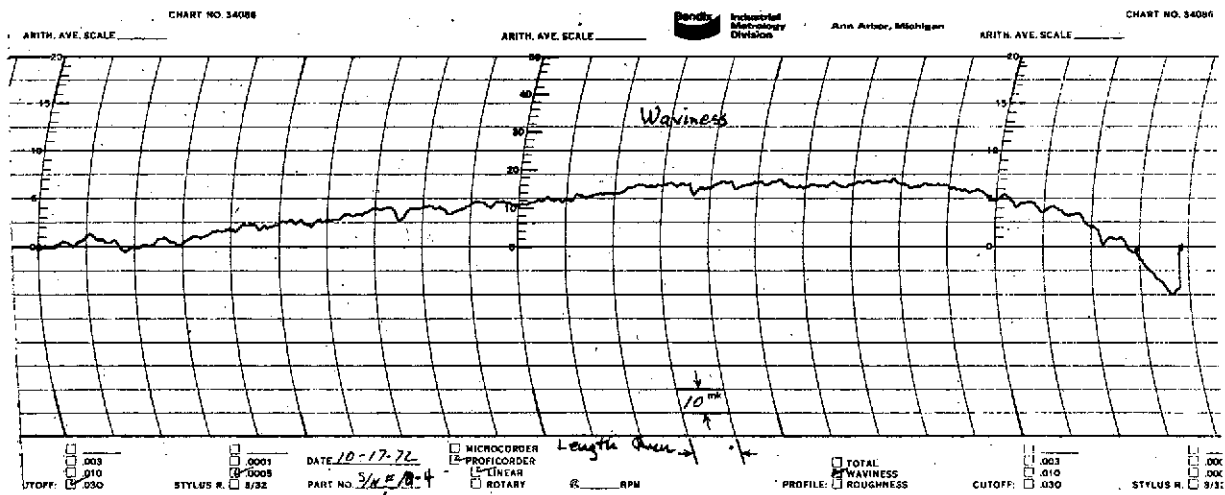


Figure 4-1j Profile of Jo Block Part # 10-4, Waviness, Length Run

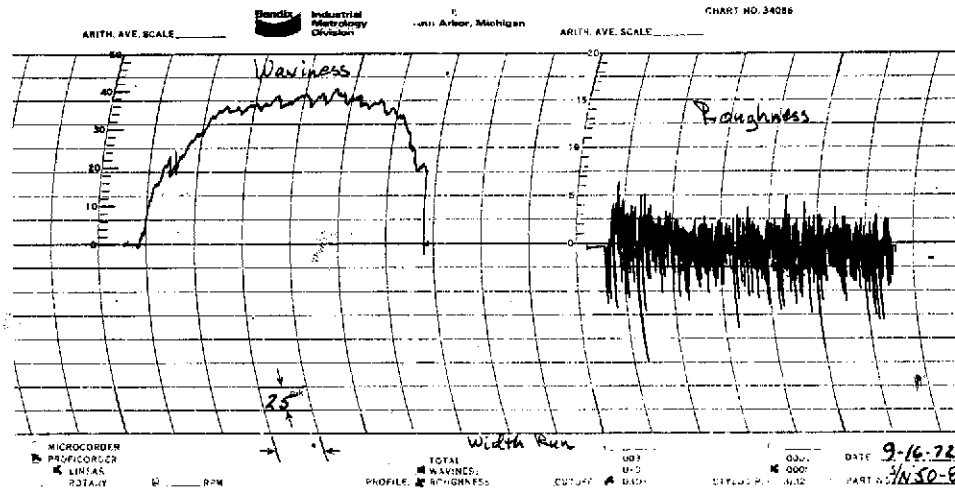


Figure 4-1k Profile of Jo Block Part # 50-8, Roughness, Width Run

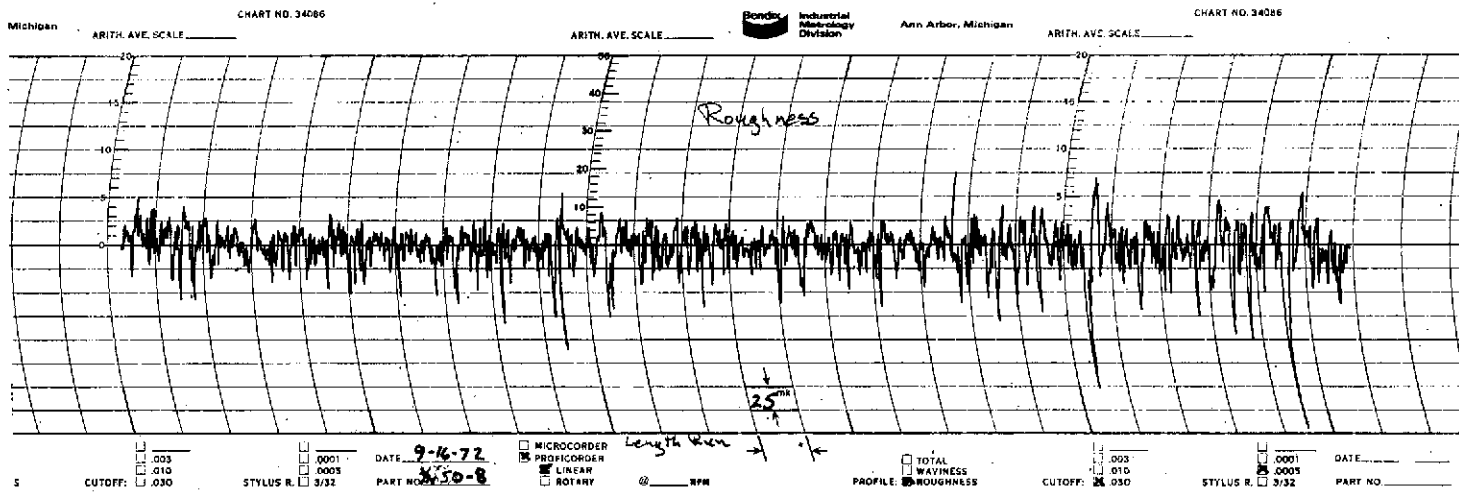


Figure 4-1l Profile of Jo Block Part # 50-8, Roughness, Length Run

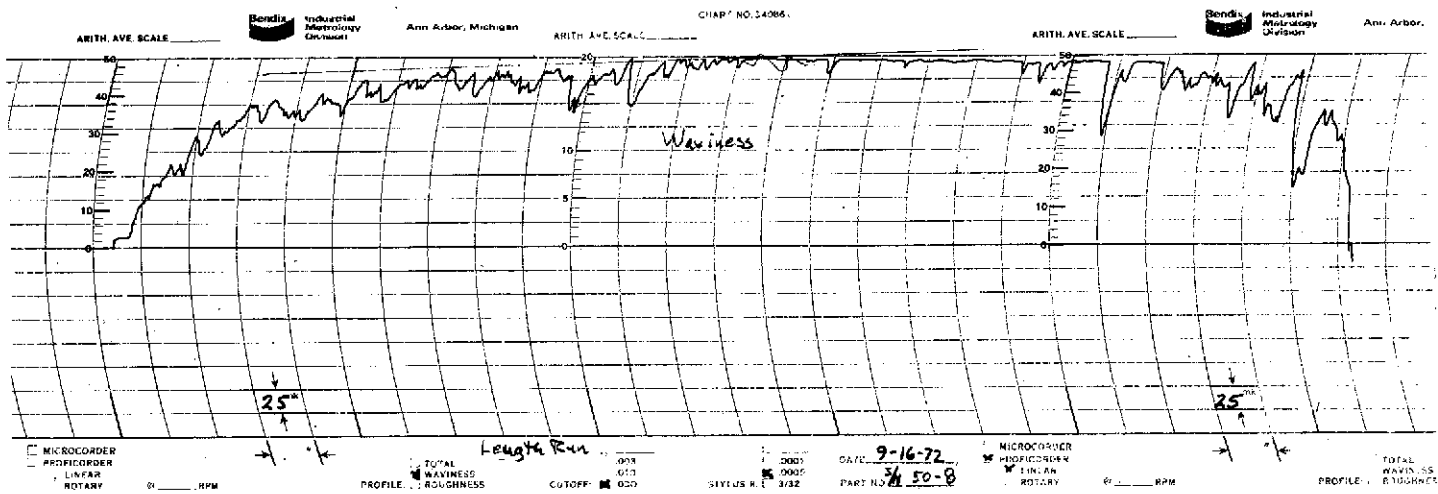


Figure 4-1m Profile of Jo Block Part # 50-8, Waviness, Length Run

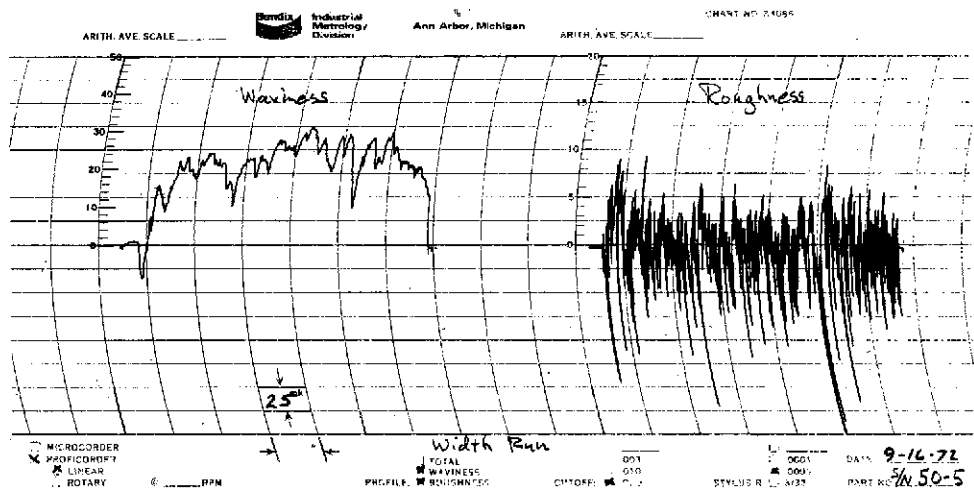


Figure 4-1n Profile of Jo Block Part # 50-5, Waviness and Roughness, Width Run

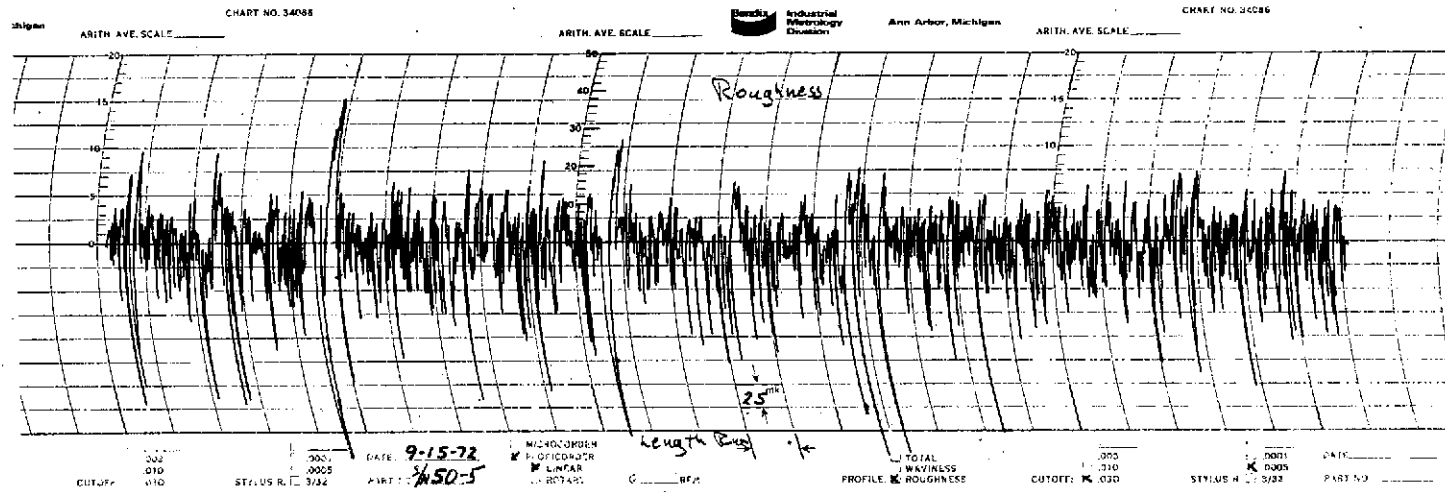


Figure 4-1o Profile of Jo Block Part # 50-5, Roughness, Length Run

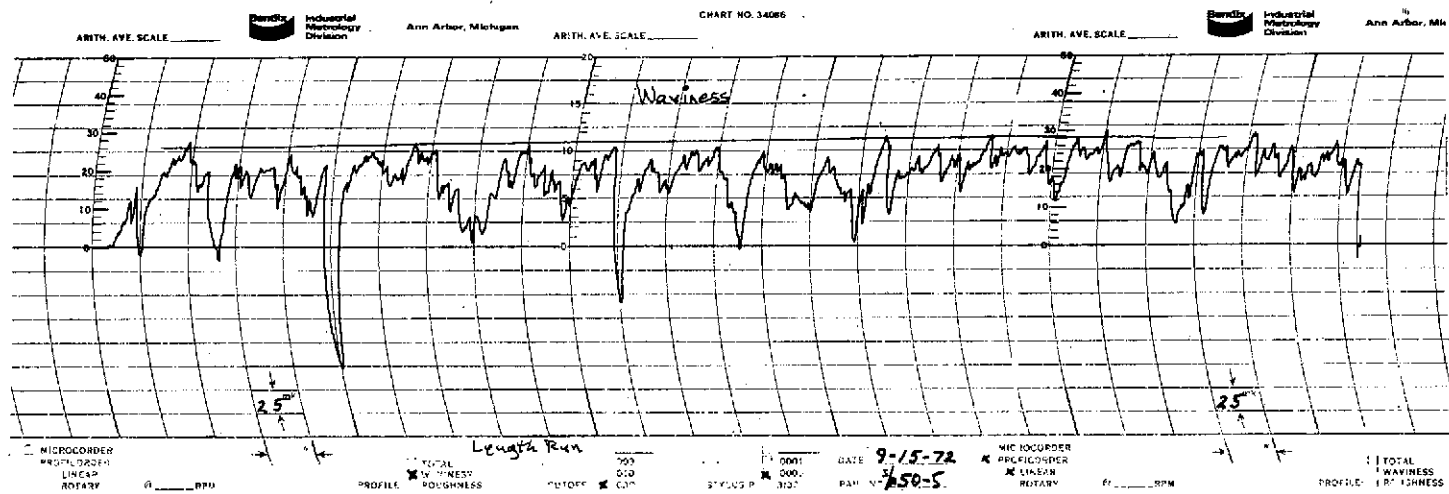


Figure 4-1p Profile of Jo Block Part # 50-5, Waviness, Length Run

A P P E N D I X 4-a

Figure 4-2

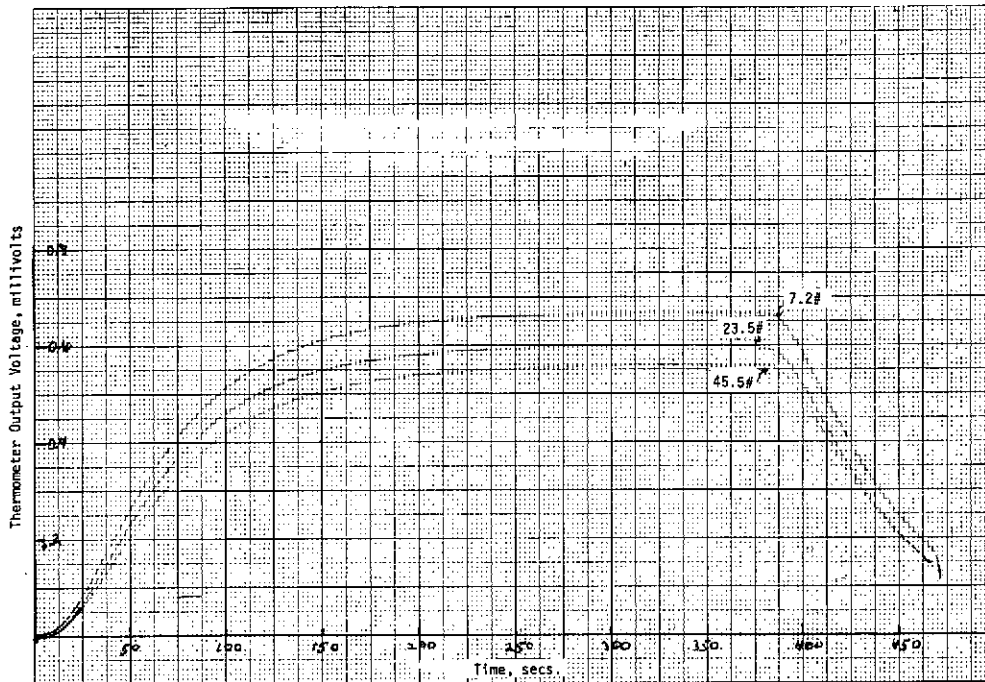


Figure 4-2a Thermometer Output Voltage vs. Time vs. Load in Vacuum for Jo Blocks 1-7 and 10-4 (10-4-72)

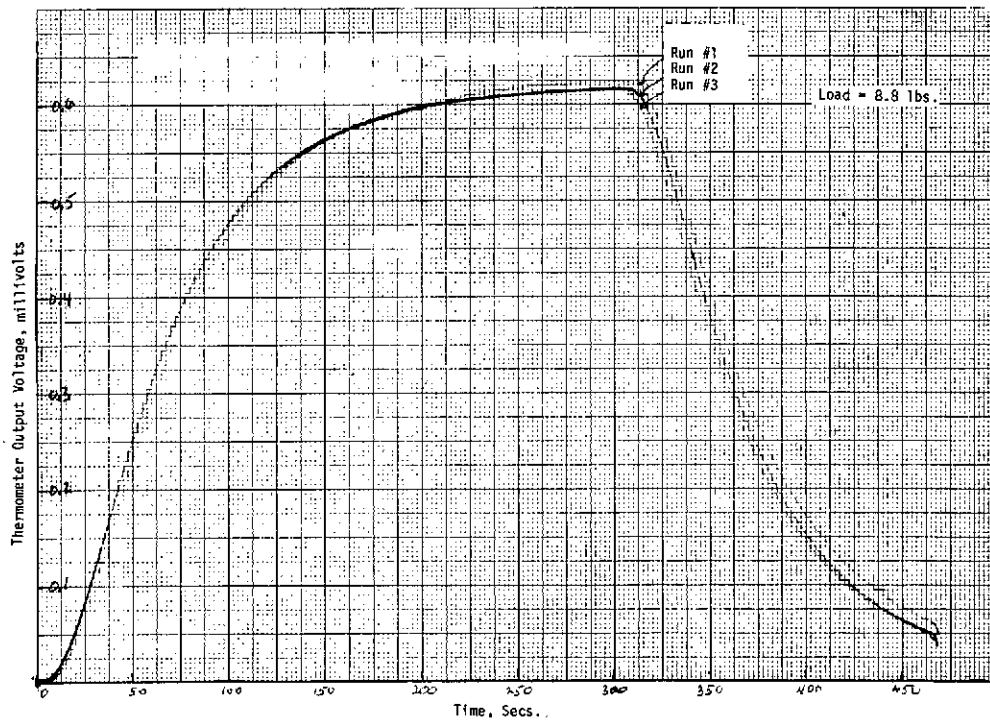


Figure 4-2b Repeatability Checks for Thermometer Output Voltage vs. Time for a Constant Load for Jo Blocks 1-7 and 10-4 (10-4-72)

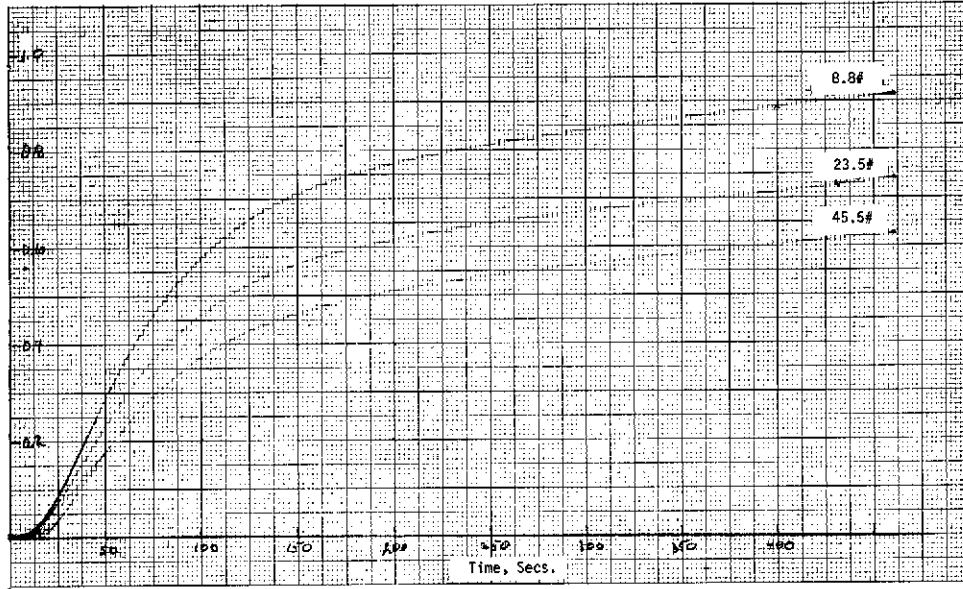


Figure 4-2c Thermometer Output Voltage vs. Time vs. Load for Jo Blocks 1-7 and 1-9 (10-4-72)

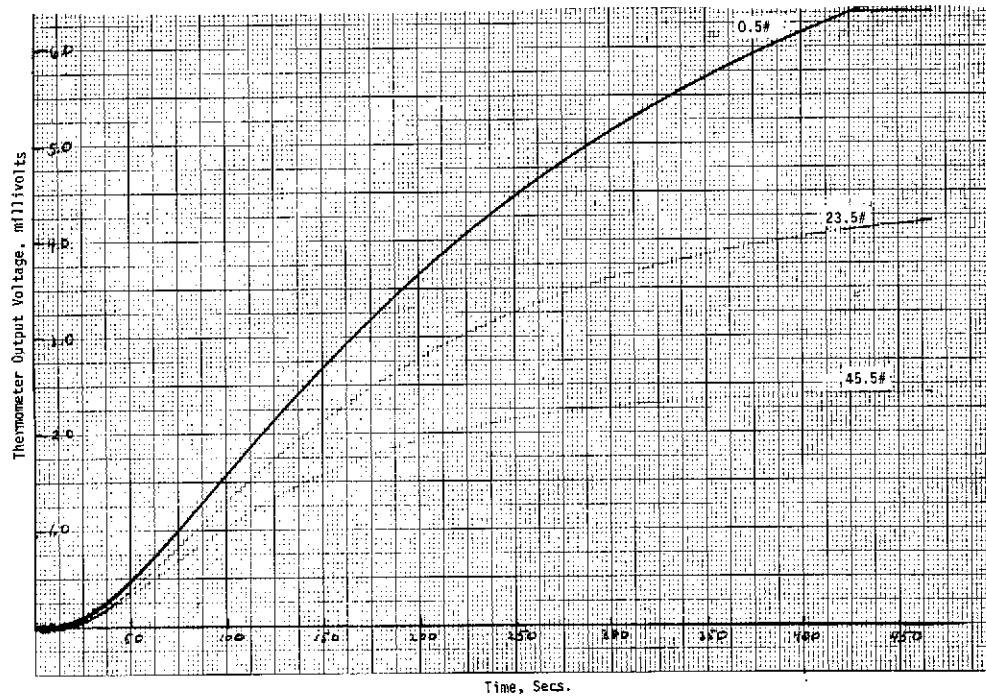


Figure 4-2d Thermometer Output Voltage vs. Time vs. Load for Jo Blocks 1-7 and 50-8 (10-6-72)

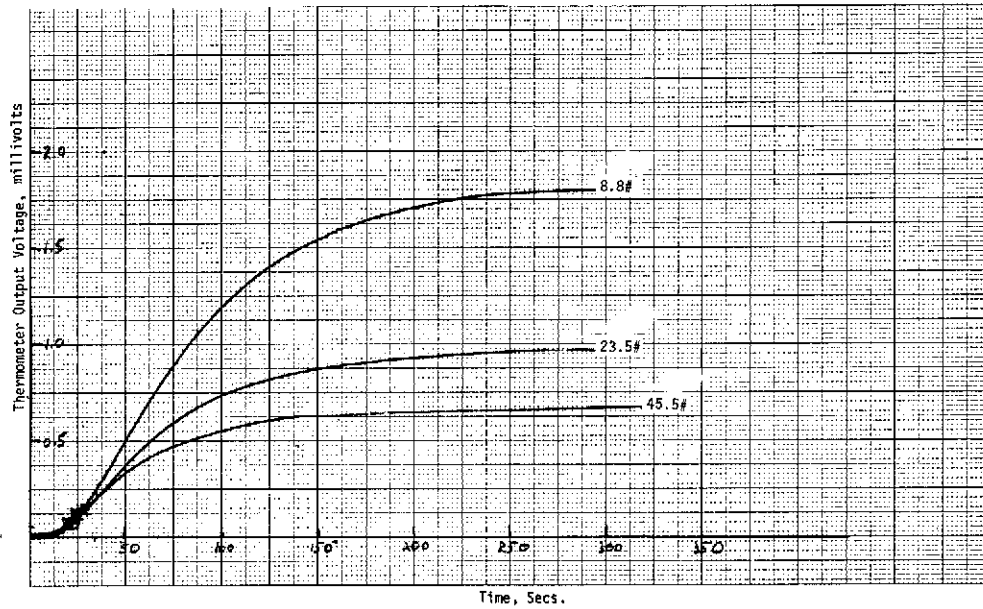


Figure 4-2e Thermometer Output Voltage vs. Time vs. Load for Jo Blocks 1-7 and 1-9 (10-11-72)

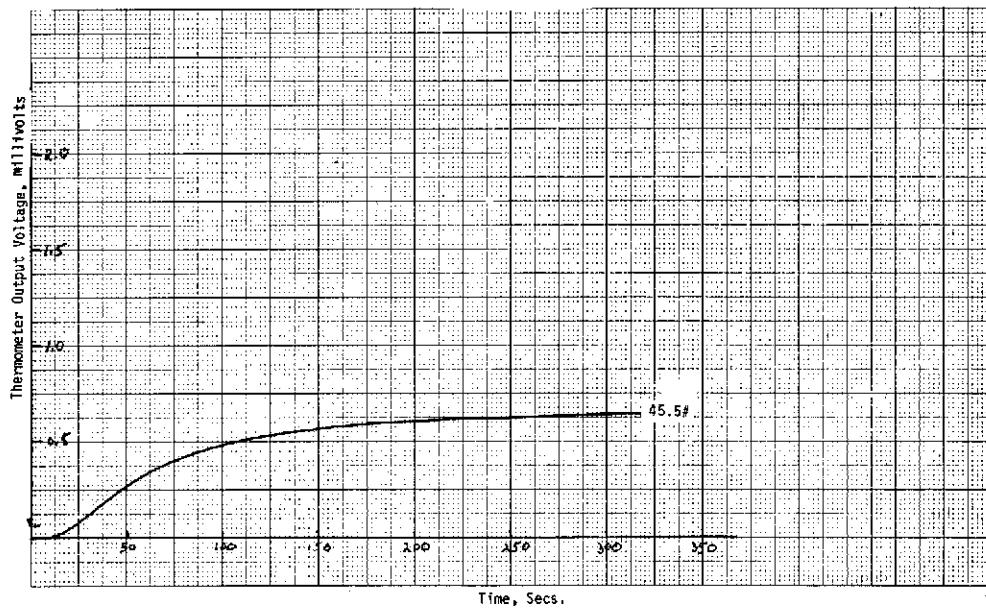


Figure 4-2f Thermometer Output Voltage vs. Time at 45.5# Load for Jo Blocks 1-7 and 1-9 (10-11-72)

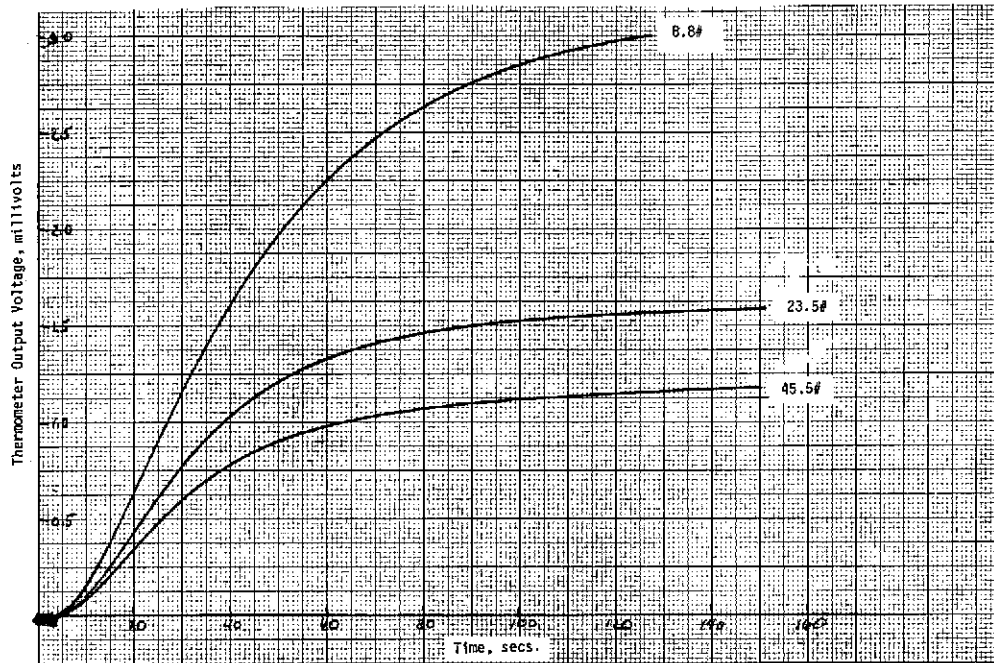


Figure 4-2g Thermometer Output Voltage vs Time vs Load for Jo Block 1-7 and 1-9A (Bead Blasted) (10-13-72)

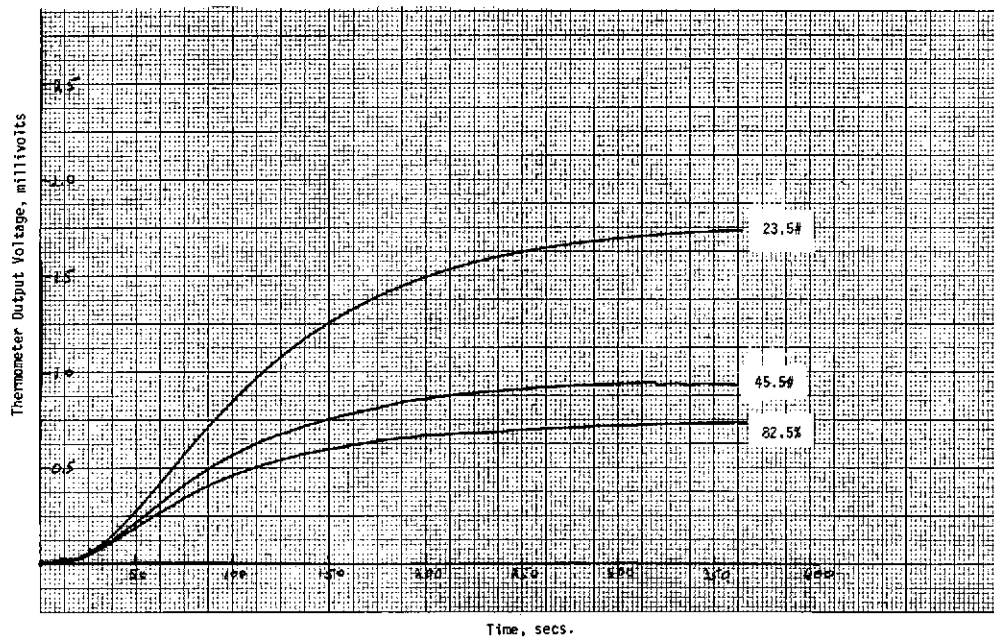


Figure 4-2h Thermometer Output Voltage vs Time vs Load for Jo Blocks 1-7 and 1-9A (Bead Blasted) (10-19-72)

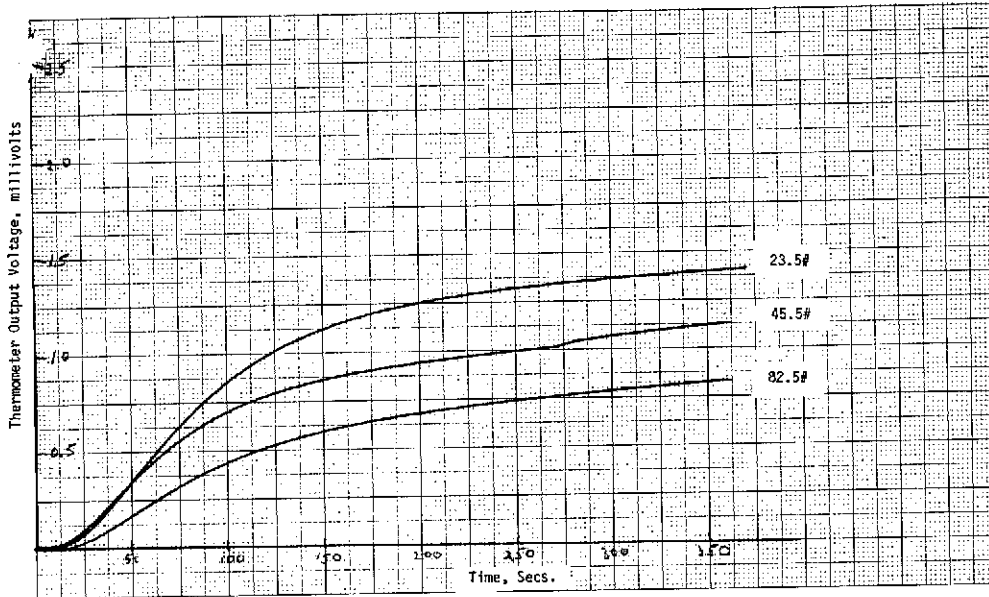


Figure 4-2i Thermometer Output Voltage vs Time vs Load for Jo Blocks 1-7 and 1-1 (10-19-72)

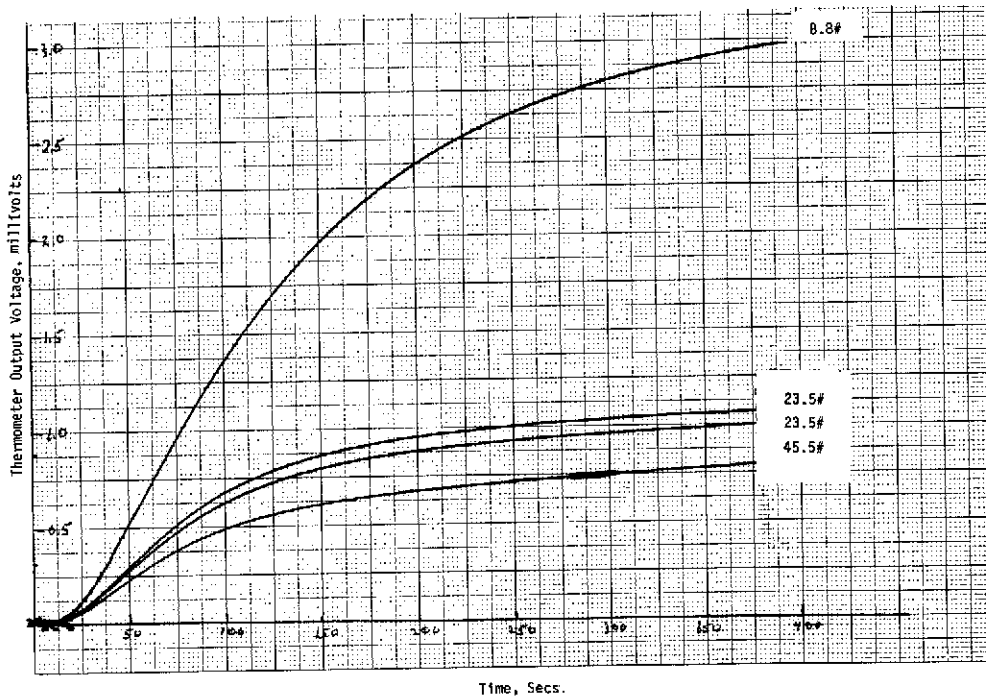


Figure 4-2j Thermometer Output Voltage vs Time vs Load for Jo Blocks 1-7 and 1-1 (10-16-72)

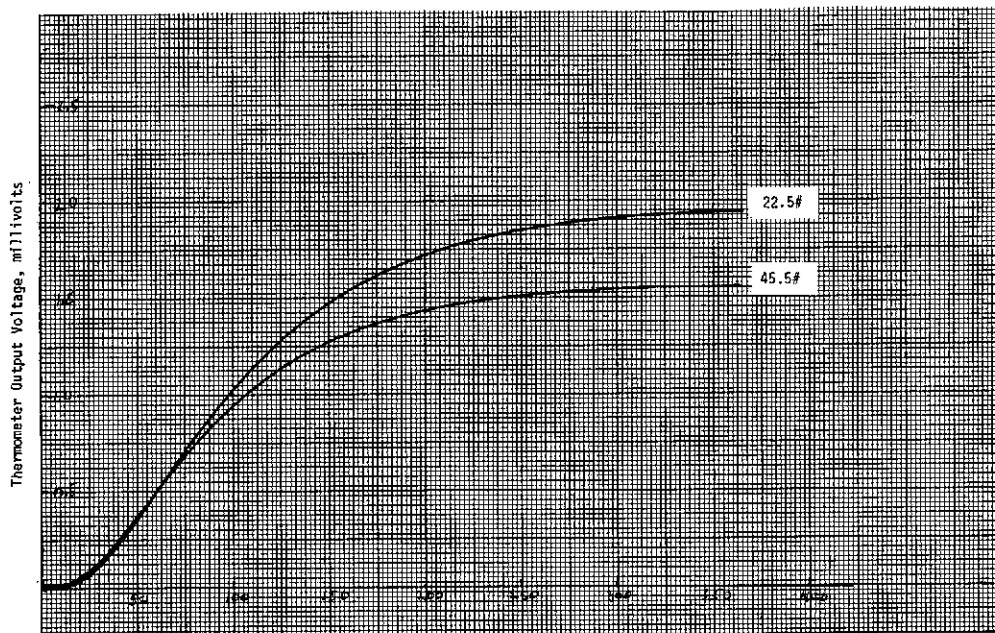


Figure 4-2k Thermocouple Output Voltage vs Time vs Load for Jo Blocks 1-7 and 1-1A (Steel Wool Roughened (10-20-72)

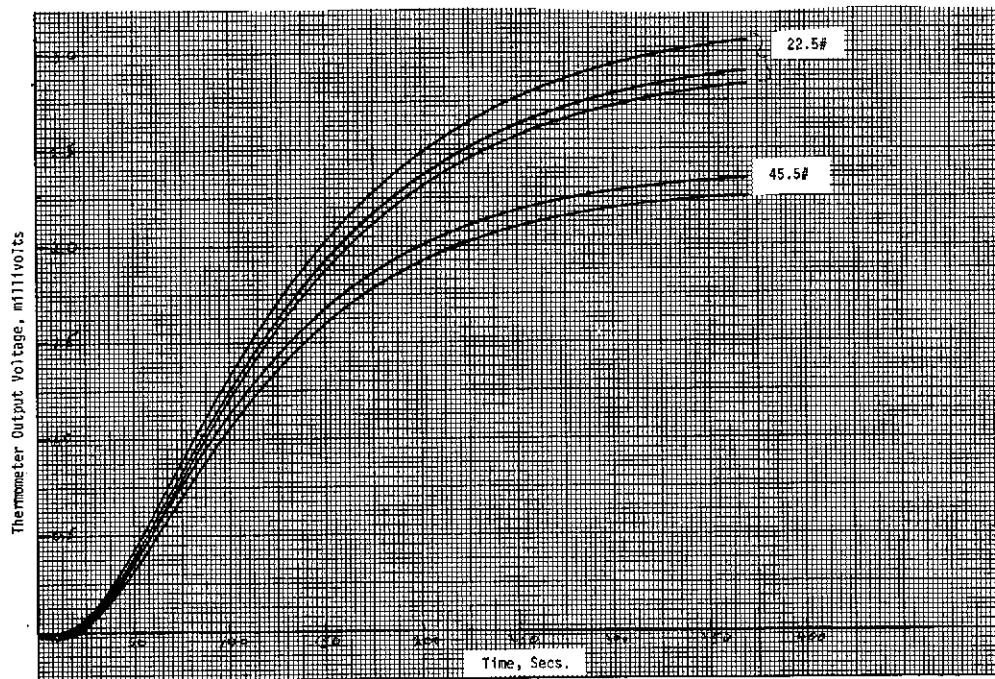


Figure 4-2l Thermometer Output Voltage vs Time vs Load for Jo Blocks 1-7 and 1-1A (Steel wood Roughened) (10-21-72)

A P P E N D I X 4-a

Figure 4-3

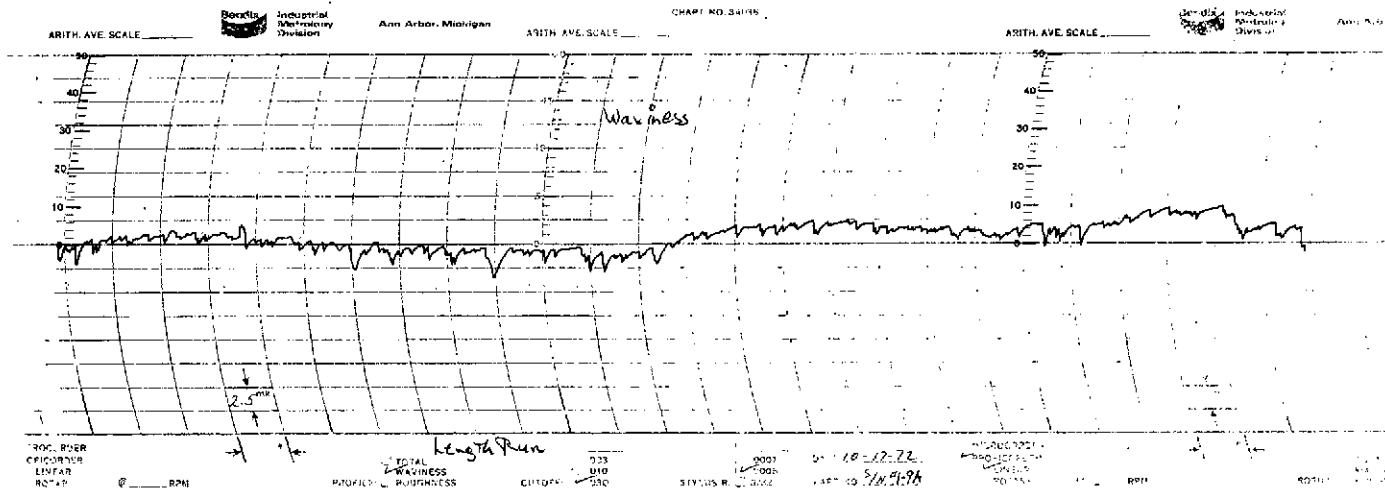


Figure 4-3a Profile of Jo Block Part #1-9A, Waviness, Length Run

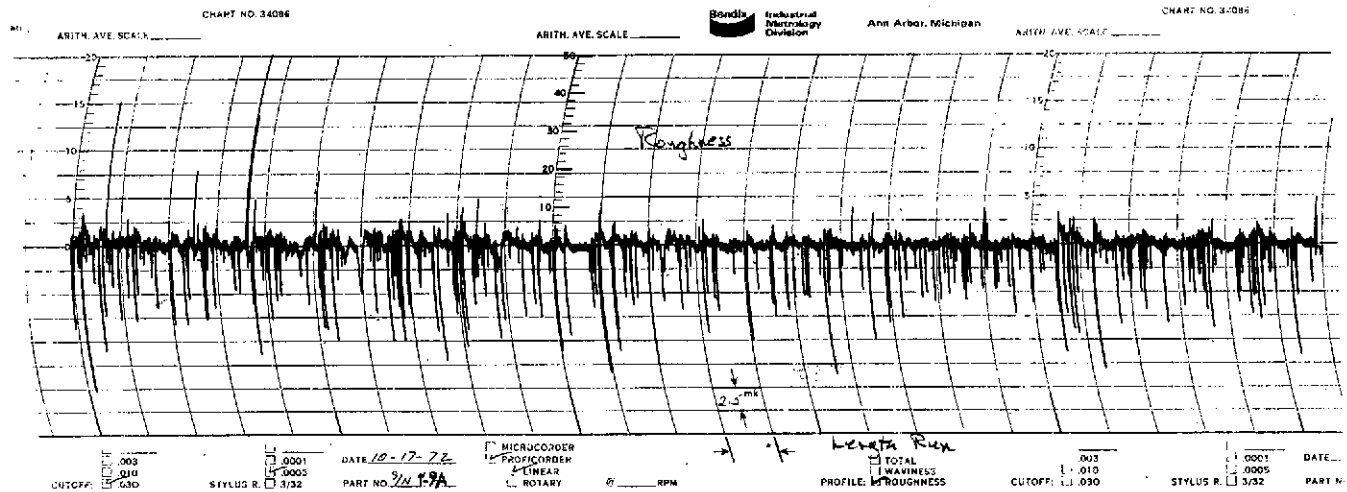


Figure 4-3b Profile of Jo Block Part #1-9A, Roughness, Length Run

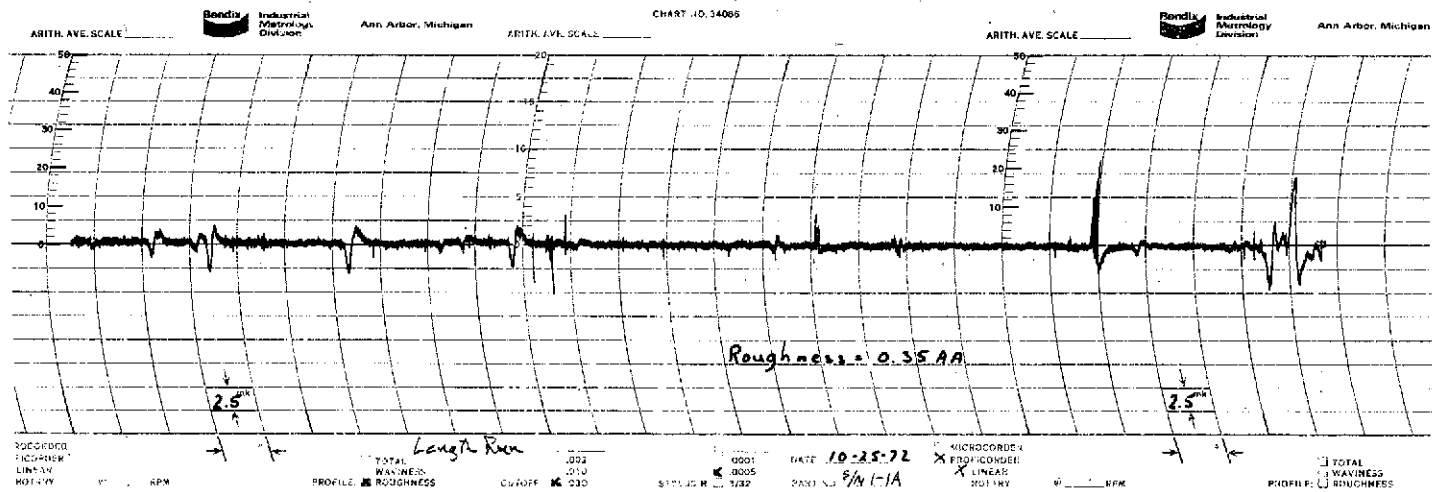


Figure 4-3e Profile of Jo Block Part #1-1A, Roughness, Length Run

5.0 COHERENT OPTICAL SIGNATURES OF MATERIAL SURFACES

5.1 INTRODUCTION

The studies described below were initiated to determine the feasibility of making measurements of surface roughness by coherent optical techniques. The results of these studies illustrate the unique correspondence between the statistical properties of a coherent wavefront reflected from that surface. It was learned that this unique relationship can be used to produce coherent wavefront signatures of surfaces which can yield quantitative identification of the surface's random parameters. These studies can be extended to the measurement of surface roughness and should prove valuable to the study of corrosion, fatigue, and wear in mechanical components since these are influenced by the roughness of surfaces. The essential features of these techniques are (1) the ability to respond to surfaces with roughnesses from .5 to 50 microinches; (2) the noncontacting, noncontaminating, and hence non-destructive nature of the techniques; and (3) the ability to determine a wide variety of statistical parameters for improved surface characterization. In addition, these techniques can be used to locate defects on a surface and to monitor performance degradation of mechanical components caused by surface-related damage.

Conventional techniques for the characterization of surfaces consist almost solely of profilometry and visual inspection. In profilometry, a mechanical stylus connected to an LVDT or other motion sensing device is moved across a surface while movement of the stylus caused by changes in surface elevation are monitored electronically. This technique and visual inspection have generally themselves been the limiting factors in many studies of surface roughness phenomena. For example, the movement of the profilometer stylus as it is drawn across the surface often causes damage and hence is a destructive measurement. Other problems relating to the sensitivity to vibration, delicate design, and general complexity of profilometers limit the use of such sophisticated instruments.

5.2 COHERENT OPTICAL SIGNATURES OF SURFACES

Coherent optical measurement techniques, stimulated by the development of holography, appear to offer new and advanced forms of surface characterization. Since it only the light beam which actually strikes the surface, optical measurement techniques are noncontacting, noncontaminating, and hence nondestructive. By reflecting light from a surface (as shown in Figure 5-1), it is possible to transfer information about that surface to the reflected optical wavefront. This information can then be stored or processed by holographically recording the wavefront or by manipulating it optically.

The basic equipment used for these studies is illustrated in Figure 5-1. It can be seen in this photograph that the light propagating from a laser is reflected by the surface to produce the wavefront signature. A projection screen was used to allow visualization of the diffracted coherent wavefront. It was the variation in the illumination across this projection screen that was actually measured to produce the signature of the surface.

A variety of these signatures is illustrated in Figure 5-2 where the wavefronts reflected from 4, 8 and 16 microinch surfaces are shown projected on the screen. It is noted that the optical signatures obtained from these three surfaces are highly distinctive, although the actual roughness of the surface is less than the wave length of light (approximately 25 microinches). In particular, it can be seen that the magnitude of the central peak of the intensity distribution varied inversely with the surface roughness. As the material surface became smoother, the central peak tended to increase. In addition, it can be seen that the intensity profile tended to spread out across the projection screen as the surface roughness increased. It is the shape of this intensity profile which is determined by the statistical parameters of the rough surface and serves to form the coherent wavefront signature used for surface characterization.

The ability of this technique to detect flaws or irregularities on surfaces was also investigated. Two optical signatures are illustrated in Figure 5-3 which demonstrate the detection of scratches.

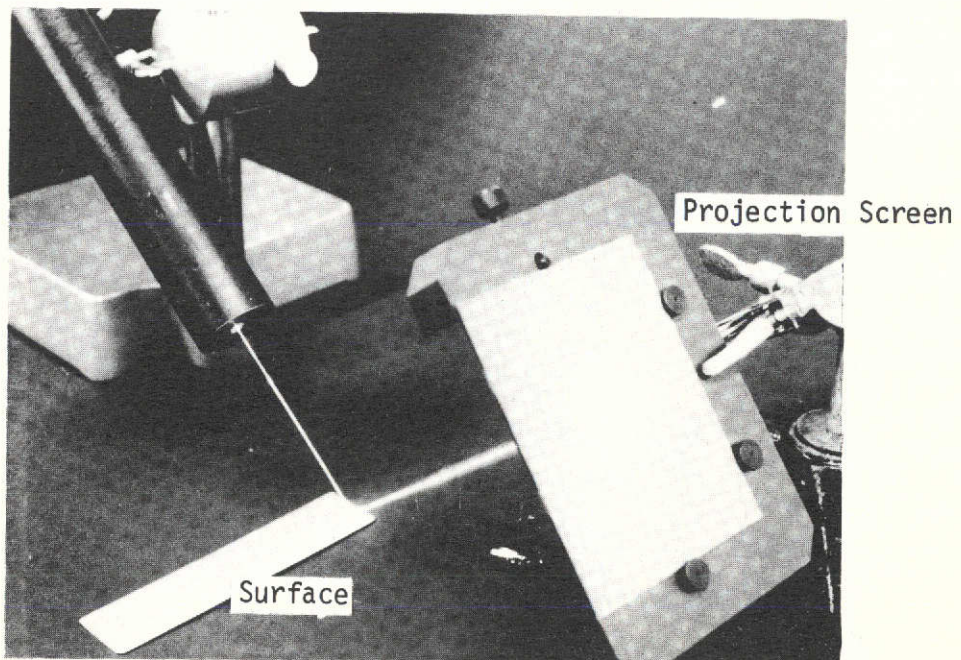
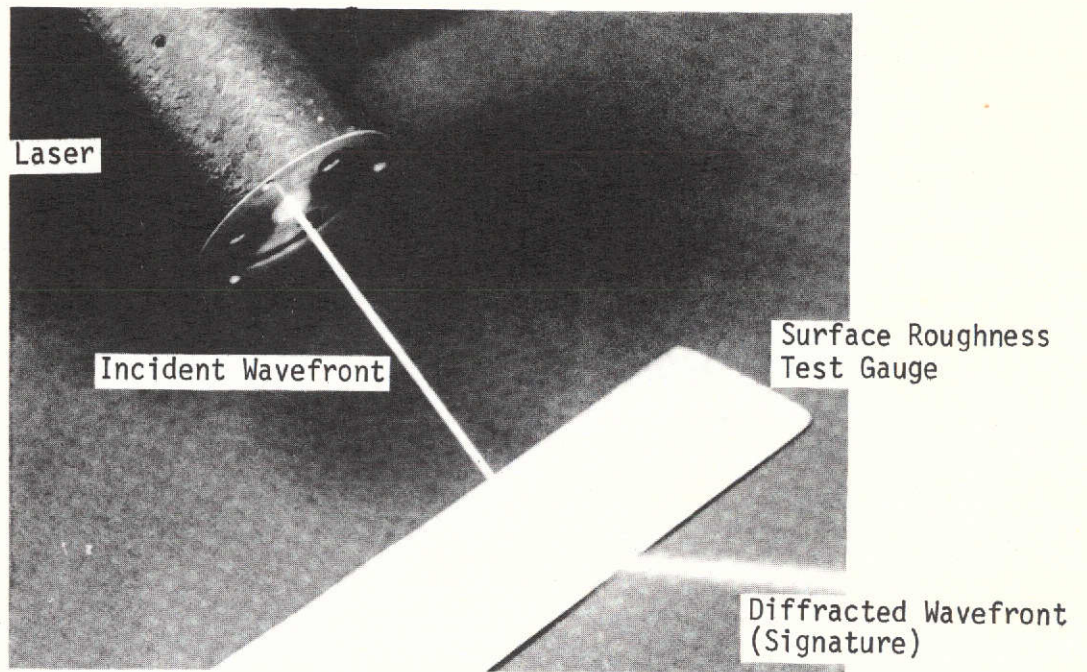
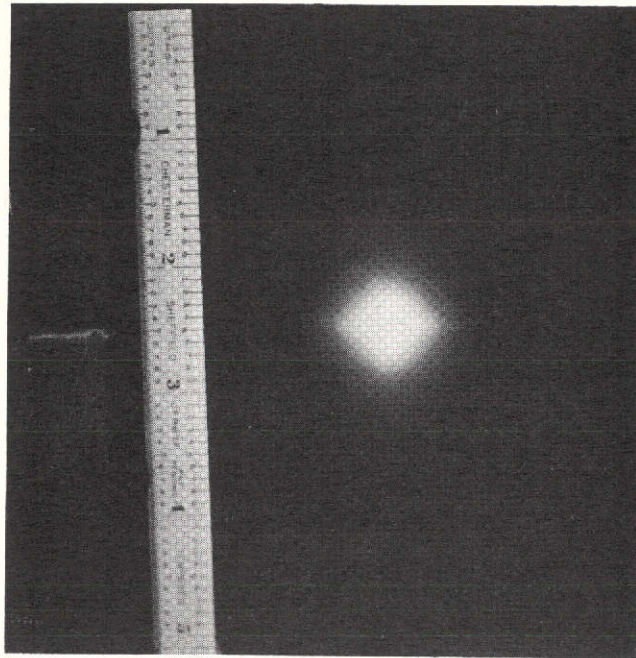
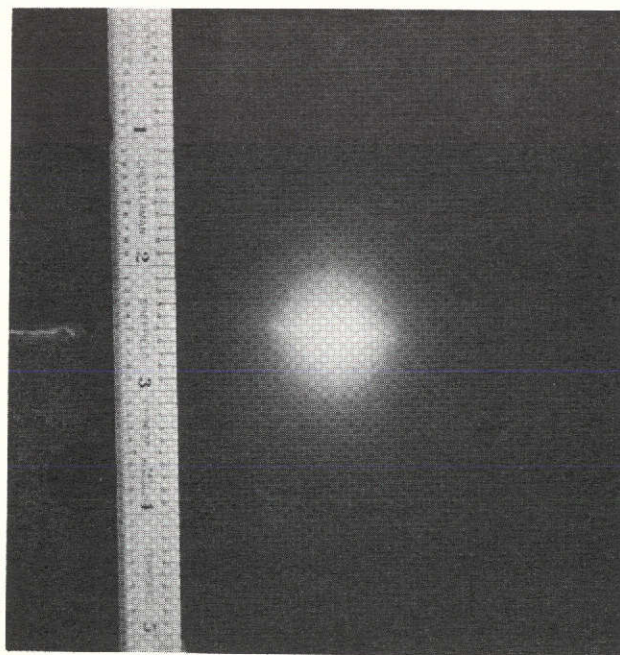


Figure 5-1. Detection of Coherent Wavefront Signatures of Rough Material Surfaces

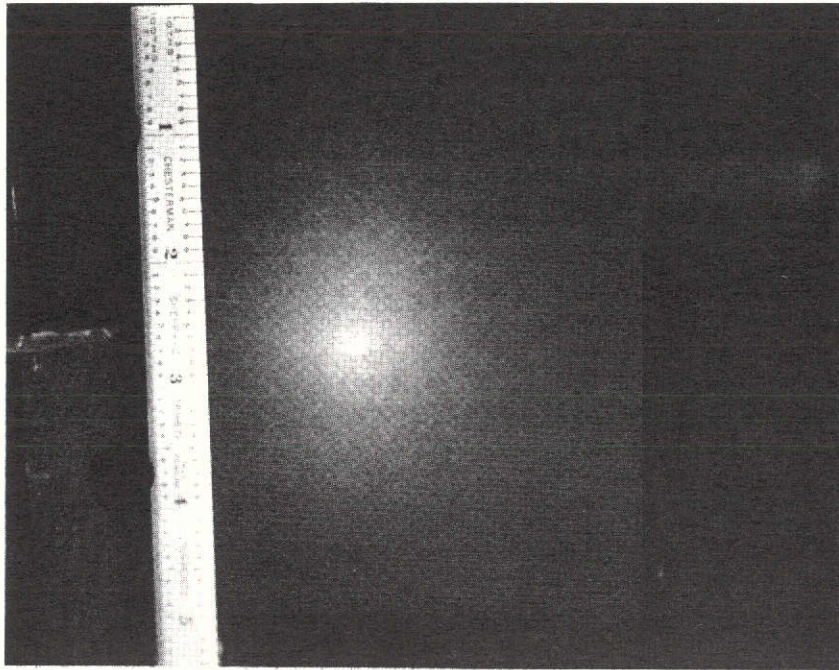


a. 4μ inch (RMS)



b. 8μ inch (RMS)

Figure 5-2. Coherent Wavefront Signatures of Material Surfaces with Varying Roughnesses



c. 16μ inch (RMS)

Figure 5-2 (Cont'd). Coherent Wavefront Signatures
of Material Surfaces With Varying Roughnesses

The photograph 5-3a shows the coherent signature obtained from a material surface free of all defects except for the normal irregularities resulting from machining processes. Comparison of this photograph with the photo of Figure 5-3b demonstrates the sensitivity with which surface flaws could be identified through coherent light signatures. Both the number and direction of the surface flaws can be determined using this technique which can be automated for fast and accurate surface inspection.



Normal Surface

Signature of Machinist Marks



Flawed Surface

Signature of Scratch

Figure 5-3. Coherent Wavefront Signatures of Surface With and Without Defects

5.3 APPLICATION OF COHERENT OPTICAL SIGNATURE TECHNIQUE TO THE LONG TERM PERFORMANCE VALVE SEAT DEVELOPMENT (SEE SECTION 2.0)

Surface quality measurements using coherent light were made during the testing of the valve design reported in Section 2.0. This design typifies the design concept of a hard/soft metal to metal seal. In principle, large yielding stresses are applied between the hard and soft faces of the seal, causing the hard poppet to coin the microscopic features of its surface into the soft metallic seat. This produces two identical surfaces which together provide the sealing interface. A metal seated valve based on this technique could be used repeatedly with low leakage and low wear. The complete description of this valve seat design is given in Section 2.0.

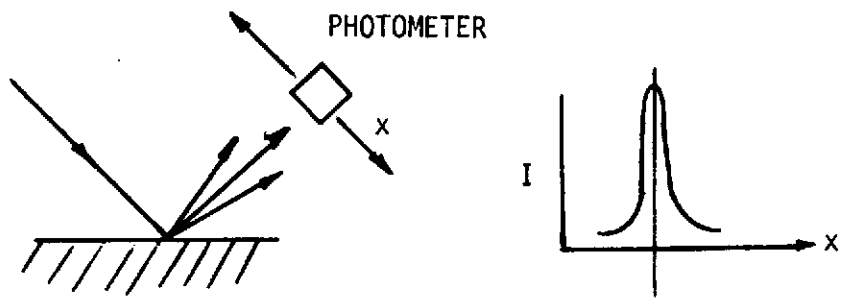
A critical portion of the program designed to test these principles centered on determining the change in quality with cycles of the two metallic surfaces. Since two different metals were used for the hard and soft surfaces of the test valve, it would be expected that the initial surface roughness of the two interfaces would be different. While the interfacial pressures should be high enough to cause the hard surface to transfer its "topological" features to the soft surface, the rate at which the transfer could take place was not known.

The proper measurement of surface roughness is critical to the characterization of overall valve performance. Any scratch or flaw in the surfaces can serve to initiate fatigue or crazing and can, therefore, constitute a potential failure site. While data on the surface roughness of both surfaces is needed as a function of valve cycling, measurements with conventional profilometers can produce such defects and severely degrade the valve performance. What is needed for the measurement of surface roughness during a performance test is a truly nondestructive technique which can provide surface roughness data without physically contacting the surface under test.

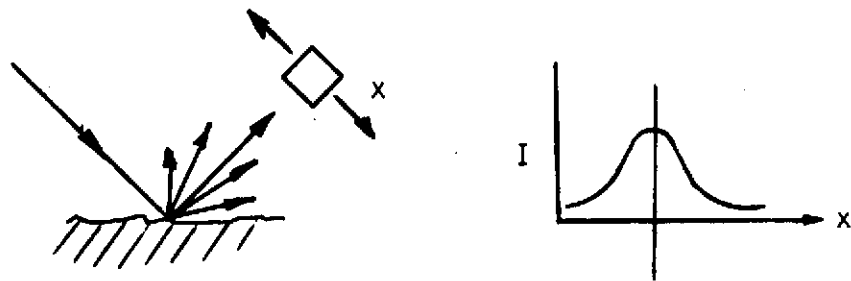
The basic principle behind the technique used on the valve seat is illustrated in Figure 5-4, where the behavior of light reflected from a variety of rough surfaces has been illustrated schematically. It can be seen in this figure that light reflected from a very smooth surface tends to maintain an angle of reflection approximately equal to the angle of incidence, to the extent that light reflected from a smooth surface remains concentrated in this single direction. However, as the surfaces become rougher, more and more light is directed toward other angles so that the reflected light pattern is less directional and more diffuse. This directionality varies with the roughness of the surfaces from which it is reflected and can be recorded by the scanning photometer shown in Figure 5-4 and used for comparison with other surfaces.

A typical optical signature has the intensity distribution shown in Figure 5-5. This intensity pattern is characterized by the parameter, w , defined as the width of the profile at half the peak intensity of the signature. (The width, w , is measured to the right of the peak to eliminate the effects of a slightly unsymmetrical profile.)

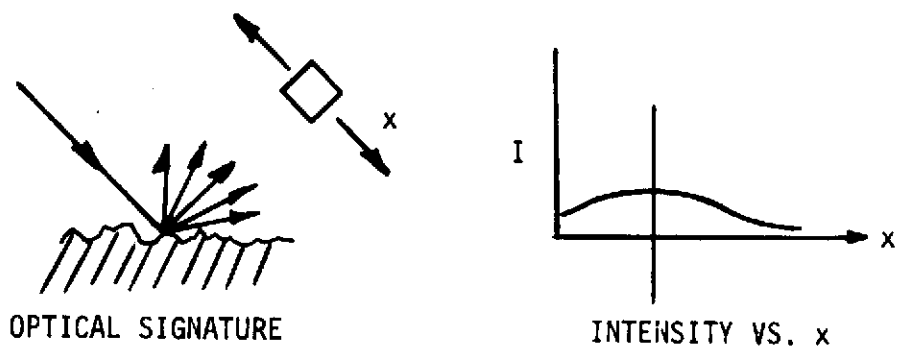
An initial calibration of the test fixture was made by inserting surfaces of known surface roughness into the apparatus, recording and analyzing their respective optical signatures and plotting the results as shown in Figure 5-6. Three points of calibration were obtained from a 2, 4, and 8 microinch test surfaces, while the fourth point, corresponding to the width of the laser beam itself, was produced by placing the traveling photometer directly in the light beam. Thus, it was possible to calibrate the response of the setup to surfaces of varying roughnesses in a manner consistent with the procedures of earlier studies. It was found from this calibration procedure that the range of surface roughnesses measurable with this optical setup varied from approximately .25 to 5.0 microinches, and was well within the range of values needed for the program.



(a) Smooth Surface



(b) Slightly Rough Surface



(c) Very Rough Surface

Figure 5-4. Variations of Optical Signature Intensity Distribution for Surfaces of Varying Roughness

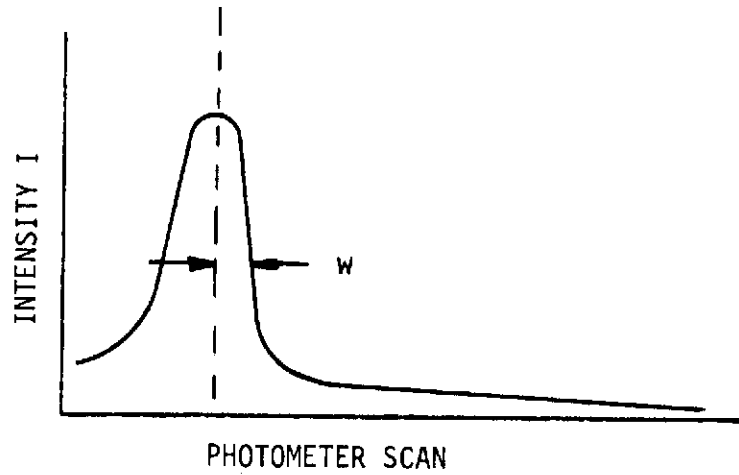


Figure 5-5. Measurement of Half Width w From the Intensity Distribution of a Typical Optical Roughness Signature

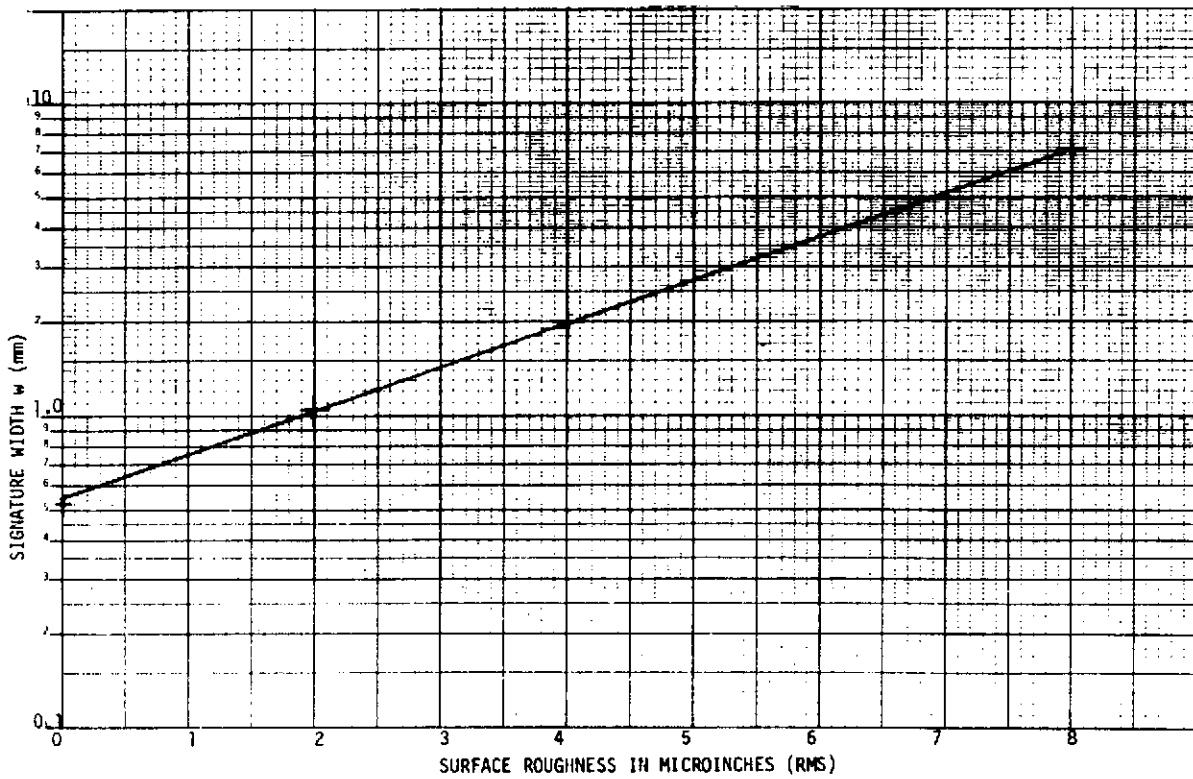


Figure 5-6. Calibration Curve

5.3.1 Testing Apparatus

The experimental setup used in these studies for optically measuring surface roughness is shown in Figures 5-7, 5-8 and 5-9. The test valve was mechanically cycled in the hydraulic machine described in Section 2.0. This machine permitted the continuous monitoring of valve motion and interfacial pressure. A mass spectrometer leak detector was connected to the system for the measurement of leak rate at various stages of the cycling. The valve seat components could be removed periodically and placed in the optical setup shown below for the assessment of sealing surface quality. Thus, it was possible to determine both the leakage and surface roughness changes as a function of the number of test cycles.

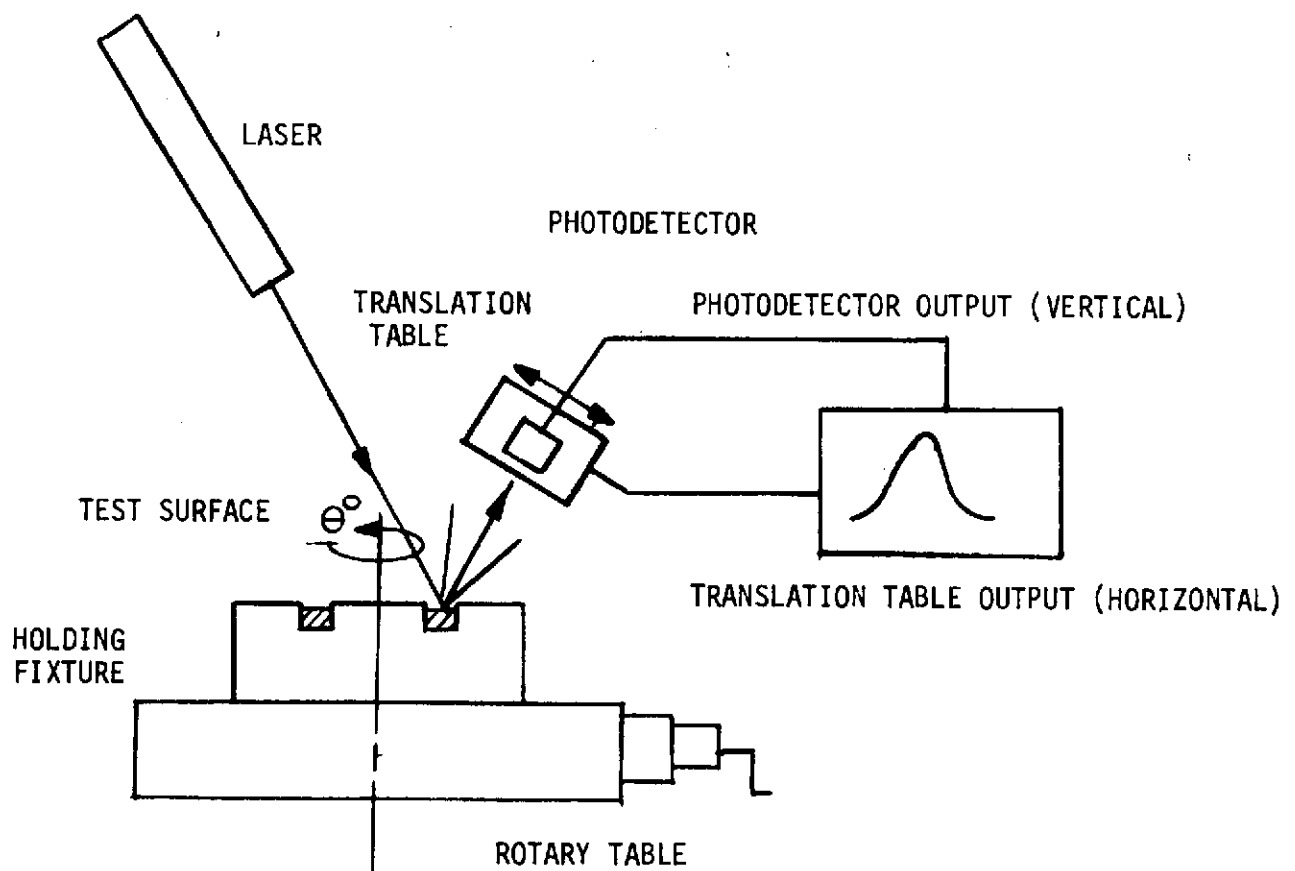


Figure 5-7. Schematic Representation of Optical Signature Test Setup

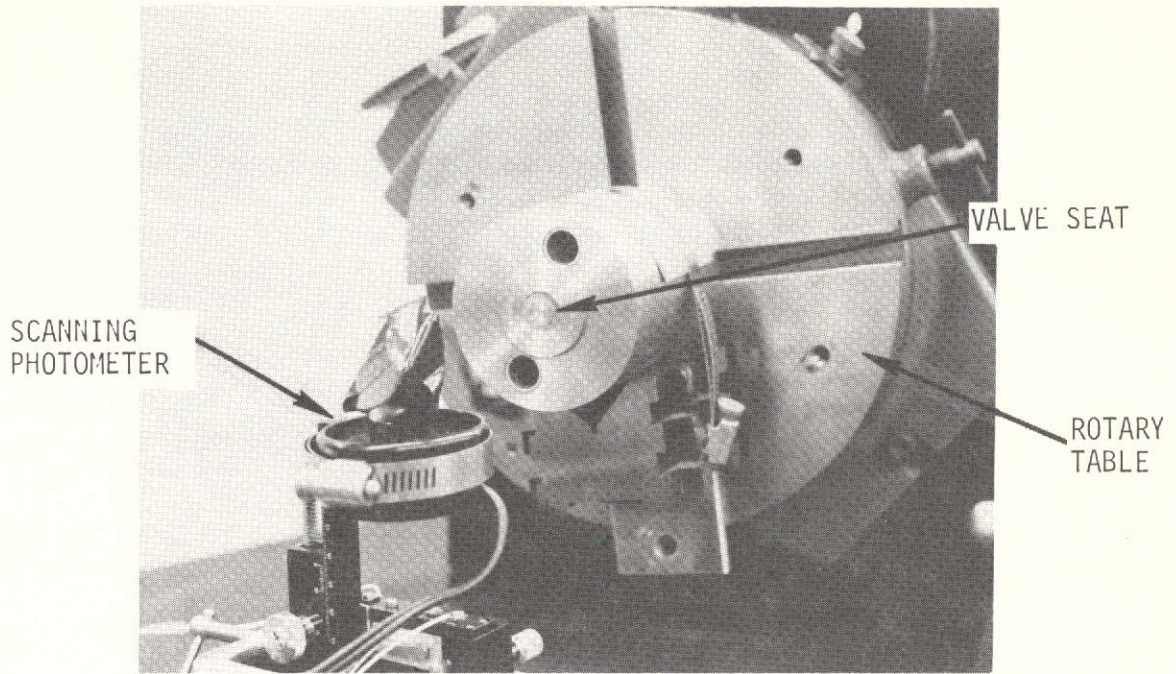


Figure 5-8. Fixture and Test Setup for Optical Signature Measurement of Valve Seat Surface

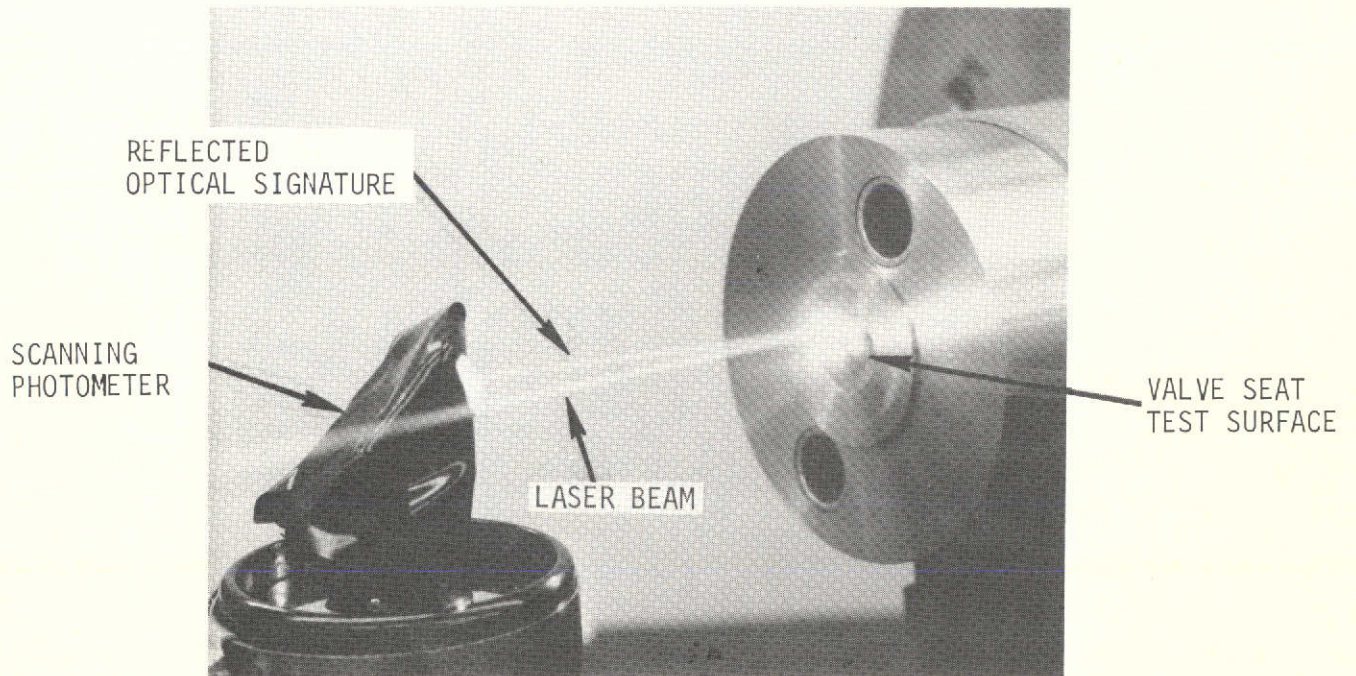


Figure 5-9. Closeup of the Optical Signature Diffracted From the Valve Seat Test Surface

The three basic components of the optical surface roughness setup shown in Figure 5-7 are 1) a 15 milliwatt HeNe laser, 2) a rotational specimen holder, and 3) a translating photometer. The specimen was mounted on the rotary table shown in Figure 5-8 to permit the placement of all portions of the test surface under the laser beam. In this manner it was possible to nondestructively measure the surface roughness at all points on the valve surface, correlated with position. The two outputs of the scanning photometer were connected to an x-y chart recorder to permit the immediate observation and recording of the coherent light signatures. Typical printout data taken from the x-y recorder is reported in Figures 5-10 through 5-13. From these data and the calibration curve of Figure 5-6, the following table was constructed.

<u>Signature</u>	<u>Cycle No.</u>	<u>θ</u>	<u>Surface Finish (Soft Seat)</u> <u>Microinches RMS</u>
Figure 5-10	0	0°	3.0
		30	2.7
		80	2.0
		130	1.3
		340	2.5
Figure 5-11	2	0°	1.3
		115	2.5
		209	1.6
		303	2.3
		355	1.9
Figure 5-12a	277	0°	1.4
		65	1.4
		82	1.4
		182	1.4
Figure 5-12b		201	1.6
		292	1.3
Figure 5-12c		303	0.8
		320	1.2
		330	1.3
Figure 5-13a	72,000	1°	1.4
		77	1.6
		100	1.4
Figure 5-13b		160	1.4
		175	1.6
		206	3.0

<u>Signature</u>	<u>Cycle No.</u>	<u>θ</u>	<u>Surface Finish Microinches RMS</u>
Figure 5-13c	72,000	216	2.0
		218	1.4
		234	2.0
Figure 5-13d		251	1.6
		256	2.0
		292	1.4

5.4 CONCLUSIONS

It was learned in the above studies that the coherent wavefront diffracted by a surface is uniquely determined by the properties of that surface and, therefore, produces an optical signature for the purposes of rough surface characterization and measurement. These coherent optical signatures varied in accordance with variations in the statistical parameters of the surface and, thus, can be used to identify and classify material surfaces created by various processes. Since these techniques provide area measurements rather than line tracings, they can be used to monitor waviness as well as linear root mean square deviation values analogous to that obtained with the conventional profilometer.

The coherent signatures can be easily recorded with either photographic or electronic devices to permit the quantitative characterization of surface roughness. By projecting the coherent wavefront signature onto photographic film or by scanning the signature with photoelectric devices, it is possible to record the coherent signature for comparison with signatures obtained from other rough surfaces or from the same surface undergoing modification through some degradation process. Optical surface roughness measurements can be made which are noncontacting, nondestructive, and sensitive to small variations in surface roughness. In view of the highly informative, experimental versatility, and inherently accurate nature of these techniques, the application of coherent optical surface rough measurements to current problems of component reliability appears worthy of further consideration. Such a study could be easily made by coupling these new coherent optical techniques with conventional wear and aging test equipment.

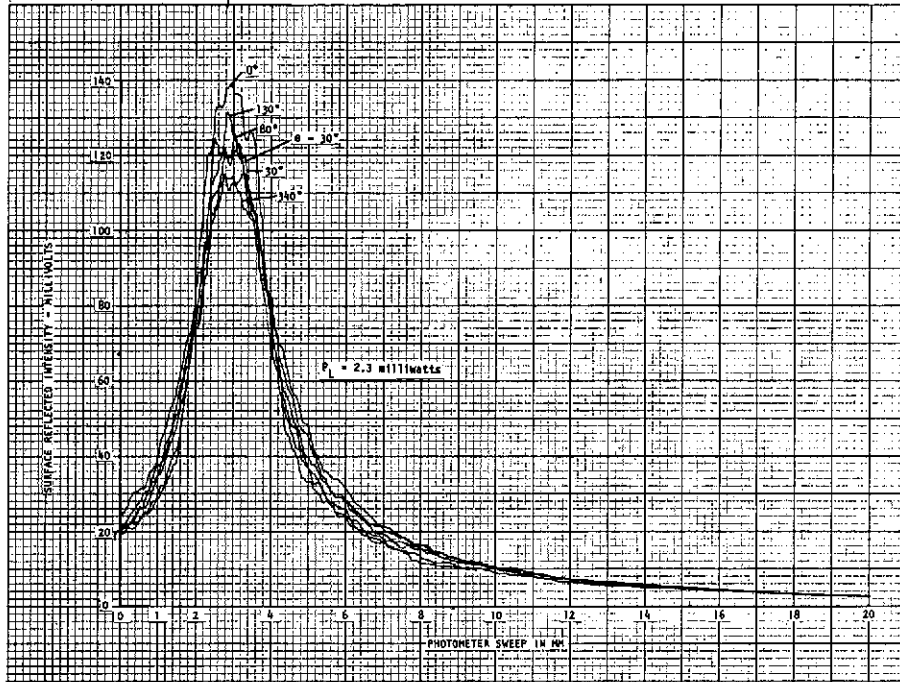


Figure 5-10. Optical Signature of 1100 Aluminum Surface, θ from 30° to 340° , Cycle No. 0

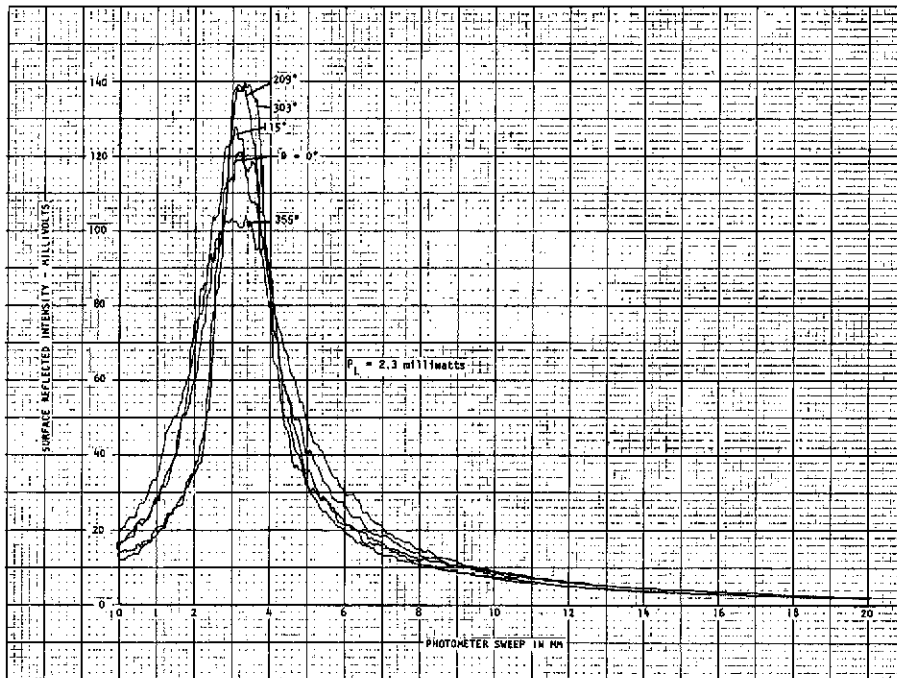


Figure 5-11. Optical Signature of 1100 Aluminum Surface, θ from 0° to 303° , Cycle No. 2

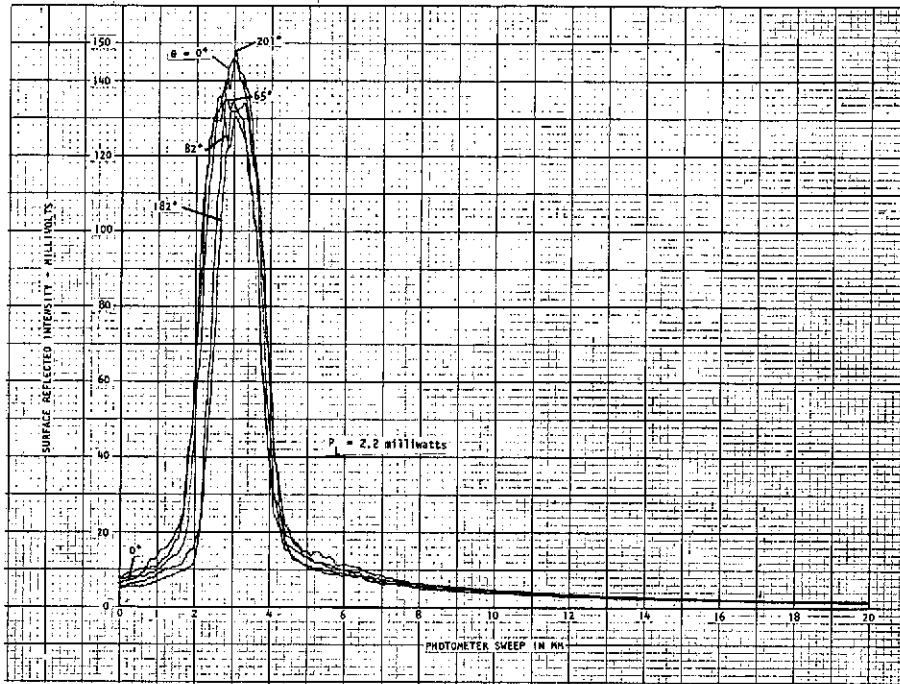


Figure 5-12a. Optical Signature of 1100 Aluminum Surface, θ from 0° to 201° , Cycle No. 277

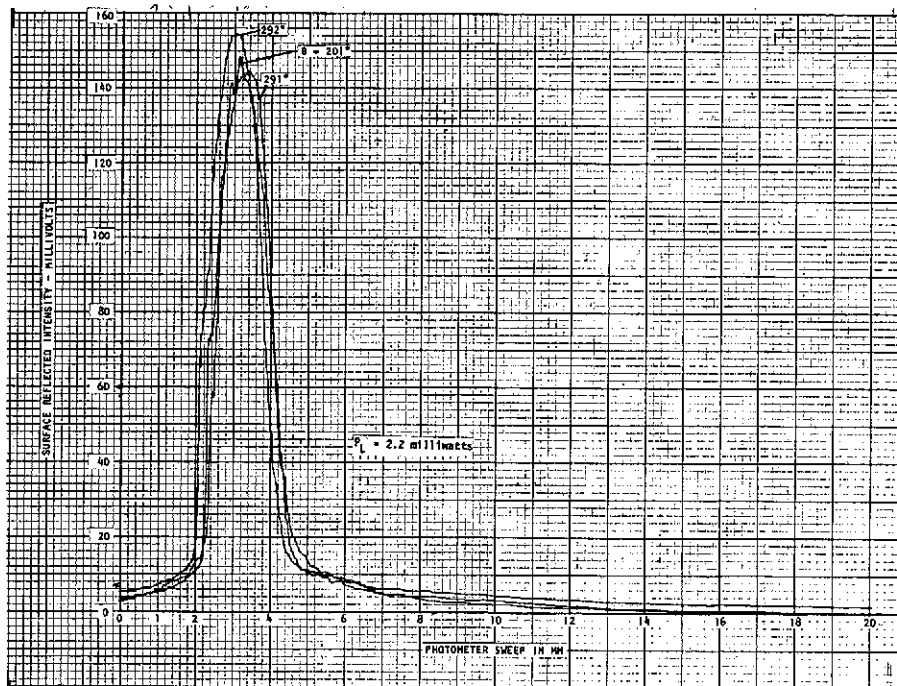


Figure 5-12b. Optical Signature of 1100 Aluminum Surface θ from 201° to 292° , Cycle No. 277

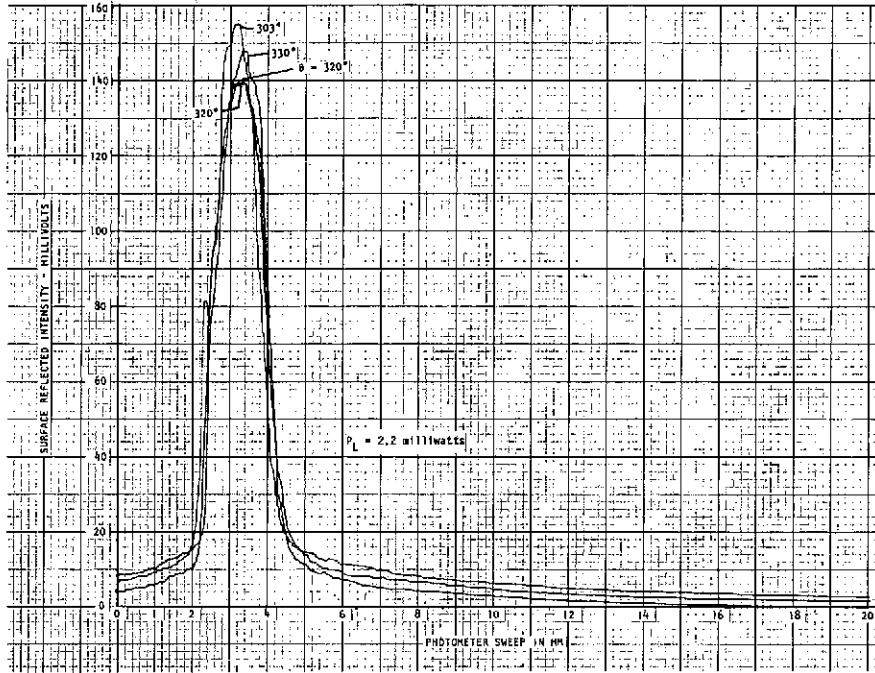


Figure 5-12c. Optical Signature of 1100 Aluminum Surface, θ from 292° to 360° , Cycle No. 277

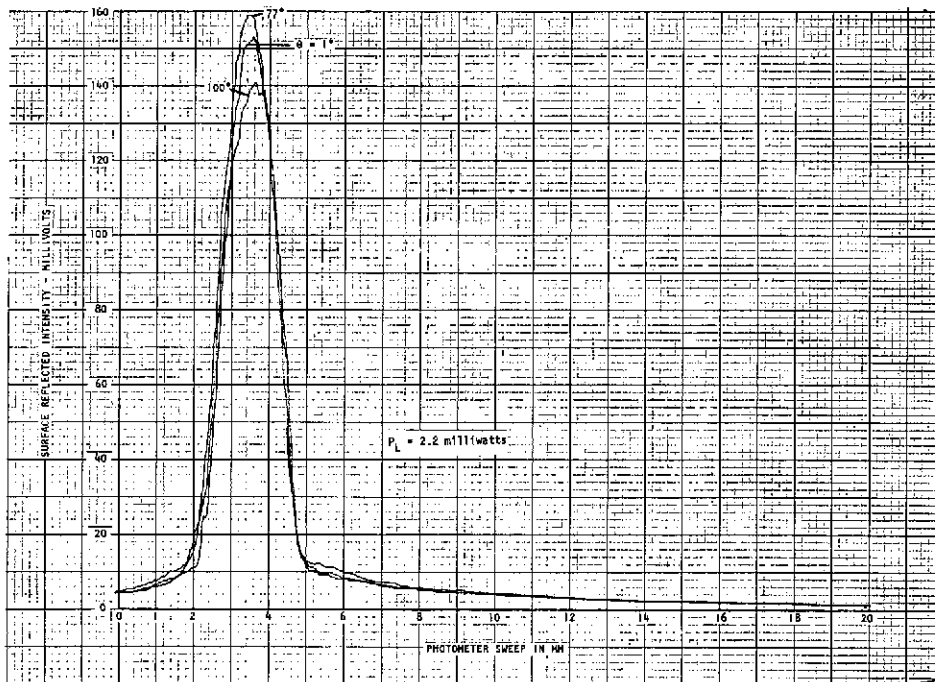


Figure 5-13a. Optical Signature of 1100 Aluminum Surface, θ from 0° to 100° , Cycle No. 72,005

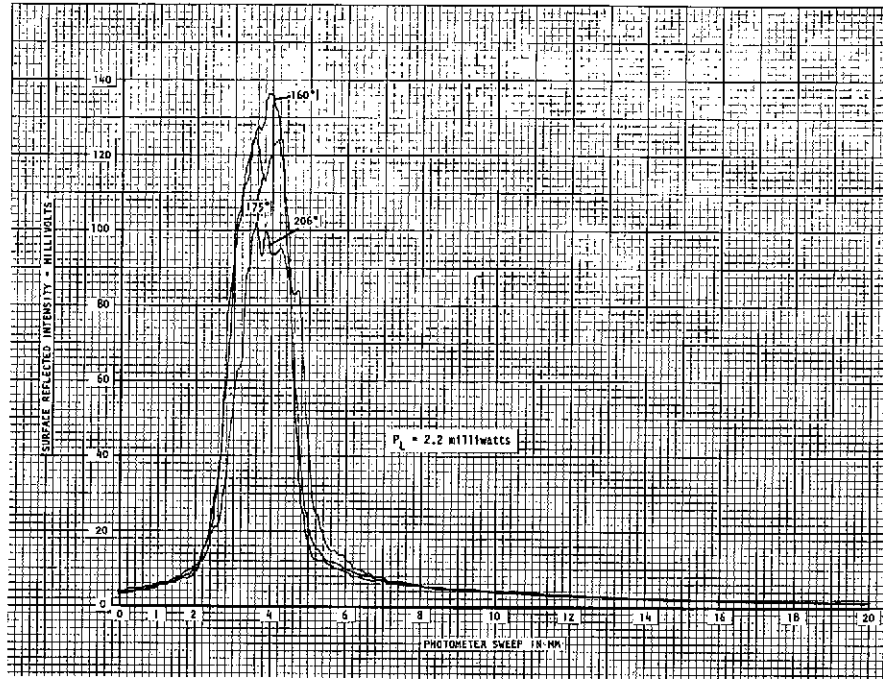


Figure 5-13b. Optical Signature of 1100 Aluminum Surface, θ from 101° to 206° , Cycle No. 72,005

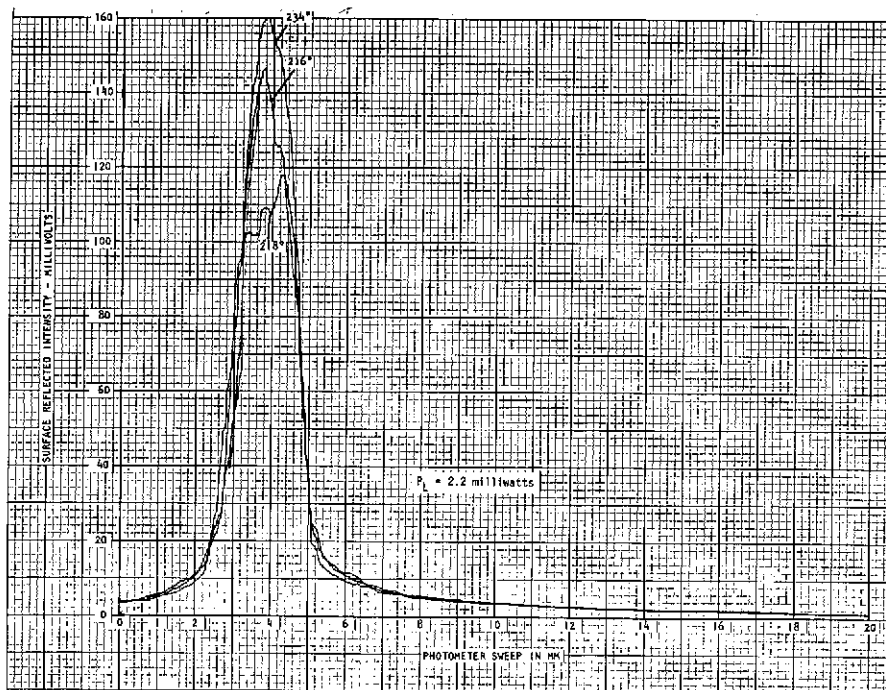


Figure 5-13c. Optical Signature of 1100 Aluminum Surface, θ from 207° to 234° , Cycle No. 72,005

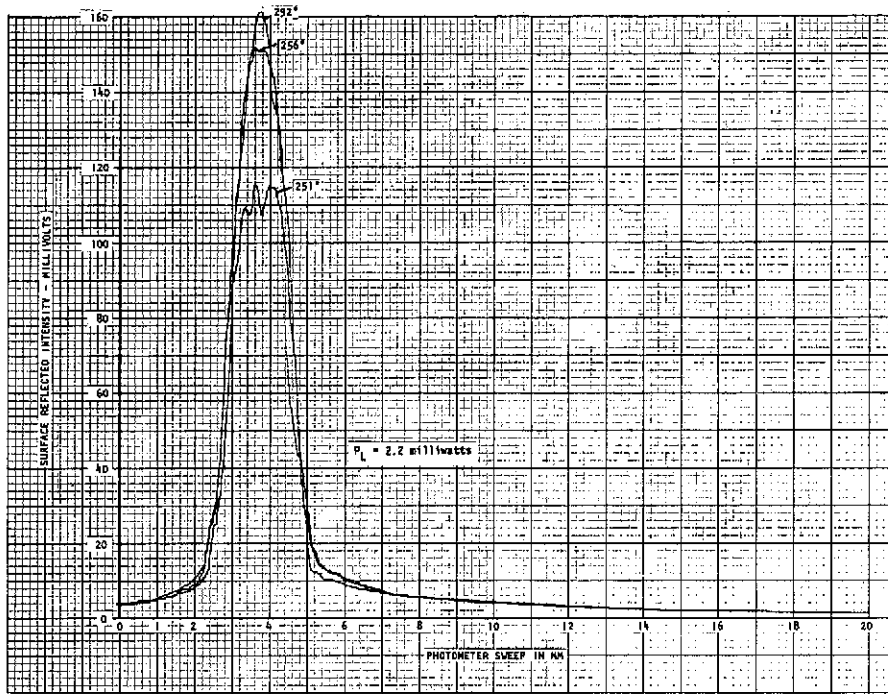


Figure 5-13d. Optical Signature of 1100 Aluminum Surface, θ from 235° to 360° , Cycle No. 72,005

6.0 FLOW TRANSIENT SIGNATURE STUDIES

6.1 INTRODUCTION

This section describes the measurement of fluid flow transients. Tests were made using an Optron electro-optic strain monitor. This system has high accuracy, a high data acquisition rate (500 measurement during a 2 millisecond transient) and a high test rate. Applications of this signature technique include measurement of valve flow transients and valve leakage measurements.

Figure 6-1 is a conceptual presentation of the system. An Optron electro-optic strain monitor is used to measure the position of a light/dark fluid interface in a precision bore tube attached to the valve. The contrasting interface can be formed by the injection of a slug (piston) of opaque dyed fluid or mercury or a solid slug into the precision bore tube before the start of the test. The bulk of the test fluid, whether propellant or a referee liquid, is transparent, or vice versa. The Optron produces an output voltage proportional to the displacement of the interface. A scope photo of this voltage versus time characterizes the transient flow properties of the valve since the displacement voltage is directly proportional to the flow volume.

The source accumulator is filled with a propellant or referee fluid which is allowed to fill the precision bore tube, and the valve. A contrasting interface slug (piston) of inert liquid or solid is injected into the precision bore tube, and recognized by the Optron. The needle valve bypass can be used to position the interface. The test valve is opened and the scope simultaneously triggered. The Optron output voltage is proportional to the instantaneous interface position, hence the output voltage versus time is directly proportional to the flow versus time.

6.2 DESCRIPTION OF APPARATUS

6.2.1 Valve Test Station

Figure 6-2a is a photograph of the valve flow transient signature test station. This unit is shown in schematic form in Figure 6-2b. The flow

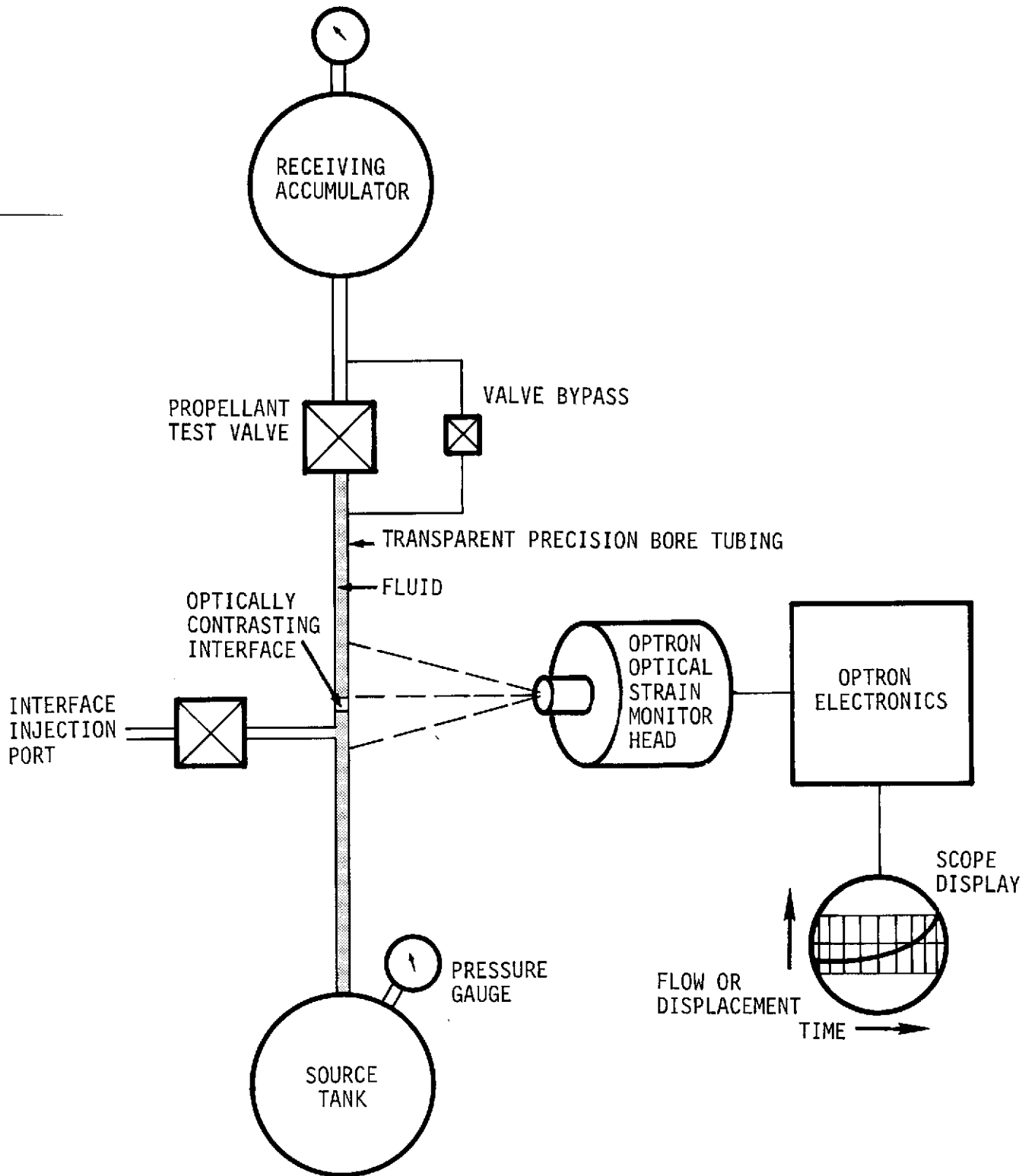
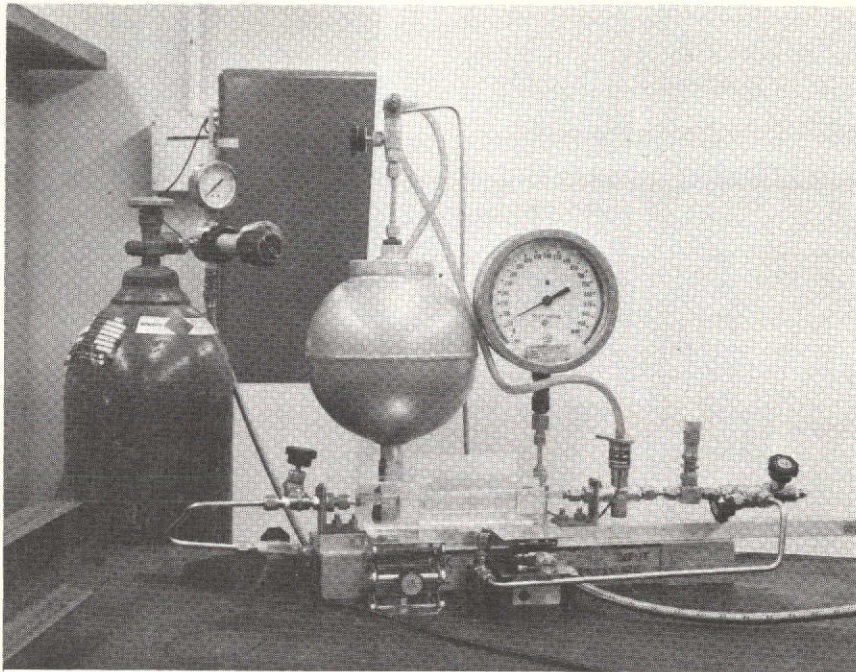
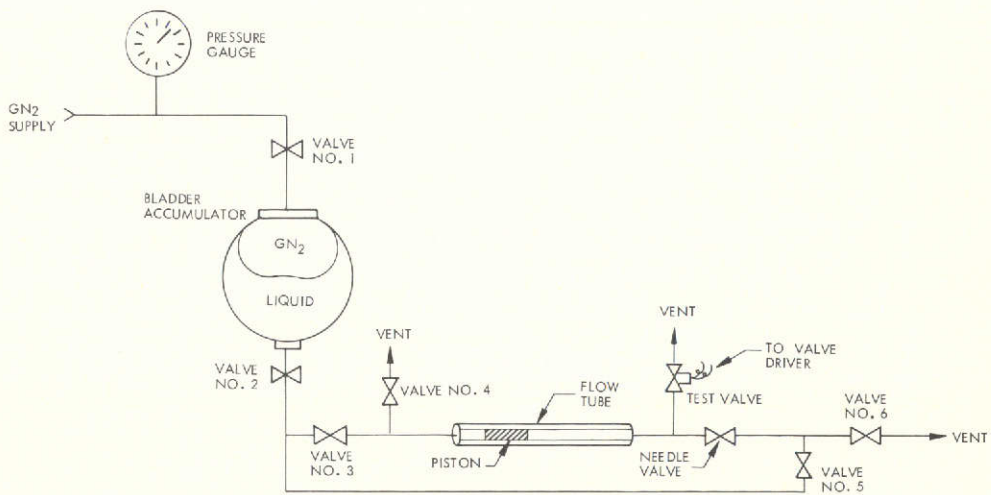


Figure 6-1. Valve Flow Transient Signature Test Schematic



a. Photograph of Test Station



b. Schematic of Valve Test Station

Figure 6-2. Flow Transient Signature Test Station

tube I.D. and piston O.D. is 2 mm diameter. The supply tank uses a neoprene bladder accumulator to eliminate pressurant bubbles in the working fluid.

A test run starts with the piston positioned near the left end of the flow tube. Valves 2 and 3 are open; valves 4, 5 and 6 are closed. The needle valve is almost all the way open; as it is turned, its stem displaces a varying amount of fluid so that it acts as a vernier control for the initial piston position. When the test valve is actuated, the piston is moved by the pressurized fluid, and this displacement is monitored by an electro-optical tracking system and recorded with a scope camera.

After the run, valve 5 is opened and valve 3 is closed. Cracking valve 4 moves the piston back to its original position. Fine adjustments of piston position are made with the needle valve while monitoring a DC voltmeter attached to the output of the electro-optical tracker. If the piston is moved considerably too far to the left, it can be repositioned by opening valve 3, closing valve 5, and cracking valve 6. If there are any gas bubbles in the system, they will be indicated by anomalous piston motion during the positioning process.

Figure 6-3 shows the relation of the electro optic tracker head to the valve test station. Both units rest on a vibration isolated granite table. The DC voltmeter used in initial piston positioning can be seen in the right hand corner of this figure.

Figure 6-1 shows the valve test station from a position near the tracker head. The piston is magnified from a 25 mm diameter x 25 mm long image. The magnification system is composed of three cylindrical lenses, one of which being the thick-walled glass flow tube itself. This system provides magnification only in the direction transverse to the motion of the piston, and prevents the tracker from losing the thin piston without introducing errors in measurements of the piston's position.

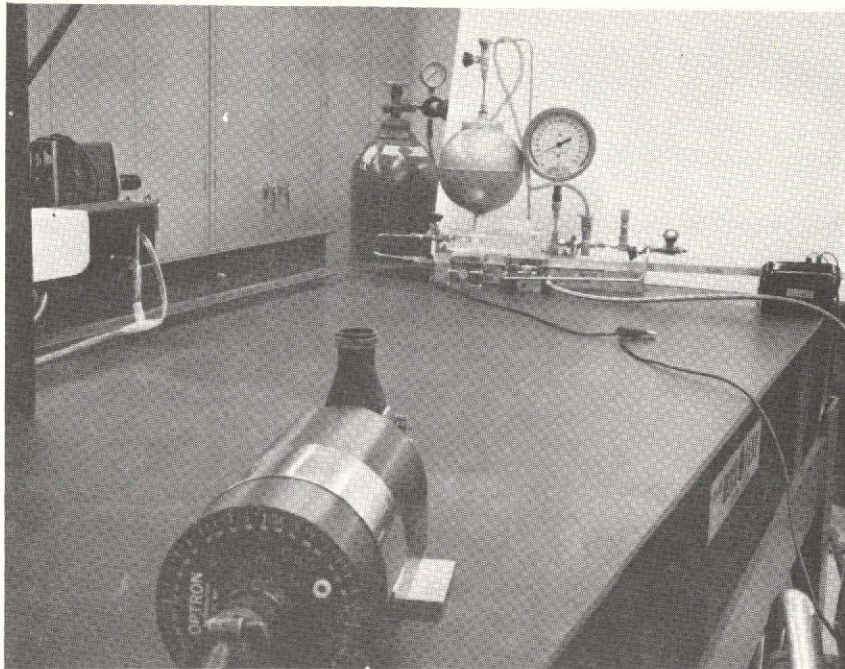


Figure 6-3. Relation of the Electro-Optic Tracker Head to the Valve Test Station



Figure 6-4. Electronic Instrumentation for Transient Flow Signature Test

6.2.2 Electronic Instrumentation

The rather elaborate electronic instrumentation used in this test is shown in Figure 6-4 and as a block diagram in Figure 6-5. The equipment in Figure 6-4 is identified as follows:

Left hand cart - Tektronix 535A scope with 53/54B plug in, used for optimizing the adjustments of the electro-optic tracker; next cart, top to bottom - two HP 467A power amplifiers for driving the valve, HP 8005A dual pulse generator for supplying both the low level valve driving pulse and the scope trigger pulse, Optron 810 electro-optic tracker (with 820 scanner, 830 multiplexer, 850 servo, and 890 test panel plug-ins), and Harrison Laboratories 6267A DC power supply for the test stand illuminator; next cart - Hughes 105A storage scope and NJE Corp. S-325 high voltage DC supply for the image dissector tube in the tracker head; left hand cart - Tektronics 555 dual beam scope (with camera) with 53/54C dual trace plug-in for recording valve voltage and current, and either a 53/54D plug-in for recording piston displacement or a type 0 operational amplifier plug-in used as a differentiator for recording flow rate; the Simpson 270 multimeter on the table was used to indicate piston position when setting up a test run.

The dual pulse generator was used to produce two 15 msec long pulses. One pulse occurred 2.5 msec before the other, and this leading pulse was used to trigger the sweeps of the two scope readouts of the electro-optic tracker. The delayed pulse was amplified by two power amplifiers connected in parallel, passed through a current measurement resistor, and applied to the valve solenoid. Both the valve voltage and current were displayed simultaneously on beam No. 2 of the recording scope, with a dual trace preamp. Beam No. 1 of the recording scope displayed either the piston position (flow volume) signal from the electro-optic tracker or the differentiated piston position signal (flow rate). A dual trace storage scope was connected in parallel with the recording scope to minimize Polaroid film consumption while adjusting the many system parameters. Another scope was AC coupled at high gain to the tracker output so that tracker servo system signal to noise ratio could be optimized and to warn of maladjustments in the optical

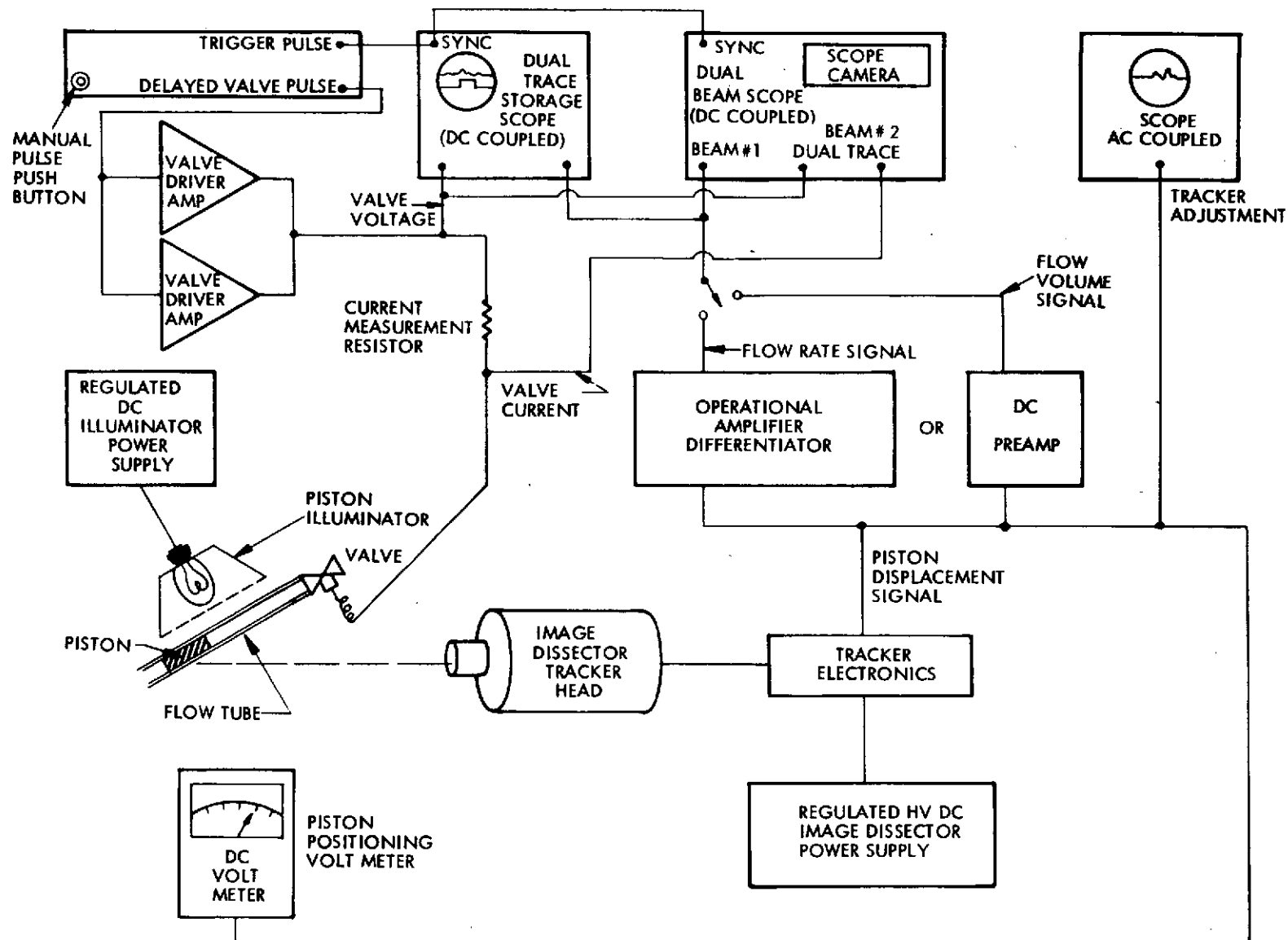


Figure 6-5. Block Diagram of Electronic Instrumentation for Transient Flow Signature Test

system. The image dissector tube high voltage power supply in the tracker main frame failed during the preliminary tests and was replaced with an external regulated HVDC supply. A low voltage regulated DC supply powered the lamps in the illuminator behind the flow tube.

6.3 RESULTS

All tests in this report were performed on a Moog propellant valve of the type described in the Summary Report of the Propellant Valve Evaluation Program (15 June 1971, 71-4781.6-165, TRW Systems). The working fluid was isopropyl alcohol; the valve actuating pulses were 15 msec long; the flow tube I.D. was 2 mm. Back pressure was one atmosphere.

6.3.1 Flow Volume Versus Time Signatures

The scale factors of the following scope photos are, top to bottom:

Piston position	18 mm/division
Valve current	500 mA/division
Valve voltage	10 V/division
Sweep speed	5 msec/division

Figure 6-6 is a scope photo of the system output with the valve disconnect from the driver. The driver output was set to produce a 24V pulse 15 msec long. The current trace remains at zero.

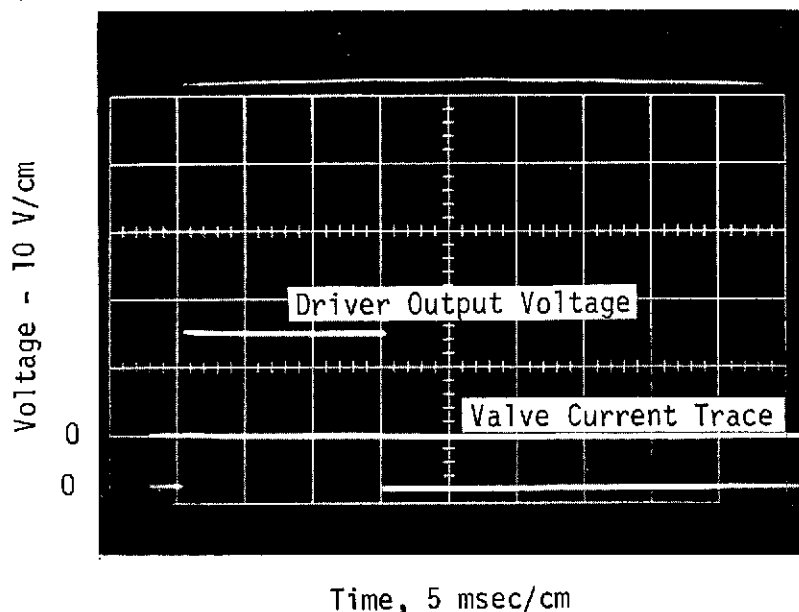


Figure 6-6. Driver Output with Valve Disconnected

Figure 6-7a shows a run made at 72 psig. Valve voltage was set at 26V; however, the voltage trace shows that a drop of a few volts occurred after about 8 msec due to driver amplifier limitations when using a single HP 417A. (This effect does not occur in the flow rate (differentiated) series where two HP 417A's were used in parallel.)

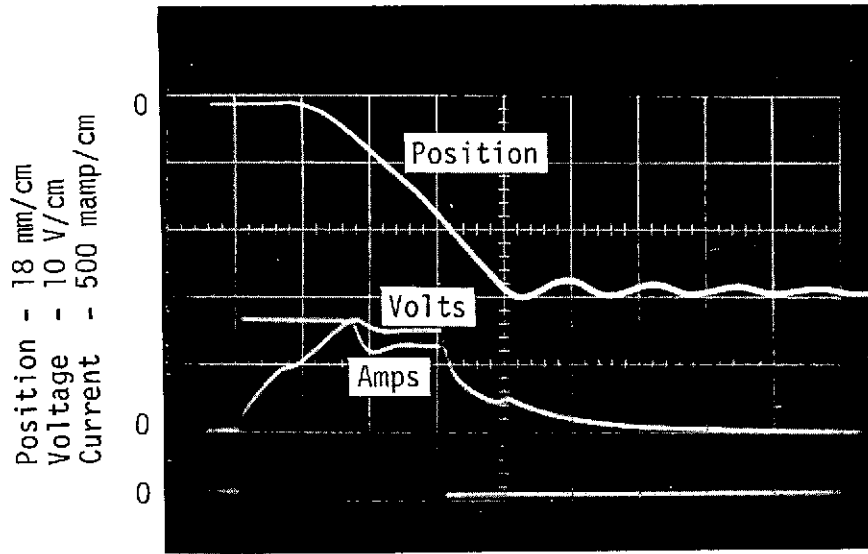
By comparing the piston position trace with the valve current trace, it can be seen that valve opening coincides with the first current inflection point after turn-on, and valve closure coincides with the inflection point after turn-off. The valve opening delay is about 4 msec and the closing delay is about 5 msec. The damped oscillations in the position trace after valve closure are due to the elasticity of the plumbing and fluid.

Figures 6-7b, c and d were made under the same conditions as shown in Figure 6-7a to demonstrate reproducibility. The only visible difference is a slight change in the amount of damping after valve closure.

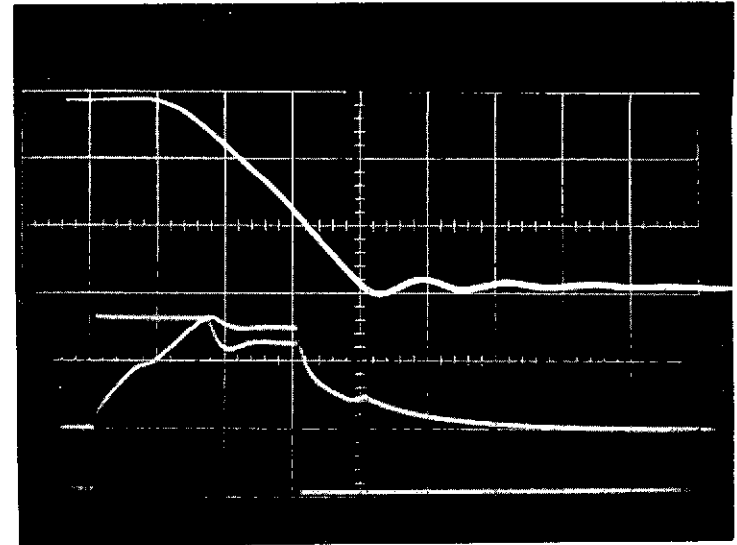
Figure 6-7e was made at 72 psig and 24V. The voltage reduction results in a slight opening delay.

Figure 6-7f was made at 72 psig and 22V. The opening delay has become quite substantial (about one msec compared to Figure 6-7d), and the total flow volume is noticeably less.

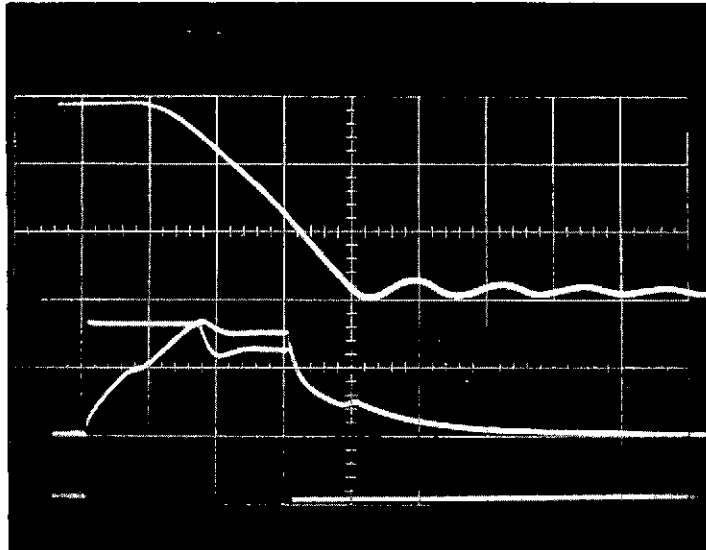
Figure 6-7g was made at 59 psig and 24V. Compared to 6-7e (72 psig and 24V), the flow volume was less. A comparison of the opening and closing process can best be made using the differentiated position (flow rate) traces, and will be discussed in the next section.



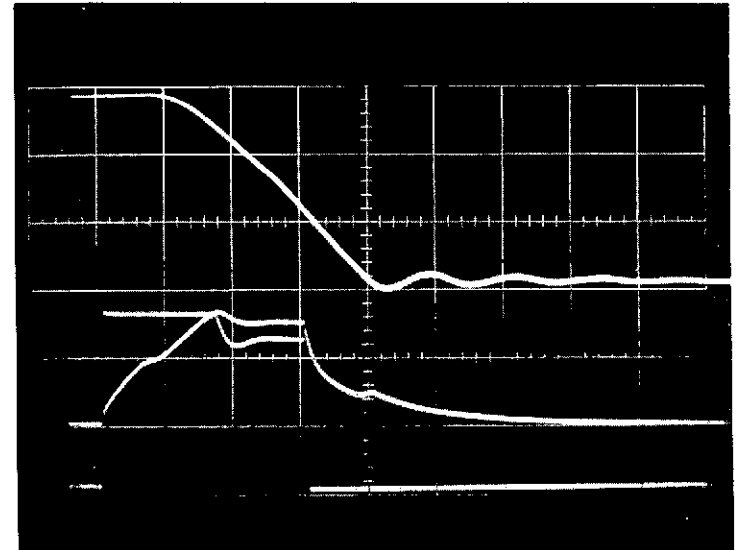
Time, 5 msec/cm
a. 26V, 72 Psig



b. 26V, 72 Psig



c. 26V, 72 Psig

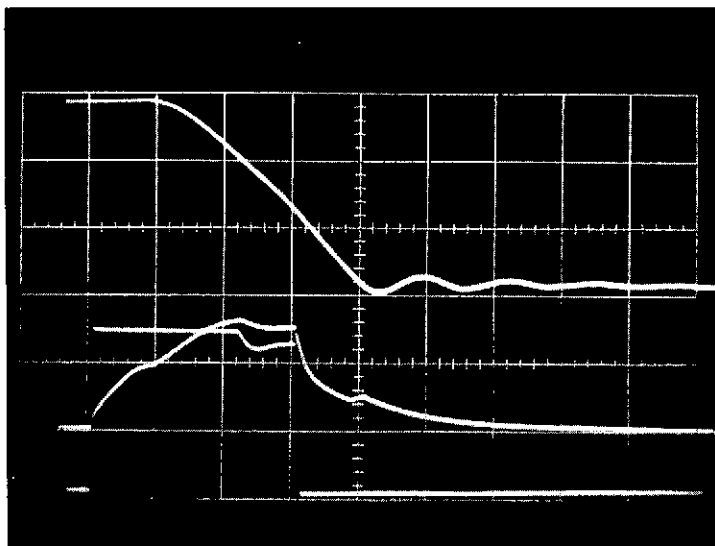


d. 26V, 72 Psig

Figure 6-7. Valve Transient Flow Signature Fluid Position; Voltage & Current Vs. Time

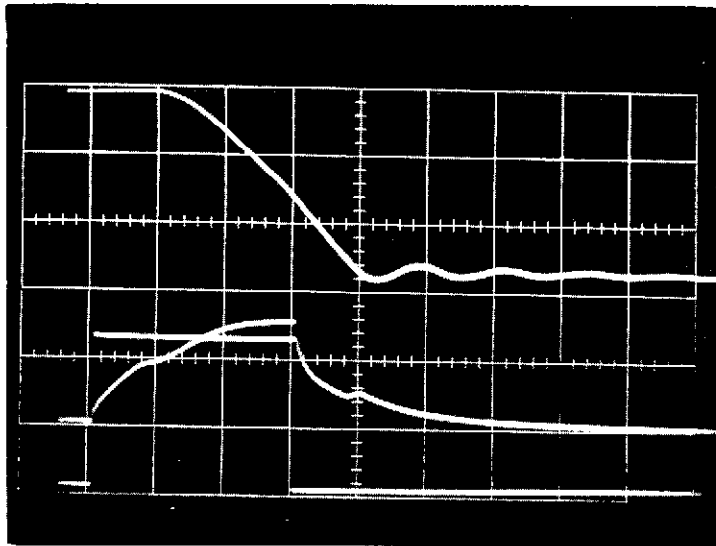
Figures 6-7h through 6-7m were made varying pressure and voltage.

This series of experiments established that the valve current inflections corresponded to valve opening and closing. Cumulative flow volume (piston position) is not a very sensitive measure of processes occurring within the valve. For this reason, the next series of experiments was performed with the position versus time signal electronically differentiated to yield flow rate versus time.

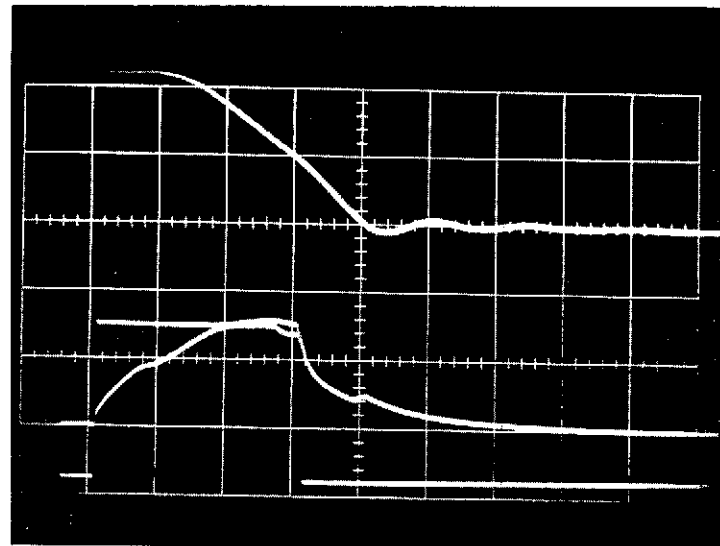


e. 24V, 72 Psig

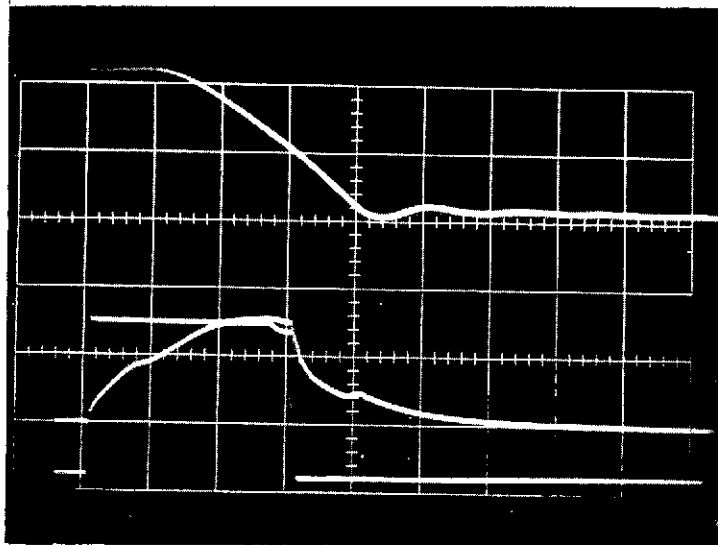
Figure 6-7. Valve Transient Flow Signature Fluid Position;
Voltage & Current Vs. Time (Cont)



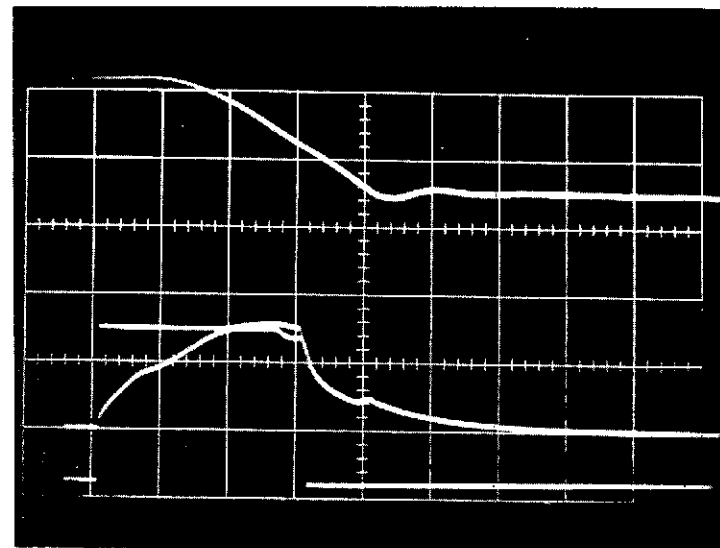
f. 22V, 72 Psig



g. 24V, 59 Psig

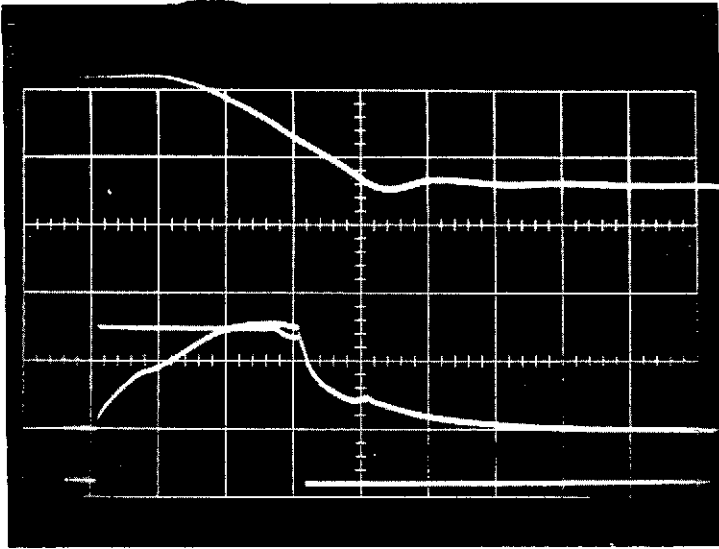


h. 24V, 46 Psig

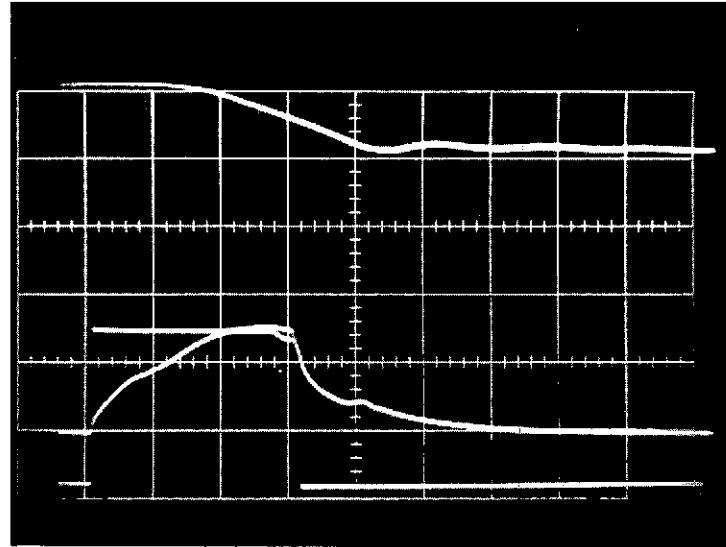


i. 24V, 36 Psig

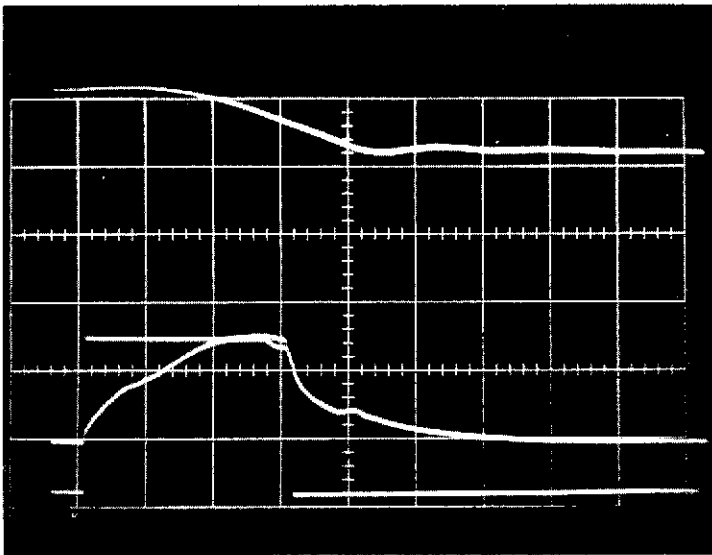
Figure 6-7. Valve Transient Flow Signature Fluid Position; Voltage & Current Vs. Time (Cont)



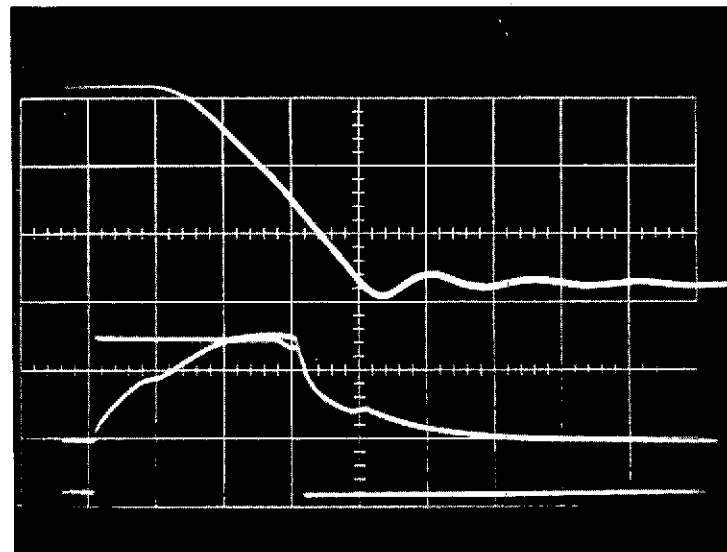
j. 24 V, 32 Psig



k. 24V, 21 Psig



l. 24V, 16 Psig



m. 24V, 86 Psig

Figure 6-7. Valve Transient Flow Signature Fluid Position; Voltage & Current Vs. Time (Cont)

6.3.2 Flow Rate Versus Time Signatures

When the piston position (flow volume) versus time signal is differentiated with respect to time, a signal representing flow rate versus time is obtained. It is to be expected that this latter signal would be a far more sensitive indicator of small changes in valve parameters and function than would the signal reported in Section 6.2.1.

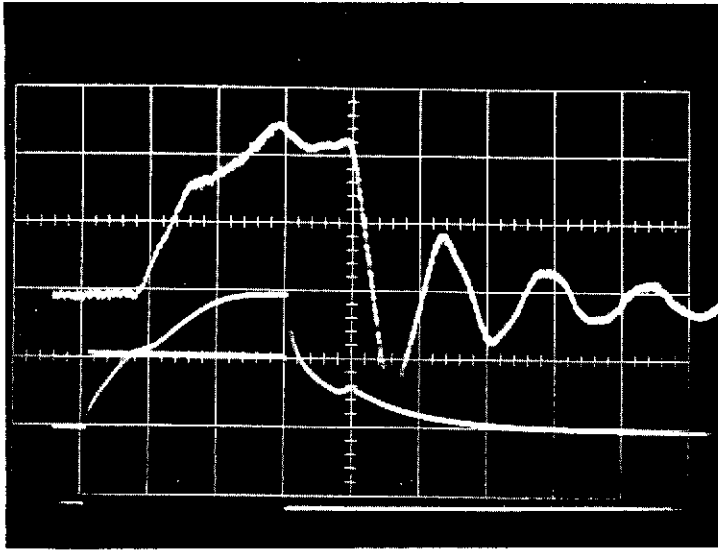
An operational amplifier was used to differentiate the position versus time signal. Analog differentiation is always a compromise between signal to noise ratio and sensitivity to time rates of change in the variable. After considerable experimentation, the differentiator time constant was set at 27 msec, and high frequency noise was controlled by the use of a 500 Hz 6 db per octave low pass filter in the output of the electro-optic tracker.

The scale factors for valve voltage, current and time are the same as in the previous series.

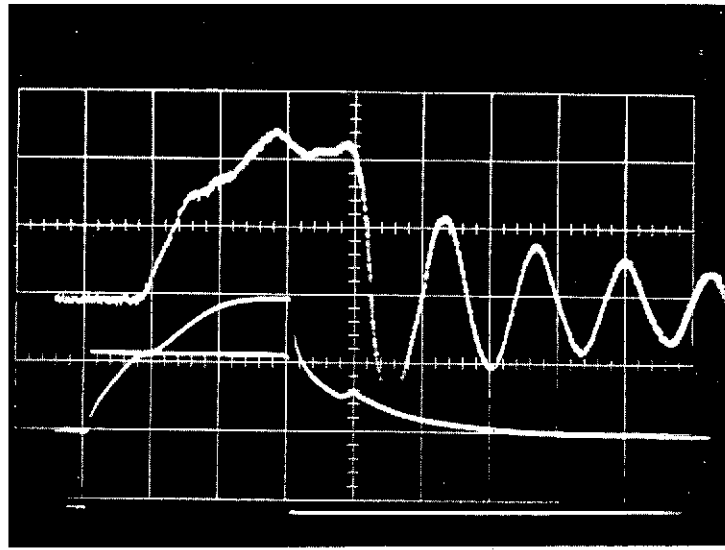
Both Figures 6-8a and 6-8b were made at 24V and 81 psig. In Figure 6-8a, the needle valve was wide open (as is the case unless otherwise stated), whereas in Figure 6-8b, it was closed. It is apparent that the condition of the needle valve did not affect the Moog valve signature; however, the damped oscillations after valve closure had a higher frequency and lower damping in the needle valve closed state, as would be expected.

The sequence of tests shown in Figures 6-8a and 6-8c through 6-8i demonstrate the effects of varying accumulator pressure on the Moog valve flow rate signature. Although there may be very minor differences in valve opening and closing times, the major changes occur between these two markers.

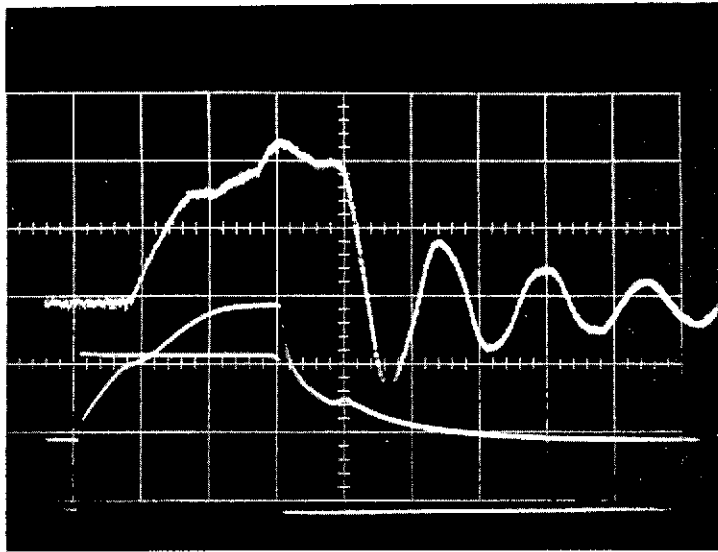
At 81 psig (Figure 6-8a), there is a flow rate reduction for about 2 msec after power off, then there is a 3 msec plateau of nearly constant flow rate before the valve closes completely and the flow rate at the piston falls to zero in another 2 msec.



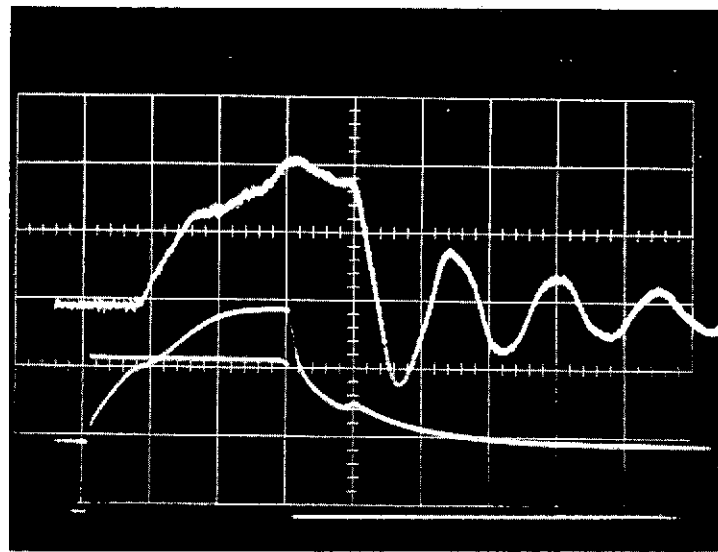
a. 24V, 81 Psig, Needle Valve Open



b. 24V, 81 Psig, Needle Valve Closed

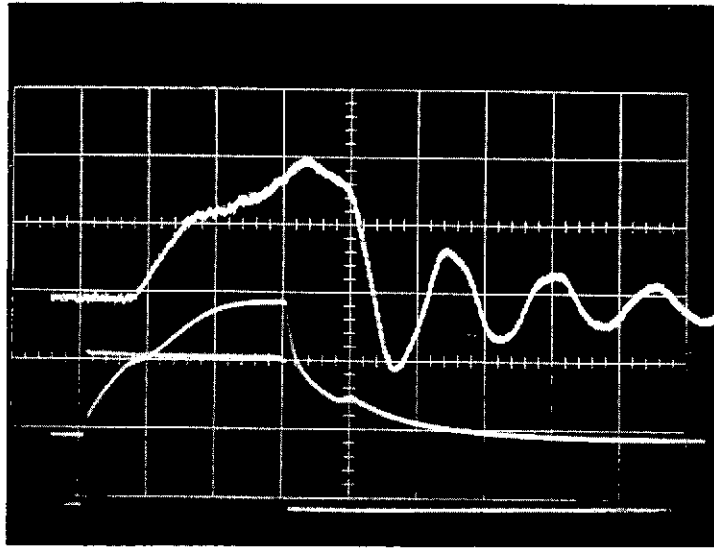


c. 24V, 71 Psig

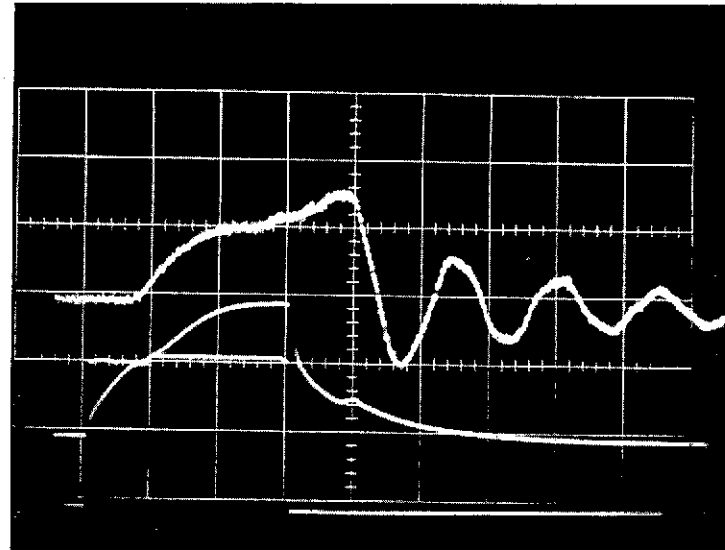


d. 24V, 61 Psig

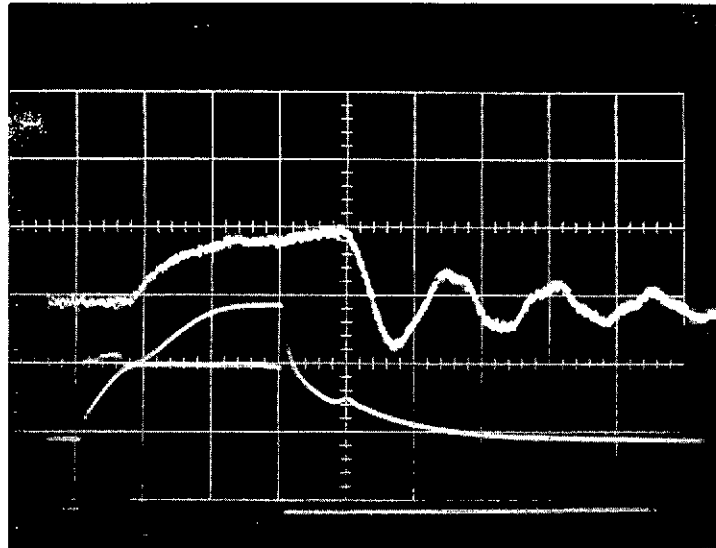
Figure 6-8. Valve Transient Flow Rate; Voltage & Current Vs. Time



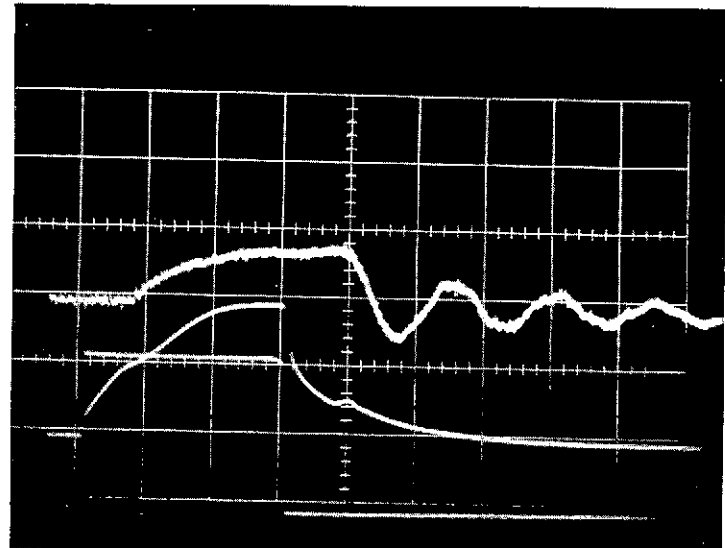
e. 24V, 51 Psig



f. 24V, 41 Psig



g. 24V, 31 Psig



h. 24V, 21 Psig

Figure 6-8. Valve Transient Flow Rate; Voltage & Current Vs. Time (Cont)

at 71 psig (Figure 6-8c), the flow rate reduction after power off occurs slower, taking about 3 msec, followed by a 2 msec plateau before cut-off.

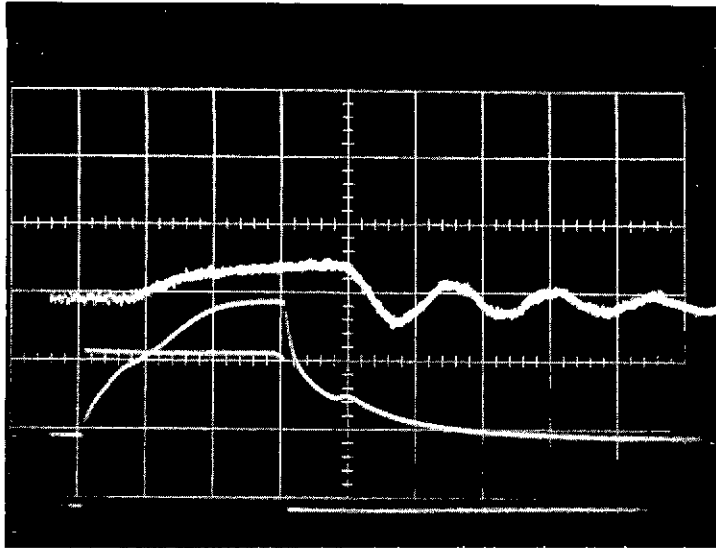
At 61 psig (Figure 6-8d), the power-off plateau has nearly vanished, and at 51 psig (Figure 6-8e), it is gone entirely.

Below 51 psig, the flow rate maximum occurs later and later after power off. It is possible that the Belleville spring loaded poppet is acting like a pump piston and briefly assisting the flow between power off and final closure.

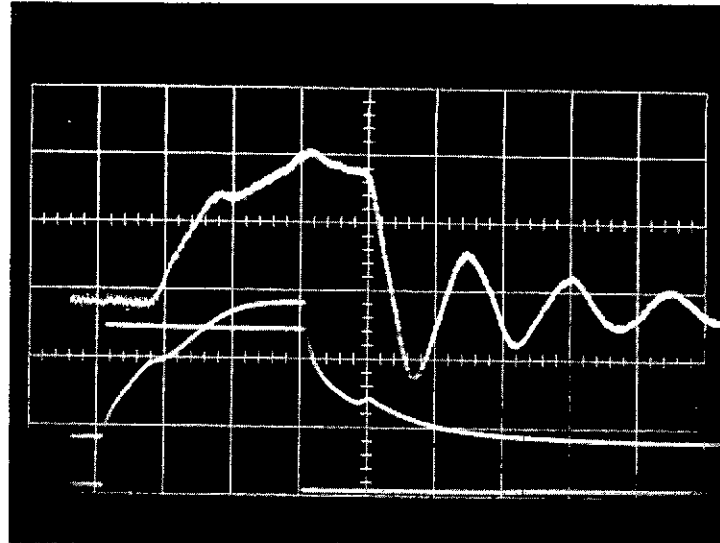
A careful study of the valve mechanism would be necessary to explain why the observed flow changes occur with variations in input pressure.

Figures 6-8j through 6-8n show a series of runs made at 24V and 66 psig to show the degree of reproducibility obtained in this technique. The signal-to-noise ratio in these preliminary experiments is such that stochastic variations in valve action under constant parameters cannot be clearly elucidated. Improved techniques, such as FM recording of the piston displacement signal followed by digital data processing could be expected to improve the S/N by at least an order of magnitude so that the currently half-buried irregularities could be characterized.

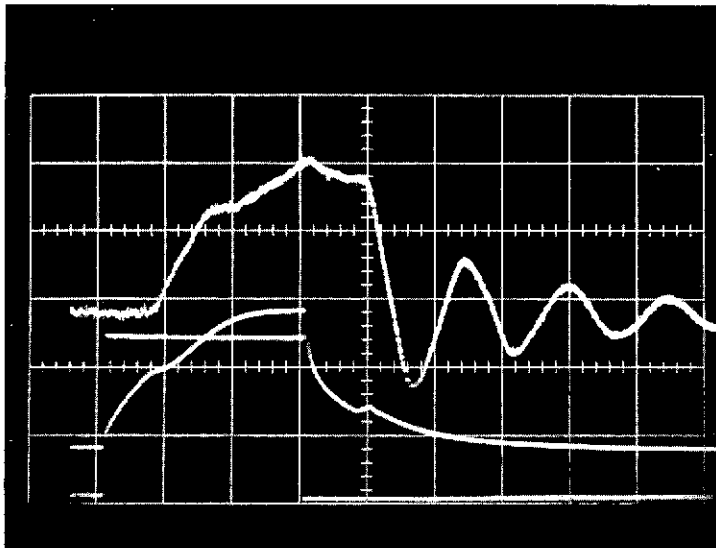
Figures 6-8o and 6-8p show two runs at 26V and 66 psig. Figures 6-8q and 6-8r show two runs at 22V and 66 psig. A comparison of these runs with the previous five at 24V and 66 psig shows that the valve opening is slightly accelerated at the higher voltage and delayed at the lower voltage, whereas higher voltages seem to slightly retard the closing and lower voltages slightly hasten it.



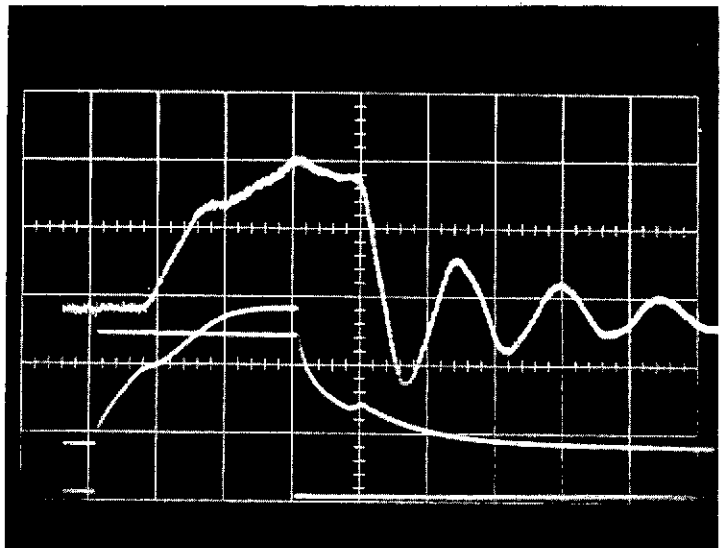
i. 24V, 11 Psig



j. 24V, 66 Psig

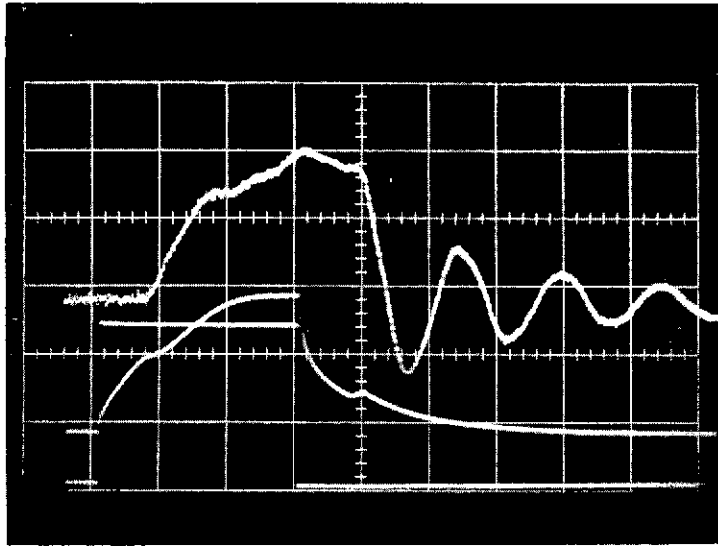


k. 24V, 66 Psig

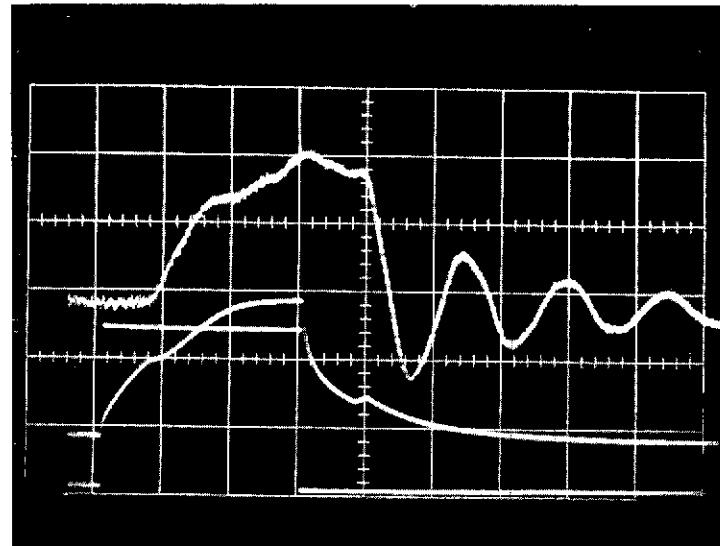


l. 24V, 66 Psig

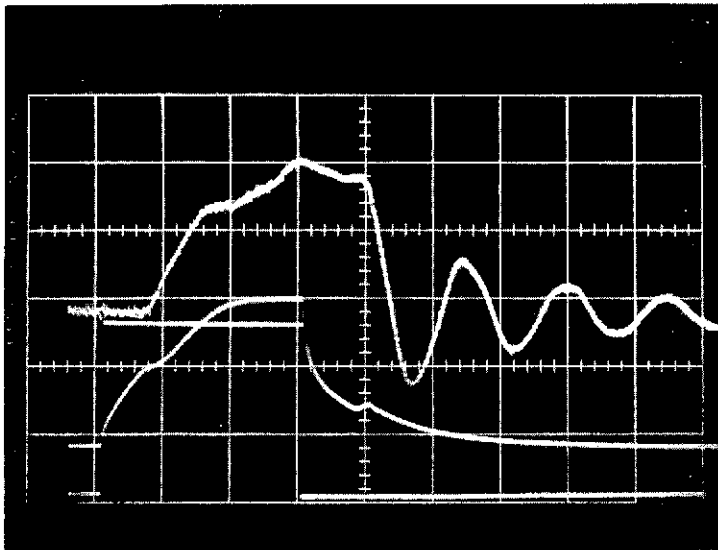
Figure 6-8. Valve Transient Flow Rate; Voltage & Current Vs. Time (Cont)



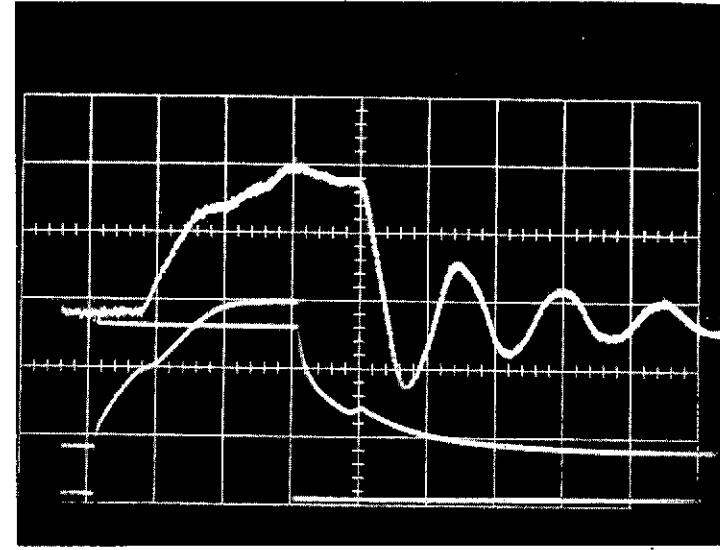
m. 24V, 66 Psig



n. 24V, 66 Psig

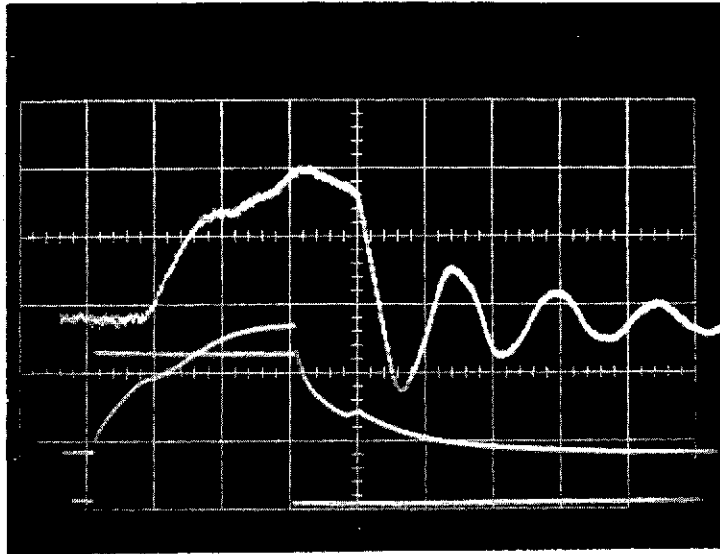


o. 26V, 66 Psig

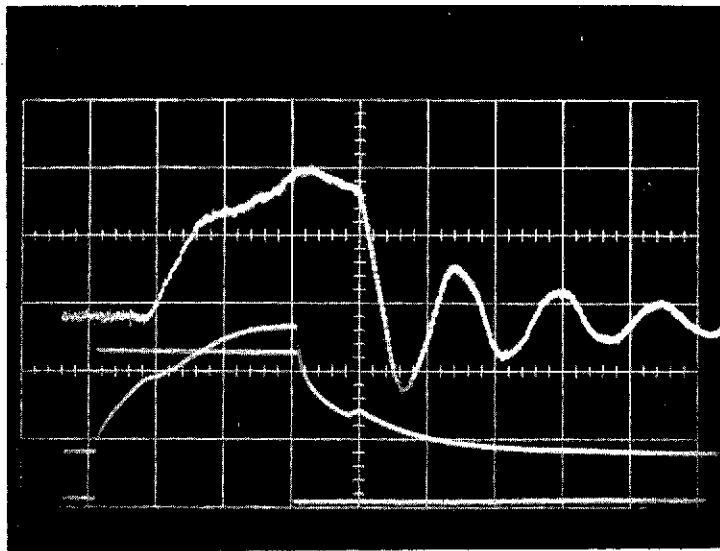


p. 26V, 66 Psig

Figure 6-8. Valve Transient Flow Rate; Voltage & Current Vs. Time (Cont)



q. 22 V, 66 Psig



r. 22V, 66 Psig

Figure 6-8. Valve Transient Flow Rate;
Voltage & Current Vs. Time (Cont)

These preliminary experiments have demonstrated that it is feasible to measure flow transient signatures in small fast-acting spacecraft valves. For practical applications, the instrumental signal to noise ratio should be improved by the use of FM recording of the piston displacement signal and the subsequent use of digital data processing to perform the differentiation. The use of these techniques should improve the S/N of the data by at least several dB.

A further improvement in signature clarity could be obtained by computer averaging of the signature over several test runs made under identical conditions. The improvement in S/N is proportional to \sqrt{n} where n is the number of runs averaged. Averaging 100 runs would yield a 10 dB improvement in S/N. If the apparatus were rebuilt with the manual valves replaced by servo valves, between one and ten test runs per second could be performed.

With the aforementioned improvements, useful data could be gathered on the change in signature versus voltage, pressure, temperature, presence of particulates, and most important, number of actuation cycles and time (involving progressive corrosion, for example). For these high precision tests, the solid piston should be fabricated so as to have the same density as the test fluid in order to eliminate inertially driven leakage errors.

6.4 FLUID LEAK MEASUREMENT

The test stand used for the valve flow transient signature tests was also used in the leakage test. As pressurized fluid leaks past the valve seats, a mercury piston moves down the capillary tube, and this movement is measured by the electro-optical strain monitor. Mercury was used to replace the solid piston of the previous experiments since both the flow rates and the inertial forces involved in this application are very small. The optical system of the electro-optical strain monitor was changed to one having a 0.15 inch full scale field of view.

With the available system parameters, leak sensitivity of the system was as follows:

1/2 mm dia flow tube - 1.34×10^5 volts cc
1 inch dia flow tube - 3.36×10^4 volts cc
2 inch dia flow tube - 8.37×10^3 volts/cc

With the tracker electronics set at a 10 Hz bandwidth, the noise level is about 2×10^{-2} volts, so for a S/N of 10 dB and a measuring period of one second, we have the following leak sensitivities:

S/N = 10 dB, 1/2 mm dia flow tube - 1.45×10^{-6} cc/sec for 1 sec
S/N = 10 dB, 1 inch dia flow tube - 5.8×10^{-6} cc/sec for 1 sec
S/N = 10 dB, 2 inch dia flow tube - 2.32×10^{-5} cc/sec for 1 sec.

If the measurement is made over a 100 second period, the respective leak sensitivities are 1.45×10^{-8} cc/sec, 5.8×10^{-8} cc/sec, and 2.32×10^{-7} cc/sec.

With a 2 mm flow tube, the downstream valves were found to have a combined leak rate averaging about 7.5×10^{-8} cc/sec at 76 psig. It was interesting to note that the leak was not steady, but rather exhibited substantial variations over periods of a minute or so.

For practical leak testing, the test station would have to be rebuilt to minimize extraneous leaks and thermal effects. Thermal expansion effects can be minimized by using:

- 1) An isothermal enclosure, allowing time for the attainment of equilibrium
- 2) A 2 mW collimated laser beam illuminator to replace the 80 W incandescent illuminator used in the test
- 3) The use of two flow tubes (test and reference) in thermal contact with each other, with the strain monitor measuring the differential displacement between the two pistons.

In spite of the unsuitability of the existent valve transient test station for this test, it was demonstrated that small fluid leaks can be measured electro-optically. It would be of interest to determine how helium leak rates correlate with liquid propellant leak rates.

7.0 SURFACE STUDIES

7.1 INTRODUCTION

Failure of a component can occur either by a bulk change in a material or by the change or degradation of a surface. A considerable amount of knowledge exists on the bulk properties of materials. Little is known about surfaces. The surface studies reported in this section were conducted by the University of Bradford, England under subcontract during the period June 1971 to December 1972.

The objective of this work was to investigate the surface characteristics of metal and solid surfaces, and to examine the use of contact angle techniques for monitoring changes at surfaces exposed to corrosive environments and the applicability of the technique to predicting the behavior of sliding surfaces in contact. Section 7.2 describes the use of the contact angle technique to examine changes occurring at various metal surfaces after treatment by corrosive liquids such as hydrazine. Section 7.3 discusses the use of the concept of critical surface tension, γ_c , in predicting frictional and wear properties of contacting materials; it is shown that although the application of the technique is limited, suitable choice of test liquids will enable the surface energy and hence the other surface properties to be determined. Section 7.4 gives results obtained using the technique of Auger Spectroscopy of an investigation of the surface composition of an inconel valve seat material.

7.2 SURFACE COMPATIBILITY STUDY

One aspect of engineering materials of all sorts which is very poorly understood is the behavior of their surfaces under various practical situations. The phenomena of friction and wear are considered in Section 7.3; here we will be concerned with the changes of the surfaces of materials in corrosive environments.

Of the various corrosion processes which have been studied, electrochemical corrosion is best understood, although there have also been studies of the interaction of metals with corrosive gases, e.g., O_2 , Cl_2 , F_2 , etc.

Little is known of the corrosion of metals by reactive liquids such as OF_2 , hydrazine, monomethylhydrazine, etc. Earlier work carried out in this laboratory (Ref. 1) showed that small changes in the conditions of preparation of polyperfluorobutene films gave rise to large changes in the wetting behavior of these films. It was therefore tempting to examine the possibility of monitoring changes occurring on the surfaces of various engineering materials in corrosive liquids by wetting techniques, i.e., by monitoring changes in contact angle of the liquid used for treating the surface or using some other test liquid, e.g., water. In particular, it was hoped that this would enable a series of tests to be set up for solid - liquid compatibility, which would not require protracted test procedures, i.e., that changes could be detected occurring at the solid surface which were not visible to the eye or by other test procedures. This part of the report, therefore, presents data obtained for changes occurring on a variety of surfaces (both specially cleaned and "as received") after treatment with hydrazine.

7.2.1 Experimental

Samples of brass, copper and stainless steel were mechanically abraded to obtain highly polished surfaces. In addition, copper plates were electropolished using a technique described by Trevoy and Johnson (Ref. 1), with a 63 - 67% (w/w) aqueous orthophosphoric acid solution; and two specimens of stainless steel plate were electropolished using an aqueous orthophosphoric acid/sulphuric acid mixture described by Perryman (Ref. 2). In addition, two surfaces of an electrolyzed inconel sample (also used for Auger studies, Section 7.4) supplied by TRW Systems Group were also examined. This sample was boiled in detergent solution and rinsed in boiling deionized water before examination. Contact angles were measured using a telescope fitted with a goniometer eyepiece, and the method of measurement was as described in previous reports (Ref. 3). All measurements were carried out with the sample in a dust free container. Hydrazine was freshly distilled from hydrazine monohydrate ($N_2H_4 \cdot H_2O$) using chromic acid cleaned glassware.

7.2.2 Results and Discussion

7.2.2.1 Electrolytically Polished Surfaces

Table 7-1 summarizes the results obtained for the electrolytically polished copper and stainless steel samples. With copper, the low contact angles ($<5^\circ$) expected of an essentially clean metal surface (Ref. 1) were not obtained if measurements were made immediately after polishing, [expt. 2(a) - (c)]. Only if the freshly polished surface was washed in a "Tide" detergent solution did the resultant surface give an angle less than 5° ; washing in a "Decon 75" solution did not give the same low angle. The angle obtained with a freshly electropolished surface was consistently $\sim 40^\circ$ [expts. 2(a), (b), (c)]; this angle increased considerably after storing a plate for 72 hours in a vacuum dessicator, indicating that contamination by vacuum grease vapor may have occurred.

The stainless steel samples gave contact angles of $<5^\circ$ immediately after polishing, without the need of a detergent wash. A 0.47% (w/w) aqueous solution of butanol spread over the surface; after rinsing with deionized water, water drops again gave angles less than 5° . However, after storing the sample "in vacuo" for 18 hours [expt. 3(b)], the contact angle for water had increased to 45° , indicating contamination of the surface. This contamination could be removed by a "Tide" detergent solution, and a chromic acid solution had no effect on this surface [expts. 3(c) and (d)]. After exposure to hydrazine for 20 hours, the contact angle for water ranged from 19 to 30° . The drops were unsymmetrical and this, together with the higher angle is good evidence for reaction of the surface with the hydrazine, although, of course, contamination could have caused the increase of angle. Stainless steel has been classified as being compatible with hydrazine.

7.2.2.2 Inconel Samples

The compatibility of the inconel samples was tested as follows:

- (a) Rough Surface. Half the face was covered with hydrazine for five minutes. No reaction could be observed, and yet the water contact angle on the treated area, 19° , differed from that on the untreated area ($35 \pm 8^\circ$). Before treatment, the water angle was 10° .

Table 7-1. Contact Angle Measurements for Water on Electrolytically Polished Copper and Stainless Steel Samples

Expt	Metal	Description of Polished Surface	Treatment of Polished Surface	Mean Contact Angle for Water θ_w	Remarks
1	Copper Plate (3 x 3.5 x 0.1 cm)	Smooth, although scratches from abrasion treatment just visible	(a) Rinsed in 10% (w/w) H_3PO_4 and water	$93 \pm 4^\circ$	Plate held "in vacuo" for 72 hours before measurement
			(b) Washed in hot detergent ("Tide") rinsed and dried	$<5^\circ$	
2	"	Smooth and specular with shallow pits where O_2 was evolved	(a) As 1 (a)	$39 \pm 5^\circ$	Angles measured immediately after polishing in expts (a)-(c); (d) immediately after (c)
			(b) "	$41 \pm 4^\circ$	
			(c) "	$39 \pm 5^\circ$	
			(d) Washed in hot detergent (Decon 75) rinsed and dried	$24 \pm 3^\circ$	
3	Stainless Steel Plate (2.5 x 2.5 x 0.1 cm)	Smooth and specular	(a) As 1 (a)	$4 \pm 1^\circ$	Angles measured immediately after polishing Retained "in vacuo" for 18 hours
			(b) "	$45 \pm 3^\circ$	
			(c) As 1(b) using Tide detergent	$<5^\circ$	No apparent reaction in chromic acid
			(d) 15 sec. dip in chromic acid (80°C) rinsed and dried	$<5^\circ$	
			(e) Immersed in freshly distilled hydrazine for 20 hrs, rinsed and dried	$25 \pm 6^\circ$	

- (b) Smooth Surface. Before treatment, the angle was $26 \pm 6^\circ$. After exposing the rough surface to liquid N_2H_4 and hence the smooth surface to its vapor, the angle was $39 \pm 2^\circ$. After five minutes contact with liquid N_2H_4 , the angle was $40 \pm 4^\circ$.

Hence, both surfaces are affected by hydrazine, as either the vapor or as a liquid. The different angles on each face may be a function of surface roughness (see Section 7.3) or of the slightly different methods of preparation.

7.2.2.3 Untreated Mechanically Abraded Samples

Preliminary Results for Brass and Copper. A mechanically polished brass block gave a water contact angle, θ_w , of $51 \pm 3^\circ$ after washing in "Tide" solution. A similarly treated copper plate gave an angle of $79 \pm 4^\circ$. The latter, after treatment with hydrazine for three and a half minutes, gave a slightly lower angle of $70 \pm 5^\circ$. The latter result, in particular, shows that the "as received" material is very different from that of a carefully produced electrolyzed material, and therefore does not reflect the properties of the clean metal. On the other hand, it is much closer to the true engineering situation. The program was therefore extended to allow further tests on mechanically polished materials, and materials passivated according to recognized procedures.

More Detailed Results for Untreated and Passivated Metals. Results were obtained for passivated alumina (prepared according to the procedure given in SRI Report No. 951581-6, Appendix A, Ref. 4), stainless steel, and the inconel sample discussed above. Advancing contact angles were measured for water and for 50% (V/V) aqueous hydrazine solutions on each of these surfaces. It was found that the advancing contact angles were time dependent, as shown in Figures 7-5 through 7-7, which are discussed in Section 7.3. In addition to these results, the advancing contact angles of a silicone oil (Midlands Silicones, MS704) were measured on the inconel surfaces, and the effect of a film of this oil was also examined. The advancing contact angle at zero time is mainly discussed in the following description of the

results, but it should be noted that the gradients of the plots of θ against time ($d\theta/dt$) are affected by the various treatments. Aqueous hydrazine solutions were used for these experiments because anhydrous hydrazine did not form stable drops on the surfaces due to a vigorous reaction with the moisture of the atmosphere.

Table 7-2 summarizes the results obtained.

- (a) Aluminum. Figure 7-1 shows the variation of θ_w with time for three drops of water (runs 2, 3, 4) on the passivated aluminum surface (after a previous experiment on the same surface, followed by repassivation). The contact angle for each run decreased steadily with time. The sample was covered with water between each experiment. The value of θ_w increased to a higher value than that of the initial drop, and then dropped again with time (runs 3 and 4). These changes of θ_w with time imply that a change is occurring at the surface of the aluminum. One possible explanation of the decrease in angle of each individual drop is that some contamination is removed from the surface which lowers the surface tension of the liquid, in turn lowering the angle. When the drop is replaced by another one, the underlying surface has now got a lower energy, and this results in a higher angle, which again decreases as further contamination is removed from the surface. The same sequence occurs in run 4. Hence, the results for the initial value of θ_w imply that the surface becomes more passive after contact with water. However, when the surface is contacted with aqueous hydrazine (run 5), the passivating layer is removed, leaving essentially a clean metal surface. This result therefore demonstrates the power of contact angle measurements in showing the removal of what is considered to be a passivating layer.

Table 7-2. Variation of Contact Angle at Zero Time With Surface Treatment of the Metal for Various Liquids

<u>Expt</u>	<u>Solid Surface</u>	<u>Treatment of Surface</u>	<u>Liquid</u>	<u>Contact Angle at t = 0</u>	<u>Remarks</u>
1	Aluminum	Passivated (see text)	Water	48.5 - 49.5°	_____
2	"	"	"	38.2 - 40.5°	Difference from Expt 1 could be due to the roughness of the surface
3	"	After treating surface with water for 15 minutes after expt 2	"	62.5 - 66.0°	Drop on same place
4	"	After further 10 minute water treatment	"	72.0 - 74.5°	Drop on same place
5	"	Freshly passivated surface	50% aqueous hydrazine	<5°	
6	Stainless Steel	2 minutes in 1% HF, 1% HNO ₃ , 98% water, rinsed, dried	Water	48.0 - 49.0°	_____
7	"	" "	50% aqueous hydrazine	23.0°	Drop gave constant value of 10 - 11° after 7 minutes
8	"	Passivated and then treated with 50% aqueous hydrazine for 15 minutes	Water	27.5 - 30.5°	_____
9	Inconel	Surface lightly abraded and treated as in expt 6	Water	94° - 98.5°	} Drop on same position on surface
10	"	" "	50% aqueous hydrazine	73.0°	
11	"	Passivated as above and treated with 50% aqueous hydrazine for 2 minutes	Water	87° - 90°	
12	"	13 minutes hydrazine treatment	Water	62.5 - 65.0°	
13	"	As in run 9	Silicone Oil	20.5 - 22.0°	Constant angle of 15 - 16° after 7 minutes
14	"	Silicone oil removed from surface, leaving thin film	Water	70° - 72.5°	Water apparently displaced the oil film
15	"	" "	50% aqueous hydrazine solution	56.5°	Constant angle of 44° after 7 minutes

NOTE: Advancing drops of the hydrazine solution were in all cases surrounded by a halo which formed at about twice the diameter of the drop. As the drop evaporated, this halo did not change position.

(b) Stainless Steel. Figure 7-2 shows the results for stainless steel (expts 6 - 8) passivated as described in the table. The contact angle of water on the fresh surface (expt 6) decreased with time, as with aluminum. Expt 7 shows the angle for a drop of aqueous hydrazine; this decreases to a constant value of about 10° . A drop of water placed on the same spot now had a lower contact angle than before, indicating that the passivating surface layers had been partly, but not completely, removed.

(c) Inconel. The inconel sample was lightly abraded with "180" grade emery paper and given the same treatment as the stainless steel sample. Figure 7-3 shows the results of four experiments on this surface. Expt 9 was carried out immediately after the passivation treatment. Several more experiments (not reported) were then carried out, which showed, among other things, that the receding angle was about 10° smaller than the advancing angle. The angle for a 50% aqueous hydrazine solution was then measured (expt 10) and found to be somewhat lower than that for pure water and decreasing more rapidly. Water was then placed on a part of the surface which had been treated with hydrazine for two minutes, and the angle (expt 11) was slightly lower than the initial value, but after 13 minutes treatment (expt 12) the value was very much lower.

Figure 7-4 shows the results for experiments 13 - 15. Expt 13 shows the result for silicone oil on a freshly prepared surface. A drop of water placed on the surface after mopping up the oil (expt 14) gave a lower value than that on the clean surface (expt 9). Hydrazine treatment (expt 15) then gave less of a decrease in contact angle than that in expt 10. Thus, treatment of the surface with an oil appears to cut down the activity of the surface towards hydrazine.

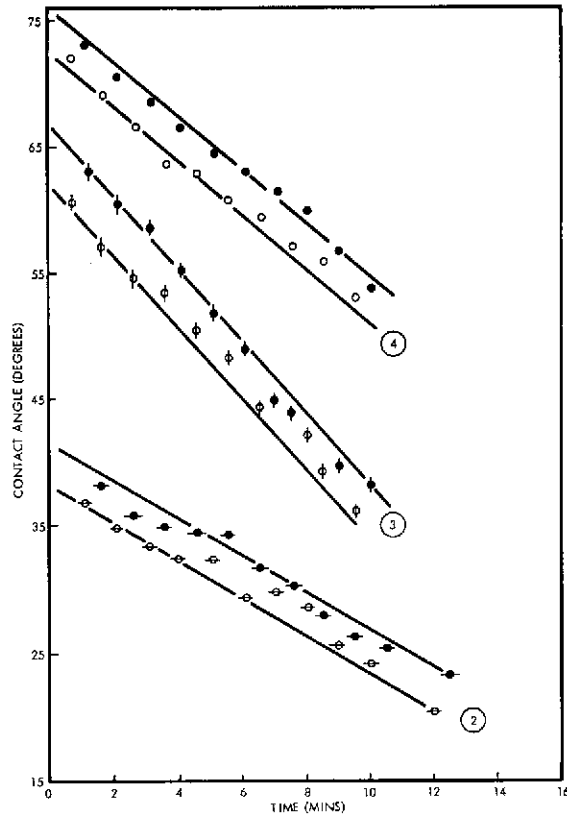


Figure 7-1. Contact Angles of Water on Passivated Aluminum

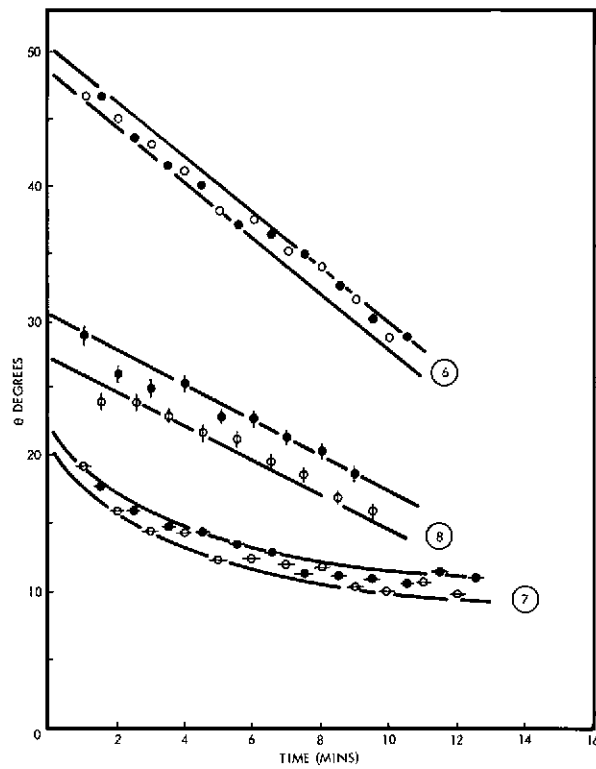


Figure 7-2. Variation of Contact Angle, θ , on Stainless Steel Surfaces as a Function of Time

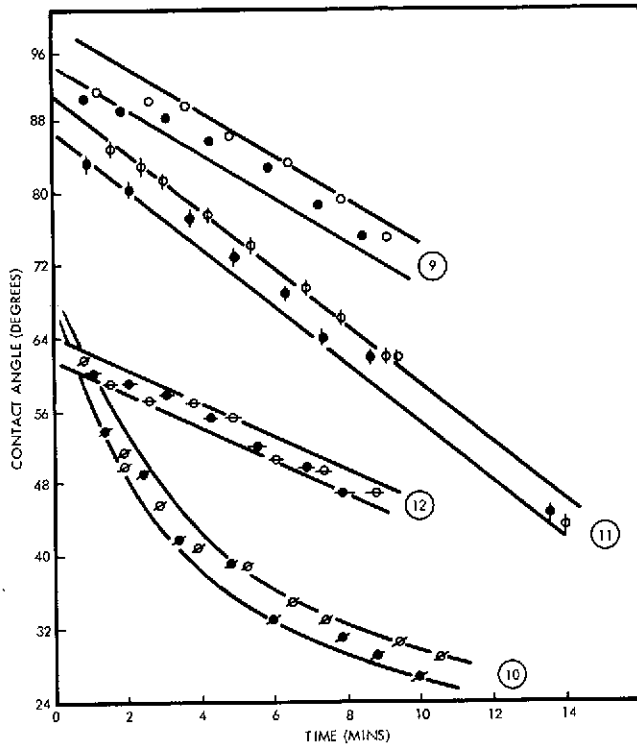


Figure 7-3. Effect of Hydrazine-Water (50/50) Solution on Inconel as Measured Through the Rate of Change of θ_w With Time

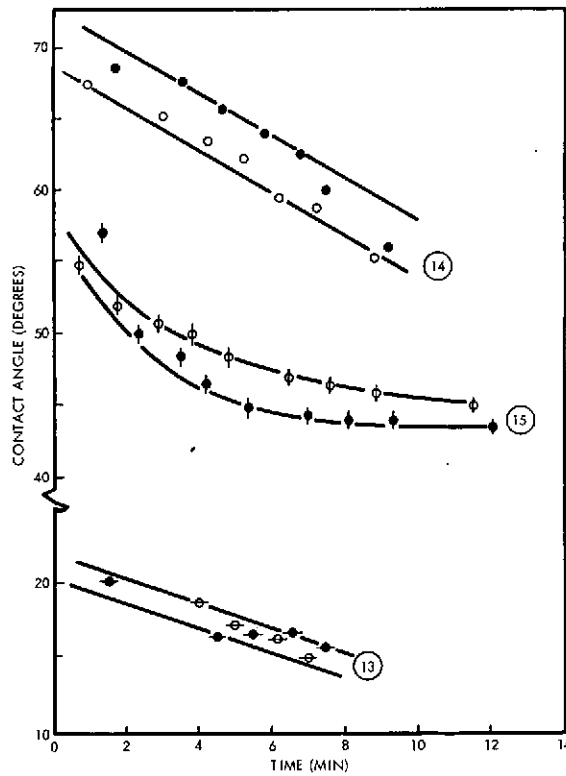


Figure 7-4. Advancing Contact Angles on Inconel and Oil-Covered Inconel Surfaces

C3

7.2.3 Conclusions

These results clearly indicate the potential of contact angle measurements in the measurement of corrosion by reactive fuels. Although the results cannot be considered as quantitative, they can be used to give valuable qualitative results for a variety of surfaces and reacting liquids, and the technique could easily be adapted for use in engineering situations.

7.3 SURFACE ENERGY AND WETTING STUDIES OF SOLIDS

7.3.1 Appraisal of the Relationships Between Surface Energy and the Physical Properties of Materials

One aspect of the work carried out in Bradford has involved an investigation of the surface properties of various solids using contact angle measurements. The work has involved the surfaces of (a) novel thin film polymers prepared by the electron bombardment technique and (b) also bulk polymers (Ref. 5) and bulk metal samples (Ref. 6). In the former work, the critical surface tensions (γ_c) of the materials were obtained using a series of pure liquids and alcohol-water solutions; in the case of the alcohol solutions, the γ_c values were lower than with pure liquids, and this was interpreted (Ref. 5) in terms of the adsorption of the alcohol molecule on the surface. The latter work with metals involved a brief study of the feasibility of using contact angle measurements to study the interaction of clean metals both with the environment and with corrosive materials such as hydrazine; although the technique is very sensitive to surface changes, it was shown that a large number of variables affected the contact angle behavior, and not the least of these was the atmospheric environment of the specimen (Ref. 6).

The surface of a solid material takes part in many processes involving that material, not only in its chemical reactivity but in its mechanical properties. Recently Rabinowicz (Ref. 7) among other authors, has developed empirical theories relating the mechanical interactions with the surface energy of the solids in question. One of the problems in establishing these relationships more fully and making them available for prediction of the mechanical properties of a material lies in the problem of measuring the surface energy. This report therefore presents (a) an outline of

Rabinowicz's theories and (b) discusses the limitations of using contact angle measurements to determine the surface energies of solids.

7.3.1.1 Mechanical Interaction of Solids

Apart from the simple case of non-lubricated adhesion between two solids (Ref. 8), solid-solid interactions are involved in two distinct but related mechanical processes, namely friction and wear; the latter may be subdivided into adhesive wear, abrasive wear, corrosive wear, and surface fatigue wear (Ref. 7).

Friction. The coefficient of friction μ between two bodies is defined by the equation:

$$F = \mu L \quad (7-1)$$

where F is the frictional force and L is the normal force between the two bodies. Generally, the coefficient of friction is independent of the area of contact and of the sliding velocity, although there are many cases where the latter, in particular, does not hold (see Rabinowicz, Ref. 7). However, the real area of contact will depend on the load, the area becoming larger as the load L becomes larger because of the flattening of asperities between the contacting materials. The real area of contact A_r is given by Equation (7-2).

$$A_r = \frac{L}{p} \quad (7-2)$$

where p is the penetration hardness of the material which is related to the ease with which the material is deformed. Also, the fractional force is given approximately by Equation (7-3).

$$F = S \cdot A_r \quad (7-3)$$

where S is the bulk shear strength of the softer of the contacting materials.

Hence, from Equations (7-1), (7-2) and (7-3)

$$\mu = \frac{S}{p} \quad (7-4)$$

The foregoing theory is relatively well established, although there have been some criticisms of it, which are dealt with in some length by Rabinowicz (Ref. 7). The values of μ calculated using Equation (7-4) are sometimes rather low, this ratio generally being of the order of 0.3. Rabinowicz (Ref. 9) has proposed that the equation should be modified by the inclusion of a term for the work of adhesion W and a factor C which depends on surface roughness, etc:

$$\mu = S/p + \frac{C \cdot W_{ab}}{p} \quad (7-5)$$

The value of W_{ab} for two materials a and b is given by Equation (7-5)

$$W_{ab} = \gamma_a + \gamma_b - \gamma_{ab} \quad (7-6)$$

It is with the determination of this term W_{ab} that we are concerned, and we will discuss it more fully below.

It is worth noting that Equation (7-5) gives reasonable agreement between observed and calculated μ values, using a rather empirical method of obtaining W_{ab} , for a series of metals. A similar relationship (Equation 7-7)

$$\mu = S/p \frac{(\gamma_c - 15)}{11} \quad (7-7)$$

has been used by West and Senior (Ref. 10) to explain results obtained by King and Tabor (Ref. 11) for polymer surfaces; here, γ_c is the critical surface tension of the solid.

Wear. Economically, wear is a very important process as it is one of the major ways in which inanimate objects lose their usefulness. The four main types of wear are often difficult to distinguish. They will be described in turn:

- (1) Adhesive wear. Here, fragments of one of two surfaces sliding over one another is transferred to the other; the fragments may subsequently be transferred back to the original surface or may form loose wear particles.
- (2) Abrasive wear. Here, a rough hard surface, sliding over a softer surface, carves grooves in it; the material of the grooves is displaced in the form of wear particles, generally loose ones.
- (3) Corrosive wear. This occurs when sliding takes place in a corrosive atmosphere. Normally, the corrosion products would form a passive layer on the surface of the material in question, but under wear conditions, attack continues. For example, aluminum is passivated by a thin layer of oxide, but under wear conditions in oxygen, the whole sample could become oxidized.
- (4) Surface fatigue wear. Fragmentation of the surface occurs due to repeated sliding over the surface.

Rabinowicz considers each type of wear in turn and discusses methods for their measurement. However, we are here largely concerned with a connection of mechanical processes with surface energy, and we will therefore only summarize some of his conclusions regarding adhesive wear.

7.3.1.2 Quantitative Description of Adhesive Wear

Experimental evidence shows that Equation (7-8)

$$V = \frac{cLx}{p} \quad (7-8)$$

holds for most cases. Here V is the volume of material worn away, L is the load and p the hardness, and x is the distance slid; c is a dimensionless constant, whose value can be predicted theoretically.

Equation (7-8) applies to the case when material is transferred from one surface to the other. The transferred material may leave the second surface if the elastic energy stored in the particle exceeds the adhesive energy which binds it to the surface.

Rabinowicz assumes that the wear particle is approximately hemispherical in shape, having a diameter, d . Hence, the elastic energy, E_e , stored in it is of the form

$$E_e = \left(\frac{\nu^2 \sigma_y^2}{2E} \right) \left(\frac{\pi d^3}{12} \right) \quad (7-9)$$

where ν is Poisson's ratio, σ_y is the normal compressive stress, and E is the Young's modulus of the material. The adhesional energy E_a acting over the interface may be written as in Equation (7-10)

$$E_a = W_{ab} \left(\frac{\pi d^2}{4} \right) \quad (7-10)$$

A particle can come off if $E_e \geq E_a$,

$$\text{or} \quad d \geq \frac{6E W_{ab}}{\nu^2 \sigma_y^2} \quad (7-11)$$

As long as small particles form and subsequently grow until they can leave the surface,

$$d = \frac{6 E W_{ab}}{\nu^2 \sigma_y^2} \quad (7-12)$$

Noting that $\nu^2 \approx 1/10$ for most materials $\sigma_y \approx 1/3p$, and $\sigma_y / E \approx \text{const} \approx 3 \times 10^{-3}$, Rabinowicz (Ref. 4) obtains for the wear particle diameter:

$$d = 60,000 \frac{W_{ab}}{p} \quad (7-13)$$

Hence, as long as W_{ab} and p can be measured, d may be estimated.

Rabinowicz derives a similar equation for the minimum load for loose particle formation:

$$L_{\min} = \pi \times 10^8 \cdot \frac{W_{ab}^2}{p} \quad (7-14)$$

The Term W_{ab} . The work of adhesion is given by Equation (7-6), i.e.,

$$W_{ab} = \gamma_a + \gamma_b - \gamma_{ab}$$

Here, γ_a and γ_b are the surface free energies of materials a and b and γ_{ab} is the interfacial tension of the interface ab. Hence, a determination of W_{ab} requires a knowledge of each of these terms. There is no satisfactory method of measuring γ_a or γ_b . The method frequently used, and adopted by Rabinowicz for metals, involves measuring the surface energy of the melt and assuming that the same value holds for the solid. He justifies this by saying that although the value increases by an amount of the order of 0.5 erg cm^{-2} per degree drop from the melting point, the value is decreased by the presence of surface oxide and contaminant films. The latter effect is reduced somewhat by the film being broken up during sliding, the value of γ tending back to the clean metal value. Rabinowicz assumes that all these changes cancel to give an effective value of γ close to the melt value. The determination of γ_{ab} is even less satisfactory; Rabinowicz cites work by McLean (Ref. 12) which shows that γ_{ab} may be between 1/4 to 1/2 of $(\gamma_a + \gamma_b)$. Although reasonable, the arguments are too empirical.

The Connection Between γ_c and γ_S . For a liquid drop on the surface of a non-deformable solid (Ref. 4 and 5):

$$\gamma_S = \gamma_{LV} \cos \theta + \gamma_{SL} + \pi \quad (7-15)$$

where γ_S is the specific free surface energy of the solid in vacuum, γ_{LV} the surface tension of the liquid against its vapor, γ_{SL} is the specific free surface energy of the solid liquid interface and π , the surface

pressure, is $(\gamma_S - \gamma_{SV})$ where γ_{SV} is the specific free energy of the solid vapor interface. The critical surface tension, γ_C , referred to previously, is the value of γ_{LV} when $\cos \theta = 1$, i.e., when the liquid just spreads over the surface. Hence, from Equation (7-15),

$$\gamma_S = \gamma_C + \gamma_{SL} + \pi \quad (7-16)$$

For low energy surfaces (i.e., $\gamma_C \lesssim 100 \text{ dyne cm}^{-1}$), it is usual to assume that $\pi \approx 0$. We have however been able to show that this is definitely not the case for water butanol mixtures (Ref. 5). Also, γ_{SL} is unlikely to be zero, as there is always some interaction between the solid and the liquid; see, for example, a paper by Owens and Wendt (Ref. 13).

However, assuming that $\pi = 0$, Owens and Wendt (Ref. 13) show that γ_{SL} is small, at least for polymeric surfaces. If this assumption is correct when $\pi = 0$, then

$$\gamma_S \approx \gamma_C + \gamma_{SL} \quad (7-17)$$

Also, for dilute aqueous butanol solutions, π arises almost entirely from the adsorption of water at the solid-vapor interface, and so

$$\pi \approx RT \int_{P=0}^{P_0} \Gamma d \ln P \quad (7-18)$$

which can therefore be evaluated if the water-vapor adsorption isotherm is known. Γ is the Gibbs excess concentration per unit area.

We can thus estimate γ_S for a solid directly from contact angle measurements using aqueous solutions if we are dealing with a case where the solute is not preferentially adsorbed. This is definitely not the case (Ref. 4 and 5) for butanol solutions on polystyrene (PS), polymethylmethacrylate (PMMA), and the thin films prepared by electron bombardment techniques (PPFB) but it may be so for cases where the solute is chosen so that its adsorption would not result in a decrease in the surface energy. This hypothesis has been tested using solutions of ethane-diol on surfaces of PMMA, PS

and Teflon (see 7.3.2). The problem of the π term requires a knowledge of the adsorption at the vapor interface, and this is also receiving attention in our laboratories.

The Term γ_{ab} . The estimation of interfacial tensions between two liquids, a liquid and a solid, or a solid and a solid is one of the outstanding problems in surface chemistry. The magnitude of the interaction depends on the type of forces involved: whether they are purely dispersional, or involve hydrogen bonding and more complex types of interaction. For example, Owens and Wendt (Ref. 12) have extended an equation first used by Fowkes for dispersion interactions between a solid and a liquid:

$$\gamma_{SL} = \gamma_{SV} + \gamma_{LV} - 2\sqrt{\gamma_S^d \cdot \gamma_L^d} \quad (7-19)$$

to include the possibility of hydrogen bonding terms:

$$\gamma_{SL} = \gamma_{SV} + \gamma_{LV} - 2\sqrt{\gamma_S^d \cdot \gamma_L^d} - \sqrt{2 \gamma_S^h \cdot \gamma_L^h} \quad (7-20)$$

The superscripts refer to dispersion contributions (d) from the liquid and the solid and to similar hydrogen bonding contributions (h).

If contact angles are measured for two liquids for which γ_L^d and γ_L^h are known, then Equation (7-16) allows γ_S^d and γ_S^h to be obtained. (This procedure also allows one to estimate γ_{SL} to check whether it is negligible - see above). Having estimated the contribution to the energy of a surface from various types of interaction (metallic interactions might be estimated using mercury drops), it is then possible to use equations similar to Equation (7-20) to estimate γ_{ab} . It should be noted that the geometric mean approach of Equations (7-19) and (7-20) is only approximate, but should prove more satisfactory than the empirical approach of McLean (Ref. 12).

7.3.1.3 The Roughness Factor in Metal to Metal Contacts

As indicated above, current theories of solid-solid interaction imply that the two surfaces are microscopically rough. Several different types of measurement have been used to show this (see Rabinowicz). It has been suggested that the advancing angle on a perfectly smooth surface (θ_r) and that on a rough surface (θ^1) are connected by Equation (7-21), where r is the surface roughness:

$$r = \frac{\cos \theta^1}{\cos \theta_r} \quad (7-21)$$

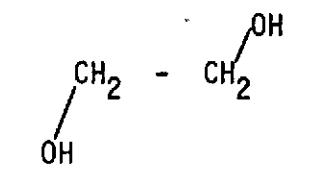
However, the theory on which this equation is based considers π to be zero (Equation 7-15) and so it is not applicable to most cases studied to date. It is possible that the method might be applicable using non-volatile liquids (which do not have an appreciable value of π), and this will be considered at a later date.

7.3.2 Experimental Studies and Some Conclusions

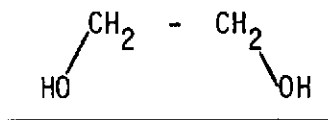
The work described below has been concerned with two separate problems arising from previous work and which both have some bearing on the present objectives.

7.3.2.1 Determination of the True Value of γ_c Using Solutions

The aim of this work is to prove or disprove the hypothesis that adsorption of the solute molecules will only occur at the solid interface if this results in a lowering of γ_c . Adsorption of butanol from aqueous solutions has previously been shown to occur on both PS and PMMA surfaces (see page 7-16); the molecule is thought to adsorb with hydroxyl groups oriented towards the surface (Ref. 4 and 5). It was decided to investigate the use of ethanediol as a solute. If this were to adsorb in the following manner:



γ_c would be about 37 dyne cm^{-1} , whereas if the adsorption occurred as:



γ_c would be about 32 dyne cm^{-1} .

Whether either of these values is obtained will depend on the surface used. If the true value of γ_c is below 32 dyne cm^{-1} ; we expect to obtain the true value from contact angle measurements. On the other hand, if the true value is above 37 dyne cm^{-1} ; we expect to find a value somewhere between 32 and 37 dyne cm^{-1} , depending on the mode of adsorption. We report below results for a variety of different surfaces.

Table 7-3 reports results obtained using PMMA ($\gamma_c = 39 - 41$ dyne cm^{-1}); the disks used were prepared from two different samples of PMMA, one with a low average molecular weight and the other with a high average molecular weight. The experimental data are shown in Figures 7-5 and 7-6. From the values of γ_c obtained of 31 - 34 dyne cm^{-1} , we must conclude that adsorption of the ethanediol is occurring as predicted, and that two-point attachment is favored, presumably as it lowers the surface energy by the greater amount. Values of $\theta_{\text{H}_2\text{O}}$ and $W_{\text{H}_2\text{O}}$ are also given, which allow us to compare our results with literature values. It is seen that the interaction of water with the low molecular weight material is different to that with the high molecular weight sample; this may reflect differences in the preparation technique, and consequent differences in the polymer surface. Also, results obtained with higher solution concentrations deviate from the straight line; this may be due to some ordering in the liquid as the solubility limit is reached.

Figure 7-7 shows results for ethanediol solutions on a PS surface similar to those used previously. γ_c is around 34 dyne cm^{-1} , and is, within experimental error, the same as the value obtained with pure liquids. It should be noted that the deviations observed with PMMA at high ethanediol concentrations (nearing the solubility limit) are also observed here.

Table 7-3. Characterization of PMMA by Aqueous Ethanediol Solutions and Pure Liquids

PMMA Use in Experiment	γ_c (dyne cm^{-1})		$\theta_{\text{H}_2\text{O}}$ (a)	$W_{\text{H}_2\text{O}}$ (b)
	From Aqueous Ethanediol	From Pure Liquids	(degrees)	(dyne cm^{-1})
Low molecular weight (170 u) ^a	34.2	38 - 41	62.5	105.0
High molecular weight. Washed with deionized water and vacuum dried (270 u) ^a	31.0	39 - 41	72.3	93.5
Literature values	-	39.0	75 - 79	90.5 - 85.6

a. PMMA was probably prepared by suspension polymerization. Figure quoted is the average particle diameter.

b. $W_{\text{H}_2\text{O}}$ = work of adhesion between water and PMMA = $\gamma_{\text{H}_2\text{O}} (1 + \cos \theta_{\text{H}_2\text{O}})$

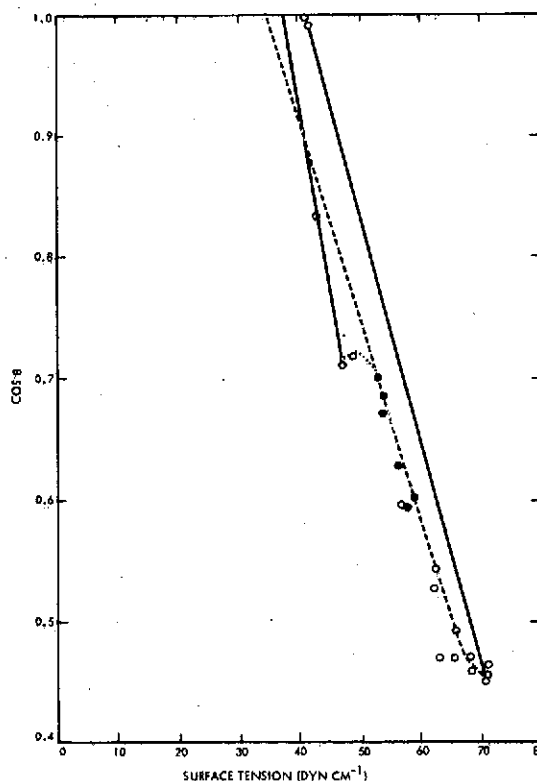


Figure 7-5. Zisman Plots for Aqueous Ethanediol Solutions (Solid Circles) and Various Liquids (Open Circles) on Low Molecular Weight Poly (Methyl Methacrylate)

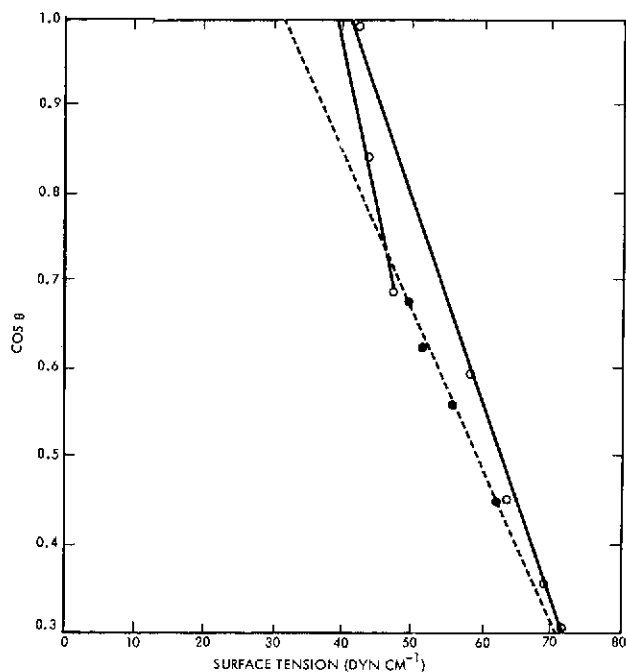


Figure 7-6. Zisman Plots for Aqueous Ethanediol Solutions (Solid Circles) and Various Liquids (Open Circles) on High Molecular Weight Poly (Methyl Methacrylate)

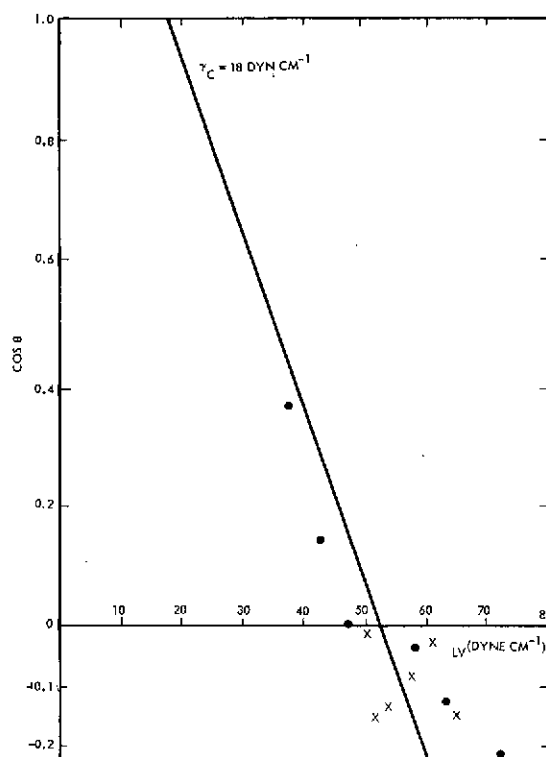


Figure 7-7. Zisman Plot for Aqueous Ethanediol ($\text{OHCH}_2 \cdot \text{CH}_2\text{OH}$) Solution and Liquids on Polystyrene

Figure 7-8 shows preliminary results obtained using Teflon (poly-tetrafluoroethylene). The sample used was not completely flat and so the results were rather erratic; the work is being repeated at present. It is clear from Figure 7-8, however, that the γ_c value obtained with ethanediol solutions is unlikely to be below the value of 18 dyne cm^{-1} obtained with pure liquids and is probably coincident with this value. Hence, it would appear that the hypothesis that adsorption does not occur on the PS and Teflon surfaces is correct, and that the ethanediol solutions can be used to characterize these surfaces. Similarly, it will be possible to use other solute-solvent combinations to characterize higher energy surfaces.

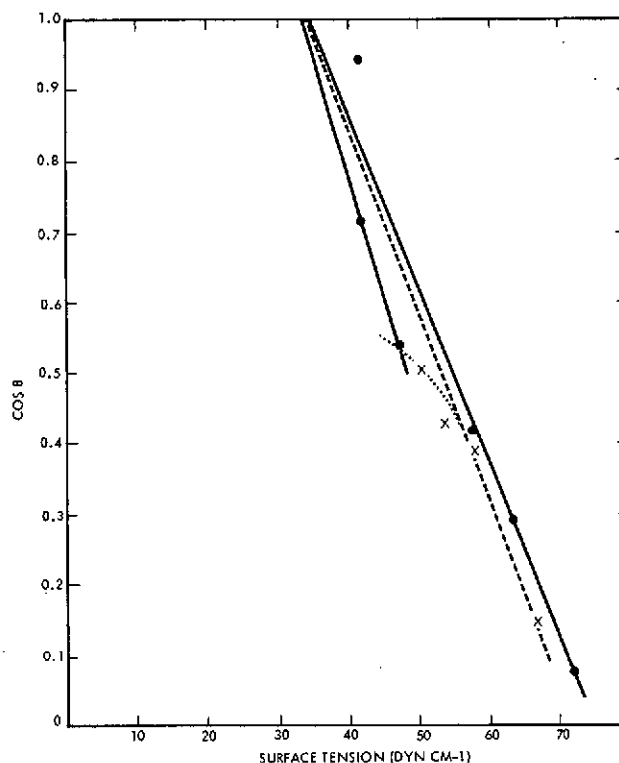


Figure 7-8. Zisman Plot for Aqueous Ethanediol Solutions (X) and Some Pure Liquids (O) on Teflon

7.3.2.2 Determination of the Butanol Adsorption Isotherm for the Solid-Liquid Interface

Results have previously been reported for the adsorption of butanol from aqueous solution at the surfaces of PS and PMMA powders.^{1*} In order to check the repeatability of these results, and to compare these results and the technique used with the results of other workers (Ref. 14), it was decided to repeat the adsorption isotherms using both the GLC analysis technique used earlier¹ and also the technique used by Vincent and Ottewill, namely the differential refractometer. The former technique was used for new samples of PMMA, whereas the latter was used with the samples of PS in previous work.

Table 7-4 gives the results for the adsorption of butanol on the powdered polystyrene; a small number of results were obtained due to limited availability of solid. However, the results showed that the technique was less sensitive than the GLC technique at the low butanol concentrations used, as so the method was abandoned in favor of the latter method. This has been used to check the earlier PMMA results, but will also be used to confirm the PS data.

Table 7-5 and Figure 7-7 show results obtained using the GLC technique for PMMA. Initially, the method used earlier¹ to obtain adsorption data, namely to use a different solid sample for each adsorption measurement was utilized, but this was found to give slightly inconsistent results, presumably due to changes in surface area of solid from sample to sample. A simple cell was therefore constructed to allow measured additions of butanol to be made and samples of the equilibrated solution to be withdrawn. This technique was found to give much more satisfactory results, and some of these are shown in Figure 7-9 and Table 7-5. The results are, in general, in good agreement with those obtained previously; any difference is probably due to slight differences in the methods of sample preparation.

Once these results have been obtained, it is hoped to attempt adsorption studies from the vapor phase; this will enable the π -term, discussed above, to be evaluated, and Equation (7-15) to be verified.

*1. M. W. Roberts, et al, Previous Reports to TRW.

Table 7-4. Adsorption of n-Butanol From Aqueous Solutions on Polystyrene, as Measured Interferometrically

Mol. Fraction Butanol, X_A	Δn	Δn^* (a)	X_A^* (b)	$\frac{n^0 \Delta X_A}{m}$ (c) m.moles g^{-1}
0.0005 ₃	0.000236 ₃	0.000232 ₃	0.00052	1.03×10^{-3}
0.0009 ₆	0.000429 ₃	0.000381 ₈	0.00085	9.70×10^{-3}
0.00132	0.000612 ₇	0.000596 ₉	0.00130	2.02×10^{-3}

(a) Δn^* = Refractive index change after adsorption

(b) X_A^* = Mol. fraction of n-butanol corresponding to Δn^* from calibration.

(c) n^0 = Total number of moles of water and butanol above polymer.

m = Weight of polymer

$$\Delta X_A = X_A - X_A^*$$

7.3.2.3 Conclusions and Suggestions for Further Work

It would appear that in order to examine the importance of surface energy in solid-solid interactions, the determination of the term W_{ab} is of paramount importance. It is therefore recommended to examine the applicability of contact angle and adsorption measurements to determining the values of the various quantities making up W_{ab} for both metal and polymer surfaces. This will entail the use of solutions such as ethanediol/water and other combinations for both contact angle measurements and adsorption measurements. The use of gas-phase adsorption techniques to determine the π -term should be developed.

Table 7-5. Adsorption of n-Butanol From Aqueous Solutions on Poly(Methylmethacrylate) as Measured Using G.L.C.

Mole Fraction X_A	Peak Area, A (arb. units)	Peak Area After ^(b) Adsorption A' (arb. units)	X'_A (c)	$\frac{N_o \cdot \Delta X_A}{m}$ ^(d) m.moles g ⁻¹
0.00045 ^(a)	-	0.014	0.00018	0.055
0.00100 ^(a)	-	0.062	0.00070	0.060
0.00139 ^(a)	-	0.041	0.00048	0.181
0.00148	0.129	0.022	0.00030	0.130
0.00203 ^(a)	-	0.126	0.00138	0.126
0.00249	0.238	0.017	0.00020	0.310
0.00395	0.336	0.115	0.00125	0.310
0.00518	0.528	0.049	0.00060	0.540
0.00683	0.724	0.145	0.00160	0.530

- a. These results were obtained using a different sample from the other results, although all results marked (a) were obtained on the same sample.
- b. A' corresponds to X'_A .
- c. X'_A = mole fraction, as read from calibration curve of A vs. X_A , after adsorption.
- d. See footnote (c), Table 7-4 (except $\Delta X_A = X_A - X'_A$)

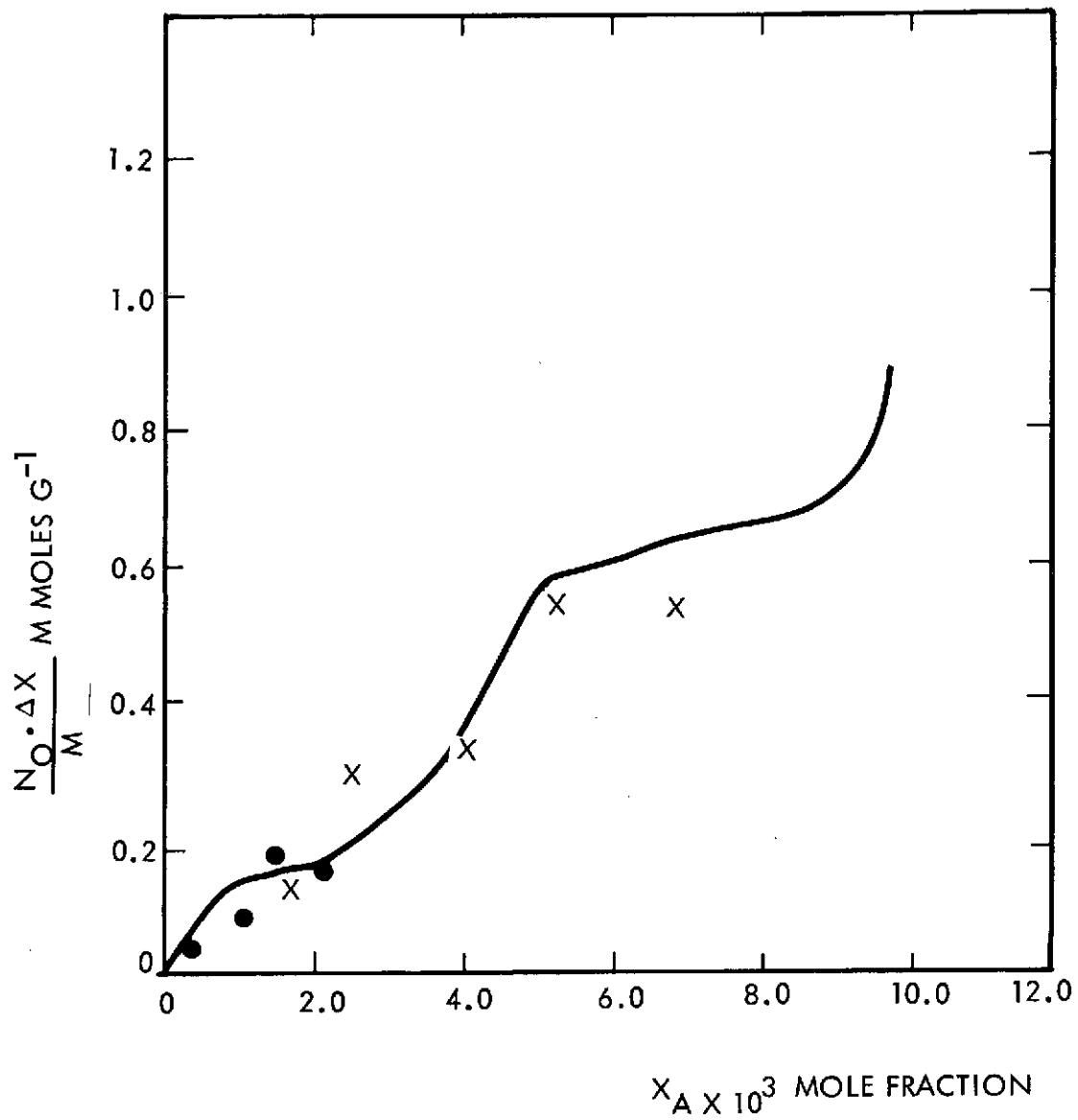


Figure 7-9. Adsorption of n-Butanol on Ball-Milled Poly (Methyl methacrylate). Solid line-data of Murphy⁽¹⁾ O, X - data of Table 7-5.

7.4 AUGER SPECTROSCOPIC STUDY OF THE SURFACES OF INCONEL

7.4.1 Introduction and Experimental

It is essential for any proper understanding of the properties of metal surfaces that they be characterized on the atomic scale. The technique of Auger Electron Spectroscopy is ideally suited for this purpose. In brief, this involves an electron beam of energy ~ 2000 eV impinging on the surface under investigation, which causes the emission of other electrons from the target. The energy of one group of these secondary electrons, the Auger electrons, is characteristic of the energy level of the atom from which they have been ejected. The theory of the method is described in Ref. 15. In the present work, a Vacuum Generators Ltd. (England) Cylindrical Mirror Analyzer Auger Spectrometer was used. The apparatus includes facilities for removing surface layers by bombarding the sample with Argon ions. The inconel sample used was the same as that used for compatibility studies (Section 7.2).

7.4.2 Results and Discussion

Figure 7-10 shows the results of examining the surface without any surface treatment, i.e., "as received". Peaks due to the presence of common surface contaminants such as sulphur, chlorine, carbon, nitrogen (trace) and oxygen were observed. A pair of peaks, attributed tentatively to potassium, were also observed, together with a relatively large group of peaks due to nickel. The nickel may have been introduced during the spotwelding process carried out to mount the sample in the spectrometer.

Figure 7-11 shows a spectrum of the same sample after ion bombardment using Argon ions for 4 hours. The sulphur and chlorine peaks are still evident, but reduced in size, the carbon peak is increased, and a new set of peaks, shown conclusively in Figure 7-12 to be due to chromium, were observed. It would therefore appear that, when the outermost layers are removed, the atoms exposed to the surface are largely carbon and chromium.

It is clear that important information regarding the atomic composition of the surface layers of metals, alloys, etc., is possible which can have an important bearing on the surface behavior. A research program to follow

this up is clearly desirable. The particular question of how important is "surface segregation" needs investigating. Some examples of this are referred to in Reference 15.

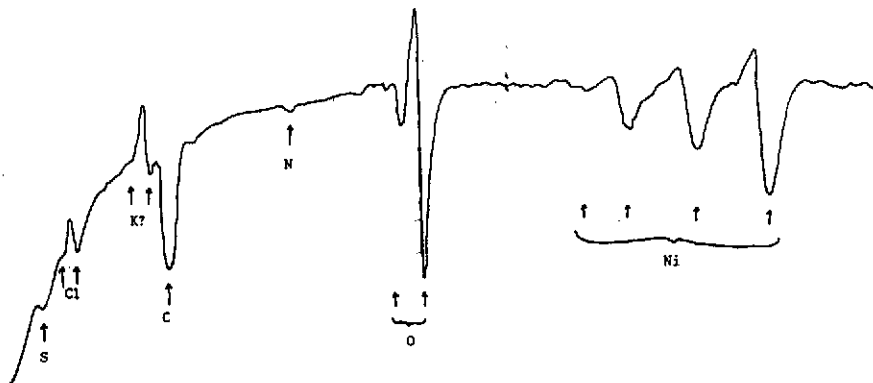


Figure 7-10. Auger Spectrum of "As Received" Inconel Sample (Unpolished Side)

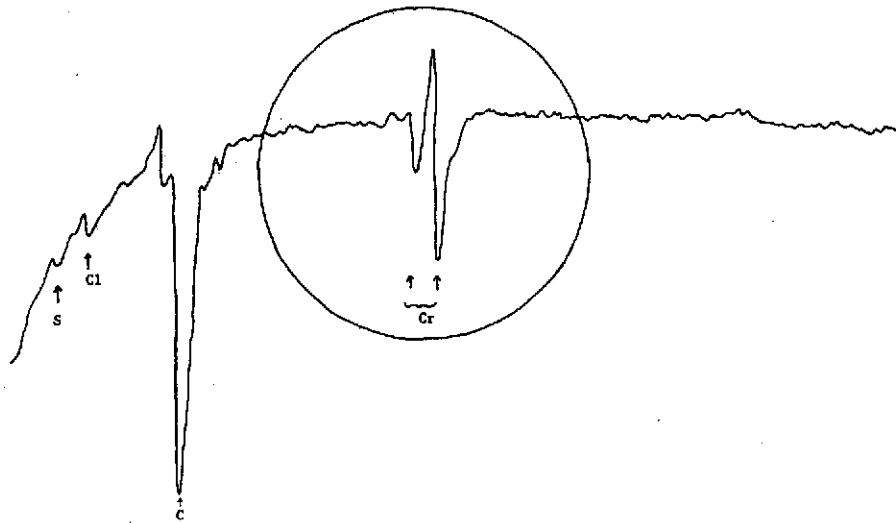


Figure 7-11. Auger Spectrum of the Sample "As Received" (Figure 7-10) After Ion Bombardment for 4 Hours by Ar^+ Ions

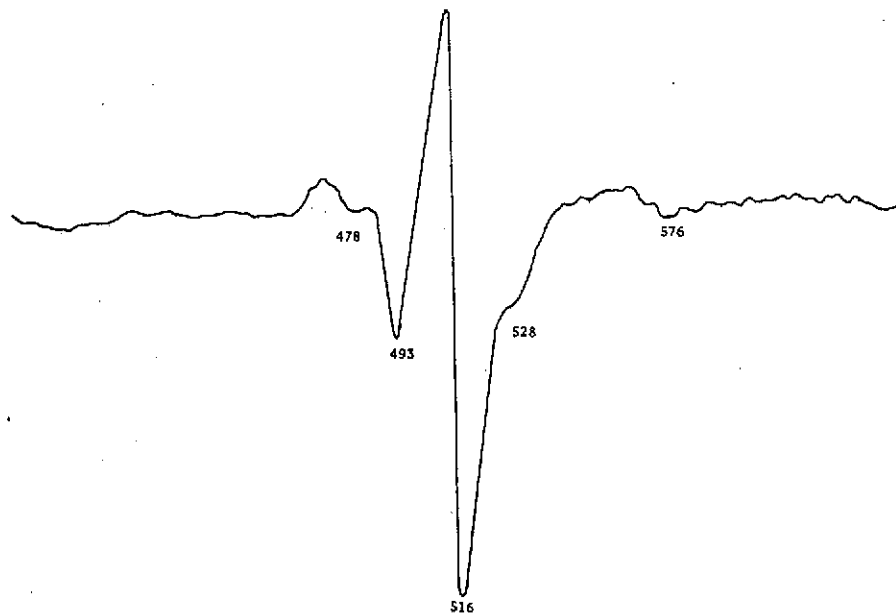


Figure 7-12. Detail of Part of Spectrum of Figure 7-11 Showing Accurate Assignment of the Peaks to Chromium

REFERENCES

1. D. J. Trevoay and H. Johnson, J. Phys. Chem., 62, 883, (1958)
2. E. C. Perryman, Metallurgia, 46, 55, (1952)
3. M. W. Roberts, et al, Final Report to TRW Systems, October 1970
4. Crutchfield, C. A., Muraca, R. F., Whittick, J. S., "The Results of Long-Term Storage Tests for Compatibilities of Spacecraft Materials with Hydrazine and Hydrazine Mixture," Report No. 951581-6, Stanford Research Institute, Menlo Park, Calif. October 1967.
5. W. J. Murphy, M. W. Roberts and J. R. H. Ross, J. Chem. Soc., Faraday Trans I, 68, 1190, (1972).
6. M. W. Roberts, et al, Quarterly report to TRW, January 1972.
7. E. Rabinowicz, Friction and Wear of Materials, Wiley, 1965.
8. K. L. Johnson, et al, Proc. Royal. Soc., A324, 301, (1971).
9. E. Rabinowicz, Metals Engineering Quarterly, 7, 4 (1967).
10. G. H. West and J. M. Senior, Wear, 19, 37 - 52, (1972).
11. R. F. King and D. Taber, Proc. Phys. Soc. (London), B66, 728 (1953).
12. D. McLean, Grain Boundaries in Metals, Clarendon Press, Oxford, (1957).
13. D. K. Owens and R. C. Wendt, J. Appl. Polymer Sci., 13, 1741, (1972).
14. R. H. Ottewill and B. Vincent, J. Chem. Soc. Faraday Trans. I, in press.
15. C. McKee and M. W. Roberts, Chemistry in Britain.

8.0 NEW TECHNOLOGY

New technology developed under this contract is reported in the following subsections:

8.1 ZERO LEAKAGE METAL VALVE SEAT FOR LONG TERM PERFORMANCE. SECTION 2.0

The design of the metal valve seat is shown in Figure 2-8, page 2-19. The metal seat is designed to avoid failure by wear, stresses, fatigue and contamination. The effects of wear on the surface roughness is avoided by refurbishing the seat during each cycle. Leakage was held to less than 10^{-8} scc/sec He for more than 30,000 cycles.

8.2 MEASURING SURFACE AND INTERFACE TOPOLOGY BY THERMAL CONTACT RESISTANCE. SECTION 4.0

Surface degradation is measured by monitoring the thermal resistance and/or the thermal time constant across an interface. Figure 4-9, page 4-37 is a schematic of the system illustrating the measurement technique. Two matched thermal sensors, each bonded across a valve poppet/seat interface are connected in a circuit designed to measure parameters such as load, surface roughness, corrosion, valve leakage, etc., as a function of time.

8.3 OPTICAL SIGNATURE OF METAL VALVE SEAT SURFACES. SECTION 5.0

The application of a HeNe Laser to a metal valve seat surface proved a new technique in characterizing valve seat surfaces finished to 2 rms or better. The diffraction pattern of the seat surface is electronically sensed and recorded on an x-y plotter.

8.4 FLOW TRANSIENT SIGNATURE TECHNIQUE. SECTION 6.0

The design of the flow transient signature test setup is illustrated in Figure 6-1, page 6-2. A liquid slug (piston) entrained in the fluid flowing in a transparent tube is tracked by an electro-optical strain monitor. During valve opening the liquid slug moves along the inlet tube and its motion (position) is converted to an electrical output. The electrical output can be recorded on an oscillograph. Also the slug can be tracked upon valve closing. The signature is a precise characteristic measurement of the transient performance of the valve.

8.5 FLUID LEAKAGE MEASUREMENT. SECTION 6.0

The same technique used in the Flow Transient Measurements using the electro-optical strain monitor can be used to measure leakages with a sensitivity better than 10^{-6} scc/sec of any fluid. See pages 6-22 and 6-23.

DISTRIBUTION LIST FOR FINAL REPORT

CONTRACT NAS 7-782

COPIES

RECIPIENT

4	Jet Propulsion Laboratory 4800 Oak Grove Drive Pasadena, California 91103 G. A. Yankura
1	NASA Ames Research Center Moffett Field, California 94035 Patents and Contracts Management
1	NASA Ames Research Center Moffett Field, California 94035 Mission Analysis Division
1	NASA Headquarters Washington, D. C. 20546 Contracting Officer
1	Patent Office
3	Office of Advanced Research and Technology NASA Headquarters Washington, D. C. 20546 Manager, Liquid Rocket Propulsion Tech., Code RPT
3	Manager, Space Storable Propulsion Tech., Code RPI
1	Office of Manned Space Flight NASA Headquarters Washington, D. C. 20546 Director, Advanced Manned Missions, MT
1	Office of Technology Utilization NASA Headquarters Washington, D. C. 20546 Director, Technology Utilization Division
1	Office of Space Science and Applications NASA Headquarters Washington, D. C. 20546 Director, Launch Vehicles and Propulsion, SV
1	NASA Lewis Research Center 21000 Brookpark Road Cleveland, Ohio 44135 Office of Technical Information

COPIESRECIPIENT

1 NASA Manned Spacecraft Center
Houston, Texas 77058
Office of Technical Information

2 NASA Marshall Space Flight Center
Huntsville, Alabama 35812
Office of Technical Information, MS-1P

1 Technical Library

1 Dale Burrows S&E-ASTN-PJ

25 NASA Scientific and Technical Information Center
P.O. Box 33
College Park, Maryland 20740

NASA FIELD CENTERS

2 Ames Research Center Hans M. Mark
Moffett Field, California 94035

1 Goddard Space Flight Center Merland L. Moseson
Greenbelt, Maryland 20771 Code 620

2 Jet Propulsion Laboratory Library
California Institute of Technology
4800 Oak Grove Drive
Pasadena, California 91103

2 John F. Kennedy Space Center, NASA Dr. Kurt H. Debus
Cocoa Beach, Florida 32931

2 Johnson Space Center J. G. Thibodaux, Jr.
Houston, Texas 77058 H. Pohl

2 Langley Research Center Ed Cortright
Langley Station
Hampton, Virginia 23365

2 Lewis Research Center B. T. Lundin
21000 Brookpark Road
Cleveland, Ohio 44135

2 Marshall Space Flight Center Hans G. Paul
Huntsville, Alabama 35812 Code R-P&VED

GOVERNMENT INSTALLATIONS

<u>COPIES</u>	<u>RECIPIENT</u>	
1	Aeronautical Systems Division Air Force Systems Command Wright-Patterson Air Force Base Dayton, Ohio 45433	D. L. Schmidt Code ASRCNC-2
1	Arnold Engineering Development Center Arnold Air Force Station Tullahoma, Tennessee 37388	Dr. H. K. Doetsch
2	Air Force Rocket Propulsion Laboratory Research and Technology Division Air Force Systems Command Edwards, California 93523	RPRPD/Mr. H. Main
1	Air Force Missile Test Center Holloman Air Force Base, New Mexico 45433	Library
1	Air Force Missile Test Center Patrick Air Force Base, Florida	L J. Ullian
1	Defense Documentation Center Headquarters Cameron Station, Building 5 5010 Duke Street Alexandria, Virginia 22314 Attn: TISIA	
1	Bureau of Naval Weapons Department of the Navy Washington, D. C. 20546	J. Kay RTMS-41
1	Picatinny Arsenal Dover, New Jersey 07801	I. Forsten Liquid Propulsion Lab.
1	Space and Missile Systems Organization Air Force Unit Post Office Los Angeles 45, California 90045	Col. Clark Technical Data Ctr.
1	Headquarters, U. S. Air Force Washington, 25, D. C. 20546	Col. C. K. Stambaugh AFRST
1	U. S. Army Missile Command Redstone Arsenal Alabama 35809	Mr. Walter Wharton
1	U. S. Naval Ordnance Test Station China Lake California 93557	Code 4562 Chief, Missile Propulsion Div.

CPIA

COPIES

RECIPIENT

1	Chemical Propulsion Information Agency Applied Physics Laboratory 8621 Georgia Avenue Silver Spring, Maryland 20910	Tom Reedy
---	--	-----------

INDUSTRY CONTRACTORS

1	Aerojet-General Corporation P. O. Box 296 Azusa, California 91703	W. L. Rogers
1	Aerojet-General Corporation P. O. Box 1947 Technical Library, Bldg. 2015, Dept. 2410 Sacramento, California 95809	R. Stiff
1	Aerospace Corporation 2400 East El Segundo Boulevard P.O. Box 95085 Los Angeles, California 90045	John G. Wilder MS-2293
1	AVCO Systems Division Wilmington, Massachusetts	Howard B. Winkler
1	Battelle 505 King Avenue Columbus, Ohio 43201	Reports Library (HAMI)
1	Beech Aircraft Corporation Boulder Division Box 631 Boulder, Colorado	J. H. Rodgers
1	Bell Aerosystems Company P.O. Box 1 Buffalo, New York 14240	W. M. Smith Leo M. Thompson
1	Bellcomm 955 L-Enfant Plaza, S. W. Washington, D. C.	H. S. London
1	Bendix Systems Division Bendix Corporation 3300 Plymouth Road Ann Arbor, Michigan 48105	John M. Brueger

COPIESRECIPIENT

1	Boeing Company P. O. Box 3999 Seattle, Washington 98124	R. Green MS 8C-76
1	Boeing Company P. O. Box 1680 Huntsville, Alabama 35801	Ted Snow
1	Missile Division Chrysler Corporation P. O. Box 2628 Detroit, Michigan 48231	Mr. John Gates
1	Wright Aeronautical Division Curtiss-Wright Corporation Wood-Ridge, New Jersey 07075	G. Kelley
1	Research Center Fairchild Hiller Corporation Germantown, Maryland	Ralph Hall
1	Republic Aviation Corporation Fairchild Hiller Corporation Farmingdale Long Island, New York	Library
1	General Dynamics, Convair Division P. O. Box 1128 San Diego, California	Library
1	Missile and Space Systems Center General Electric Company Valley Forge Space Technology Center P. O. Box 8555 Philadelphia, Pa.	F. Mezger F. E. Schultz
1	Grumman Aircraft Engineering Corp. Bethpage, Long Island New York 11714	Joseph Gavin
1	Honeywell, Inc. Aerospace Division 2600 Ridgway Road Minneapolis, Minn.	Mr. Gordon Harms
1	Hughes Aircraft Co. Aerospace Group Centinela and Teale Streets Culver City, California 90230	E. H. Meier

COPIESRECIPIENT

1	Reliability Analysis Center ITT Research Institute 10 West 35th Street Chicago, Illinois 60616	H. A. Lauffenburger
1	Walter Kidde and Company, Inc. Aerospace Operations 567 Main Street Belleville, New Jersey	R. J. Hanville
1	Ling-Temco-Vought Corporation P. O. Box 5907 Dallas, Texas 75222	Library
1	Arthur D. Little, Inc. 20 Acorn Park Cambridge, Massachusetts 02140	Library
1	Lockheed Missiles and Space Co. Attn: Technical Information Center P. O. Box 504 Sunnyvale, California 94088	J. Guill
1	Lockheed Propulsion Company P. O. Box 111 Redlands, California 92374	Library
1	The Marquardt Corporation 16555 Saticoy Street Van Nuys, California 91409	Library Horst Wichman
1	Baltimore Division Martin Marietta Corporation Baltimore, Maryland 21203	Mr. John Calathes (3214)
1	Denver Division Martin Marietta Corporation P. O. Box 179 Denver, Colorado 80201	Dr. Morgenthaler A. J. Kullas G. Skartvedt
1	Orlando Division Martin Marietta Corporation Box 5837 Orlando, Florida	J. Ferm
1	McDonnell-Douglas Astronautics 5301 Bolsa Avenue Huntington Beach, California 92647	J. L. Waisman Dr. D. English

COPIESRECIPIENT

1	McDonnell-Douglas Corporation P. O. Box 516 Municipal Airport St. Louis, Missouri 63166	R. A. Herzmark
1	Aeronutronic Division Philco Ford Corp. Ford Road Newport Beach, California 92663	Library
1	Astro-Electronics Division Radio Corporation of America Princeton, New Jersey 08540	Y. Brill
1	Rocket Research York Center Redmond, Washington 98052	F. McCullough, Jr.
1	Space & Information Systems Division Rockwell International 12214 Lakewood Boulevard Downey, California 90241	Library
1	Rocketdyne Division (Library 586-306) Rockwell International 6633 Canoga Avenue Canoga Park, California 91304	Dr. R. J. Thompson
1	Scientific Service Bureau, Inc. P. O. Box 375 Morrisplains, New Jersey 07950	T. F. Seamans
1	Stanford Research Institute 333 Ravenswood Avenue Menlow Park, California 94025	Dr. Gerald Marksman
1	Sundstrand Aviation 2421 11th Street Rockford, Illinois 61101	R. W. Reynolds
1	Thiokol Chemical Corp. Aerospace Services Elkton Division Bristol, Pennsylvania	Library
1	Thiokol Chemical Corporation Huntsville Division Huntsville, Alabama 35807	John Goodloe

COPIESRECIPIENT

1	TRW Systems Group TRW Incorporated One Space Park Redondo Beach, California 90278	G. W. Eilverum
1	Tapco Division 23555 Euclid Avenue Cleveland, Ohio 44117	P. T. Angell
1	Florida Research and Development Pratt and Whitney Aircraft United Aircraft Corporation P. O. Box 2691 West Palm Beach, Florida 33402	R. J. Coar
1	Research Laboratories United Aircraft Corporation 400 Main Street East Hartford, Connecticut 06108	Erle Martin Dr. C. Brown
1	United Technology Center 587 Methilda Avenue P. O. Box 358 Sunnyvale, California 94088	Dr. David Altman
1	Vickers, Inc. Box 302 Troy, Michigan	Library